

Magnetite Nanotubes and Nickel Nanorods of Low Aspect Ratios: From Synthesis to Application in Ferrofluidic Suspensions

Dissertation
zur Erlangung des Doktorgrades
an der Fakultät MIN
Fachbereich Physik
der Universität Hamburg

vorgelegt von
Robert Zierold

Hamburg, 2013

Gutachter der Dissertation:

Prof. Dr. K. Nielsch
Prof. Dr. A. Hütten
Prof. Dr. B. J. H. Stadler

Gutachter der Disputation:

Prof. Dr. K. Nielsch
Prof. Dr. H. P. Oepen

Datum der Disputation:

10.07.2013

Vorsitzender des Prüfungsausschusses:

Prof. Dr. M. A. Rübhausen

Vorsitzender des Promotionsausschusses:

Prof. Dr. P. H. Hauschildt

Dekan der MIN-Fakultät:

Prof. Dr. H. Graener

Abstract

Magnetic nanoparticles which are suspended in a carrier medium can be utilized to influence the viscosity of the liquid suspension by an applied magnetic field. Such liquid suspensions are called magnetic fluids and usually consist of spherical particles.

In this thesis, elongated magnetite nanotubes and nickel nanorods with aspect ratios below ten are synthesized by two different template-based preparation routes. First, atomic layer deposition of iron oxide is combined with geometrically tunable porous alumina templates. The iron oxide deposition process, the subsequent reduction process as well as the structural and magnetic properties of thin films and magnetite nanotubes are studied. Second, nickel/copper multilayered electrodeposition in a porous template allows for the synthesis of long, multisegmented nanowires. A selective wet-chemical etching of the sacrificial copper phase results in short nickel nanorods.

For reference, the magnetic field- and shear frequency-dependent (magneto)viscosity of a commercial ferrofluidic suspension based on spherical cobalt ferrite particles is studied. Comparative measurements of the viscoelastic properties of nickel nanorod and iron oxide nanotube suspensions, in terms of the magnetoviscous effect, the shear thinning, and the shear moduli are presented and discussed. Based on these results, the differences in the magnetic field- and in the shear frequency-dependent viscoelastic behavior of spherical and elongated particle suspension are clearly derived.

Finally, hybrid suspensions are introduced which consist of spherical nanoparticles and a small amount (in the ppm range) of inorganic, elongated additive particles, namely nickel nanorods and superparamagnetic iron oxide nanotubes. The hybrid suspensions reveal an increase in the response behavior of their magnetoviscous effect compared to the pure liquid suspensions. Moreover, a concentration-, magnetic field-, and shear frequency-dependent sol-gel transition is found in such hybrid ferrofluids. Clustering around the elongated objects is derived as reason for the observed enhancement in the magnetoviscous properties of the inorganic hybrid suspensions.

Kurzfassung

Magnetische Nanopartikel, die in einer Trägerlösung suspendiert sind, können dazu verwendet werden, die Viskosität der Suspension durch ein angelegtes Magnetfeld zu beeinflussen. Solche Suspensionen werden im Allgemeinen magnetische Flüssigkeiten genannt und bestehen üblicherweise aus runden Partikeln.

In dieser Doktorarbeit sollen längliche Magnetit-Nanoröhren und Nickel-Nanostäbchen (mit Aspektverhältnissen kleiner als zehn) auf zwei unterschiedlichen Syntheserouten, unter Verwendung von maßgeschneidertem, nanoporösem Aluminiumoxid als Maske, hergestellt werden. Im ersten Fall wird die Atomlagenabscheidung von Eisenoxid dazu verwendet, die Porenwände zu beschichten und auf diesem Weg Eisenoxide-Nanoröhrchen herzustellen. Der Eisenoxid-Abscheidungsprozess, die anschließende Reduktion sowie die strukturellen und magnetischen Eigenschaften von dünnen Magnetit-Schichten und Magnetit-Nanoröhren werden untersucht. Weiterhin erlaubt die elektrochemische Abscheidung von Nickel/Kupfer-Multischichten in einer porösen Membran die Synthese von langen, segmentierten Nanodrähten. In einem selektiven, nasschemischen Ätzprozess wird die Kupfer-Opferschicht entfernt und es verbleiben kurze, magnetische Nanostäbchen.

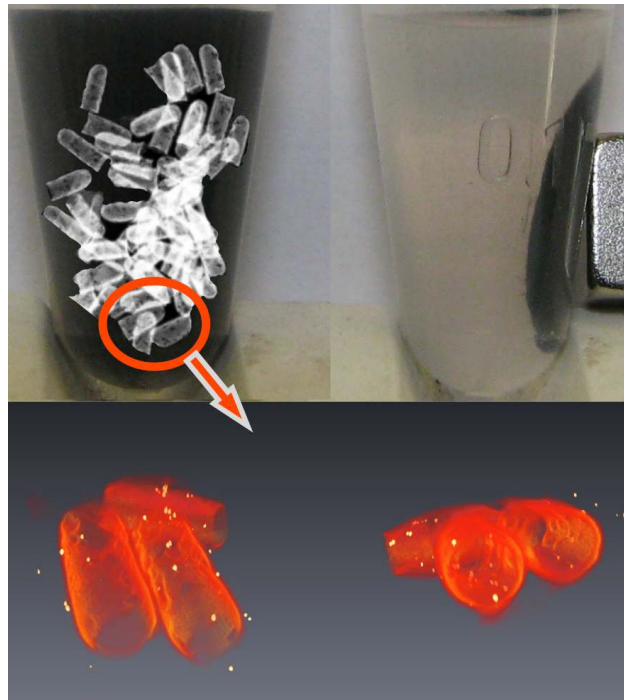
Als Vergleichsprobe wird die magnetfeld- und scherfrequenzabhängige Magnetoviskosität eines kommerziellen Ferrofluides (basierend auf sphärischen Kobaltferritpartikeln) experimentell bestimmt. Im Anschluss werden Messungen der viskoelastischen Eigenschaften von Suspensionen, basierend Nickel-Nanostäbchen und Eisenoxid-Nanoröhren, im Hinblick auf den magnetoviskosen Effekt, das scherverdünnende Verhalten sowie die Schermodule vorgestellt und diskutiert. Aufbauend auf diesen Ergebnissen werden die Unterschiede der magnetfeld- und der scherfrequenzabhängigen viskoelastischen Eigenschaften von kugelförmigen und länglichen magnetischen Partikeln in einer Trägerlösung herausgearbeitet.

Weiterhin werden hybride Suspensionen eingeführt, die hauptsächlich aus sphärischen Nanopartikeln und einer sehr geringen Menge (im ppm-Bereich) von anorganischen, länglichen Nanoobjekten, im Detail Nickel-Nanostäbchen und superparamagnetische Eisenoxid-Nanoröhren, bestehen. Diese hybriden Ferrofluide zeigen eine signifikante Vergrößerung des magnetoviskosen Effektes im Vergleich zu den reinen (ursprünglichen) Suspensionen. Darüber hinaus kann ein konzentrations-, magnetfeld-, und scherfrequenzabhängiger Sol-Gel-Übergang in solch hybriden, magnetischen Flüssigkeiten gefunden werden. Der Grund für die beobachtete Verbesserung der Magnetoviskosität in den anorganischen Hybrid-Suspensionen ist Agglomeration und Bindung der runden Nanopartikel um bzw. an die länglichen Objekte.

Contents

1	Motivation & Scope of the Work	1
2	Introduction & Background	5
2.1	Magnetism	5
2.2	Rheology	16
2.3	Magnetic Fluids	20
3	Templated Synthesis & Structural Investigation	33
3.1	Template Preparation & Two-Dimensional Scale-Up	34
3.2	Atomic Layer Deposition: From Thin Films To Nanotubes	36
3.3	Magnetic Properties of Iron Oxide Thin Films	49
3.4	Iron Oxide Nanotubes by Atomic Layer Deposition	61
3.5	Three-Dimensional Scale-Up: Synthesis of Nickel Nanorods	72
4	Magnetic and Magnetorheological Properties of Liquid Suspensions	81
4.1	Piezo-Membrane Axial Vibrator	81
4.2	Reference Ferrofluid Based on Spherical Nanoparticles	83
4.3	Elongated Nanoparticle Liquid Suspensions	90
4.4	Shear Thinning in Ferrofluidic Suspensions	99
4.5	Shear Moduli of Ferrofluids	106
4.6	Magnetorheological Properties of Ferrofluids: A Wrap-Up	109
5	Hybrid Magnetic Fluids	111
5.1	Nickel Nanorods as Additive	111
5.2	Superparamagnetic Iron Oxide Nanotubes as Additive	121
5.3	A Hypothesis for the Enhanced MVE in Hybrid Suspensions	123
6	Summary and Outlook	127
	Bibliography	131
A	Appendix	155
A.1	Templated Synthesis & Structural Investigation	155
A.2	Physical Properties of Particles and Ferrofluids	163

1 Motivation & Scope of the Work



The magnetism of solid materials consciously touches our daily life in terms of fridge magnets, door magnets or in school on white/black boards. More hidden, but also in permanent daily use, is the magnetism in a hard disk drive of a computer. The list of everyday magnetic applications is almost infinitely long: audio loud speakers, microwaves, magnetic stripe cards, (electro)magnetic motors and sensors, just to name a few. The commonality of all these examples is the manifestation of (permanent) magnetism in solid state. A plethora of devices is conceivable based on the magnetic properties of materials which can be influenced by and utilized with external magnetic fields.

The magnetism in liquids, however, was veiled for a long time and has only been observed in extraordinary fluids such as superfluidic helium-3 or under-cooled transition metal melts.[Leg77] [Pau78] [Wil96] Applying a magnetic field would affect the properties of such magnetic liquids. One property of a fluid is its *viscosity*. Influencing the viscosity by an external magnetic field would expand the range of applications in our daily life. However, practical applications of under-cooled melts

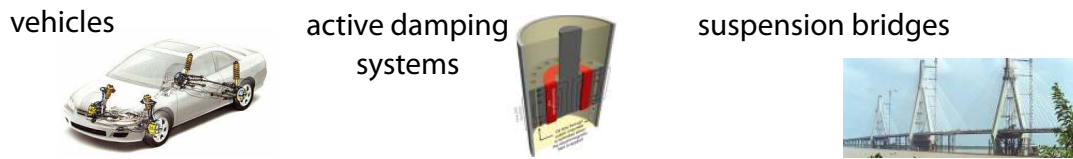


Figure 1.1: Application of magnetic fluids utilizing the magnetic field dependence of their viscosity. Pictures are taken from [Aer13] and [Lon13]. The photograph displays the Dong Ting Lake Bridge in China.

or superfluidic helium are not feasible today due to the extremely complex handling of those, and alternatives have to be found to influence the viscosity of a liquid by an external magnetic field. Suspending solid magnetic particles—with a size range from a few nanometers up to several microns—into a carrier liquid transfers the microscopic magnetic field-dependent solid particle properties to the macroscopic fluid-mechanical behavior of the fluid. In detail, the viscosity of the liquid suspensions can be tuned by the strength of the externally applied magnetic field. Such liquid suspensions are called *magnetic fluids* and are nowadays used in damping systems as displayed in figure 1.1. Other applications of magnetic nanoparticle suspensions are cooling liquids, in medical drug delivery, or as magnetic resonance imaging contrast agent, depending on the size of the particles as well as other properties and specifications, e.g. material, magnetic moment, toxicity, stability, to name a few.[Ber96] However, the shape of the particles is almost always limited to being spherical. Only few reports can be found in the literature applying elongated particles in magnetic fluids: either the yield of the manufacturing process is not sufficient, or the shape control in the synthesis is deficient because of the high sensitivity to the growth conditions.

In this thesis, two different template-based (scaled-up) preparation approaches are presented, which allow for the synthesis of elongated magnetic nanoparticle ferrofluids consisting either of low-aspect ratio iron oxide nanotubes (section 3.4) or short nickel nanorods (section 3.5). *Atomic layer deposition* and a subsequent *thermal reduction* process allow for the synthesis of high-quality *magnetite* thin films and nanotubes. First principle studies of the magnetic properties of the such prepared iron oxide thin films are presented (section 3.3). Subsequently, the synthesis and the characterization of iron oxide nanotubes are presented in detail. The nickel nanorods suspensions are synthesized by electrodeposition in a *porous alumina membrane* utilizing the thickness of the membrane—the third dimension—to drastically the nanorod yield. *Multisegmented* nanowires with a length of several microns serve as precursor for short nanorods. Suspending iron oxide nanotubes or nickel nanorods in a carrier liquid results in a *ferrofluid* consisting of elongated particles. Shear frequency- and magnetic field-dependent viscosity measurements of these elongated particle suspensions are compared with measurement results of a commercially available reference magnetic fluid consisting of spherical particles (chapter 4).

Undeniable differences in terms of *magnetoviscous* properties are observed and discussed. Finally, *hybrid* magnetic fluids are prepared by mixing elongated objects into a commercial ferrofluid fluid based on spherical nanoparticles (chapter 5). These bimodal liquid suspensions are characterized with respect to their response onto an applied magnetic field and as a function of the shear frequency. An exceptional magnetoviscous response is accompanied by a transition from a *sol-like* state to a *gel-like* behavior of the hybrid suspension already in moderate magnetic fields.

This thesis reveals the potential of elongated nanoparticles in the field of magnetic fluids either as pure liquid suspension or as additive in commercially available magnetic fluids. The synthesis routes and measurement results presented in this work encourage investigation of elongated particle ferrofluids and might pave the way for novel applications in our daily life.

2 Introduction & Background

This chapter is thought to give a sufficient introduction and background to the physics needed to follow through the thesis. The chapter consists of three parts: first, a short general introduction to magnetism is given, followed by a second section about the basics of rheology. Third, *magnetic fluids* are introduced and a state of the art literature survey is presented dealing with *ferrofluids*, *magnetorheological fluids* and *magnetic hybrid suspensions*. Standard textbooks and further overview literature, e.g. review articles, are cited in particular since only a selected fraction of the three research fields will be addressed herein.

2.1 Magnetism

Herein, the focus is on the theory of magnetism needed to describe and to discuss the observed phenomena of this thesis. For a general introduction to the topic of magnetism, reference is made to standard magnetism textbooks, e.g. [Jil91], [Aha96], [Cul09] or [Spa10], to name a few. This section closes with a brief summary of the magnetic materials that this work is built upon. The CGS unit system is still the primarily used system in the field of magnetism, whereas the SI units have been prevailed in the research field of rheology. This thesis sticks to these conventions. The introduction to magnetism as well as the magnetic characterization of samples is given with respect to the CGS unit system, whereas the magnetic field-dependent rheology studies are presented in SI units without any further notice.

2.1.1 Introduction to Magnetism

A material with magnetization \vec{M} responds to an externally applied magnetic field strength \vec{H} with the magnetic induction \vec{B} .

$$\vec{B} = \vec{H} + 4\pi\vec{M} \quad (2.1)$$

The magnetization is a property of the material and is defined as the sum of the magnetic moments \vec{m} per volume V of the material.

$$\vec{M} = \frac{\sum \vec{m}}{V} \quad (2.2)$$

The energy of a magnetic dipole with the moment \vec{m} in an external magnetic field in free space amounts to

$$E = -\vec{m} \cdot \vec{H}. \quad (2.3)$$

A ferromagnetic material shows a spontaneous magnetization below the Curie temperature, and its magnetization can be saturated to the value M_s at sufficiently high fields. At this stage, all individual magnetic moments point parallel to the externally applied magnetic field.

$$M_s = \frac{\sum |\vec{m}|}{V} \quad (2.4)$$

The total energy E_t of a ferromagnet, as discussed here, is the sum of four main contributions: the exchange energy E_x , the Zeeman energy E_z , the demagnetization energy E_d related to the ‘shape anisotropy’, and the magnetocrystalline anisotropy energy E_a . Contributions of the magnetoelastic anisotropy—some directions of the magnetization are preferred due to internal strain—are neglected herein. Minimization of the total energy results in the micromagnetic structure of the ferromagnetic sample.

$$E_t = E_x + E_z + E_d + E_a \quad (2.5)$$

In the following paragraphs, the individual energy contributions will be briefly introduced and discussed.

Exchange Energy

The exchange energy E_x is the driving force for the spontaneous ordering of the magnetic moments in a ferromagnet. The energy amounts to

$$E_x = -2J_{12}\vec{S}_1 \cdot \vec{S}_2 \quad (2.6)$$

in the Heisenberg model for the simplest case of two spins \vec{S}_1 and \vec{S}_2 located at neighboring atoms. J_{12} denotes the exchange integral, also called exchange constant, of the two electron wave functions: $J_{12} > 0$ and $J_{12} < 0$ correspond to a parallel and antiparallel alignment of the spins, respectively. The magnetic moment of a spin is

$$\vec{m} = g\mu_B\vec{S} \quad (2.7)$$

with the Landé factor g and the Bohr magneton μ_B . In a solid material with a huge number of atoms the exchange energy can be written as

$$E_x = A \int \left(\nabla \frac{\vec{M}}{M_s} \right)^2 dV. \quad (2.8)$$

A denotes the exchange stiffness constant which is related to the exchange constant and depends on the material as well as on the temperature.

Zeeman Energy

The Zeeman energy E_z describes the interaction of the magnetization with an externally applied magnetic field. Derived from the energy of a magnetic dipole in a magnetic field, the energy amounts to

$$E_z = - \int \vec{M} \cdot \vec{H} \, dV \quad (2.9)$$

and is minimized for $\vec{M} \parallel \vec{H}$. Thus, a parallel alignment of the magnetization to the applied magnetic field is energetically favorable.

Demagnetization Energy

A sample is magnetized in an external magnetic field. Since the magnetic field lines are directed from the north to the south pole by definition, an internal magnetic field is created which is opposed to the externally applied magnetic field. This internal field is called demagnetizing field \vec{H}_d . The origin is the gradient of the magnetization of the sample because magnetic monopoles do not exist ($\nabla \cdot \vec{B} = 0$).

$$\nabla \cdot \vec{H}_d = -4\pi \nabla \cdot \vec{M} \quad (2.10)$$

The demagnetization energy describes the energy of the magnetization in such a demagnetizing field.

$$E_d = -\frac{1}{2} \int \vec{M} \cdot \vec{H}_d \, dV \quad (2.11)$$

In detail, the demagnetizing field of a body depends on the particular shape of the sample and can become a complex function of location in the sample. However, the demagnetizing field is proportional to the magnetization for a homogeneously magnetized ellipsoid and is expressed by

$$\vec{H}_d = -\bar{N}\vec{M}. \quad (2.12)$$

\bar{N} denotes the demagnetizing tensor which becomes diagonal when the magnetization is parallel to one of the rotational axes. The trace of the demagnetizing tensor $N_x + N_y + N_z$ amounts to 4π in the CGS unit system. Analytical solutions for the demagnetizing factors (N_i) are only found for spheres or ellipsoids. Demagnetizing factors for other shapes have to be numerically approximated. In general, the demagnetizing factor is larger along the short axis than along the long axis for an elongated object. Therefore, it is easier to saturate a sample parallel to the long axis/axes—along a cylinder or in-plane in a film—leading to an experimentally observed ‘shape anisotropy’.

direction	α_1	α_2	α_3	energy
cube edges $\langle 100 \rangle$	1	0	0	0
face diagonal $\langle 110 \rangle$	$\frac{1}{\sqrt{2}}$	$\frac{1}{\sqrt{2}}$	0	$\frac{1}{4}K_1$
body diagonal $\langle 111 \rangle$	$\frac{1}{\sqrt{3}}$	$\frac{1}{\sqrt{3}}$	$\frac{1}{\sqrt{3}}$	$\frac{1}{3}K_1 + \frac{1}{27}K_2$

Table 2.1: Tabular overview of the directional cosines and the magnetocrystalline anisotropy energy for a cubic symmetry along different, depicted directions. The direction as well as the energy of the easy, the intermediated and the hard axis can be determined by inserting K_1 and K_2 .

Anisotropy Energy

The energy term E_a denotes the ‘magnetocrystalline anisotropy’ which has its origin in the interaction of the spin magnetic moment with the crystal lattice, the so-called spin-orbit coupling. Thus, the symmetry of the magnetocrystalline anisotropy is the same as of the crystal structure of the material.

All materials investigated in this thesis exhibit a cubic crystal at room temperature. The magnetocrystalline energy E_a can be written as

$$E_a = K_1(\alpha_1^2\alpha_2^2 + \alpha_2^2\alpha_3^2 + \alpha_3^2\alpha_1^2) + K_2(\alpha_1^2\alpha_2^2\alpha_3^2) + \dots \quad (2.13)$$

with the temperature-dependent anisotropy constants K_1 and K_2 . α_i denotes the directional cosine of the magnetization vector—projection of the magnetization to each axis normalized to the length of the magnetization vector. The direction with the minimized energy is the preferred direction, the so-called easy axis. The direction cosines and the magnetocrystalline anisotropy energy are calculated for different, depicted directions in table 2.1. The cubic magnetocrystalline anisotropy is often dominated by the first term. Depending on whether K_1 is positive or negative the energy landscape—and thus the direction distribution of easy and hard axes—changes drastically as illustrated in figure 2.1 for magnetite at two different temperatures (and neglected K_2).

Surface Contribution

In thin films and nanostructures, an additional contribution to the total energy of a magnet has to be taken into account, which is related to the enhanced surface-to-volume ratio of magnetic atoms. This term is called ‘surface anisotropy’ and has its origin in a symmetry break at the surface: interacting spins at the surface have not the same number of neighboring spins as in the volume part of the sample. Hence, the exchange energy at the surface is altered. The energy contribution E_a^s can be approximated by

$$E_a^s = \frac{1}{2}K_s \int \left(\frac{\vec{M}}{M_s} \cdot \vec{n} \right)^2 dS \quad (2.14)$$

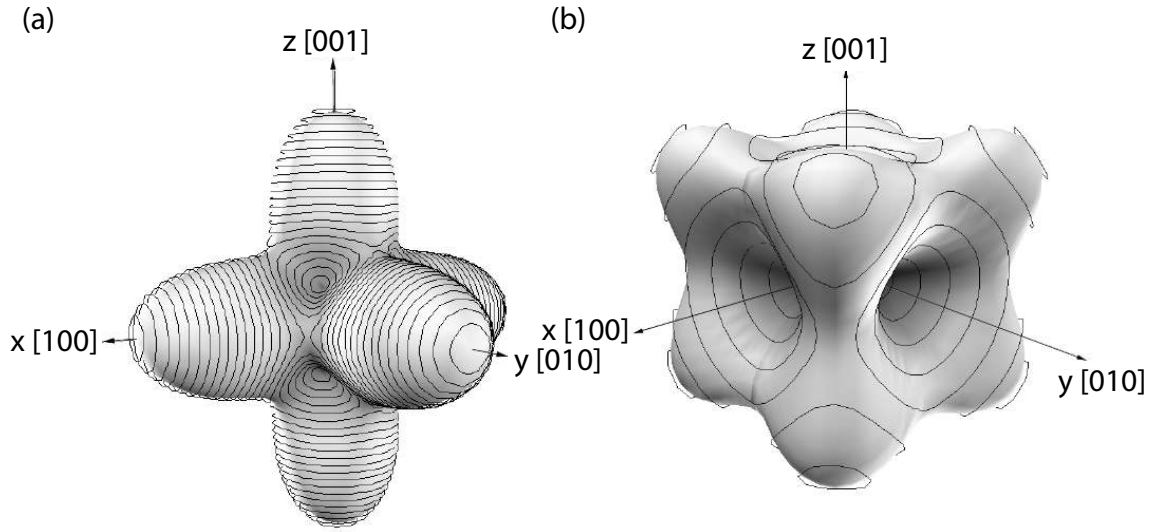


Figure 2.1: The magnetocrystalline energy landscape of cubic magnetite (a) with a $K_1 < 0$ at 293 K and (b) $K_1 > 0$ at 126 K. (a) The easy and the hard axes are along the $\langle 111 \rangle$ and the $\langle 100 \rangle$ directions, respectively. (b) The easy axes point along the $\langle 100 \rangle$ directions for $K_1 > 0$, whereas the $\langle 111 \rangle$ directions become magnetically hard. Picture is adapted from [Mux00].

in which K_s denotes a general surface anisotropy constant and \vec{n} the unit vector which is normal to the surface element $d\vec{S}$. In a scenario with an uniaxial anisotropy of a thin film with the thickness t , the effective anisotropy constant K can be defined by

$$K = K_v + 2\frac{K_s}{t} \quad (2.15)$$

with a contribution of the volume K_v and the contribution of the surface K_s . Indeed, K_s depends on the material and is in the order of 0.1 erg cm^{-3} . Experimental investigation of the effective anisotropy constant allow for the determination of the surface anisotropy constant. In specific cases, as observed in Co/Au or Co/Pt multilayers, the surface anisotropy causes a perpendicular—to the thin film—magnetization anisotropy.[Wel95] [Zep89]

Domain Formation

One way to minimize the total energy of a ferromagnet is the formation of magnetic domains. Magnetic domains are areas in which all the atomistic magnetic moments are parallel aligned. However, the direction of orientation varies from domain to domain and can lead to a complex micromagnetic structure of the sample. A demagnetized magnetic material tries to minimize the stray field as much as possible by the formation of differently aligned domains. The border between two magnetic

domains at which the magnetic moments change their pointing direction is called domain wall and is associated with a certain amount of energy. Hence, the interplay between exchange energy—parallel alignment of the spins preferred—and the anisotropy energy—all magnetic moments parallel to a preferred (crystallographic) axis—results in the total energy of the domain wall. The exchange energy would result in a rather thick wall, whereas the anisotropy energy would lead to a thin wall. Hence, energy minimization defines the absolute wall thickness l_d which scales for an uniaxial anisotropy with

$$l_d \propto \sqrt{\frac{A}{K}}. \quad (2.16)$$

Again, A denotes the exchange stiffness of the exchange energy contribution. If the size of a ferromagnet is reduced down to the nm-scale it becomes energetically favorable—depending on the material’s magnetic properties and geometry—to avoid domain wall formation and to form single-domain particles.

2.1.2 From Single-Domain to Superparamagnetic Behavior

Stoner and Wohlfarth described the hysteretic behavior of an uniaxial anisotropic, spheroidal single-domain particle analytically and explained its magnetization reversal mechanism by a coherent/parallel rotation.[Sto48] The model was expanded by Jacob and Bean to a chain of interacting, single-domain spheres.[Jac55] For the first time, non-coherent reversal mechanisms like the symmetric or asymmetric fanning reversal were discussed. Both models build the fundament of the modern magnetization reversal research; for instance, the curling and the transverse domain wall model find loan in the fanning and in the coherent reversal, respectively. One has to mention that both models are often used for a first simple approximation of individual magnetic nanowires with an easy axis along the long axis of the wire forming the uniaxial anisotropy.

Further size reduction can decrease the total magnetic anisotropy energy up to a value comparable to the thermal energy. The temperature at this point is usually (far) below the Curie temperature at which the exchange energy is overcome. Thus, a single ‘macroscopic’ magnetization vector of the nanoparticle can be defined as a sum of all atomistic moments (per particle volume)—also called macrospin approximation. Its magnetic energy landscape provides (local) minima which can be regarded as easy axes—at least two, usually antiparallel to each other. When the thermal energy overcomes the energy barrier separating the minima, the direction of the ‘macroscopic’ magnetization vector can switch. Thus, a measurement time much longer than the dwell time in one minimum will give a zero net magnetic moment of the particle. However, when a magnetic field is applied, one minimum is preferred. As a consequence, the macrospin magnetization will point along the magnetic field

direction similar to a paramagnet, in which the individual atomistic moments are forced to align parallel to an externally applied magnetic field. In contrast to paramagnetism, a larger (initial) susceptibility as well as saturation in moderate magnetic fields can be observed. The behavior is called superparamagnetism, and is size- as well as measurement time-related.

Magnetic Relaxation: The Intrinsic Model of Néel or the Extrinsic One of Brown

At a given temperature there is a finite probability to switch the direction of a particle's magnetization. The residual time in a local energy minimum for a magnetically uniaxial anisotropic nanoparticle is called Néel relaxation time τ_N and can be expressed by

$$\tau_N = \tau_0 \exp\left(\frac{KV}{k_B T}\right). \quad (2.17)$$

Therein, τ_0 denotes a material-dependent, characteristic time in the range from 10^{-9} s to 10^{-10} s. KV is the height of the energy barrier consisting of a general anisotropy constant K and the magnetic volume of a particle V . The thermal energy $k_B T$ is expressed by the Boltzmann constant k_B and the absolute temperature T . When the experimental measurement time τ_m is much longer than τ_N , the magnetization can change its direction in the particle several times, leading to a measured zero net magnetic moment. The particle is in the so-called unblocked—superparamagnetic—state. When the temperature is decreased, τ_N becomes larger until it equals the measurement time τ_m . This temperature is called blocking temperature T_B below which the particles are blocked and act as ferromagnets with a remanent magnetic moment. The blocking temperature can be calculate by

$$T_B = \frac{KV}{\ln\left(\frac{\tau_m}{\tau_0}\right)k_B}. \quad (2.18)$$

The measurement times in typical laboratory setups vary from 1 s to 100 s, as a consequence, $\ln\left(\frac{\tau_m}{\tau_0}\right)$ typically ranges from 20 to 25. Therefore, the experimentally determined blocking temperature allows for the estimation of the particle volume if the anisotropy constant is known, or vice versa.

The internal random flip of the magnetization is sometimes denoted by ‘intrinsic’ superparamagnetism to distinguish it from the Brownian relaxation mechanism which might result in an experimentally observable ‘extrinsic’ superparamagnetism. Assuming a hard magnetic, perfect sphere which is able to rotate by Brownian motion in a fluid, a relaxation time similar to τ_N can be defined as follows:

$$\tau_B = \frac{3V\eta}{k_B T}, \quad (2.19)$$

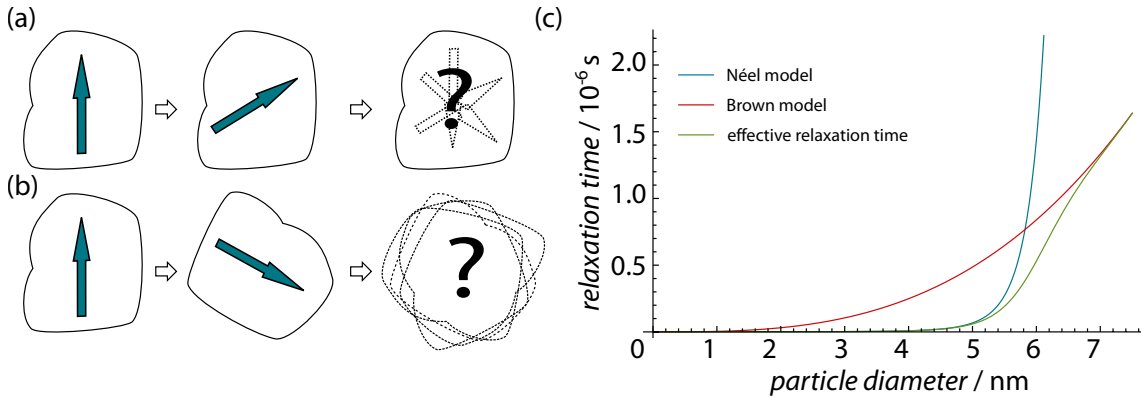


Figure 2.2: Schematic illustration of the Néel and Brown relaxation mechanisms in (a) and (b), respectively. The macroscopic magnetic spin freely rotates inside the particle during Néel relaxation. In contrast, the magnetization is pinned in the Brown model, but the particle itself is able to rotate. (c) Plot of the different relaxation times, namely Néel (blue), Brown (red) and effective (green), calculated as a function of the particle diameter. The parameters for the calculation are: cobalt ferrite nanoparticles with a magnetocrystalline anisotropy of $K_1 = 2.6 \times 10^6 \text{ erg cm}^{-3}$ (in SI units $2.6 \times 10^5 \text{ J m}^{-3}$) suspended in a carrier medium with a viscosity of 10 mPas at a temperature of 293 K. The characteristic time scale is chosen to be 10^{-9} s. An interception of the Néel and the Brown relaxation mechanism can be determined at 5.8 nm, below which the Néel relaxation is dominant. The energy barrier increases for increasing diameters due to the magnetocrystalline anisotropy—the magnetic moment is pinned—and the Brown relaxation mechanism becomes more favorable.

with the viscosity η of the surrounding carrier medium. Again, when the measurement time becomes much longer than τ_B , the particles will rotate and thus change the ‘macroscopic’ magnetization direction with respect to the measurement setup—but not to the particle itself—leading to a zero net magnetic moment of the sample. Both relaxation mechanisms are schematically displayed in figure 2.2 to point out the differences.

In an ensemble of non-interacting, magnetic (nano)particles which are suspended in a liquid carrier medium—a so-called *ferrofluid*—both relaxation mechanisms will occur in parallel. An effective relaxation time can be defined as

$$\tau_{eff} = \frac{\tau_N \tau_B}{\tau_N + \tau_B} \quad (2.20)$$

and will be dominated by the relaxation mechanism with the lower time scale as displayed in figure 2.2(c) at the example of cobalt ferrite nanoparticles.[Fan89]

If the suspended particles deviate from a spherical geometry, have a surrounding dead magnetic layer, or possess an organic shell, the volume in the Néel relaxation (equation 2.17) and the Brownian relaxation (equation 2.19) is not the same. Only the magnetic volume influences the Néel mechanism, whereas the hydrodynamic

	magnetite Fe_3O_4	nickel	cobalt ferrite CoFe_2O_4
magnetism	ferri-	ferro-	ferri-
M_s (RT) [emu cm^{-3}]	480	485	360
crystal structure	spinel	fcc	spinel
K_1, K_2 (RT) [10^5 erg cm^{-3}]	-1.35, -0.44	-0.45, 0.23	26.3

Table 2.2: Magnetic properties of magnetite, nickel and cobalt ferrite. M_s is the saturation magnetization. K_1 and K_2 denote the magnetic crystalline anisotropy constants.

volume determines the Brownian relaxation time. The hydrodynamic volume is defined as the hypothetical volume of a perfect, hard sphere with the same diffusion properties as the suspended particle.

2.1.3 Magnetic Materials

Besides diamagnetic and paramagnetic materials, which only respond to an externally applied magnetic field, ferro-, ferri- and antiferromagnetic materials possess permanent, ordered, magnetic moments. The transition metals (Co, Ni, Fe), their alloys as well as their binary and ternary oxides are the most popular and known representatives. The three ‘magnetic’ materials—namely, magnetite, nickel, and cobalt ferrite—used in this thesis are briefly introduced by a short overview (table 2.2) of the most relevant magnetic parameters needed for this work. Magnetite is presented in more detail since synthesis and preparation of stoichiometric Fe_3O_4 was one aim of this work (subsection 3.2.3).

Magnetite

The three stable oxides of iron are magnetite (Fe_3O_4), hematite ($\alpha\text{-Fe}_2\text{O}_3$) and maghemite ($\gamma\text{-Fe}_2\text{O}_3$). Among these phases, the ferrimagnetic magnetite shows the highest magnetization of 480 emu cm^{-3} compared to $< 10 \text{ emu cm}^{-3}$ for hematite and 400 emu cm^{-3} for maghemite.[Cor03] Magnetite belongs to the spinel crystal structures AB_2X_4 in which A and B represent the cations and X an anion—mostly oxygen or sulfur. For detailed information about this mineral class, please refer to the review article by Hill *et al.* from 1979.[Hil79] Expression of the chemical formula by $[\text{Fe}^{3+}][\text{Fe}^{3+}\text{Fe}^{2+}][\text{O}^{2-}]_4$ —a so-called ‘inverse’ spinel structure—represents the distribution of the iron ions at the tetrahedral (A) and octahedral (B) sites. The magnetic cubic cell consists of eight Fe^{3+} ions in tetrahedral structure and each eight Fe^{2+} and Fe^{3+} ions on octahedral places (figure 2.3 (a)). Antiferromagnetic coupling of the two sublattices results in the observed ferrimagnetism in magnetite.

A phase transition at $\approx 120 \text{ K}$ is a unique feature of magnetite, designated after Verwey who formulated a first conception of its origin.[Ver39] The first indication of the transition was already measured by Renger *et al.* in the susceptibility of a

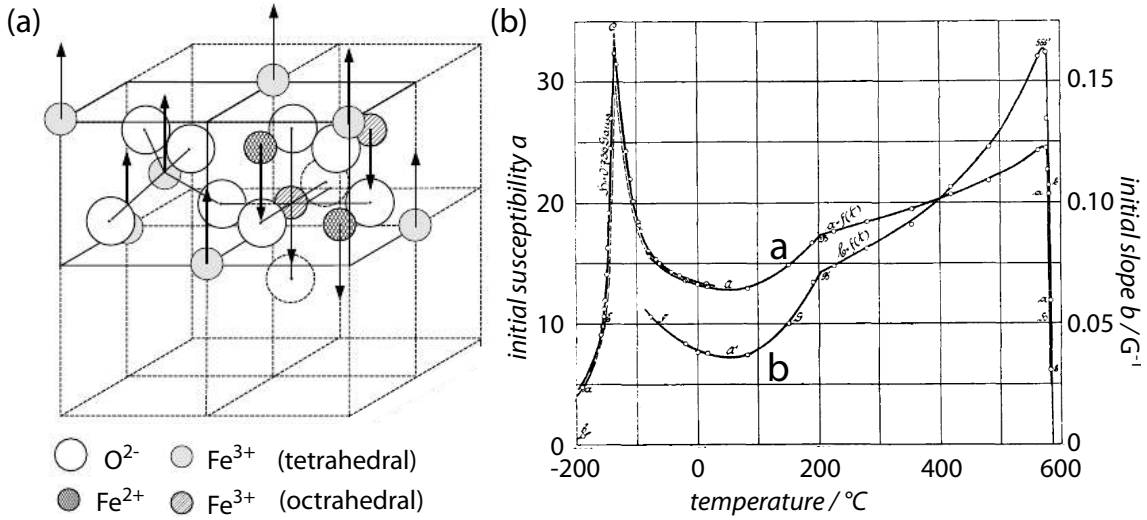


Figure 2.3: (a) Illustration of the cubic inverse spinel crystal structure of magnetite at room temperature. The 16 Fe^{3+} ions are equally distributed on the tetrahedral and octahedral sites of the crystal, whereas the eight Fe^{2+} ions are only located at the octahedral sites. (b) First published observation of the Verwey transition in temperature-dependent susceptibility $\chi = a + bH$ measurement of a macroscopic magnetite sample. [Ren13] Figure adapted from Renger’s PhD thesis (1913); axes were re-labeled for clarity.

synthetic polycrystal in 1913 (figure 2.3(b)). [Ren13] A change of the ionic crystal structure occurs at the transition temperature T_V from a cubic inverse spinel ($T > T_V$) to a less symmetric monoclinic structure ($T < T_V$). As a consequence, the electronic band structure is varied resulting in a change of the related physical properties, namely magnetism (susceptibility change), electrics (conductivity drop), mechanics and thermodynamics (peak in the heat capacitance). The Verwey transition is one of the best explored phase transitions, but still under hot debate. Walz published 2002 a topical review in which he summarized the research and opinions from the first discovery in 1913 through the Mott conference in Cambridge in 1979 to the beginning of the 21st century. [Wal02] Common sense (related to this work) is: only high-quality, stoichiometric magnetite owning a negligible amount of impurities shows this single, first order transition. Stoichiometry deviations of more than 1.2% turns the transition into a (continuous) second order transition until a disappearance of the Verwey transition can be determined above four percent impurities. [Ara86] [vdZ96] [Koh12] Confinement of at least one dimension can cause a shift of the Verwey temperature to lower temperatures until a complete suppression of the phase transition can occur. [Orn10] Several reasons are still under discussion, namely internal strain—related to the growth or mechanical interaction with the substrate—or the loss of the long-range order of Fe^{2+} and Fe^{3+} on the octahedral sites in thin films, which is a requirement for the Verwey transition. [Mou04]

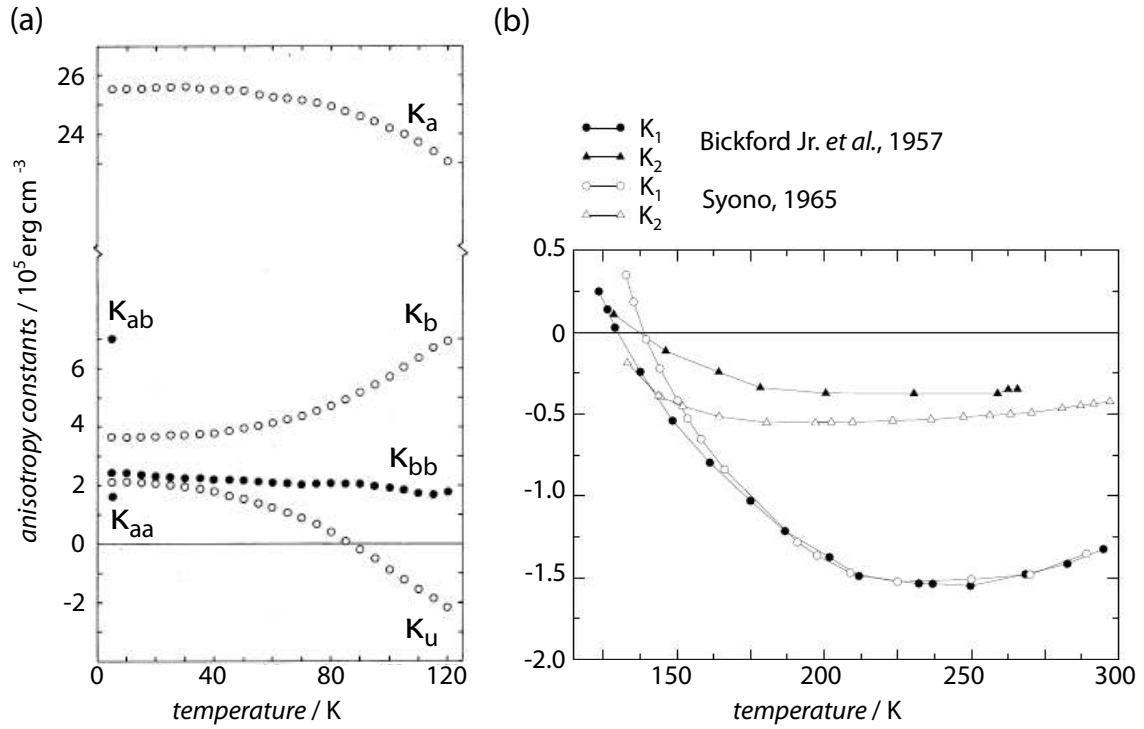


Figure 2.4: (a) and (b) display the temperature-dependent evolution of the magnetocrystalline anisotropy constants below the Verwey temperature and above, respectively. The absolute value of the magnetocrystalline anisotropy constant κ_a below the Verwey temperature is at least one order of magnitude larger than K_1 of the cubic magnetocrystalline anisotropy above the Verwey transition. (a) is adapted from [Abe76]. (b) Data was taken from [Bic57] [Sy65]; figure itself is adapted from [Mux00].

At around 130 K, slightly above the Verwey transition, the magnetocrystalline anisotropy constant K_1 changes its sign (see figure 2.4). The intersection point at which K_1 equals zero is called *isotropic* or *spin-reorientation* point and is a Verwey transition-independent reorientation of the spins from the $\langle 111 \rangle$ axes to the $\langle 100 \rangle$ directions (figure 2.1). Exactly at the isotropic point other anisotropy terms, like the much smaller second term of the magnetocrystalline anisotropy K_2 , the demagnetization field, or surface and magnetoelastic anisotropy, will determine the magnetic properties of a magnetite sample. As already mentioned, the crystal structure changes to a monoclinic structure with a slight tilt of the c -axis at the Verwey transition. Thus, the magnetocrystalline anisotropy energy of Fe_3O_4 below the Verwey transition can be written as

$$E_a = \kappa_a \alpha_a^2 + \kappa_b \alpha_b^2 + \kappa_{aa} \alpha_a^4 + \kappa_{bb} \alpha_b^4 + \kappa_{ab} \alpha_a^2 \alpha_b^2 - \kappa_u \alpha_{111}^2 \quad (2.21)$$

in which α_a , α_b are the directional cosines of the magnetization with respect to the a - and b -axis, respectively. κ_i denotes the corresponding magnetocrystalline anisotropy

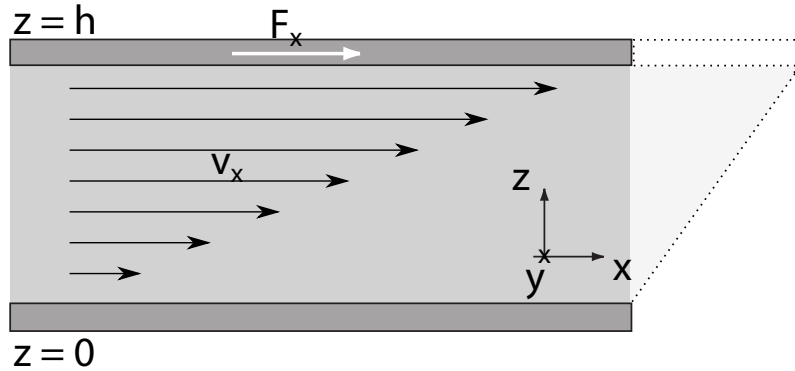


Figure 2.5: Scheme to derive the basic values of rheology from the simple ‘two plates’ model. A liquid is sheared by moving an upper plate at $z = h$ with a force F_x . As a consequence, a velocity gradient $\frac{dv_x}{dz}$ is formed. The picture is adapted from [Mez06].

constants. Abe *et al.* added an additional uniaxial anisotropy term $\kappa_u \alpha_{111}^2$ to give respect to the small rhombohedral distortion— α_{111} denotes the directional cosine with respect to the elongated cube diagonal [111].[Abe76] [Mux00] Moreover, the authors showed that the monoclinic magnetocrystalline anisotropy constants (κ_i except κ_u) are about ten times larger than K_1 (comparison of (a) and (b) in figure 2.4). Muxworthy and McClelland concluded in their review article: "Consequently, the relative importance of the monoclinic magnetocrystalline anisotropy to the domain structure is far greater than the cubic magnetocrystalline anisotropy." [Mux00]

2.2 Rheology

The following section is thought to give a short introduction to rheology of liquids and liquid suspensions, and vocabulary as well as physical values used in this. For a further, more detailed overview, please refer to standard textbooks like “Rheology: principles, measurements, and applications” by Macosko or “The Rheology Handbook: For Users of Rotational and Oscillatory Rheometers” by Mezger.[Mac94] [Mez06] More specific information regarding rheology of colloidal suspensions can be found in the text books by Tadros or Mewis.[Tad10] [Mew11]

2.2.1 Basic Concepts

The basic concepts of rheology can be explained by a simple model of two plates as displayed in figure 2.5. A force F_x moves an upper plate with the area A spanned in the x - y -plane in the x -direction—whereas, a lower plate is fixed—leading to a shear stress τ in the liquid placed in between

$$\tau = \frac{F_x}{A}. \quad (2.22)$$

A velocity gradient—the so-called *shear rate* $\dot{\gamma}$ —is formed in the liquid sample due to adhesion at the plates. The laminar flow of the liquid induced by such shear stress is called *shear flow*.

$$\tau \propto \dot{\gamma} = \frac{dv_x}{dz} \quad (2.23)$$

The *vorticity* Ω of a flowing fluid with the velocity vector field \vec{v} is defined as

$$\Omega = \nabla \times \vec{v}, \quad (2.24)$$

and is a measure of the ‘local rotation’ of a fluid element. Conceptually, the vorticity describes the rotation of a particle—or a fluid volume element—in a shear flow with a rotation axis perpendicular to \vec{v} . The vorticity of a simple shear flow (as displayed in figure 2.5) points along the y-axis (into the sheet plane).

2.2.2 Viscosity

Ideal viscous fluids, for which the proportionality in equation 2.23 holds, are called *Newtonian fluids*. The constant of proportionality of shear stress and shear rate (equation 2.23) is called the viscosity coefficient η with the SI-unit Pa s and can be interpreted as an internal friction coefficient.

$$\eta = \frac{\tau}{\dot{\gamma}} \quad (2.25)$$

The viscosity of Newtonian fluids depends only on the temperature and on the pressure. Examples for such fluids are water, low molecular oils, glycerin but also the blood plasma. In contrast to Newtonian fluids, the viscosity of ‘non-Newtonian’ fluids is a function of the shear rate. The viscous behavior of those can be quite complex depending on their internal structure. In general, two main types of such non-Newtonian behavior can be defined, namely shear thickening and shear thinning behavior as displayed in figure 2.6. Some reasons for shear thinning behavior are explicitly mentioned here, since the investigation of this effect in *ferrofluids* will be part of this thesis (section 4.4). In particular, one has to consider shear rate-dependent orientation of the particles, elongation of dispersed drops, or breakage of agglomerates as a possible origin. Polymer solutions, polymer melts, gloss paints, colloidal suspension are listed as examples for shear thinning fluids.

Various phenomenological models are established to describe the shear thinning behavior as a function of the shear rate. The simplest phenomenological model is a ‘Power Law’ by Ostwald and de Waele

$$\eta = K\dot{\gamma}^{n-1} \quad (2.26)$$

with the consistency K and the flow behavior index n . [Ost33] [Mez06] If the flow behavior index equals one, the fluid behaves as a Newtonian fluid, whereas $n > 1$

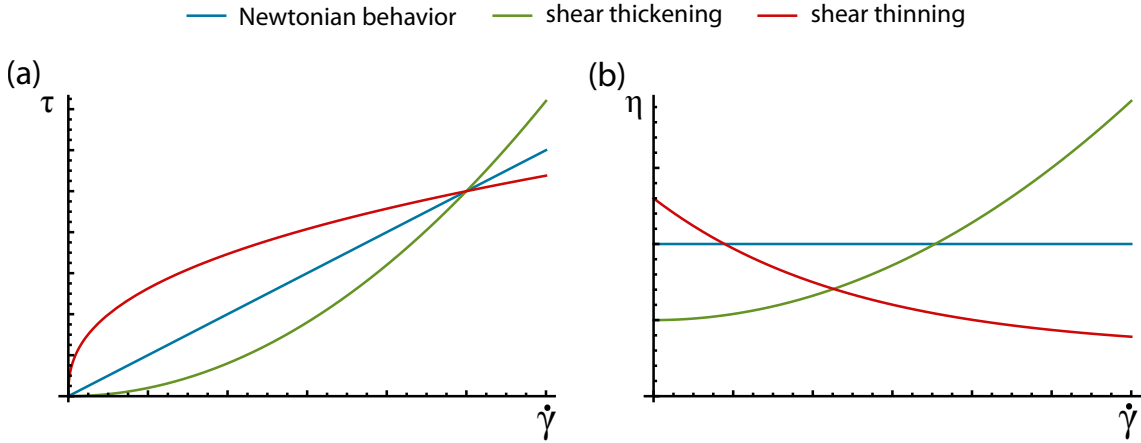


Figure 2.6: Schematic plot of the shear stress (a) and the viscosity (b) as a function of the shear rate. An ideal ‘Newtonian’ fluid is denoted in blue, a liquid which shows shear thickening or shear thinning in green and red, respectively. The latter represents the behavior of ferrofluids as investigated in the chapter 4. The interceptions of the curves have no physical meaning.

or $n < 1$ describes a shear thickening (dilatant) or a shear thinning (pseudoplastic) fluid, respectively. The Herschel-Bulkley relationship, which describes the majority of flow curves in a wide shear rate range, is an extension of this model with an additional term related to the yield stress τ_0 ¹.

$$\eta = \frac{\tau_0}{\dot{\gamma}} + K\dot{\gamma}^{n-1} \quad (2.27)$$

At vanishing yield stress, the Herschel-Bulkley relationship changes over to the ‘Power Law’ by Ostwald/de Waele.

2.2.3 Viscoelasticity

Viscoelastic materials display viscous as well as elastic behavior at the same time. The latter is a property usually related to solids. Once an applied shear stress is removed, the materials turns back in the original—non-deformed—state. A material specific value (in the linear elastic regime) is the shear modulus G which describes the relation between shear stress τ and the resulting deformation γ of the solid.

$$G = \frac{\tau}{\gamma} = \frac{\eta\dot{\gamma}}{\gamma} \quad (2.28)$$

¹The yield stress is defined as stress which has to be applied until a material is plastically deformed. However, the determined value of the yield stress is not only dependent on the material but also on the experiment, the apparatus used and the applied data evaluation model.

Many non-Newtonian fluids reveal viscous as well as elastic properties, and thus have to be treated as viscoelastic. Oscillation tests enable the experimentalist to determine and to separate the viscous and elastic properties of complex fluids or substances from each other.

A sinusoidal, oscillatory shear stress with the angular frequency ω results in a sinusoidal response function of the deformation with the phase displacement δ

$$\tau(t) = \tau_A \sin(\omega t) \quad (2.29)$$

$$\gamma(t) = \gamma_A \sin(\omega t + \delta) \quad (2.30)$$

in which τ_A and γ_A denote the shear stress and the deformation amplitude, respectively. Two limits can be assigned: on the one hand, the ideally elastic case with a phase shift δ of zero—shear stress and deformation are ‘in-phase’, and on the other hand, the ideally viscous limit in which τ and γ are ‘out-of-phase’ ($\delta = 90^\circ$). Thus, the phase shift for viscoelastic materials is in between

$$0^\circ < \delta < 90^\circ. \quad (2.31)$$

The shear modulus in oscillatory experiments is defined as complex shear modulus G^*

$$G^* = G' + iG'' \quad (2.32)$$

with the storage modulus $G' = \frac{\tau_A}{\gamma_A} \cos \delta$ and the loss modulus $G'' = \frac{\tau_A}{\gamma_A} \sin \delta$. G' is a measure for the stored deformation energy, whereas the latter depicts the energy lost during deformation. The stored energy is used to revert the deformation after a load. Therefore, G' represents the elastic behavior of a sample. In contrast, the energy which is dissipated through internal friction during the deformation cannot be used to return to the initial state before load. The material is irreversibly deformed; accordingly, G'' describes the viscous property of a sample.

The phase shift can be also denoted as loss factor

$$\tan \delta = \frac{G''}{G'} \quad (2.33)$$

describing the ratio of viscous to elastic behavior of a sample. In the limiting cases, $\tan \delta$ amounts either to zero or to infinity for ideally elastic or viscous behavior, respectively. Between the limiting cases, two different states occur, namely liquid-like and gel-like behavior. Moreover, a transition point can be defined at which the two states transforms into each other:

a sol-like (liquid-like) state	$\tan \delta > 1$	$G'' > G'$
a gel-like state	$\tan \delta < 1$	$G'' < G'$
a sol-gel transition point	$\tan \delta = 1$	$G'' = G'$.

Since the viscosity and the shear modulus are related as shown in equation 2.28, the viscosity becomes complex, analog to equation 2.32.

$$\eta^* = \frac{G^*}{i\omega} = \eta' - i\eta'' \quad (2.34)$$

The real and the imaginary part of complex the viscosity η^* can be derived to

$$\eta' = \frac{G''}{\omega} = \frac{\tau_A \sin \delta}{\gamma_A \omega} \quad (2.35)$$

$$\eta'' = \frac{G'}{\omega} = \frac{\tau_A \cos \delta}{\gamma_A \omega}. \quad (2.36)$$

with the absolute value

$$|\eta^*| = \sqrt{(\eta')^2 + (\eta'')^2}. \quad (2.37)$$

In 1958, Cox and Merz stated the later so-called ‘Cox-Merz rule’

$$|\eta^*(\omega)| = \eta(\dot{\gamma} = \omega) \quad (2.38)$$

based on comparative experiments of a steady flow rheometer with an elastovisco-ometer.[Cox58] This rule enables the experimentalist to compare the viscosity measured in a steady shear flow rheometer as a function of the shear rate with the absolute value of the viscosity as a function of the (shear) frequency determined in an oscillatory rheometer. The ‘Cox-Merz rule’ is established in the engineering field of rheology since then. Chae *et al.* showed the validity of the rule for magnetic dispersions in 2001.[Cha01] Since an oscillatory measurement platform was used in this work, the viscosity was measured as a function of the ‘shear frequency’. However, the reader should have the equivalence of ‘shear rate’ and ‘shear frequency’ based on the ‘Cox-Merz rule’ in mind.

To conclude, the viscous behavior of a sample can be described by using either G'' or η' , whereas the elastic property can be denoted by the corresponding counterparts G' and η'' . Indeed, the use of complex shear moduli has prevailed over the complex viscosity parts in industrial practice and engineering. However, for liquids, liquid suspensions, polymer solutions and polymer melts the absolute value of the viscosity $|\eta^*|$ is still used as third instance to give a complete and quickly graspable picture of the material investigated.

2.3 Magnetic Fluids

While the former two parts presented the basic concepts of magnetism and rheology, this section combines major elements of both in terms of ‘magnetic fluids’. First,

the simple *rotational magnetoviscosity* model is presented followed by more complex concepts that include chain and cluster formation. Second, the segue from a ‘real’ *ferrofluid* to a *magnetorheological fluid* is discussed. Third, a (literature) survey of liquid suspensions consisting of elongated particles is presented. Last, *hybrid* liquid suspensions are introduced which consist of mixtures of different (magnetic) particles. For further information about ferrofluids and ferrohydrodynamics the textbooks of Rosensweig, Odenbach and Berkovsky are recommended.[Ros85] [Ode02a] [Ber96]

2.3.1 Ferrofluids: From Rotational Magnetoviscosity to Chain Formation

Liquid suspensions of magnetic nanoparticles react to an applied magnetic field by an apparent viscosity increase. This phenomenon was independently observed by Rosensweig and McTague for the first time in 1969.[Ros69] [McT69] In the following decades, theoretical calculations tried to explain this magnetic field-dependent increase by a model, later called rotational magnetoviscosity.[Shl72] [Mar73] [Shl80] A liquid suspension consisting of (permanent) magnetic, spherical nanoparticles is assumed. Furthermore, interaction between the particles is neglected which can be true for highly-diluted suspensions possessing a small volume concentration Φ as in the work by McTague.[McT69] A simplified sketch of the rotational magnetoviscosity concept is presented in figure 2.7 (a). A particle with a fixed magnetic moment m rotates in a shear flow due to viscous friction. The (fixed) magnetic moment tries to follow the externally applied magnetic field H which is applied with a certain angle β to the vorticity. However, the mechanically induced rotation of the particle results in a deviation of the pointing direction of the magnetic moment inside the particle from the direction of the external magnetic field. Thereby, the free rotation of the (nano)particle is hindered by the competition between magnetic torque antagonized by the mechanical one. As a consequence, the apparent viscosity is increased.

The difference of the viscosity η_r between the measured viscosity in an applied magnetic field and the viscosity of the ferrofluid without magnetic field η_0 is given by

$$\eta_r = \frac{3}{2}\eta_0\Phi \cdot \frac{\alpha - \tanh \alpha}{\alpha + \tanh \alpha} \cdot \langle \sin^2 \beta \rangle. \quad (2.39)$$

α describes the ratio of magnetic to thermal energy.[Shl72]

$$\alpha = \frac{m\mu_0 H}{k_B T}. \quad (2.40)$$

However, the experimentally observed viscosity values are often orders of magni-

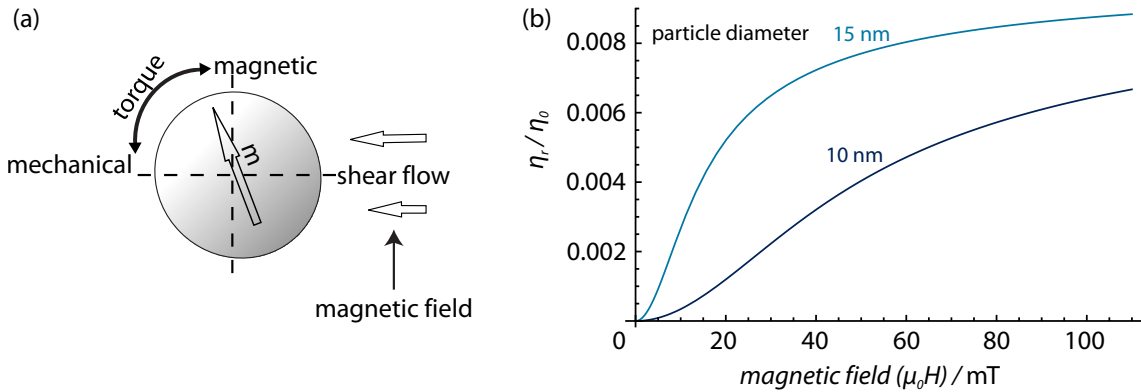


Figure 2.7: (a) Schematic drawing of the rotational magnetoviscosity concept in the limiting case that the shear flow, the vorticity—defines the rotation axis of the particle which is parallel to the normal of the sheet plane—as well as the applied magnetic field are perpendicular to each other (figure adapted from [Ode04]). The free rotation of the particle is hindered by an interaction between magnetically and mechanically induced torque. (b) Calculated rotational viscosity (equation 2.39) normalized to the carrier liquid viscosity η_0 (10 mPas) for two cobalt ferrite nanoparticle suspensions (diameter 10 nm and 15 nm in dark and bright blue, respectively; volume concentration 0.66 %)

tude larger than the theoretically predicted ones.² Additionally, a strong dependence with respect to the applied shear frequencies is experimentally found which can also not be included in the rotational magnetoviscosity model.[Ode04] Therefore, other explanations and models have to be considered. The calculated, normalized rotational viscosity η_r/η_0 of a ferrofluid—as used in chapter 4: cobalt ferrite particles, diameter 15 nm, volume concentration 0.66 %—is plotted in figure 2.7 (b) as a function of the applied magnetic field. The experimentally observed normalized viscosity increase (refer to figure 4.6 (a)) differs orders of magnitudes from the calculated values, and reveal a different response to the applied magnetic field.

To differentiate the interpretation of the measurements from the concept of rotational magnetoviscosity and its reason, the general term ‘magnetoviscous effect’ was defined as viscosity increase from zero to applied magnetic field $\eta(H)$ normalized to the zero-field viscosity.[Ode98] [Ode02a]

$$\text{MVE} = \frac{\eta(H) - \eta_0}{\eta_0} \quad (2.41)$$

A simplified picture is given in figure 2.8(a). In the upper panel, the mono-disperse, (permanent) magnetic nanoparticles are homogeneously distributed in the carrier liquid. By applying a magnetic field only the rotational magnetoviscosity increases the apparent (measured) viscosity as sketched in the left, lower panel. If

²One has to consider that only particles above the superparamagnetic limit in the size distribution—possessing a fixed magnetic moment—contribute to the rotational viscosity.

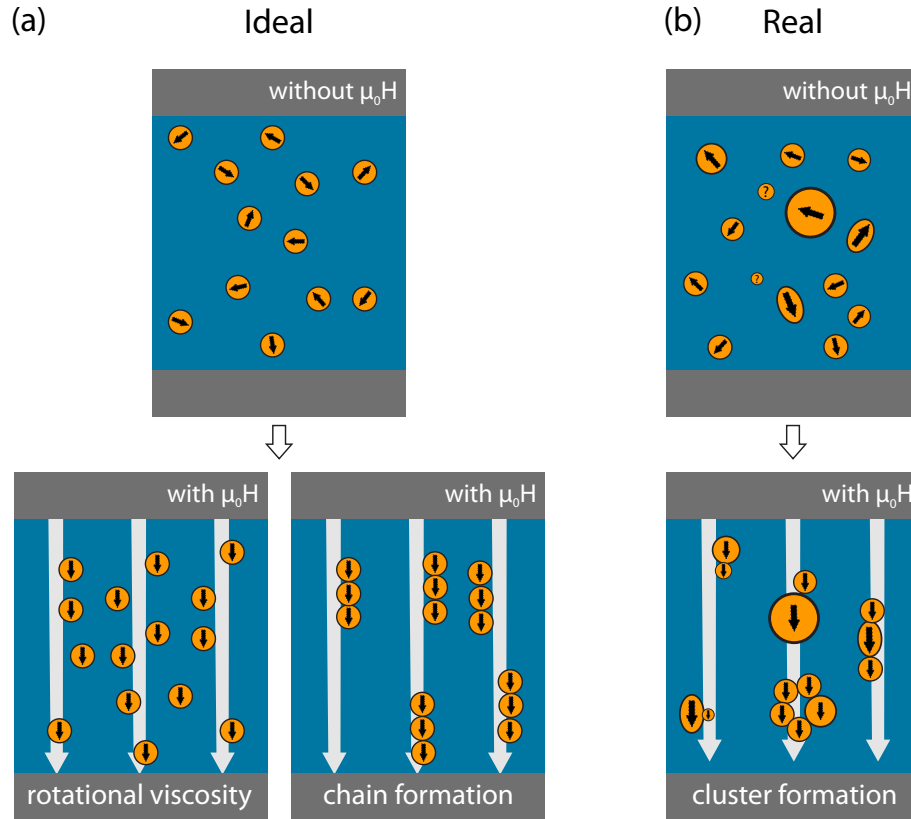


Figure 2.8: Simplified scheme of the chain/cluster formation in (a) ‘ideal’ ferrofluids assumed in theory and (b) in ‘real’ ferrofluids possessing a certain size distribution and/or (slightly) varying shapes. The upper panels and lower panels display the situation without and with applied magnetic field, respectively. In detail, the two lower panels of (a) show the model of rotational magnetoviscosity (left) and the concept of chain formation (right).

particle interaction is additionally taken into account, magnetic field-induced chain formation (displayed in the lower, middle panel) can be assumed as a reason for the larger apparent viscosity response to the applied magnetic field compared to the rotational magnetoviscosity concept.[Cha80] [Ode98] Moreover, the shear thinning effect—apparent MVE decrease with increasing shear frequencies—can be explained by this model, too. High shear frequencies, and thus high shear forces, cause the breaking of the chains and results in a shear frequency-dependent MVE. Zubarev developed a model presuming straight, rigid and non-interacting chains which allows for a shear frequency-dependent calculation of the chain length, and thus of the MVE.[Zub92] [Zub00] [Zub02] The in-situ experimental proof of chain formation in ferrofluids upon an applied magnetic field was given by scanning electron microscopy, neutron scattering experiments and cryogenic transmission electron microscopy.[Hay75] [But03b] [But03a] [Wie06]

In reality, all synthesis routes of ferrofluids result in a certain size distribution, and

occasionally in a variation of shapes, as sketched in the upper panel of figure 2.8 (b). The strength of the magnetoviscous effect is determined by the absolute amount of larger particles in the liquid suspension leading to microstructure formation due to enhanced particle-particle interaction.[Ode00] [Kan02] [Thu03] [Ode04] Two kinds of internal heterogeneous structures in ferrofluids are mainly observed in an external magnetic field: on the one hand, chains with a wide length variation and on the other hand, drop-like aggregates (lower panel in figure 2.8 (b)).[Zub06] Moreover, energy considerations of particle and (resulting) microstructure interactions predict other complex structures, e.g. rings, tubes, scrolls, which might influence the properties of the ferrofluids further.[Yoo10] [Tan12]

2.3.2 Ferrofluids or Magnetorheological Fluids?

Besides ferrofluids, the so-called magnetorheological fluids are forming the second class of magnetic fluids. Ferrofluids behave in an external magnetic field like fluids with an increased apparent viscosity, whereas magnetorheological fluids solidify. Thereby, shear modulus and yield stress, alter over several orders of magnitude, from a liquid-like to a solid-like state. The listed references—mainly review articles—are thought to give a comprehensive overview and introduction to the topic of magnetorheological fluids and application of them.[Gin96] [Ash96] [Gin98] [Jol99] [Tao01] [Bos02] [Krö03] [Bic06] [Gon06] [dV11]

An exact distinction between ferrofluids and magnetorheological fluids is rather difficult since various intrinsic and extrinsic properties have to be taken into account. Intrinsic properties are related to the properties of the individual particle itself, namely particle size and magnetic state; extrinsic properties belong to the liquid suspension, e.g. concentration of particles and stability. The following two paragraphs present the commonly defined attributes for ferrofluids and magnetorheological fluids. A summarizing, tabular comparison of the properties of ferrofluids and magnetorheological fluids is shown in table 2.3.

	ferrofluid	magnetorheological fluid
particle size	nanometer range (around superparamagnetic limit)	typically several hundreds of nm up to tenths of μm
magnetic state	mainly superparamagnetic, only a few permanent magnetic particles	permanent magnetic in single or even multi-domain state
vol. concentration	below ten percent	above ten percent
stability	good (small size and superparamagnetism)	poor due to sedimentation and agglomeration
B field response	viscosity increase	solidification

Table 2.3: Typical properties of ferrofluids and magnetorheological fluids.

As already mentioned, ferrofluids consist of nanoparticles with a size (distribution) below the superparamagnetic limit—the critical diameter is material dependent.

Thus, most particles of the liquid suspension reveal superparamagnetic behavior resulting in minimized magnetic interactions. As a consequence, the tendency to form agglomerates is reduced. Furthermore, functionalization by surface charges or by a surfactant layer—steric or electrostatic hindrance or a combination of them—as well as a low volume concentration (usually below 10 %) reduces the interaction further. Brownian motion of the nanoparticles prevents from sedimentation of them. Thus, a good long-time stability performance is achieved ranging from several months up to years with only small changes in the (magneto)viscous properties. Upon applying an external magnetic field, the viscosity increases due to the formation of non-interacting chains. The larger particles—only a few in the size distribution—are above the superparamagnetic limit in a single-domain, permanent magnetic state and act as ‘seed’ for the chain formation. But in contrast to magnetorheological fluids, ferrofluids still possess the typical properties of a liquid. The formed chains can break under high shear frequencies leading to the experimentally observed shear thinning effect. After removal of the magnetic field the initial zero-field viscosity is reached again without any remaining, previously magnetic field-induced structures.

In contrast, magnetorheological fluids consist of a high volume concentration (up to 30 %) of ferro-/ferrimagnetic particles—far above the superparamagnetic size limit. The diameter ranges from few hundreds of nanometers up to several microns with a broad size distribution. Therefore, permanent magnetic particles in single-domain or even multi-domain states are predominantly present. Strong magnetic interaction results inevitably in agglomeration which can only be (minimally) reduced by (surface) functionalization. Moreover, the large size of the individual particles reduces the Brownian motion and thus triggers significant sedimentation. Both features result in a poor stability compared to the ferrofluidic suspensions. The major difference between ferrofluids and the magnetorheological fluid is revealed upon the reaction to an externally applied magnetic field. Magnetorheological fluids solidify and change their liquid-like off-field state to a solid-like state featuring high yield stress and shear moduli in the kPa range, or even higher. Strong (magnetic) particle-particle interaction is caused by an increase in the particle size up to the micrometer range as well as by a volume concentrations of several ten percent. Thus, thick and strongly interacting, cross-linked chains are formed upon an applied magnetic field. As a consequence, a stable network is formed leading to the experimentally observed solidification of the colloidal suspension. The formed microstructures could be partially stable after removing the magnetic field. Such permanent structures can change the viscous properties of the fluid in the field-off-state after applying a magnetic field compared to the properties in the initial state before applying a magnetic field.

Taking all the facts into account, the liquid suspensions of elongated nanoparticles prepared in this thesis can be attributed to the ferrofluid class. Although all individual particles are permanent magnetic and much larger than 20 nm, the low

volume concentration (< 0.1 vol %) and moreover the response of the viscosity on the applied magnetic field allows for a clear identification of ferrofluidic properties. Liquid suspensions which change from a sol- to a gel-like behavior are presented in chapter 5. However, a clear solidification as observed in magnetorheological fluids cannot be found. Consequently, all liquid suspensions presented herein are called ferrofluids.

Both types of magnetic fluids are mainly employed in magnetically controlled damping systems depending on the specific purpose such as application in bridges, cars, or audio loudspeakers, to name a few of them.[Zhu12] Moreover, ferrofluids find use in heat transfer and sealing systems.[Ber96] Utilizing superparamagnetic particles in liquid suspensions is a growing field in medicine and clinical studies: in particular, one has to mention the application as contrast agents in magnetic resonance imaging, in drug- and gene-delivery, or in magnetic hyperthermia treatment of cancer.[Goy08] [Pan09] [Kri10]

2.3.3 Liquid Suspensions Consisting of Elongated Nanoparticles

Publications regarding magnetic fluids—including ferrofluids as well as magnetorheological fluids—are mainly dealing with spherical particles. Various synthesis routes are known and well described in the aforementioned review articles. For the preparation of elongated nanoparticles, like nanowires or nanotubes, various preparation methods are published, e.g. template-based approaches,[Huc00] vapor-solid-liquid growth mechanisms,[Wan08] or wet-chemical self-assembly to name a few of them.[Rao09] However, literature on elongated magnetic particle suspensions including measurements of their magnetoviscous properties is quite rare. A sufficient volume concentration of magnetic material can often not be achieved because of the limited yield per synthesis batch. Nevertheless, such (extremely) diluted liquid suspensions of elongated magnetic objects have been applied in research fields like (bio)medicine, optics or mechanics. For instance, magnetic field-assisted gene or drug delivery might provide novel paths in cancer therapy,[Sal03] [Yue11] and the alignment of magnetic nanorods/-wires can be exploited to manipulate the optical transmission of a colloidal suspension.[Kle09] Furthermore, nickel nanorods can be applied as intrinsic probe for the measurement of the shear modulus of a ferrogel.[Ben11]

Only a few publications can be found dealing with the manipulation of the viscoelastic properties of colloidal elongated particle suspensions. One has to mention the work by Lopez-Lopez *et al.*, Bell *et al.* and de Vicente *et al.* in the field of magnetorheological fluids.[LL07] [Bel08] [dV09] [dV10] In the area of ferrofluids, only the research group of Prof. Birringer (Saarland University) has explored the potential of transition metal nanorods for applications as ferrofluids.[Doe07] [Gün08] The PhD thesis of Dr. Christian Lang and the out-coming publication "Magnetic nanorods: Genesis, self-organization and applications" by Birringer *et al.* are men-

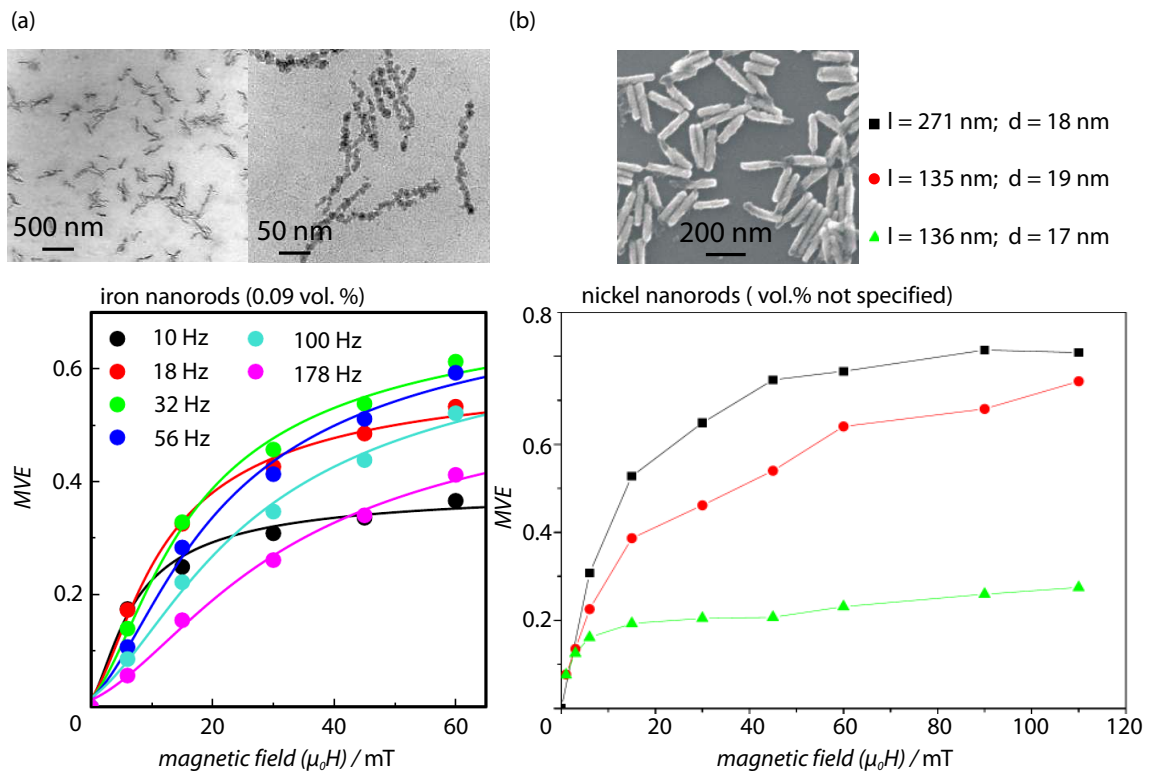


Figure 2.9: (a) Transmission electron microscopy images of the iron nanorods and the MVE as a function of the applied magnetic field for a liquid suspension of them (0.09 vol %) at different shear frequencies.[Lan05] (b) Scanning electron microscopy image of nickel nanorods synthesized by Günther. The MVE of nickel nanorod ferrofluids (concentration not mentioned) with different rod lengths in dependence of the applied magnetic field.[Gün11]. In both cases, a saturating behavior of the MVE is apparent, which is attributed to the elongated shape of the suspended particles. (A detailed discussion of such a behavior is given in subsection 4.3.3 in chapter 4.) Original data and images have been published by Lang [Lan05] and Günther [Gün11] for subfigures (a) and (b), respectively. For the sake of clarity, adaption, image processing, and rearrangement were performed.

tioned in particular, since magnetoviscosity measurements of one colloidal nanorod suspension are presented and discussed.[Lan05] [Bir08] Iron nanorods were synthesized by a magnetic field-assisted aerosol synthesis route. Indeed, the shape of the nanorods can be described as chain of connected grains/particles with aspect ratios between 20 and 25 at a mean diameter of 11 nm (figure 2.9 (a)). The iron nanorods were suspended in heptane leading to a final magnetic volume concentration Φ of 0.09%. The determined MVE (normalized to the volume concentration Φ of the liquid suspension) was one to two orders of magnitude larger than the normalized MVE of a reference ferrofluid. Moreover, a reduced shear thinning effect was also observed in the nanorod suspension, thus showing the promising properties of such

elongated nanoparticle ferrofluidic suspensions. Annegret Günther of the same research group synthesized liquid suspensions consisting of nickel nanorods—length from 80 nm to 240 nm and a diameter (22 ± 5) nm—via electrodeposition in porous anodic alumina and subsequent release from the supporting template.[Gün11] In her PhD thesis, she studied the hydrodynamic properties of such colloidal suspensions in terms of the rotational diffusion coefficient. In the last chapter as an outlook, a magnetic field-dependent as well as a shear frequency-dependent measurement is shown (figure 2.9 (b)). However, neither a detailed physical explanation nor a comparison with standard ferrofluids was given in the framework of her thesis.

Martsenyuk *et al.* derived an expression for the viscosity increase $\Delta\eta$ in a standard ferrofluid which can be used to deduce a magnetic field-dependent $\Delta\eta$ for elongated magnetic particle suspensions.[Mar74] [Lan05] [Bir08] Solving the Fokker-Planck equation, valid for homogeneous small shear flows, results into

$$\Delta\eta = \frac{1}{4}\Phi\tau_{\perp}M(B)B, \quad (2.42)$$

in which $\Delta\eta = \eta(B) - \eta_0$ denotes the difference of the apparent viscosity in an applied magnetic field $\eta(B)$ —magnetic induction in vacuum $B = \mu_0 H$ —to the viscosity without magnetic field η_0 .

The transversal relaxation time τ_{\perp} is a function of the Brownian relaxation time and of the Langevin function $L(\alpha) = \coth \alpha - \frac{1}{\alpha}$ in which $\alpha = \frac{mB}{k_B T}$

$$\tau_{\perp} = \frac{2\tau_B}{2 + \alpha L(\alpha)}. \quad (2.43)$$

The Langevin function is also used to approximate $M(B)$, which denotes the field-dependent magnetization of the ferrofluid and can be approximated under the assumption of small shear frequencies with $M(B) = M_s L(\alpha)$. Furthermore, the geometry of the particle is related to the Brownian relaxation time via the rotational diffusion coefficient D_r by

$$\tau_B = \frac{1}{2D_r}, \quad (2.44)$$

which amounts for a sphere with the volume V to

$$D_r^{sphere} = \frac{k_B T}{6\eta V}. \quad (2.45)$$

Inserting the latter equation as well as 2.43 and 2.44 into equation 2.42 allows for the derivation of the rotational viscosity which equals equation 2.39 for $\beta = 90^\circ$ —magnetic field perpendicular to the vorticity.

$$\Delta\eta = \frac{3}{2}\eta_0\Phi \cdot \frac{\alpha - \tanh \alpha}{\alpha + \tanh \alpha} \quad (2.46)$$

Unfortunately, no analytical solution exists for the rotational diffusion coefficient of rod-like particles. The problem has been tackled in the slender-body theory by several authors.[Bro60a] [Bro60b] [Bre74] [Tir80] [Bro81] [Tir84] [Ilg02] [Ilg03] All authors showed that the rotational diffusion coefficient D_r of a spheroid or a cylinder with the (geometric) particle volume V can be expressed by

$$D_r = \frac{k_B T}{6\eta V c_n}. \quad (2.47)$$

The correction term c_n is a function of the aspect ratio n which is defined as the ratio of the length l to the diameter d and correlates the (geometric) particle volume with the hydrodynamic volume. However, the models of the several authors differ slightly depending on the boundary conditions and the exact shape of the particle. If the latter equation as well as 2.43 and 2.44 are inserted into equation 2.42, one ends up with

$$\Delta\eta = \frac{3}{2} c_n \eta_0 \Phi \cdot \frac{V B M_s}{k_B T} \cdot \frac{L(\alpha)}{2 + \alpha L(\alpha)}. \quad (2.48)$$

Further simplification can be proceeded by normalizing η_r to the carrier liquid viscosity $\text{MVE} = \Delta\eta \eta_0^{-1}$, using an aspect ratio-dependent correction term $C_n = \frac{3}{2} c_n$ and α as the ratio of magnetostatic to thermal energy.

$$\text{MVE} = C_n \cdot \Phi \cdot \frac{\alpha - \tanh \alpha}{\alpha + \tanh \alpha} \quad (2.49)$$

The shape correction function C_n is compared for several models in figure 2.10 revealing a good agreement for all models at aspect ratios below ten—deviation <12%. In brief, the derived equation 2.49 can be treated as an increase of the viscosity based on the model of the rotational viscosity but this time for non-interacting, elongated nanoparticles.

2.3.4 Hybrid Suspensions

Bimodal hybrid magnetorheological fluids prepared by mixing two different liquid suspensions—either a ferrofluid with a magnetorheological fluid or suspensions consisting of differently shaped particles—have been utilized to mitigate the sedimentation of the larger particles.[Chi01] [Par01] [Shi04] [LL05] [Wer06] [Igl12] The enhanced stability performance is attributed to a cloud of (functionalized) nanoparticles around the micron-sized spheres formed due to the permanent magnetic moment of the latter. The cloud of nanoparticles prevents the permanent magnetic microspheres for irreversible agglomeration and improve the re-dispersion after a magnetic field has been applied. Similar improvements in the sedimentation have also been observed by Ngatu *et al.* who replaced micron-sized iron spheres in a magnetorheological fluid by electrodeposited μm -long nanowires (diameter 260 nm).[Nga08] Thus,

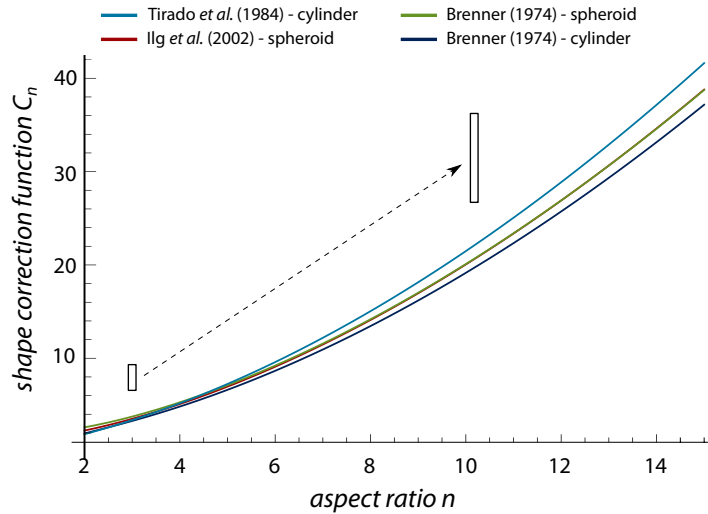


Figure 2.10: Plot of the shape correction functions C_n in dependence of the aspect ratio n for several models: for blunt-ended cylinders (bright blue and dark blue) [Tir84] [Bre74] as well as prolate spheroids (green and red) [Bre74] [Ilg02] [Ilg03]. The two differently derived shape functions for the prolate spheroids match well, only a slight deviation can be observed at small aspect ratios (≈ 2), whereas the shape functions for the cylinders differ more prominently caused by the different approximations made. The exact equations for the different models are displayed in the appendix A.2. The scheme illustrates the geometry of an object with increasing aspect ratio.

both major bottlenecks of magnetorheological fluids can be overcome or at least minimized by preparation of hybrid magnetorheological suspensions.

Moreover, adding non-magnetic (micron-sized) materials to a magnetorheological fluid increases its field-dependent viscous stress. [Lev97] [Uli10] Simulation by Ulicny *et al.* showed that the interactions of magnetostatic (only magnetizable spheres), short-range repulsive (all spheres), and hydrodynamic forces could be responsible for the observed effect. However, the authors themselves motivate further investigations to tackle that problem in detail. At the same time, a drastic increase in the apparent viscosity of a ferrofluid was reported upon the addition of a small number of elongated, non-magnetic tobacco mosaic virus particles (TMV) to a commercially available liquid suspension consisting of cobalt ferrite nanoparticles (figure 2.11 (a)–(c)). [Wu10b] [Wu10c] In contrast to the ‘hand-waving’ explanation of Ulicny and co-workers, Wu *et al.* showed that the observed increased MVE is due to electrostatic interaction between positive surface residues of the tobacco mosaic viruses and negatively charged magnetite particles. Thereby, large virus-magnetic nanoparticle clusters as displayed in subfigure (d) are formed which increase the apparent viscosity significantly. If the surface of the tobacco mosaic viruses mainly carries negative residues, no additional MVE can be observed since the cluster formation is hindered by repulsive electrostatic interaction. [Wu10b]

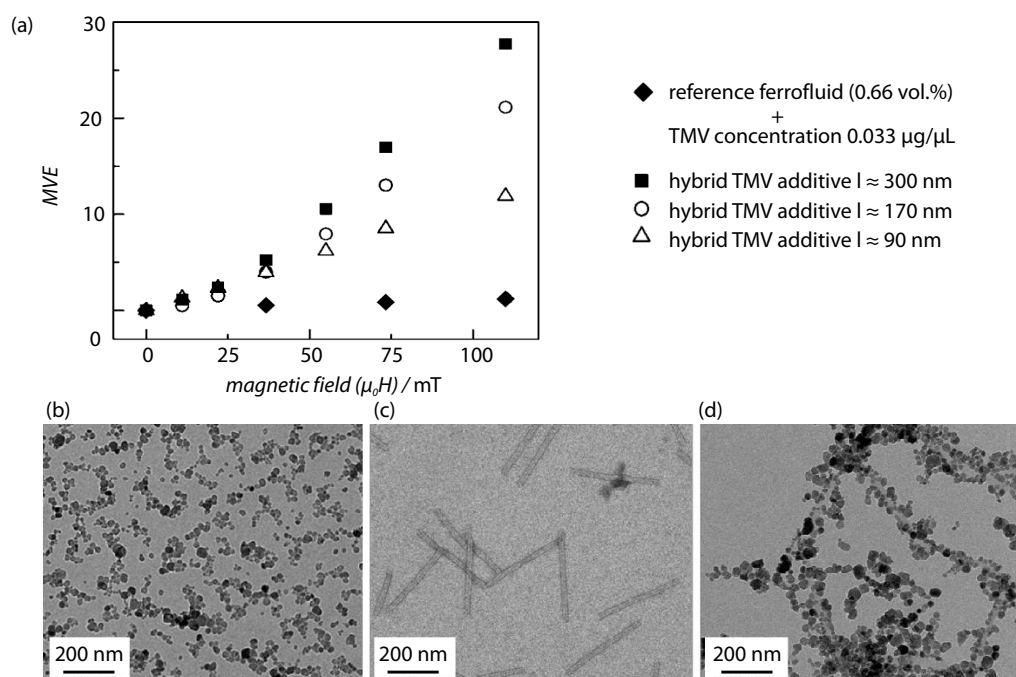


Figure 2.11: (a) MVE of a spherical particle ferrofluid and three hybrid suspensions—tobacco mosaic viruses with different length served as organic additives—as a function of the applied magnetic field. The observed MVE increases with increasing length of the TMV particles at a constant additive concentration. (b)–(d) TEM images of the spherical particles, the viruses and the clusters. Original data and images have been published by Wu *et al.*[Wu10b] For the sake of clarity, image processing and rearrangement were performed.

2.3.5 Sum-Up

A list of keywords is given as a short summary of this chapter. The topics will appear later in this work and run like a common thread through the thesis:

- magnetite, its unique Verwey transition and the isotropic point,
- superparamagnetism,
- complex viscosity and shear moduli,
- ferrofluids and hybrid magnetic liquid suspensions,
- the concept of rotational magnetoviscosity and the extension for elongated particles,
- chain and microstructure formation as reason for the observed MVE,
- shear thinning effect.

3 Templated Synthesis & Structural Investigation

Wet-chemical preparations methods for spherical (or polygonal) magnetic nanoparticles allow, on the one hand, for the synthesis of sufficiently concentrated liquid suspensions with a narrow particle size distribution.[Lu07] [Tej09] But on the other hand, varying the shape from spherical to elongated particles, and perhaps even to tubular ones, turns out to be quite difficult because of the high sensitivity to growth conditions, and only few reports are published.[Par00] [Cor01] [Liu06] [Wu10a] Template-assisted synthesis routes overcome this problem, since the geometrical parameters, namely length and diameter, are exactly and independently tunable from a few nanometers up to several microns.[Whi93] [Gar99] [Huc00] [Pri05] [Ara07] [Ana09] However, the major shortcoming of a template-based synthesis approach is the yield of nanoobjects per batch which is bound to the limited substrate size.[Mar94] Sample sizes in research laboratories usually range from a few square millimeters to a few square centimeters. To increase the template area by only one order of magnitude, all synthesis processes have to be reconsidered and have to be appropriately adjusted to allow for a technical scale-up. This chapter starts with a brief description of the template preparation and the necessary scale-up of which (section 3.1). The second part (section 3.2) deals with atomic layer deposition (ALD), an unique technique based on sequential self-limited gas-surface reactions. A short, general introduction to ALD is given followed by a detailed description of the ALD processes of the two materials used in this work, namely silica and iron oxide. Structural and magnetic characterization of iron oxide thin films shed light onto the synthesis process, its quality, and the magnetic properties of these films (as shown in section 3.3). The fourth part (section 3.4) merges the template preparation with ALD to synthesize iron oxide nanotubes. A preparation route for iron oxide nanotubes of low aspect ratios is described and the results of structural as well as magnetic investigation of the iron oxide nanotubes are presented. Finally, a synthesis approach for nickel nanorods is introduced in section 3.5. The third dimension of a porous template is utilized by nickel-copper-multilayer electrodeposition. Subsequent selective etching of the sacrificial copper layers in the multisegmented nanowires allows for the preparation of short, magnetic nickel nanorods.

3.1 Template Preparation & Two-Dimensional Scale-Up

The template-based synthesis route chosen in this work bases on the use of porous anodic alumina as template. It is well known that controlled electrolytic oxidation of pure aluminum can result in the formation of nanopore arrays.[Kel53] [Dig69] A two step-anodization process leads to a hexagonally self-ordered porous anodic alumina (AAO) membrane with approximately 10% porosity as schematically displayed in figure 3.1 (a) and figure 3.2 (a) and (b).[Mas95] [Nie02] After removal of the porous alumina layer of the first anodization by chromic acid, concave hemispheres remain on the aluminum chip at the former positions of the alumina pore extremities at the barrier layer. These indentations serve as seeds for the pore growth in the second anodization. A scheme of the major reactions during anodization is shown in figure 3.1 (b). The aluminum is oxidized to Al^{3+} in an acidic electrolyte by a certain applied electric field. Further reaction of the aluminum ion with water leads to the formation of aluminum oxide. The arising hydrogen of this reaction is reduced at the cathode. Simultaneously, localized electric field-enhanced dissolution of the Al_2O_3 results in a pore growth in the alumina layer. Self-ordering of the pores occurs due to the minimization of the apparent mechanical stress during the electrochemical oxidation process of the aluminum metal.[Jes98] The anodization process itself, and thus the resulting pore structure (geometry, ordering, growth rate) depends mainly on the electrolyte, process temperature and applied oxidation potential.[Li98a] [Li98b] General, approximated relationships between the applied voltage and the geometrical properties are:

- interpore distance $\sim 2.5 \text{ nm V}^{-1}$
- pore diameter $\sim 0.9 \text{ nm V}^{-1}$
- barrier layer thickness $\sim 1.5 \text{ nm V}^{-1}$

The anodization of aluminum chips with an area of a few square centimeter was well established in the group in 2008. However, a rough calculation of the amount of nanoobjects needed for ferrofluidic suspensions—one nanopore corresponds to one nanotube—made a scale-up of the synthesis inevitable. Since the chambers of the atomic layer reactors used in this work can only deal with substrate sizes up to four inch diameter, the Al substrate size was increased to 10 cm in diameter finally corresponding to a nanoporous membrane area of 64 cm^2 . A scale-up of the complete anodization setup was performed as displayed in the appendix in figure A.1. The platinum wire typically used in electrochemistry was replaced by a silver wire for economical reasons. Pt is known to be outstanding inert against etching and oxidation. However, in the acidic electrolytes used in this work, namely oxalic and sulfuric acid, the silver is passivated by a thin, conductive and stable silver oxide

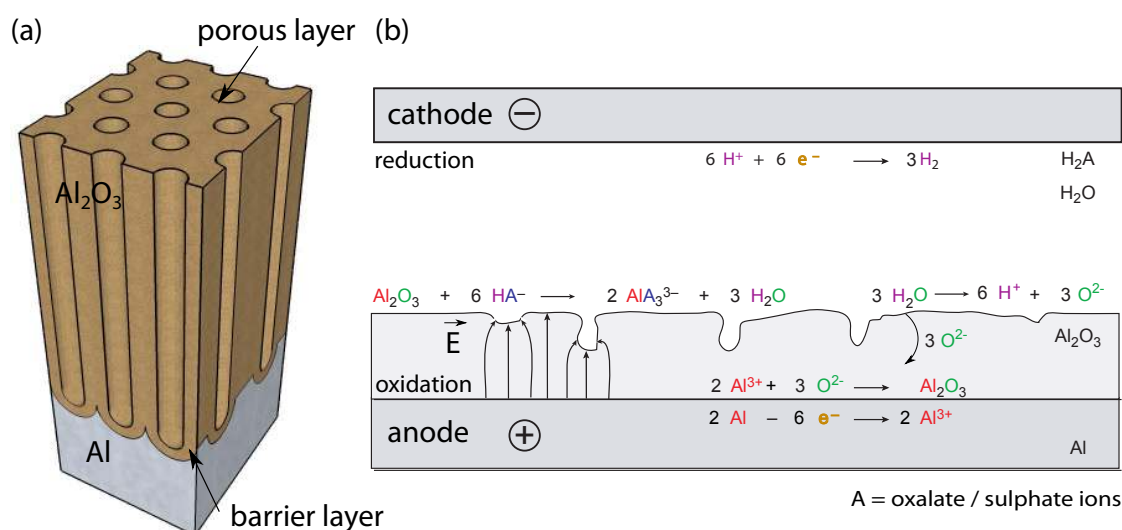


Figure 3.1: (a) Scheme of a hexagonally ordered, nanoporous alumina membrane grown by electrolytic oxidation of aluminum. (b) Schematic drawing of the electrolytic oxidation process of aluminum and the electrical field-enhanced alumina dissolution. Chemical equations symbolically represent the major chemical reactions during the process.

layer. Prior the first anodization, an electropolishing process has to be applied to flatten the surface of the Al substrate. Current densities in the order of 0.4 A cm^{-2} (substrate area) are flowing through the cell/electrolyte/aluminum chip in the first seconds. Again for economical reasons, a cheap solution was invented to overcome the problem of the high electrical power consumption. Two motorbike Pb/Pb(SO₄)₂ batteries each with 12 V were connected in series resulting in an electropolishing voltage of 24 V allowing for the supply of more than 25 A during the first seconds. For further, more detailed information about the process conditions and the scale-up used in this work please refer to the experimental section of Zierold *et al.*[Zie11]

Accurate adjustment of the pore length by controlling the overall charge (density) passed through the system during the anodization reaction allows for tuning the aspect ratio of the prospective iron oxide nanotubes. A linear relationship between pore depth and charge density was found by scanning electron microscopy (SEM) images of the cross section of the prepared porous membranes (figure 3.2 (a)). Additionally, performed transmission electron microscopy (TEM) of released nanotubes¹ support the linear behavior (as displayed in subfigure (c)). The pore length can also be adjusted by the anodization time—being experimentally much more simple and suitable than a charge density controlled setup—under the condition that all parameter which influence the absolute current flowing during anodization, such as anodized area, electrolyte concentration and temperature, oxidation voltage, to name a few of them, are kept constant (figure A.2 in the appendix).

¹The synthesis and release procedure is described in more detail in section 3.4.

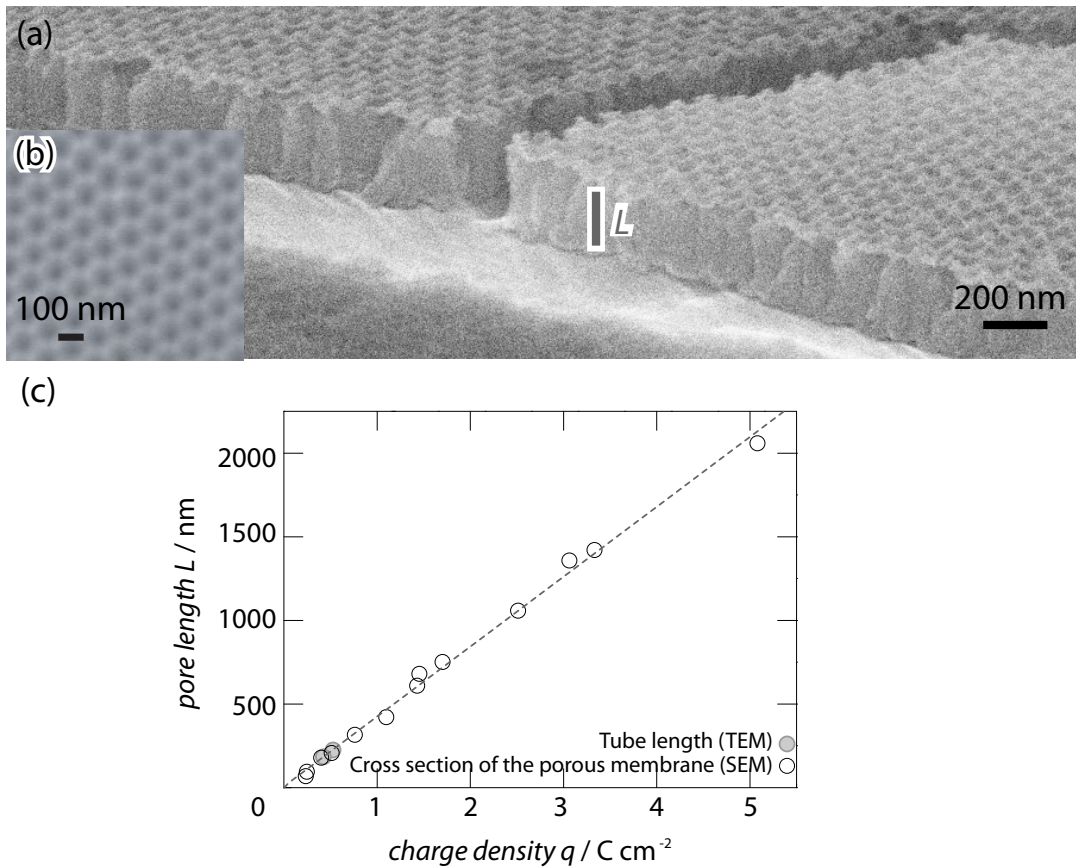


Figure 3.2: SEM images of a tilted cross section (a) and a top side (b) of porous anodic alumina membranes grown in oxalic acid solution. The pore length L is plotted as a function of the total transferred charge per unit area q during the oxidation process. The pore diameter amounts to (40 ± 5) nm. Data points displayed by open and filled circles correspond to cross-sectional SEM images of the porous alumina membranes and TEM images of released nanotubes, respectively. The linear fit amounts to $L = (417 \pm 7) \text{ nm cm}^2 \text{ C}^{-1}q + (7 \pm 15) \text{ nm}$.

3.2 Atomic Layer Deposition: From Thin Films To Nanotubes

Atomic layer deposition (ALD) provides the unique ability—compared to the standard physical and chemical vapor deposition techniques—to perfectly mold porous alumina templates without shadowing effects. A short introduction into the principles of ALD is given, followed by the description of the developed deposition process for silica. Finally, the iron oxide process and its subsequent thermal reduction is presented.

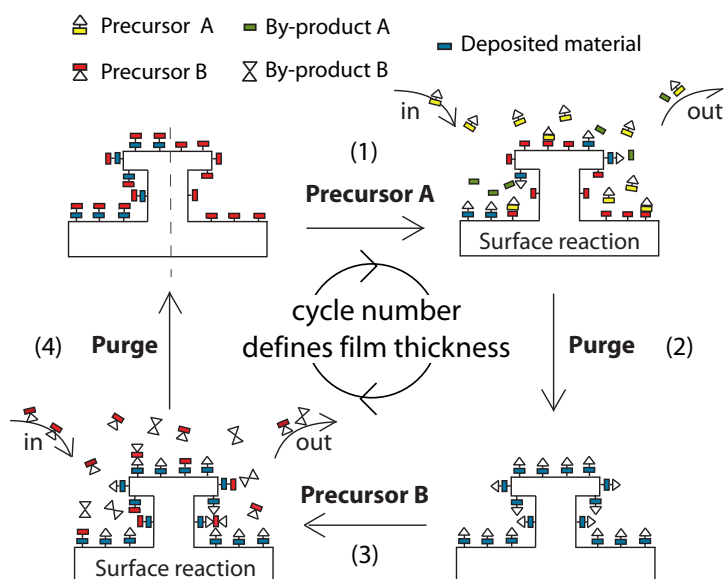


Figure 3.3: Schematic drawing of an ALD cycle with two different precursor species. One ALD cycle consists of a pulse of precursor **A** (1) which reacts in a self-limiting manner with the surface. After purging of the chamber (2), the precursor **B** is brought to the intermediated surface, reacts there in a self-terminating behavior, and deposits a monolayer of the desired material (3). Subsequently, the reaction chamber is purged again (4). Since the (resulting) surface residues after one ALD cycles can react with precursor **A**, a sequential deposition routine is possible allowing for an exact thickness control by adjusting the number of cycles.

3.2.1 General Introduction of ALD

Contrary to the classical chemical vapor deposition, atomic layer deposition allows for conformal deposition by using sequential, self-limiting gas-solid surface reactions. Since the deposition is not limited by the absolute mass transport of precursor molecules, homogeneous coatings with sub-nm control thickness can be achieved even on three-dimensional substrates. ALD is diffusion-limited which means on the one hand, no line-of-sight from precursor source to the substrate is required. But on the other hand, the molecules need sufficient time for diffusion and surface-side reaction. In general, atomic layer deposition provides continuous, pinhole-free films with a low content of residual impurities.[Puu05] [Geo10] [Mii13]

A typical ALD cycle consists of four steps as displayed in figure 3.3:

1. *Pulse 1:* The substrate is defined by certain surface species and the precursor **A** is brought to the substrate's surface.
2. *Purge 1:* After the completed, self-terminating surface reaction, the non-used precursor **A** molecules as well as the reaction by-products are pumped away and the reaction chamber is purged.

3. *Pulse 2*: At this point, the substrate remains in an intermediate surface state. The second precursor **B** is pulsed into the ALD chamber and reacts in self-limiting manner with the residues of **A** chemisorbed to the substrate.
4. *Purge 2*: After the completed gas-solid surface reaction, the reaction chamber is purged from the by-products and the non-used precursor **B** molecules. The surface groups after one ALD cycle allow for a next reaction with precursor **A**.

After one ALD cycle—in the ideal case—the substrate presents the same surface residues as at the beginning, but an additional monolayer of the desired material has been deposited. It is obvious that the thickness of the film deposited by ALD can be adjusted by the total amount of cycles proceeded. Since typical deposition rates of ALD processes range from 0.1 Å to 1.5 Å, thickness control in the (sub-)nm range can be achieved.

At the “[...]case study for the trimethylaluminum/water process” Puurunen describes the most important features and main characteristics of ALD in detail. A large and almost complete summary of ALD processes till 2005 is given in this review.[Puu05] George’s review published in 2010 summarizes the major trends and important developments in the ALD community in the last decade.[Geo10] Especially new ALD process technologies (like plasma-enhanced, roll-to-roll, atmospheric-pressure or spatial resolved ALD) and (polymer) molecular layer deposition (MLD) have to be mentioned, since the amount of publications and contributions to international conferences has drastically increased in the last years.[Kes11] [Les11] Recently, Miikkulainen from the Puurunen group published a review article about ALD in general, processes and trends with over 2300 references.[Mii13] Due to its self-limiting nature, ALD is outstandingly suited for the coating of high-aspect ratio (nano)structures. In such substrates, such as opals, nanoporous membranes, bio-materials, and nanoparticles, to name a few, ALD is often the only suitable technique to reach a conformal coating without shadowing effects.[Kne07] [Bae11]

Two ALD reactors have been used in the framework of this thesis. In the beginning, the depositions were carried out in a commercially available *Savannah 100* system *Ultratech, Inc.* (formerly *Cambridge Nanotech, Inc.*). Expansion of the ALD research activities of the Nielsch group led to an increased demand of ‘user time’ in 2009. Unfortunately, budget limitations did not allow for purchasing a commercial reactor (minimum price 120 000 \$). Thus, a home-made ALD reactor operating in stop-mode—the vacuum pump can be disconnected from the chamber by an extra valve allowing for long exposure times which are necessary to coat high-aspect ratio samples homogeneously—was designed and constructed.² The reactor is displayed

²The main construction work had been performed by Reinhold Meißner (technician, Physics Department, University of Hamburg) with support by the mechanical workshop of the Institute for Applied Physics. The controlling software was programmed by Stephan Martens (PhD student, Physics Department, University of Hamburg).

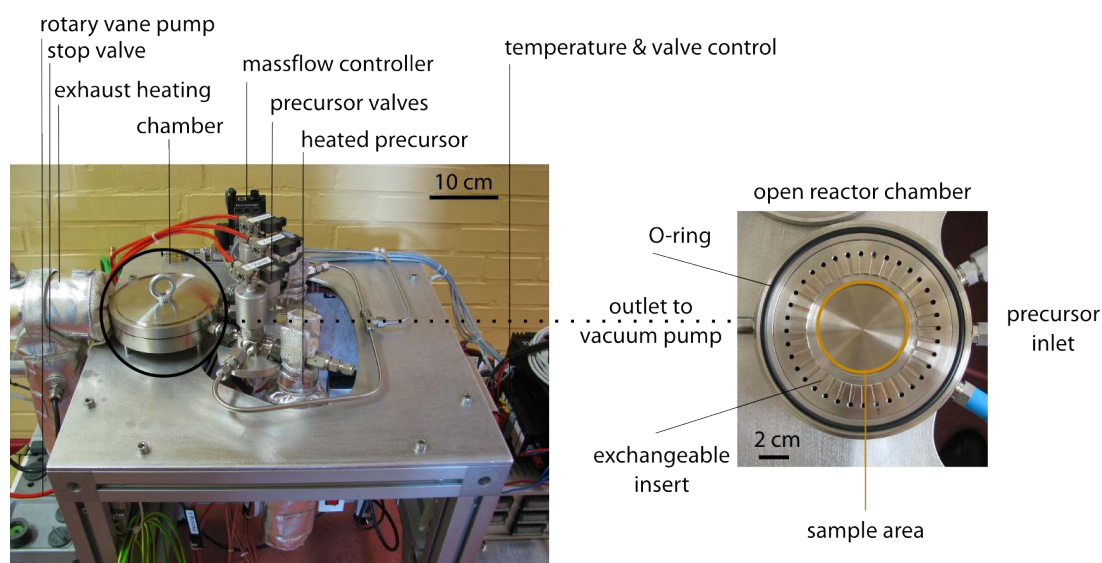


Figure 3.4: Photographs of the first home-made ALD reactor and of the opened reaction chamber. The main parts are labeled. Please note that the stop valve, which allows for long diffusion times of the precursor in the reaction chamber, is covered by the heating jacket. The exchangeable insert (displayed in the right photograph) allows for an improved homogeneity of the precursor flow and/or suitable adjustment of the chamber area (highlighted in yellow) depending on the specific sample specifications.

in figure 3.4 and allows for the mounting of three precursors in parallel. The specifications, such as chamber and precursor temperature, vacuum, chamber size, pulse times, to name a few of them, are comparable to commercially available starter models, but for less than a fourth of the market price. After an initial test phase, the home-made setup has been integrated in the everyday laboratory equipment and has been applied for the sample preparation in this thesis. Since then, four more ALD reactors have been built in our group, partly for specific research activities, namely ALD deposition on powders or into nanochannels with an aspect ratio—length to pore opening—of more than 10 000.

3.2.2 ALD of Silicon Dioxide

To enable the wet-chemical release of the synthesized iron oxide nanotubes (section 3.4) from the supporting porous alumina template, deposition of outer and inner protective tubular layers are inevitable. Since the template used in this work is aluminum oxide, the ‘gold standard’ alumina ALD process from trimethyl aluminum + water cannot be used. Even though the quality of the alumina films deposited by ALD is better in terms of refractive index, density, impurities, etc. compared to the electrochemical synthesized AAO membranes, the wet-chemical etching selectivity between AAO and ALD-prepared alumina is too low.

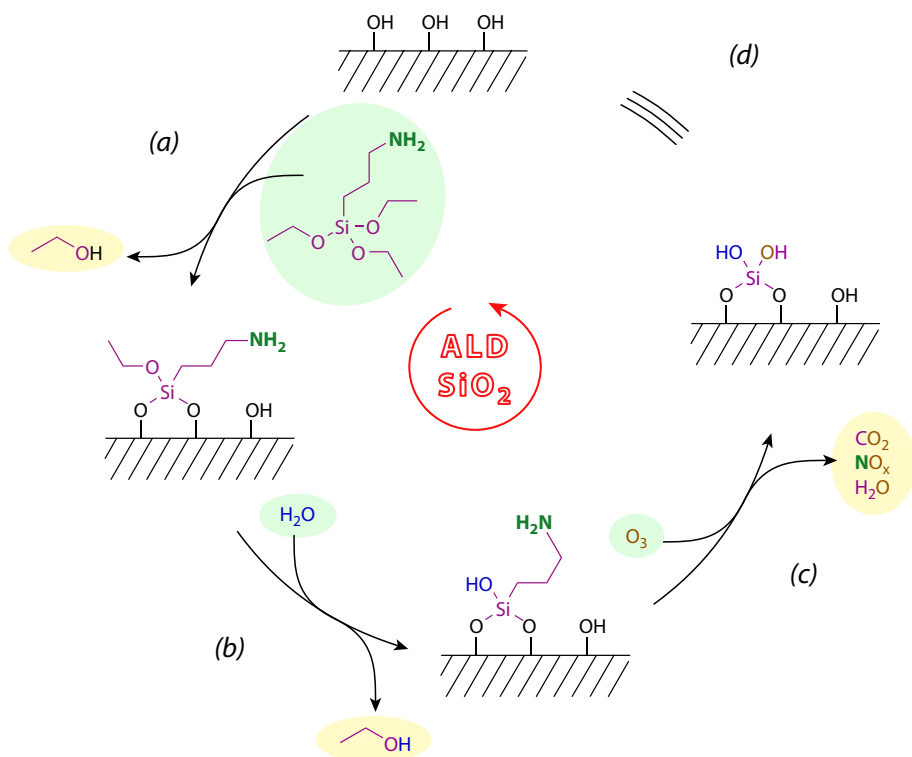


Figure 3.5: Schematic explanation of the developed three-step silica deposition process. (a) Chemisorption of the 3-aminopropyl triethoxysilane via self-catalysis at the surface hydroxy groups. (b) Self-catalytic hydrolysis of the ethoxy groups of the silan precursor with water. (c) Combustion reaction with ozone to remove the aminoalkyl moiety. (d) Hydroxy groups are present on the surface of the deposited silica unit.

Silicon dioxide is well known for its resistivity against acidic and alkaline solution. Furthermore, it exhibits insulating properties and promises sufficient biocompatibility, thus providing a wide possible range of application in electronics or medicine. However, an applicable ALD silica process was not available back then. Therefore, and with regard to precursor availability, costs and process conditions, a novel, low-temperature deposition process for silicon dioxide was developed. The details of the ALD process itself as well as the physical properties of the silica have been published elsewhere.[Bac08] [Hil10] Only a short description of the deposition process and the properties of the deposited silica are presented herein. Fergusson *et al.* proposed a deposition reaction of tetraethoxysilane $\text{Si}(\text{OEt})_4$ and water in presence of an ammonia catalyst.[Fer04] It was known from surface functionalization chemistry that a triethoxysilane bearing an aminoalkyl moiety can be hydrolyzed without additional catalyst. The labilizing process of the strong Si–O bond can be called *self-catalytic*, since the silane molecule carries the catalyst in form of a functional moiety within itself, and works as substrate and catalyst at the same time. The three-step process

is schematically shown in figure 3.5. First, anchoring and chemisorption onto the substrates is achieved by a self-catalyzed hydrolysis process of the ethoxy moieties with surface hydroxy groups (a). Second, the remaining ethoxy groups are removed by self-catalytic hydrolysis with the water acting as the second precursor (b). In the third step, the catalyzing aminoalkyl moiety is burned by oxidation with ozone (c), resulting in one deposited layer of silica which presents Si–OH bonds at the surface allowing for a repetition of this cycle (d).[Bac08]

The growth rate of this process is found to be (0.6 ± 0.1) Å per cycle, constant in a substrate temperature range from 120 °C to 250 °C and independent of the precursor pulse times—minimum tested pulse times were 1 s, 0.3 s and 0.1 s for the silane, water and ozone, respectively—and exposure times. X-ray photoelectron spectroscopy (XPS) and elastic recoil detection analysis (ERDA) reveal almost stoichiometric silicon dioxide with a few amount of nitrogen and hydrogen impurities. The carbon level is below the detection limits of the setups used. X-ray diffraction data in combination with atomic force microscopy reveals an amorphous silica film with a rms roughness of 1.5 Å. The small deviation of the refractive index $\Delta n = 0.008$ measured by spectroscopic ellipsometry and compared to literature (bulk) confirms the high quality and the chemical purity of the film. Rapid thermal annealing (RTA) of the as-deposited film reduces the amount of impurities down to a level comparable to thermally grown silica. Furthermore, RTA significantly improve the wet-chemical etching resistivity in buffered hydrofluoric acid and the electrical properties, e.g. dielectric constant, breakdown voltage, conductance.[Hil10]

3.2.3 ALD of Iron Oxide Thin Films and Reduction to Magnetite

Iron oxide is in special interest of scientists and engineers because it provides substantial potential for various applications, e.g. as catalyst, in solar cells, in gas sensors, and for solid oxide fuel cells, just to name a few of them.[Cor03] Iron oxide deposited by ALD has been applied for basic research on magnetic domain wall movement in magnetite nanotubes,[Bac07] [Esc08] [Bac09] [Pit09] [Alb10] [Alb11] catalytic oxidation of water, [Gem12] solar cells,[Kla11] ferrofluids,[Zie11] and synthesis of ferrite films and nanotubes by using a supercyclic ALD process.[Cho10b] [Cho11]

Atomic Layer Deposition

Several ALD processes for the deposition of various iron oxide phases are published. A comprehensive overview is given in table 3.1. However, the most ALD recipes offer a lack of feasibility for our purpose. Either the growth rate is too small, the high temperature processes are not suitable for our home-made ALD reactor setup, granular films are obtained (especially at high temperatures), significant carbon

precursors	process temperature	deposited phase	reference
FeCp ₂ O ₂	350 °C to 500 °C	phase mixture	[Roo08] [Sch09] [Sch11]
FeCp ₂ O ₃	170 °C to 200 °C	amorphous	[Mar11]
	> 200 °C	α-Fe ₂ O ₃	[Mar11] [Kla11]
Fe(acac) ₃ O ₂	20 °C to 150 °C	not reported	[dR02]
Fe(thd) ₃ O ₃	160 °C to 310 °C	α-Fe ₂ O ₃ on Si(100)	[Lie05]
	160 °C to 310 °C	γ-Fe ₂ O ₃ on MgO(100)	
FeCl ₃ H ₂ O	350 °C to 400 °C	γ-Fe ₂ O ₃	[Aro08]
	> 400 °C	α-Fe ₂ O ₃	
Fe ₂ (O ^t Bu) ₆ H ₂ O	130 °C to 170 °C	not reported	[Bac07]

Table 3.1: Literature overview of investigated iron oxide ALD processes. The FeCp₂-O₃ process was mentioned by Escrig and co-workers for the first time in 2008, but without studying the process itself.[Esc08]

incorporation is observed, or the self-limiting nature of ALD couldn't be proven in high-aspect ratio nanostructures.

The synthesis route for magnetic iron oxide nanotubes—using ferrocene plus ozone as precursors and a subsequent reduction process in argon-hydrogen-atmosphere (figure 3.6)—was mentioned the first time by Escrig *et al.* in 2008.[Esc08] In the following years, this process was applied several times for the synthesis of magnetic iron oxide nanotubes and the physical study of the magnetic reversal mechanisms in nanostructures.[Bac09] [Pit09] [Alb10] [Cho10a] [Alb11] However, a complete study of this ALD process based on precursor combustion was first published in 2011.[Mar11] In the same year, the appearance of the Verwey transition was measured in iron oxide nanotubes synthesized by ALD for the first time, proving the high quality magnetite phase achieved by the reduction process.[Zie11] The growth rate of 1.4 Å cycle⁻¹ proposed by Martinson *et al.* could not be reached in the ALD setups used in this work. Depending on the specific ALD reactor and the ozone generator attached to, growth rates have been established in stop-mode operation between 0.15 Å and 0.3 Å per cycle. A plot of the film thickness determined by X-ray reflectivity as a function

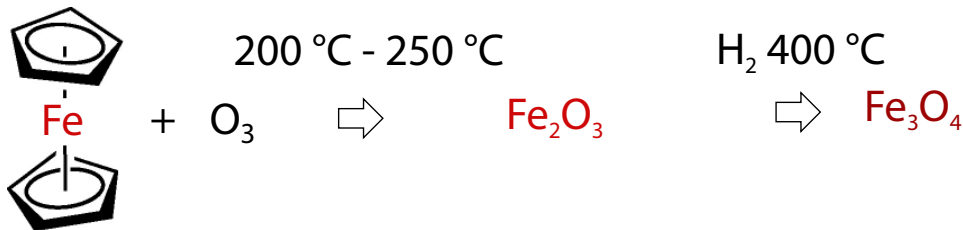


Figure 3.6: Reaction scheme the iron oxide deposition. An iron oxide layer is formed in a combustion process of ferrocene with ozone. Subsequent forming gas annealing converts the amorphous film (Fe₂O₃) into the ferrimagnetic magnetite (Fe₃O₄) phase.

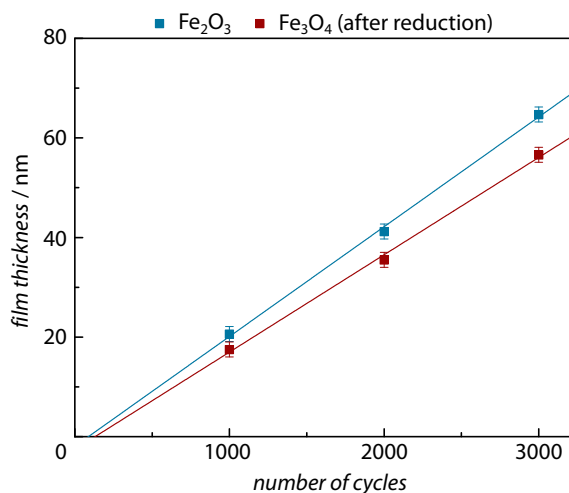


Figure 3.7: X-ray reflectivity measurements allow for thickness determination as a function of the number of ALD cycles. The growth rate can be determined by a linear fit and amounts to 0.22 \AA per cycle with a nucleation delay of around 80 cycles. After reduction, each thickness was reduced by about ten percent leading to a ‘magnetite synthesis growth rate’ of 0.20 \AA per ALD cycle.

of the number of ALD cycles is shown in figure 3.7 revealing a linear growth.³ A nucleation delay—positive intercept with the x-axis—can be found and amounts to ≈ 80 cycles. This observation is in good agreement with the published value by Martinson and co-workers taking the six to seven times reduced growth rate into account. Especially, ozone dose times of more than 200 s are needed to reach a constant, saturated growth rate. Since our reactors are operated in stop-mode with a permanent nitrogen flow ranging from 10 sccm to 50 sccm, such long pulse/exposure time would result in an unwanted, complete ventilation of the chamber and might cause a parasitic CVD. However, at the experimental parameters accessible by our setups, Martinson *et al.* reported similar growth rates.[Mar11]

The iron oxide films deposited at a temperature of $200 \text{ }^\circ\text{C}$ are amorphous as revealed by XRD analysis.⁴ Increasing the deposition temperature to $230 \text{ }^\circ\text{C}$ results in a polycrystalline iron oxide thin film, in which α - as well as the γ Fe_2O_3 could be assigned (Starting point of the in-situ XRD measurements as displayed in figures 3.8 (a), 3.9 (a). A complete $\theta/2\theta$ before thermal treatment is displayed in figure A.4 in the appendix.) This observation is in good agreement with the publication of the Elam group which detected the hematite phase at a deposition temperature of $250 \text{ }^\circ\text{C}$ and predominantly amorphous material at $200 \text{ }^\circ\text{C}$.[Mar11]

³XRR measurements and data evaluation were performed by Lewis Akinsinde (technician) and Charlie Le Lam (master student, Physics Department, University of Hamburg (2012))

⁴Private Communication from Sven Barth (Institute of Materials Chemistry, Vienna University of Technology (Austria)) in the framework of a collaboration project (2012).

Reduction process

The conversion from the iron oxide as deposited into the magnetite phase occurs in a reduction reaction, in which oxygen is partly removed from the film. Thus, a part of the Fe^{3+} is reduced to Fe^{2+} —the oxidation state is changed. A comparative overview of iron oxide reduction processes with respect to reduction time, reduction temperature, and forming gas atmosphere was given by Pineau *et al.* in 2006.[Pin06] A general parameter set can be extracted for the reduction of iron oxide nanostructures to magnetite from several references:[Reg81] [Bac07] [Gav07] [Wan09] [Sal11]

- temperature range between 300 °C to 400 °C for minutes up to a few hours,
- a volume ratio of 5 % to 10 % hydrogen in an inert gas,
- atmospheric pressure,
- a permanent flow of the forming gas.

However, optimization and adjustment of the reduction process on-site, especially in terms of temperature and time, has to be executed since over-reduction (to iron or wustite FeO) or incomplete reduction is conceivable.[Pin06] [Pin07]

In this work, not only the template synthesis approach was scaled up, but also the reduction setup had to be enlarged to allow for the reduction of templates up to a diameter of 10 cm. For finance restraints and simplicity, a simple setup shown in the appendix in figure A.3 was developed consisting of a stainless steel vessel placed on a hotplate. A short description of the reduction procedure is given there, too. For a detailed review of the optimized reduction parameters, please refer to the master thesis of Charlie Le Lam (Physics Department, University of Hamburg (2013)).[Lam13]

A significant thickness loss is found by XRR measurements of the film thickness after reduction as displayed in figure 3.7. The removal of oxygen as well as the crystallization of the previously amorphous iron oxide film can result in a densification. This observation is corroborated by observed voids in the iron oxide layer obvious in high-angle annular dark-field scanning TEM images of three-layered magnetite nanotubes (figure 3.20 in section 3.4).

In-situ X-ray diffraction measurements during reduction of iron oxide thin films (figures 3.8, 3.9) were performed within a collaboration between the research group of Prof. Nielsch (Physics Department, University of Hamburg) and the research group of Prof. Detavernier (Department of Solid State Science, University of Ghent (Belgium)).⁵ XRD data were recorded while heating an iron oxide film (thickness of (55 ± 5) nm) with a heating rate of 0.2 °C s^{-1} in helium-hydrogen atmosphere (95/5) (figure 3.8). Four lines can be assigned to the hematite and maghemite phase in figure 3.8 (a) between 30° and 40° in the $\theta/2\theta$ range at temperatures up to 200 °C. The two weakest peaks—attributed to the maghemite phase—disappear

⁵Experiments and data evaluation were proceeded by Jolien Dendooven in the group of Christophe Detavernier (University Ghent (Belgium)) (2012).

at approximately 300 °C and the major (104) peak of α -Fe₂O₃ at 33.2° becomes more prominent indicating a re-crystallization to the hematite phase. At about 350 °C, the both remaining hematite peaks loose intensity and three new patterns arise at 35.5°, 30.1° and 37.1° corresponding to the (311), (220) and (222) crystal plane of magnetite, respectively. At 420 °C the peaks abruptly disappear and only the major (110) peak of α -iron is present. Figure 3.8 (b) displays three $\theta/2\theta$ cross sections of figure 3.8 (a) at different temperatures. At 200 °C—drawn in blue—the (104) peak of hematite is obvious, whereas only the two major peaks of the magnetite phase can be identified at a temperature of 400 °C (green). Further increase of the temperature up to 600 °C results in the formation of iron denoted by the peak at 45°. Time-dependent in-situ XRD measurement during reduction can reveal information about the kinematics of the reduction process as displayed in figure 3.9 (a) and (b). While the XRD data were recorded, the as-deposited sample (thickness of 55 ± 5 nm) was heated up to 400 °C—with the maximum heating rate of the setup (3°C s^{-1})—in the forming gas atmosphere and was then kept constant for the rest of the measurement. After 100 s two peaks at around 33.2° and 39.3° representing hematite are obvious—the final temperature had not been reached at this point. As soon as the reduction temperature is reached, the hematite peaks vanish and the three major peaks of magnetite appear. However, after around 10 min the peaks get weaker and the (110) peak of iron appears. With ongoing time, the peak intensity of the magnetite phase decreases and the prominent iron peak becomes more prominent. Additionally, one may identify (in subfigure (b)) a new, small signature at 36.3° which can be attributed to an intermediated (metastable) wustite phase and which is later completely reduced to pure iron. This observation is in agreement with the review article by Pineau, who proposed different reduction paths depending on the applied reduction temperature.[Pin06]. The absence of the wustite phase in the temperature-dependent measurements is attributed to the shorter averaging times (5 s) compared to the time-dependent measurements (30 s). On the one hand, reducing the average time is necessary to ensure sufficient resolution on the temperature scale; but on the other hand, the reduced averaging results into a lower signal-to-noise ratio, and thus some peaks might not be resolved.

One may wonder if the reduction process is the same in the in-situ XRD and in the home-made oven setup. XRD and magnetization measurements after the reduction in the home-made oven reveal a similar temperature window. Reduction below 360 °C and above 450 °C lead to a disappearance of the Verwey transition—a unique property of magnetite—indicating over and under reduction. However, the time-dependence of the in-situ reduction process cannot be confirmed in the home-made setup. Reduction times between 10 min and 90 min do not change the properties of the obtained magnetite, significantly. This discrepancy might be attributed to the different forming gases (Ar/H₂ 95/5 used in Hamburg; He/H₂ 95/5 used in Ghent), different flow rates or different (local) temperatures in the reduction setup. The

exact reason remains open for further studies. The in-situ XRD analysis is a powerful tool to win insights in the reduction process and to determine the exact time and temperature window to avoid under- or over-reduction. Two further experiments are already planned: first, a study of the XRD signal as function of time at different temperatures, and second, an investigation of the reduction process of an iron oxide film capped with a thin layer of Al_2O_3 or SiO_2 also deposited by ALD.

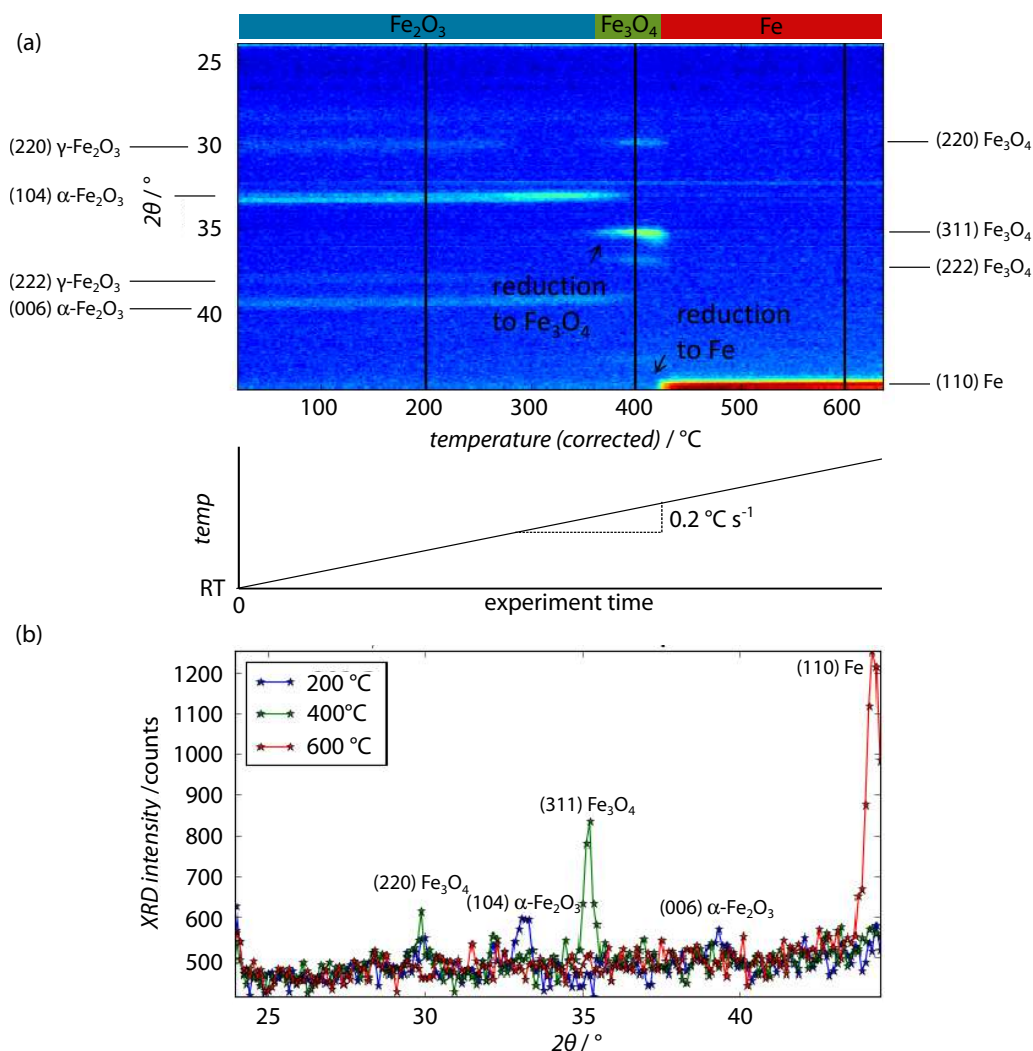


Figure 3.8: In-situ X-ray diffraction measurements of an as-deposited iron oxide thin film (thickness 55 nm): (a) Variation of the intensities as a function of temperature. The heating rate amounted to 0.2 °C s^{-1} . The mixed-phase iron oxide after ALD is converted at around 350 °C to the magnetite phase until it is over-reduced to pure iron at 420 °C . The temperature profile is schematically displayed below. (b) $\theta/2\theta$ cross sections at three different temperatures. At the depicted temperatures 200 °C (blue), 400 °C (green) and, 600 °C (red) the peaks can be attributed to maghemite (JCPDS 39-1346), hematite (JCPDS 80-2377), magnetite (JCPDS 85-1436) and iron (JCPDS 87-0721), respectively.

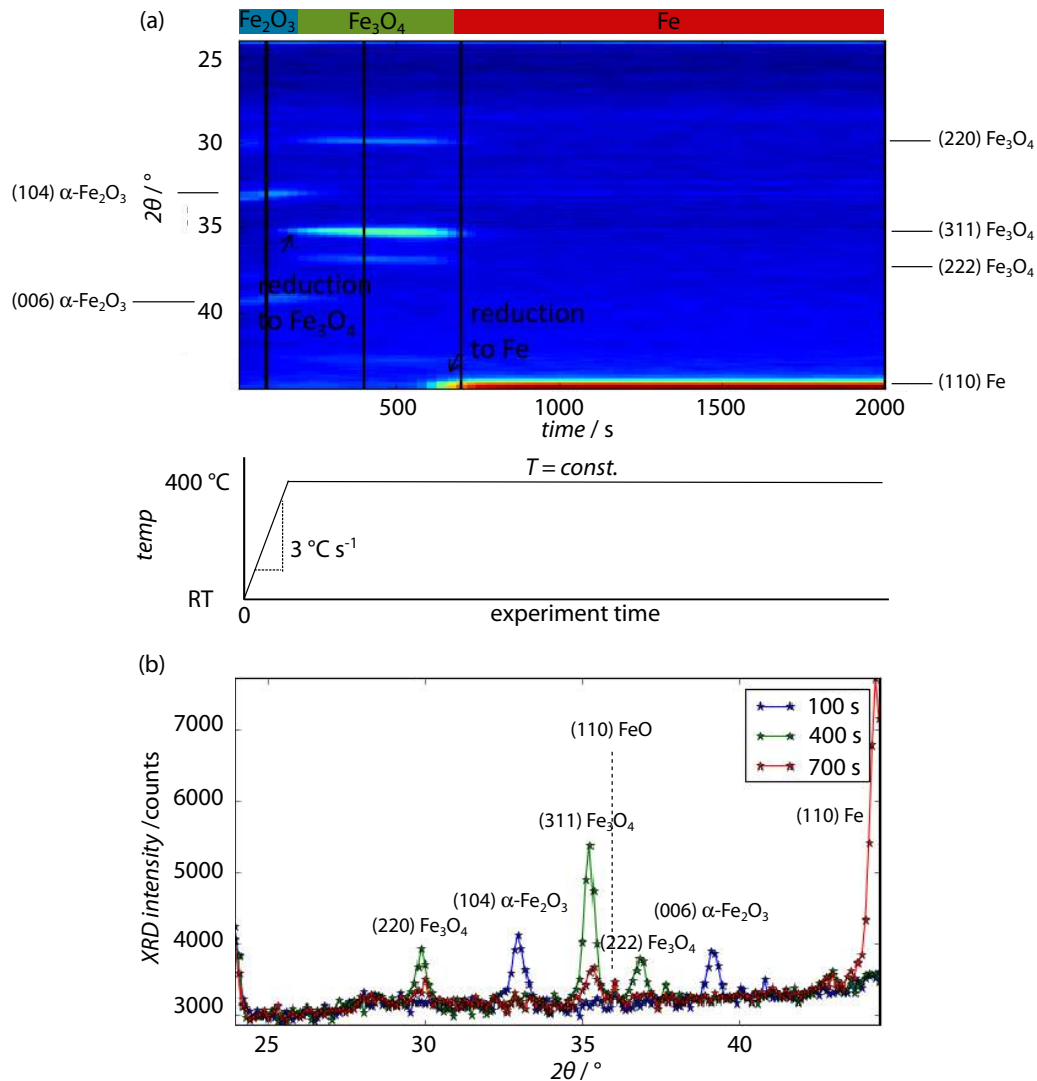


Figure 3.9: In-situ X-ray diffraction measurements of an as-deposited iron oxide thin film (thickness 55 nm): (a) Variation of the intensities as a function of time. XRD data were recorded while the sample was heated from room temperature with the maximal heating rate of 3°C s^{-1} up to 400°C . Then, the temperature was kept constant during data acquisition. The temperature profile is schematically displayed below. Reduction to magnetite occurs after 150 s; over-reduction to iron starts after 10 min. (b) $\theta/2\theta$ cross sections after three different times 100 s (blue), 400 s (green) and 700 s (red). At 100 s only the hematite phase is apparent, which is later (400 s) completely converted to magnetite. Further reduction results in iron via a reaction path about the metastable wustite phase—the major peak of magnetite decreases, the (110) peak of iron appears, and an additional (small) peak show up which we attribute to the FeO phase (JCPDS 84-0302).

3.3 Magnetic Properties of Iron Oxide Thin Films

Utilizing SQUID (superconducting quantum interference device) and vibrating sample (VSM) magnetometry⁶ shed light onto the magnetic properties and the internal magnetic microstructure of magnetite thin films prepared by ALD and subsequent reduction. The section is split into two parts: first, a magnetite thin film with a thickness of 60 nm is investigated as a function of the temperature, the externally applied magnetic field, and the angle between magnetic field and film plane. Second, the magnetic properties are studied in dependence of the film thickness which is reduced down to a few nanometers.

3.3.1 Magnetic Characterization of a Magnetite Thin Film

Temperature-dependent measurements

Temperature-dependent measurements, namely *Field-cooled* (FC), *Zero-Field-Cooled* (ZFC), and *remanence*, reveal a sharp change in the normalized magnetic moment as a function of the temperature at around (122 ± 1) K. This prominent feature is obvious in all three in-plane (a) as well as out-of-plane (b) measurements (figure 3.10) and can be attributed to the Verwey transition, which is characteristic for magnetite. Therefore, the occurrence of the transition can be used as a measure for the optimization of the reduction process— Fe_3O_4 formation—with regard to argon-hydrogen flow, reduction time and reduction temperature due to its sensitivity in terms of stoichiometry and impurity content.[Ara86] [vdZ96] [Koł12] In a field-cooled measurement a magnetic field, here 1000 Oe, is applied and the magnetic moment is measured during cool-down. Starting at 250 K in both mounting configurations, the magnetic moment raises by cooling down; at the Verwey transition a drop in the magnetic moment can be observed. Interestingly, in the out-of-plane direction the increase of the magnetic moment above the transition is more steep, whereas in the in-plane configuration the decrease below the Verwey temperature is more prominent. A contrary behavior can be observed in the remanence measurement after a magnetic field of 1000 Oe is applied at 5 K. The magnetic field is switched off, and subsequently, the magnetic moment is measured during warm-up. A positive and a corresponding negative peak in the magnetic moment can be observed at 122 K in the in-plane and out-of-plane measurement, respectively. The Verwey transition could also be proven in a zero-field-cooled measurement—sample cool-down without applied magnetic field, warm-up and measuring in an applied field. In the in-plane measurement, a steep increase near to the Verwey transition can be observed followed by the same decrease as in the field-cooled measurement. In the out-of-plane direction the Verwey transition is manifested by a sharp peak with a similar moderate increase and decrease below and above the transition temperature.

⁶MPMS-2, MPMS-XL, and VersaLabTM all instruments by Quantum Design, Inc.

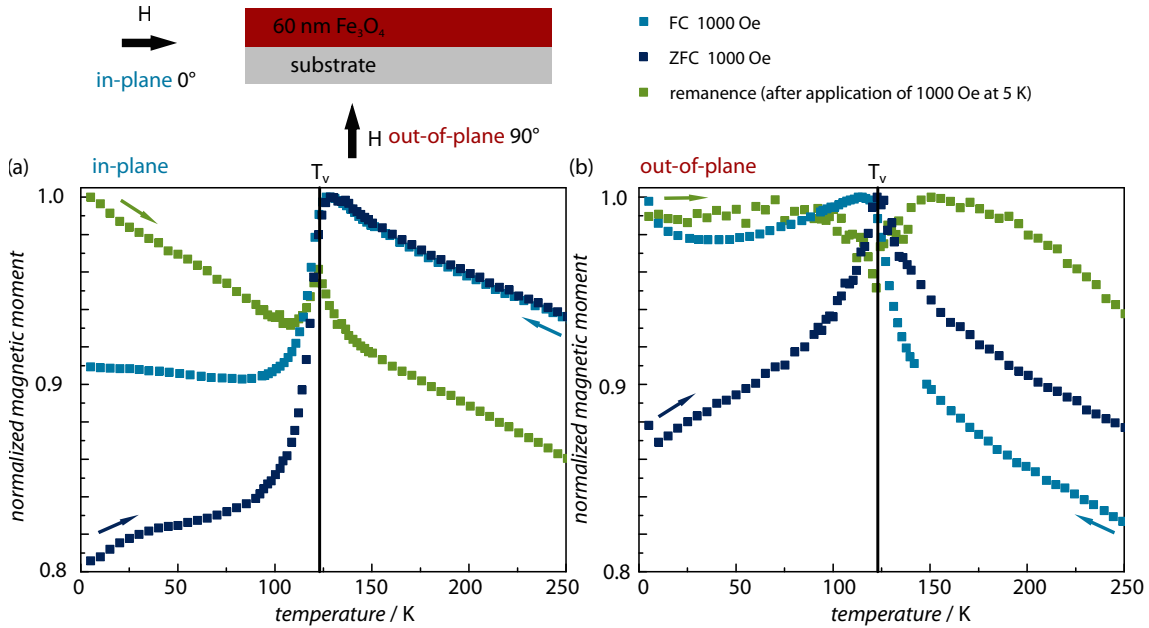


Figure 3.10: Temperature-dependent ZFC, FC and remanence measurement for the in-plane (left) and out-of-plane (right) mounting configuration. The magnetic field used for all measurements amounted to 1000 Oe. The Vervey transition at (122 ± 1) K is obvious by a distinct fingerprint in all measurements and is highlighted by a vertical line. The scheme at the top illustrates the nomenclature.

The results of temperature-dependent measurements of the coercive field are displayed in figure 3.11. The general trend of the coercive field as a function of the measurement temperature is in both mounting configurations the same. However, at temperatures below the Vervey transition (122 K), the in-plane coercive field is larger than the coercive field in the out-of-plane direction, whereas the out-of-plane coercivity is larger compared to the in-plane ones at temperatures above the Vervey transition. Starting at low temperatures a significant drop of the coercive fields can be observed, until a minimum is reached at 130 K. Subsequently, the coercive fields increase again and reach an almost constant value at around 400 Oe to 450 Oe. The Vervey temperature—depicted from the remanence measurement in figure 3.10—is highlighted with a vertical line and matches with the position of the highest slope. However, the position of minima in both measurement configurations clearly occurs at a higher temperature ((130 ± 1) K) and can be attributed to the isotropic point at which K_1 of the magnetocrystalline anisotropy vanishes and which is independent of the Vervey transition.[Abe76] [Bol05] [Bat06]

At this point of the thesis, the differences in the course of the curves comparing the in-plane with the out-of-plane experiments cannot be explained in detail. The in-plane measurements reveal a similar behavior as the observations by Bataille *et al.*

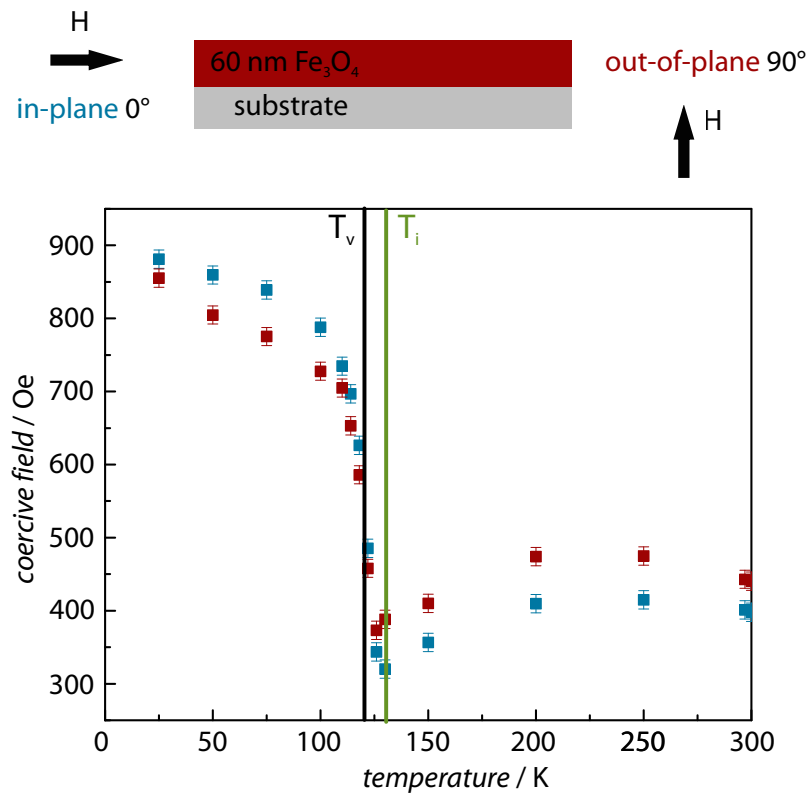


Figure 3.11: Plot of the coercive field (a) as a function of the temperature. Each data point corresponds to values taken from a magnetization isotherm measured at the corresponding temperature. Raising the temperature results in a steep decay of the coercive field until a minimum is reached. This minimum is attributed to the isotropic point of magnetite and is highlighted by a vertical green line.

who attribute the abrupt increase of the coercive field in the ZFC measurement to: “The frozen magnetic domains are suddenly free to relax in this temperature range, as would happen for frozen magnetic nanoparticles whose anisotropy barrier decrease.”[Bat06] At the Verwey transition a change of the crystal occurs, this re-orientation can result in a loss of the ordering of the magnetic moments in the FC measurement—normalized magnetic moment drops by freezing the sample—or in an orientation of the magnetic moments parallel to the magnetic field direction in the ZFC measurement—normalize magnetic moment increases by heating the sample. It is striking that a positive peak is revealed in the in-plane remanence measurement, whereas a dip is determined in the out-of-plane remanence measurement. Such an observation might be explained by an alignment of the magnetic moments from the out-of-plane to the in-plane measurement. The course of the ZFC and FC curves in the out-of-plane measurement are different compared to the in-plane experiments and cannot be explained in such simple terms. However, it can be stated that

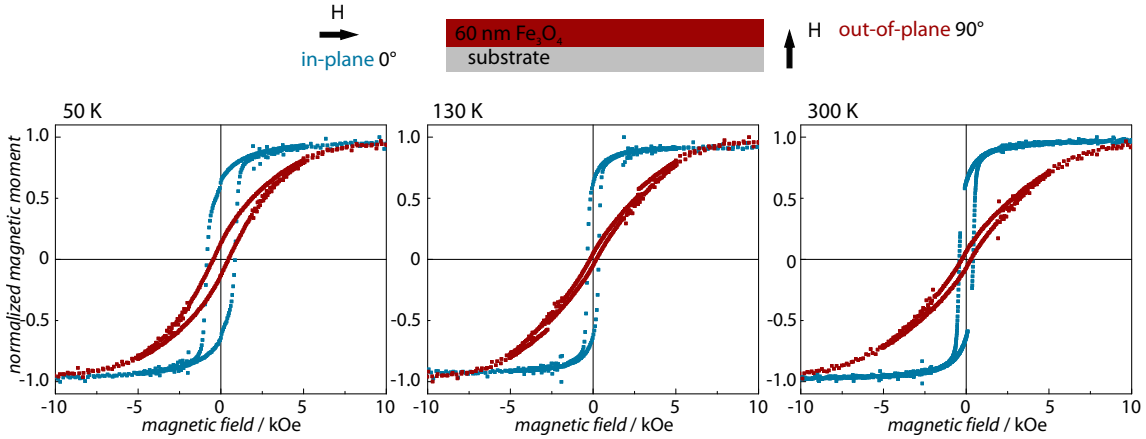


Figure 3.12: Magnetizations isotherms of an iron oxide thin film measured at three temperatures in the in-plane and the out-of-plane configuration. From left to right: 50 K, 130 K, 300 K. Reduced squareness and enlarged saturation field identify the out-of-plane direction to be harder than the in-plane direction. The scheme at the top illustrates the nomenclature.

the Verwey transition can be detected by all temperature-dependent studies and in both mounting configurations, whereas the isotropic point is only detectable in temperature-dependent measurements of the coercive fields.

Magnetization isothermal measurements

Magnetization isotherms are displayed in figure 3.12 for three different temperatures (from left to right: 50 K, 130 K, 300 K) for in-plane and out-of-plane drawn in blue and red, respectively. The easier direction is the in-plane direction: first, the squareness—remanence normalized to the saturation magnetic moment—is higher in the in-plane direction than in the out-of-plane direction. Second, the saturation field—magnetic field at which saturation occurs—is lower compared to the out-of-plane direction. The minimum of the coercive field at the isotropic point at 130 K is obvious in the magnetization isotherm for both mounting configurations (compare middle panel of figure 3.12 with the outer panels). Furthermore, saturation in the out-of-plane direction seems to be reached more easily at 130 K than at the other temperatures emphasizing the disappearance of one anisotropy term, namely the magnetocrystalline anisotropy.

To shed light onto the magnetic properties of the magnetite thin films, a technique called first-order reversal curve (FORC) analysis was utilized. A specific footprint of the local interaction field H_u distribution and the coercive field H_c distribution in the sample can be derived. FORC measurements base on a data set of minor loops taken in the following procedure:

1. the sample is saturated,
2. the measurement is started at a *reversal field* H_r smaller than the saturation field H_s ,
3. the magnetic moment of the sample is measured with increasing magnetic field up to saturation,
4. sequentially, the reversal field is step-wise reduced until negative saturation is achieved.
5. Important in this procedure is that the step width of the reversal field and the step width in the measurement magnetic field are equal ($\Delta H_r = \Delta H$).
6. The color in the FORC diagrams is mapped to the value of the FORC distribution function

$$\rho = -\frac{1}{2} \frac{\partial^2 M(H, H_r)}{\partial H \partial H_r},$$

red denoting the highest and blue the lowest values, respectively.

Coordinate transformation of the set reversal fields as well as the measured coercive fields and data processing allow for obtaining contour plots of interaction field and the coercive field as displayed in figure 3.13. This procedure has been established in our group by Philip Sergelius within the framework of his Bachelor's thesis.[Ser11] The specific features in the plots can be interpreted to achieve insight into sample-intrinsic magnetic properties, such as domain states, interaction fields, and thermal relaxation processes, usually not accessible by standard (temperature- and magnetic field-dependent) measurements.[Pik99] [Rob00] [Pik01] [Pik05] FORC diagrams of a 60 nm thick film are presented in figure 3.13 for the two different measurement mounting configurations, namely in-plane and out-of-plane.⁷ A footprint of mean field interacting, permanent magnetic single-domain (SD) particles can be identified in the in-plane FORC measurement displayed in figure 3.13 (a).[Rob00] [Rob06] Typical signatures of SD behavior are the closed contours around a distinct maximum, the negative shift of the maximum on the interaction field axis—corresponding to a positive (stabilizing) mean field—and the flattening of the pattern at the lower side. The maximum on the coercive field axis corresponds to the mean coercivity in the sample and equals the coercive field determined by SQUID magnetometry. A different trace can be determined in the out-of-plane measurement (figure 3.13 (b)). On the one hand, the diverging wide-spread, non-closed contours at the origin and the symmetry on both sides of the coercive field axis (at $H_u = 0$) can be attributed

⁷Measurement and data evaluation was performed by Philip Sergelius and Tim Böhnert (Physics Department, University of Hamburg (2012)).

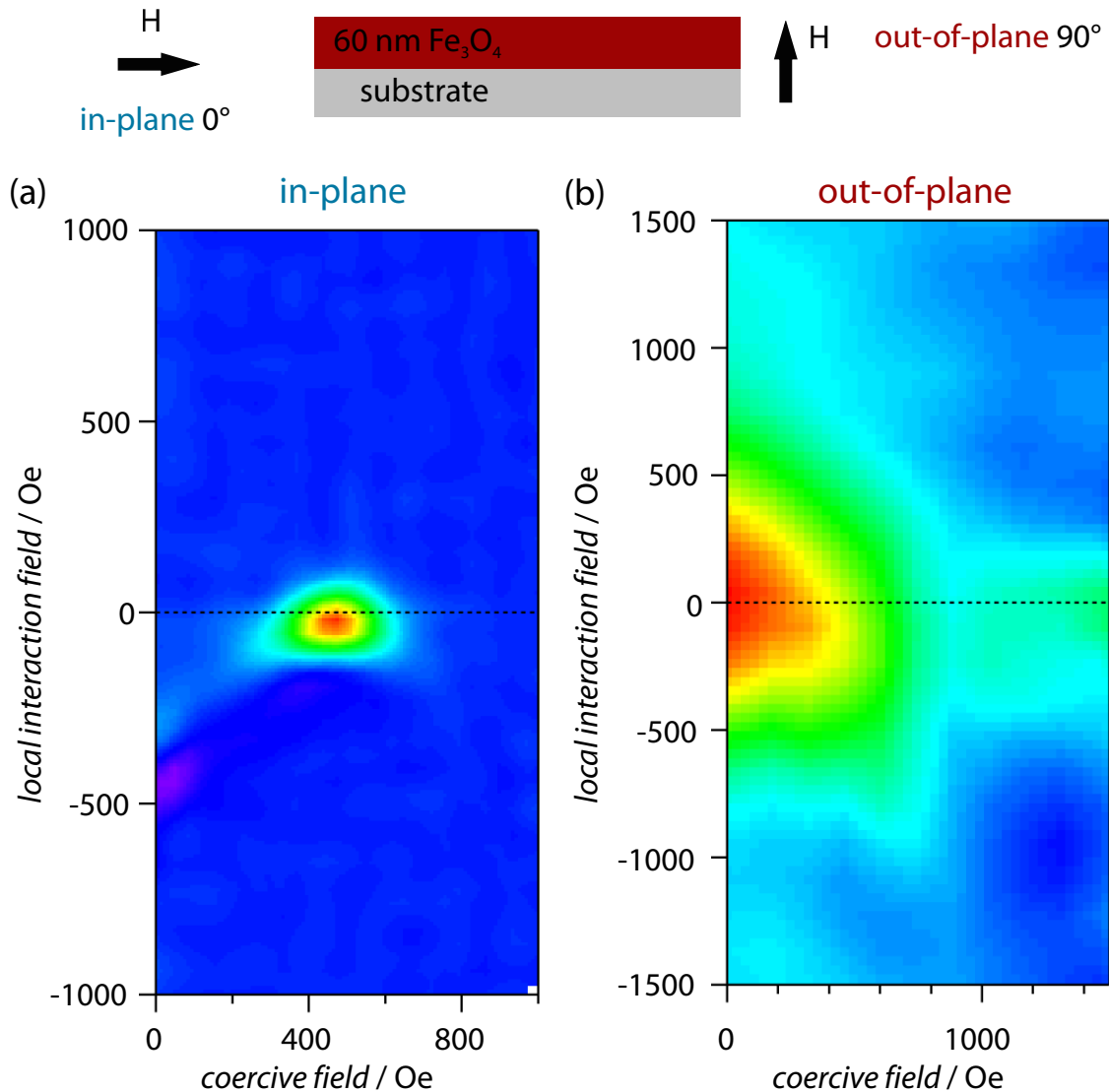


Figure 3.13: VSM FORC measurements taken at 300 K for an in-plane (a) and an out-of-plane (b) mounting configuration. The contour plot allows for the determination of the local interaction field and coercive field distribution. (a) In-plane measurements reveal the footprint of an interacting single-domain particle system. The mean coercive field (maximum) corresponds to the SQUID measurement of the film. (b) A different signature is obvious in the out-of-plane configuration. Non-closed, diverging contours represent MD/PSD micromagnetic states in the magnetite thin film. The scheme at the top illustrates the nomenclature.

to a multi-domain (MD) state. The exact physical origin of this diverging MD contour pattern is presently unknown. However, domain wall pinning as well as domain wall nucleation and annihilation are most frequently discussed and used to explain such patterns.[Rob00] On the other hand, traces attributed to pseudo-single-domain (PSD) behavior can be found, too. In particular, the backward curvature in the contour line below the zero interaction field axis is an indication to such a characteristic.[Rob00] PSD behavior is known for magnetite in an intermediated size range between pure single-domain and truly multi-domain states.[Mux02] Dunlop gives a literature summary of the suggested origins for such mixed state patterns, such as mixtures of MD and SD grains in the sample, domain wall moments, imbalanced and surface moments, and in size changeable closure domains, to name a few of them.[Dun02a] [Dun02b] Williams and Dunlop suggested a dominant vortex domain state in cubic as well as elongated magnetite particles in a size from 0.1 μm to 0.7 μm based on micromagnetic simulations.[Wil95] The magnetization reversal is mainly attributed to vortex nucleation and subsequent propagation, whereas domain wall movement is found to appear first in larger grains. A final conclusion whether the iron oxide film is in a MD-state, a PSD-state, or even a mixture of them, cannot be stated and remains open for further investigation.

Angular-dependent measurements

The idea of a transition in the domain structure—and/or a change in the magnetization reversal mechanism—is supported by angular-dependent SQUID measurements (figure 3.14 (a), data displayed for measurement at 300 K). The squareness decreases by rotating the sample from in-plane (0°) to out-of-plane (90°); further rotation increases the squareness again. This behavior is expected for rotating the magnetization away from the easy-axis to the hard-axis and back. However, the coercivity as a function of the rotation angle reveals a different, non-monotonic behavior. Starting the rotation from the in-plane direction the coercive field increases monotonically until around 60° rotation angle where the value of the coercivity suddenly drops and reaches a minimum in the out-of-plane configuration. Further rotation follows the same (mirrored) trend back and results finally in a ‘M’-shaped curve. Such a behavior of the coercivity is well-known for a transition in the type of the magnetization reversal mechanism in one-dimensional nanostructures, for instance the change of the domain wall type from vortex to transverse as a function of the iron oxide nanotube’s wall thickness or the rotation angle.[Esc08] [Bac09] [Alb11] Jacobs and Bean predict a magnetization reversal mechanism transition in their model ‘chain-of-spheres’—single-domain particles aligned in a chain—which was previously often used to model one-dimensional nanowires.[Jac55] In their model, the magnetization reverts in the fanning mechanism (near a parallel alignment of the chain and the external magnetic field) until a critical angle is reached and the magnetization flips coherently (parallel) in the individual single-domain particles. For granular thin

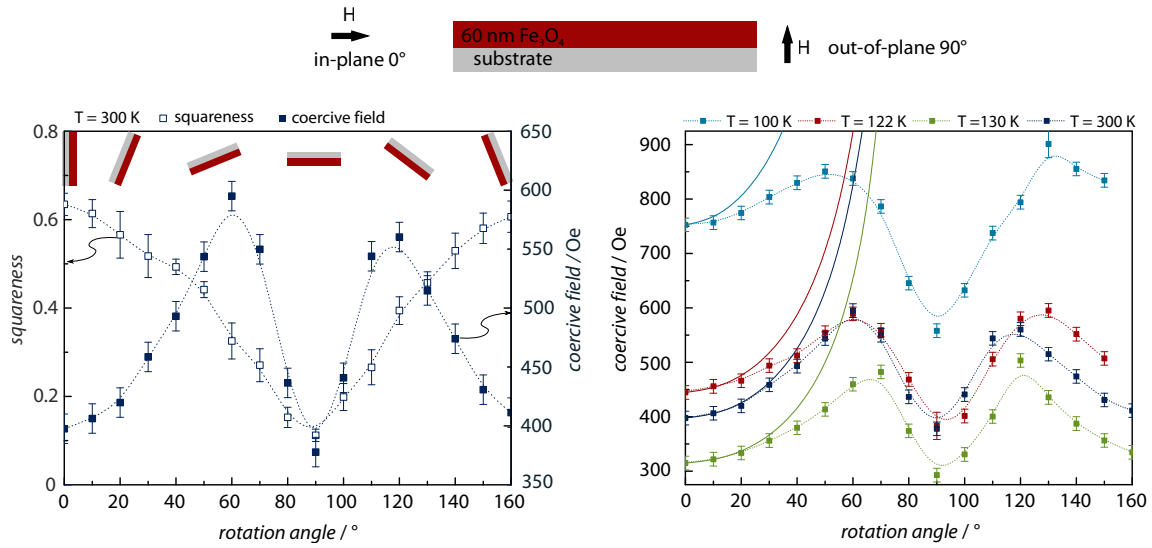


Figure 3.14: Plots of the angular-dependent SQUID measurements of the squareness as well as the coercive field at 300 K (a) and the coercivity for four different temperatures (b). Each data point corresponds to values taken from a magnetization isotherm measured at the corresponding angle. The ‘M’-shaped behavior of the coercivity can be attributed to a transition in the magnetization reversal mechanism from (incoherent) single-domain particle switching to reverse domain formation and growth. The scheme at the top illustrates the nomenclature. The solid lines (left side) are plots of the $1/\cos$ -relation representing domain wall motion. All lines drawn in (b) serve as guide to the eyes.

films such curves are reported, too, revealing an angular-dependent transition of the magnetization reversal from domain wall propagation near in-plane to individual particle/grain switching in the out-of-plane direction.[Vic87] [Ran90] [Wan91] The often assumed, simple $(1/\cosine)$ -relation for a reversal mechanism via domain wall motion is plotted in subfigure 3.14 (b) in solid lines. Especially at low temperatures, a strong deviation to the measured coercive fields is obvious. Thus, domain wall motion near the in-plane direction seems to be unlikely in this iron oxide thin film. Additionally, the MD/PSD states determined by the FORC measurements indicate a more complex magnetization reversal mechanism in the out-of-plane configuration than individual particle switching. Gau and Brucker observed a similar ‘M’-shaped behavior and attributed the abrupt decrease of the coercive field (near the out-of-plane direction) to “[...] reverse-domain nucleation and growth. Likely reverse domain nucleation sites are surface irregularities and physical or chemical defects.”[Gau85] Moreover, the authors attribute incoherent rotation mechanisms such as fanning or curling to be responsible for the angular-dependence of the coercive field at angles below the transition point (near in-plane). The specific footprint of the observed behavior is invariant in temperature (3.14 (b)), despite the absolute values and the ‘M’-width. At the isotropic point at 130 K, the curve is shifted to

lower coercive fields since the first constant of the magnetocrystalline anisotropy vanishes. Additionally, the drop in the coercivity around the out-of-plane configuration appears more narrow than at other temperatures. The formation of reversed domains is reduced since a decreased (magnetocrystalline) anisotropy would favor domain walls with a larger wall width. Thus, incoherent magnetization reversal of interacting individual particles or grains is preferred over reverse domain formation at low angles. As a consequence, a shift of the abrupt drop closer to the out-of-plane (90°) configuration is observable. However, surface anisotropy, demagnetization fields in grains, surface roughness, or grain boundaries can act as nucleation sites for the formation of reverse domains leading to the MD/PSD behavior observed in the FORC measurements.[Liv81] [Zha01] To summarize, taking the FORC measurements as well as the angular-dependent measurements of the coercive field into account, the magnetization reversal is attributed to an incoherent reversal mechanism near in-plane, whereas reverse domains formation and growth is expected in the out-of-plane direction.

Turning back to the beginning, at the point where the different temperature-dependent measurements were shown (figure 3.10 as well as 3.11) and different behavior around the Verwey transition in the in-plane and out-of-plane configuration were observed: the suggested explanation for the in-plane direction in terms of a particle system can be validated. However, the behavior in the out-of-plane configuration still cannot be explained because the temperature-dependent interplay between magnetocrystalline anisotropy, demagnetization field as well as the domain structure and its reversal has to be taken into account.

3.3.2 Magnetic Properties of Iron Oxide Films with a Thickness Down to a few Nanometers

Film thickness-dependent measurements performed at 300 K reveal a decreasing trend of the coercive field (a) as well as the saturation magnetization (b) with decreasing film thickness t (figure 3.15). Between 10 nm and 30 nm nominal film thickness the coercive field is almost constant at (400 ± 50) Oe and the saturation magnetization amounts to the literature value of (480 ± 10) emu cm $^{-3}$. However, thinner films reveal drastically decreased values of both properties. Power law functions $H(t) = H_c(1 - at^n)$ and $M(t) = M_s(1 - bt^l)$ can be phenomenologically fitted to saturation magnetization and coercive field, respectively.[Orn10] The fit parameter H_c equals to (510 ± 82) Oe. The exponent n and the scaling factor a (with the dimension of nm n) amount to -2 ± 1 and to 25 ± 39 , respectively. A similar fit can be proceeded on the saturation magnetization as a function of the film thickness. The fitting parameter $M_s = (482 \pm 6)$ emu cm $^{-3}$ matches perfectly with the literature value reported for magnetite. The parameter $l = -4 \pm 1$ is a factor eight smaller than the reported value by Orna *et al.* indicating that the decay of the saturation

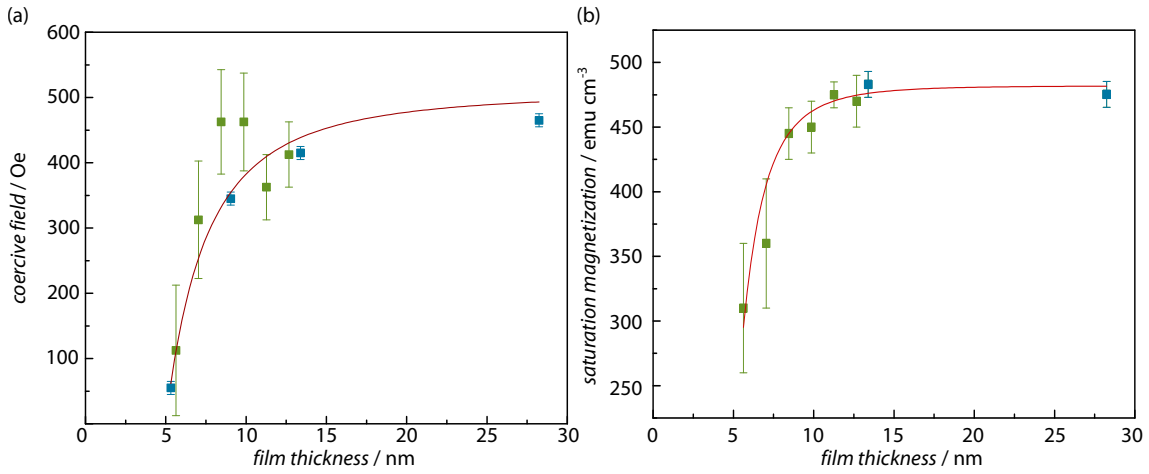


Figure 3.15: Plot of the coercive field (a) and the saturation magnetization (b) as a function of the film thickness measured at 300 K in the in-plane mounting configuration. Both magnetic properties decrease with reduced film thickness. Blue and green data points corresponds to two different sample series. The larger error bars for the green measurements are caused by the reduced sensitivity of the SQUID DC head compared to the RSO head. The red lines are fits of power law equations to the measured data.

magnetization is much steeper than in the epitaxial films grown by pulsed laser deposition, in which the decrease of the saturation magnetization already starts at film thicknesses of around 50 nm. The third fitting parameter b amounts to 285 ± 612 .⁸ The decreasing values of the coercive field and the saturation magnetization can be explained by the evolution of grain sizes with film thickness. Thinner ALD-deposited films are converted by reduction in polycrystalline films possessing a smaller mean-size of grains compared to thicker films. However, if the grains become too small (and maybe separated due to the volume shrink during reduction) superparamagnetic behavior is expected. The decrease in the coercive field can be explained by the lower energy barrier of the grain/particle which has to be overcome. An apparent reduction of the saturation magnetization in thin (granular) films can be caused by several reasons, e.g. surface oxidation which results in a ‘dead’ magnetic layer, surface spin canting or spin disordering at the enlarged surface of nanoparticulate grains.[Tan91] [Coe71] [Kod96] [vdH96] Moreover, an incomplete saturation of the samples would also cause a reduced ‘apparent’ saturation magnetization. Especially if the magnetic film thickness becomes too thin, the magnetic background of the substrate can lead to large errors in the (apparent) saturation magnetization. In epitaxial thin films—as investigated by Orna and co-authors—similar superparamagnetic

⁸The large fit errors of a and b already indicate a wide value range allowing for appropriate fits. By fixing the other parameters a critical thickness in the range from 0 nm to 8 nm can be calculated at which the H_c and M_s vanish. This estimation is in good agreement with the experimental observations.

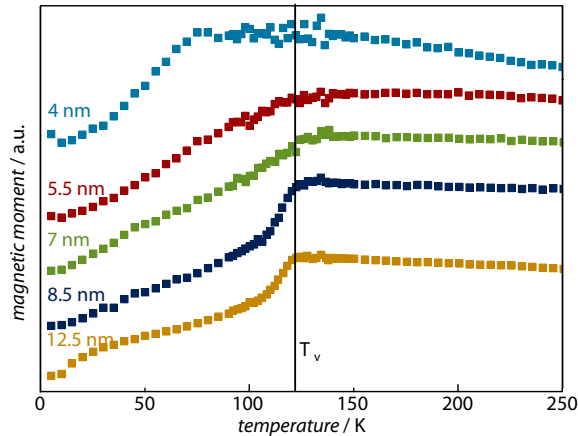


Figure 3.16: ZFC measurements at 1000 Oe of various film thicknesses in the in-plane mounting configuration. The Verwey transition becomes less prominent with decreasing film thickness. However, for all film thicknesses from 5.5 nm to 12.5 nm the observable plateau is approximately reached at the Verwey temperature of 122 K highlighted by a vertical line. For the thinnest film a maximum at a much lower temperature is obvious. This feature cannot be explained by a shifted Verwey transition, instead it is attributed to a blocking temperature of the smallest—superparamagnetic—grains which occur during the reduction process due to a volume loss.

phenomena are observed which are attributed in this particular case to antiphase boundaries in the epitaxial films.[Orn10] Across these boundaries the cation lattice is disturbed while the oxygen lattice remains still leading to a single crystalline film. The structural areas separated by an antiphase boundary turns out to be magnetically frustrated or (anti)ferromagnetically coupled, thus leading to magnetic domain structure. The energy barrier of an individual domain can be decreased—depending on the antiferromagnetic exchange coupling, the boundary area as well as the state of frustration—up to a value that thermal fluctuation of the magnetic moment in the domain is possible.[Voo98] [Eer04] Furthermore, the antiferromagnetic coupling between adjacent domains often serves as an explanation for the ‘apparent’ reduced saturation magnetization—the antiferromagnetic coupling hinder a complete saturation in moderate magnetic fields.[Mar96] [Mou04] [Orn10]

Zero-field-cooled measurements are displayed in figure 3.16 for various film thicknesses. The Verwey transition is evident at film thicknesses above 8.5 nm, whereas the specific signature—strongly raising magnetic moment—is lost towards thinner films. However, a clear shift of the Verwey transition to lower temperatures with decreasing film thickness cannot be identified as reported in literature by other authors.[Sen97] [Li98c] [Orn10] A broad size distribution of grains can result into a transition temperature distribution not allowing for the determination of a single transition temperature. At the thinnest film (4 nm), the raise of the magnetic moment is shifted to a lower temperature value and forms a maximum. This feature is

particularly not attributed to a shifted Verwey transition, instead the appearance of a blocking temperature for superparamagnetic grains is seen as the reason. Superparamagnetism might be another explanation for the vanishing distinct transition temperature. An increased mean of the grain size distribution at intermediated film thicknesses can result in a broad blocking temperature peak around the Verwey temperature, and thus can hide the transition. Electrical transport measurements as performed by Li and co-workers can allow for resolving the Verwey transition in resistance measurements not covered by the superparamagnetism.[Li98c] However, precision electrical transport measurements performed by Johannes Goth (Physics Department, University Hamburg, (2012)) at film thicknesses below 10 nm exhibited resistances higher than $1 \text{ T}\Omega$ in a voltage range $\pm 30 \text{ V}$ at temperatures from 75 K to 300 K. Therefore, one can conclude that the film is composed out of grains which are not connected to each other. On the one hand, this result supports the hypothesis of the volume shrinkage and the formation of nanoparticulate grains which will act superparamagnetic below a certain size. On the other hand, electrical transport measurements cannot be performed on such films to reveal whether the Verwey temperature decreases with decreasing film thickness or not. Spatially resolved Raman spectroscopy might allow for determination of a size-dependent shift.⁹

Escrig *et al.* and Bachmann *et al.* compared theoretically calculated coercive forces of iron oxide nanotube ensembles as function of wall thickness to experimentally determined coercivities.[Esc08] [Bac09] For thin wall thicknesses $\leq 8 \text{ nm}$ a significant deviation between theory and experiment is observed. Structural imperfections of the tubes, thermal instabilities, finite length of the tubes, or shape irregularities are listed as possible explanations. Based on the result of this subsection, the assumptions of them can be validated and specified: (extremely) thin coatings result in a nanoparticulate, non-closed film with a grain size distribution around the superparamagnetic limit finally leading to reduced coercive fields. Moreover, for prospective projects dealing with magnetite in elongated nanoobjects, measurements at the isotropic point (130 K) are suggested to minimize the influence of the magnetocrystalline anisotropy.

The data shown in this section present measurement results of granular magnetite thin films synthesized by ALD and a subsequent reduction process. Optimized synthesis process parameters have led to polycrystalline, stoichiometric magnetite thin films proven by in-situ XRD as well as by the appearance of the Verwey transition and the isotropic point for the first time in ALD films. Furthermore, VSM FORC and angular-resolved SQUID measurements predict a change of the magnetic structure (SD to MD/PSD) and of the magnetization reversal mechanism from the in-plane to the out-of-plane direction. Reduced film thicknesses (below 10 nm) reveal a decrease of the magnetization and the coercive field. Moreover, the clear footprint of the Ver-

⁹A collaboration for that purpose has been started with the research group of Anna Fontcuberta i Morral (School of Engineering, EPFL (Switzerland)) in the end of 2012.

wey transition vanishes and is replaced by a peak in the ZFC measurements which can be attributed to the transition between blocked and unblocked nanoparticulate grains.

However, detailed investigation and description of the temperature-dependent micromagnetic domain states and its reversal mechanism in thin films is out of the scope of this thesis. Therefore, further magnetic characterization (e.g. angular-resolved or temperature-dependent FORC as well as time-dependent relaxation measurements) are suggested. Continuing studies can shed new light onto the (intrinsic) micromagnetic properties of magnetite thin films deposited by ALD.

3.4 Iron Oxide Nanotubes by Atomic Layer Deposition

The combination of nanoporous alumina templates with atomic layer deposition of iron oxide allows for the synthesis of magnetic nanotubes which are embedded in the membrane after synthesis. A releasing procedure consisting of several steps allows for the preparation of nanotube liquid suspension. The detailed synthesis parameters can be found in the experimental sections of [Wu10c] and [Zie11].

3.4.1 Synthesis and Characterization of Ferrimagnetic Magnetite Nanotubes

The synthesis route is schematically displayed in figure 3.17. After template preparation by 2-step anodization (a) and pore widening (b) to remove the conical structure at the pore entrance of the membrane, a thin layer of silicon dioxide is deposited onto the pore walls acting as protective outer layer (c). Thereby, the silica is also deposited on the top side of the membrane, and thus connects the embedded silica nanotubes. Anisotropic reactive ion etching (RIE) is applied to remove these *interconnects*¹⁰ (d). Subsequently, the sample is coated by ALD with iron oxide and a second silica layer (e). Once again, the tubes are connected on the top of the template by the deposited layers. The silica layer on top—corresponding to the inner protection layer of the nanotube—is etched again by selective RIE in same process conditions as previously. Subsequently, the iron oxide is removed by means of Ar⁺-ion bombardment¹¹ (f). The dry etching procedure is a crucial prerequisite to allow for a complete dispersion of the nanotubes, otherwise the nanotubes remain connected and form large blocks as shown in figure A.5 in the appendix. Thermal reduction (g) of the iron oxide to magnetite is conducted in argon-hydrogen atmosphere in same conditions as used for the synthesis of magnetite thin films. The

¹⁰CHF₃ flow 25 sccm, process pressure 20 mTorr, power 75 W

¹¹Ar flow 20 sccm, process pressure 10 mTorr, power 200 W

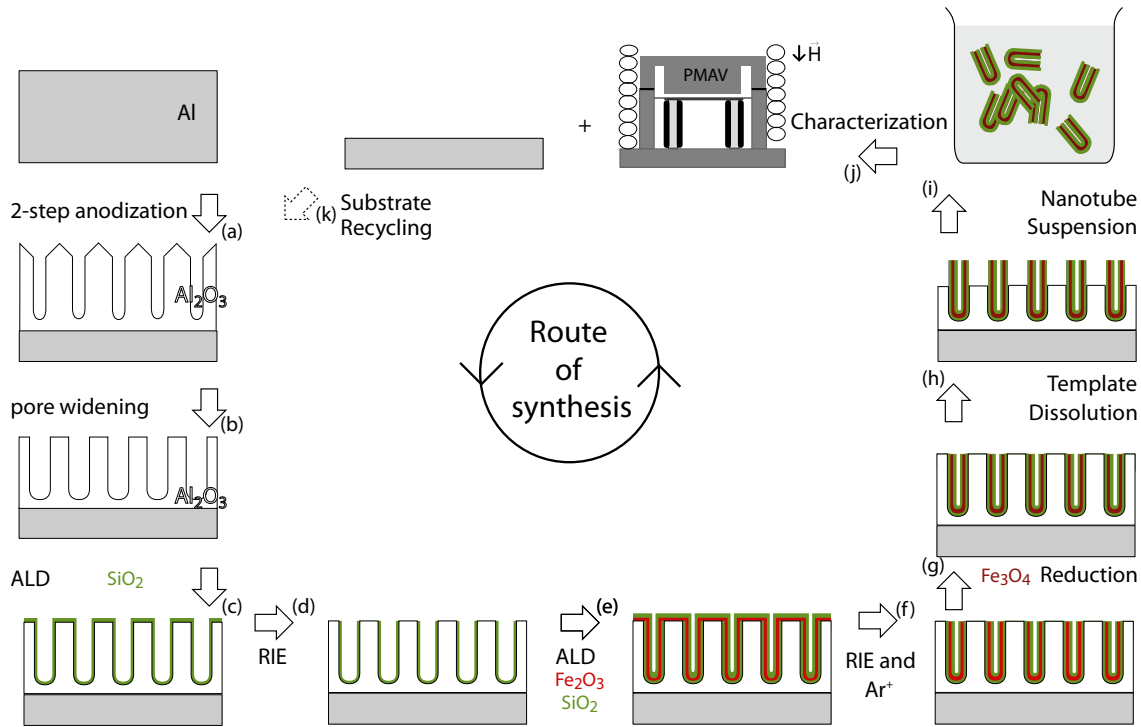


Figure 3.17: Schematic drawing of the synthesis route for ferrofluidic suspensions containing iron oxide nanotubes: (a) 2-step anodization followed by pore widening (b) and ALD of silica (c). The connecting film on the top of the membrane is removed by RIE (d). Further ALD of iron oxide and silica (e) results in three-layered nanotubes embedded in the template. Subsequently, RIE and argon sputtering (f) disconnect the nanotubes from each other. The as-deposited iron oxide is converted into magnetite by a reduction process (g). Selective template removal (h) results in a nanotube suspension (i), which can be further investigated (j), and a recyclable aluminum substrate, which can be directly used again for a second anodization (k).

supporting alumina template is selectively etched (h) and the tubes are released to the acidic solution. However, the nanotubes are protected by a silica shell against etching. Short ultrasonication, vacuum-enhanced filtration, and several (3–8) washing steps result in a nanotube suspension ready for further characterization (i,j). Since chromic acid is used for the selective etching, the underlying aluminum substrate is not attacked and the long-range order of the hemispherical indentations is retained. Thus, the aluminum chip can be directly reused for the nanotube synthesis without operating the time- and material-consuming electropolishing process and first anodization (k).

Three-layered magnetic nanotubes with an average length of (190 ± 20) nm and a mean tube diameter of (85 ± 10) nm were used to investigate the structural properties. Aberration-corrected high-resolution transmission electron (AC-HR-TEM)

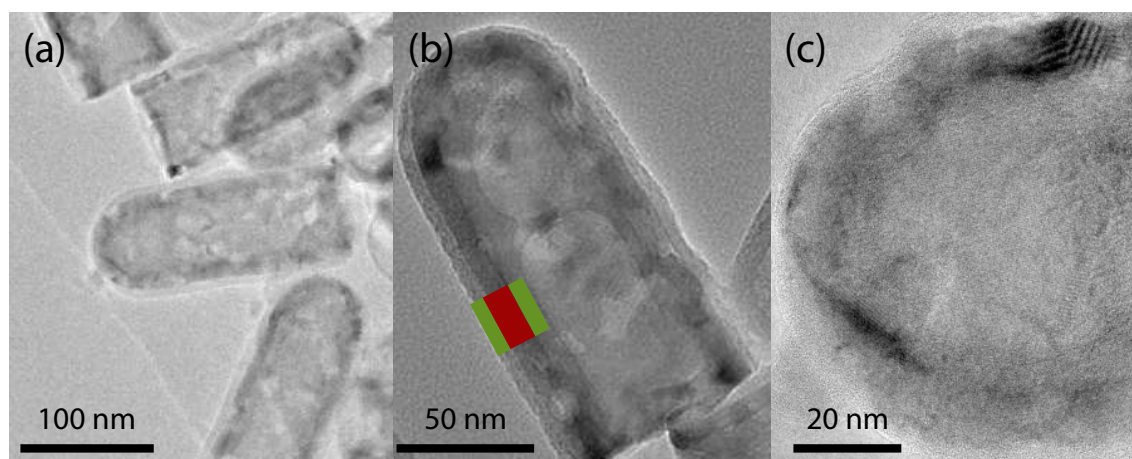


Figure 3.18: HR-TEM micrographs display the three-layered structure SiO_2 (green)- Fe_3O_4 (red)- SiO_2 (green) of the iron oxide nanotubes with an average length of (190 ± 10) nm and a mean tube diameter of (85 ± 10) nm in subfigure (a,b). Magnified HR-TEM reveals an amorphous silica shell, whereas the iron oxide layer is polycrystalline after forming gas annealing.

microscopy was applied to resolve the three-layer structure—consisting of $\text{SiO}_2/\text{Fe}_3\text{O}_4/\text{SiO}_2$ —of the nanotube’s wall (figure 3.18).¹² The layer thicknesses for silica and iron oxide of these tubes amount to (6 ± 1) nm and (8 ± 2) nm, respectively. At high-magnification the polycrystalline microstructure of the iron oxide layer is apparent; whereas the continuous silica layer remains amorphous even after the thermal heat treatment applied during the reduction process. A polycrystalline spinel magnetite structure is confirmed by the ring pattern in selected area electron diffraction (SAED) of a dried nanotube ensemble (figure 3.19 (a) and 3.21 (b)) as well as by the fast Fourier transform of a HR-TEM of a single nanotube (figure A.6 in the appendix). The observation of the spinel structure is consistent with the grazing-incidence X-ray diffraction pattern shown in figure 3.19 (b) which was taken of a nanotube ensemble dried on a piece of silicon. A Gaussian fit to the XRD (311) peak allows for estimation of the mean crystallite size to around 16 nm by using the Scherrer equation.[Sch18] [Lan78]¹³ High-angle annular dark-field (HAADF) scanning TEM micrographs (figure 3.20) display a homogeneous distribution of iron atoms along the entire length of all tubes. Minor voids—apparent as darker spots in

¹²HR-, dark-field, and high-angle annular dark-field scanning transmission electron microscopy studies were performed by Johannes Biskupek in the group of Ute Kaiser at Ulm University (Electron Microscopy Group of Materials Science).

¹³ $d = \frac{K\lambda}{B(2\theta)\cos\theta}$ being B the full-width-at-half-maximum (FWHM) in rad, λ the wavelength of the X-ray beam (Cu $K\alpha$ in our case), and θ the peak position. K denotes the Scherrer constant which amounts between 0.7 to 1.1 depending on the shape of the particle and the diffracting crystal plane. Herein, we used for estimation of the mean grain size d the value $K = 0.9$.

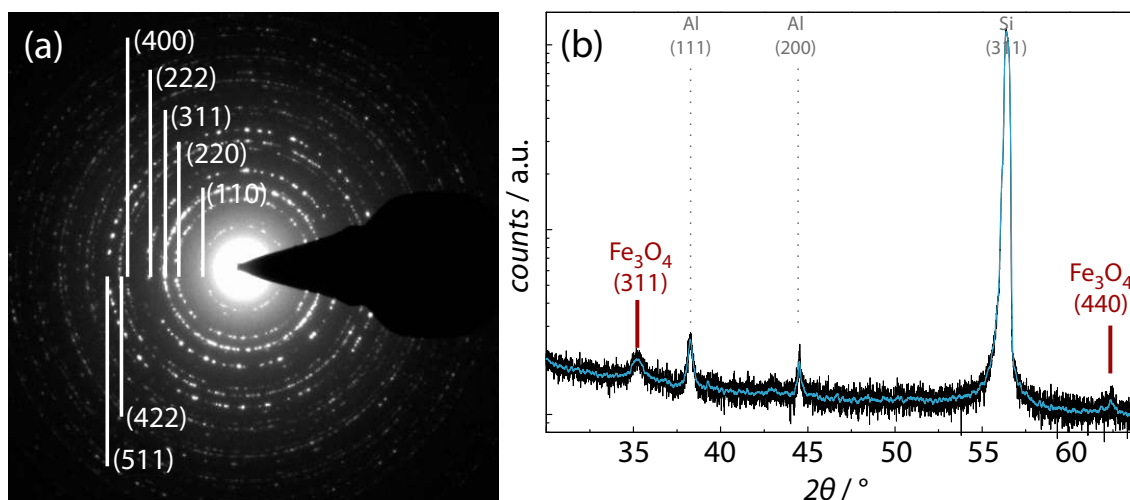


Figure 3.19: The pattern of selective area electron (left) and grazing-incidence X-ray (right) diffraction—both performed on a dried suspensions of iron oxide nanotubes—indicates a polycrystalline (spinel) structure of magnetite in the nanotube wall. The electron diffraction rings as well as the X-ray peaks are labeled to the corresponding magnetite crystal planes. The prominent (311) silicon peak originates from the substrate holder, and the aluminum peaks likely arise from contamination during the releasing process of the nanotubes.

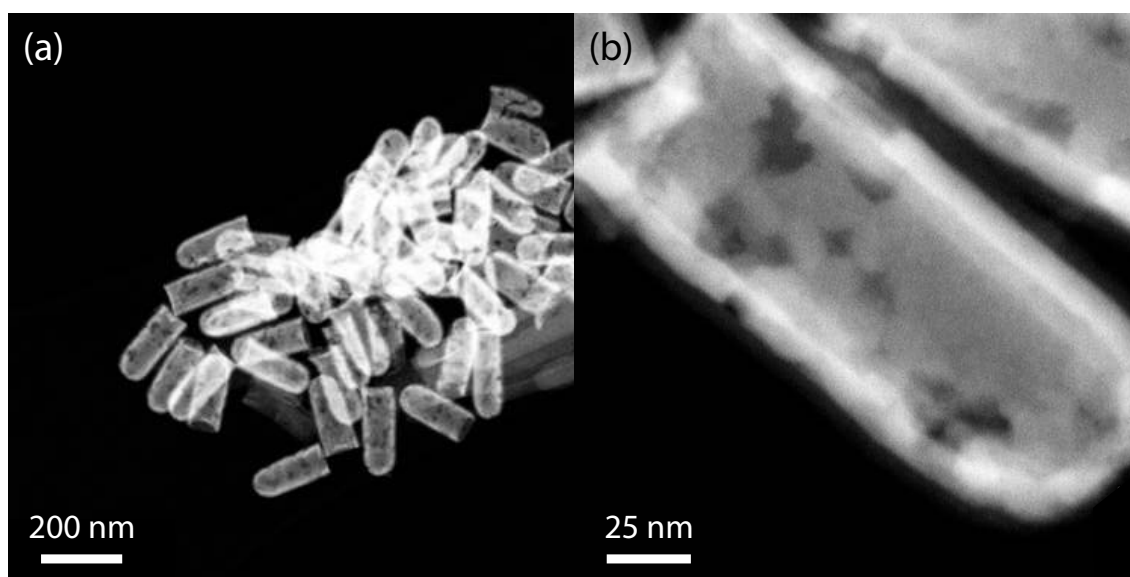


Figure 3.20: High-angle annular dark-field scanning TEM images display the homogeneously distributed iron atoms along the entire tube length. (a) A small distribution in the length and the diameter of the tubes is obvious. (b) Magnification of a single nanotube: minor voids are visible in all nanotubes. These voids are probably caused by a volume shrinkage during the reduction process.

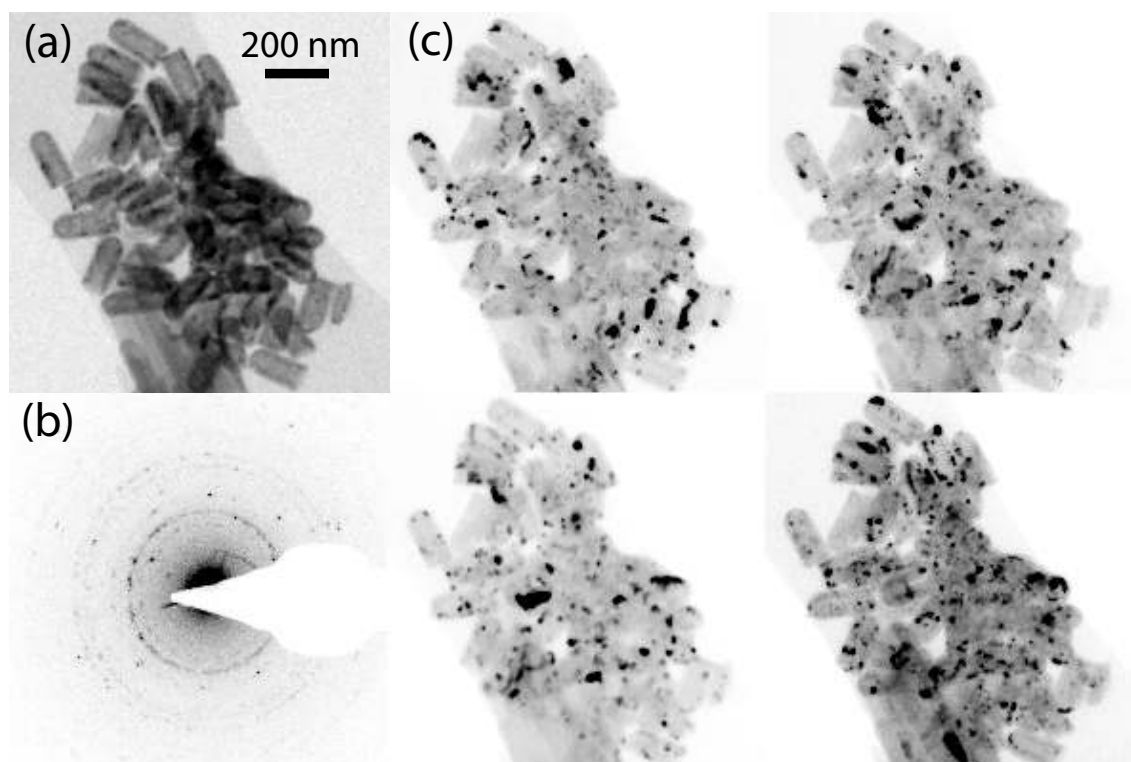


Figure 3.21: HR-TEM micrograph (a) and SAED (b) of the nanotubes investigated by dark-field TEM imaging at an aperture around the 311 diffraction ring (c). A polycrystalline, granular structure of the magnetite in the nanotubes' wall is revealed. For the sake of clarity, the SAED image as well as the dark-field micrographs have been processed. The original micrographs are shown in the appendix in figure A.7 in the appendix.

the images—are present which most likely originate from the volume shrinkage during the reduction step. Dark-field TEM imaging (figure 3.21 (c)) using the aperture around the second diffraction ring (311 plane) supports the idea of the granular, polycrystalline magnetite structure in the iron oxide wall. The grain size shows a wide distribution from a few to several tens of nanometers—the value determined by XRD might be a reasonable mean value of crystallite size distribution. Furthermore, at least some of the grains observed around the 311-diffraction ring seem to be elongated with a long axis parallel to the tube axis. Under the assumption that this observation is also valid for differently oriented crystallites, the shape anisotropy of the individual grains will mainly determine the magnetic anisotropy of the nanotube.

SQUID magnetometry was used to determine the magnetic properties of magnetite nanotubes. Magnetization isotherms measured on a dried nanotube suspension reveal reduced coercive fields and remanences for the out-of-plane measurement configuration—applied magnetic field is perpendicular to the long axis of most

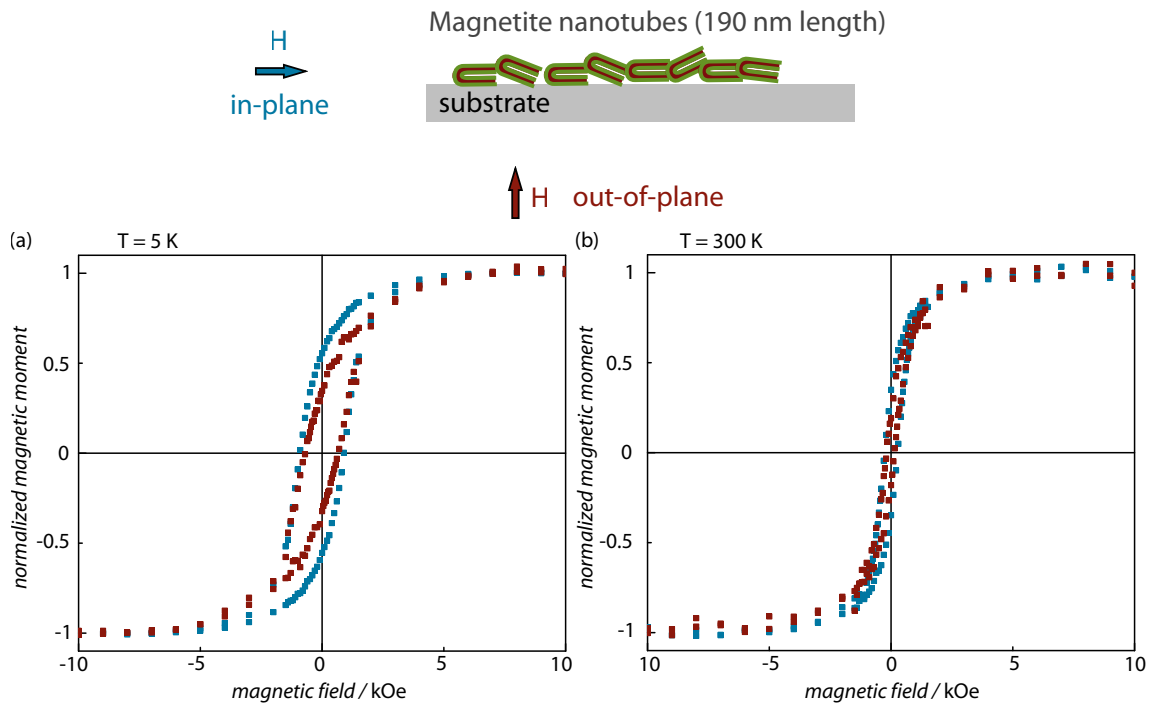


Figure 3.22: Normalized magnetization isotherms at 5 K (a) and 300 K (b) of magnetite nanotubes dried on a silicon substrate and measured in two different mounting configurations. The scheme at the top of the figure illustrates the nomenclature for the in-plane and out-of-plane measurement.

tubes—compared to the in-plane measurement as displayed in figure 3.22.¹⁴ The coercive field at 5 K is measured to be (910 ± 25) Oe and (690 ± 25) Oe for the in-plane and the out-of-plane configuration, respectively. The same feature can be identified in the squareness determined at 5 K which amounts to $(55 \pm 2)\%$ and to $(35 \pm 2)\%$ for the in-plane and out-of-plane measurement, respectively. Furthermore, it is obvious that the saturation field is reached earlier in the in-plane than in the out-of-plane measurement. Raising the measurement temperature to 300 K (figure 3.22 (right)) results in a lowered magnitude of the coercive fields and the remanent magnetizations. However, the observation of reduced values for the two different measurements configuration (in-plane/out-of-plane) can be confirmed in the coercive field (270 Oe/160 Oe) as well as remanences (35%/20%). To conclude, these measurements indicate a magnetic easy axis parallel to the long axis of the nanotube.

The reason of this easy axis along the tube axis is supposed to be rather the shape anisotropy of the individual grains than the shape anisotropy of the tube

¹⁴In that specific case, the nanotubes were suspended in water and were dried in an applied magnetic field parallel to the substrate plane provided by two NdFeB magnets. The in-plane direction correspond to the magnetic field during the drying process.

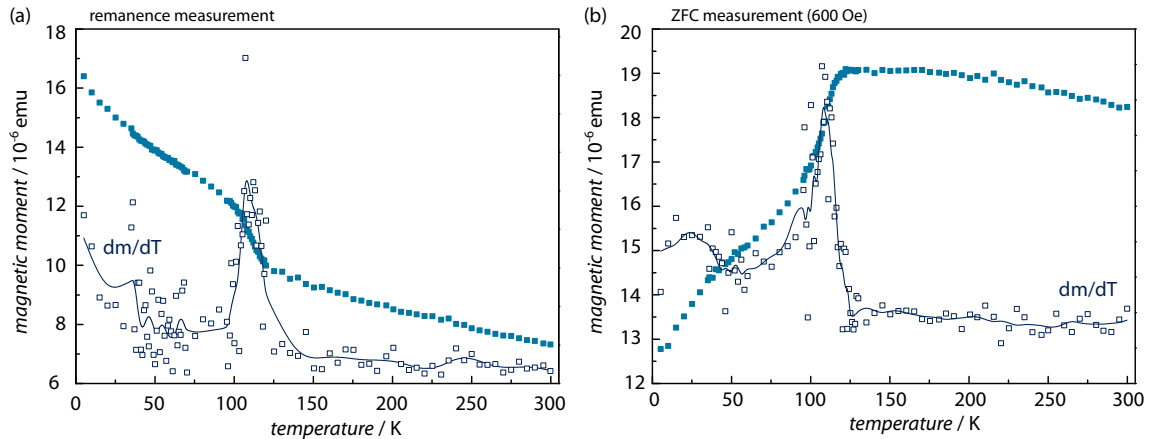


Figure 3.23: Temperature-dependent remanence (a) and ZFC (b) measurements. A drastic change of the magnetic moment during warm-up is apparent and is attributed to the Verwey transition at around 107 K observed in magnetite nanotubes for the first time. The abrupt change is highlighted by a maximum in the first derivative of the magnetic moment over temperature drawn in dark blue. The lines drawn serve as guide to the eyes.

itself. Furthermore, the iron oxide layer in the wall of a nanotube consists of individual, partially separated grains. However, a sufficient amount of grains might possess a slightly longer axis parallel to the tube axis than perpendicular leading in total to an easy axis parallel to the nanotube axis. The large drop in the coercive fields and the remanences from 5 K to 300 K can be explained by a number of grains being smaller than the critical volume for superparamagnetism corresponding to a blocking temperature of ≤ 300 K. This hypothesis is supported by the drop in the remanence measurement of more than 50 % from 5 K to 300 K as well as the strongly rising magnetic moment far below the Verwey transition in a ZFC-measurement as shown in figure 3.23 (a) and (b), respectively. The 8 nm wall thickness of the explored tubes are at the limit until which constant, (almost) bulk-like values could be observed in thin films; thus it is not surprising that first indications of superparamagnetism could be observed. For comparison reference is made to section 3.2, and especially to the figures 3.10, 3.15 and 3.16. Moreover, the remanence and the ZFC-measurement in figure 3.23 reveal the Verwey transition observed in ALD-synthesized iron oxide nanotubes for the first time. A peak in the first derivative dM/dT —corresponding to the highest slope of the curve—can be attributed to the Verwey transition at (107 ± 2) K. This value is slightly decreased compared to the thin film measurements presented in section 3.3. However, this observation agrees with previous studies on thin films and electrodeposited nanowires for which similarly reduced transition temperatures were reported as well.[Sen97] [Kle95] [Car05] [Orn10] In all these publications, the shift of the Verwey transition to lower temperatures is generally attributed to mechanical strain in the films or nanostructures. Such a scenario is also conceivable for the nanotube in which the curved iron oxide

layer is sandwiched between two silica layers. In contrast, the granular iron oxide films deposited by ALD are neither capped with a silica layer nor are their surfaces curved. Thus, ALD-deposited, granular thin films might exhibit less strain than the nanotubes and epitaxial films—leading to a Verwey transition close to the bulk value. The observation of the Verwey transition reflects the improved synthesis conditions compared to earlier studies of the Nielsch group.[Esc08] [Bac09] [Pit09] [Alb10] [Cho10a] [Alb11] Moreover, the high quality of the silica shell is shown which protects the magnetite layer in the highly oxidizing chromic acid solution used in the release procedure.

3.4.2 Synthesis of Superparamagnetic Nanotubes

A liquid suspension of superparamagnetic nanotubes is supposed to show a better stability against agglomeration and sedimentation than a liquid suspension consisting of permanent magnetic nanotubes. The thermally fluctuating magnetization in the nanoobject would hinder dipolar magnetic interactions, and thus the agglomeration is supposed to be reduced. In section 3.3 (figures 3.15 and 3.16) it was shown that iron oxide films reveal superparamagnetic behavior if the thickness is reduced to ≤ 5 nm. Therefore, the iron oxide layer thickness sandwiched between the silica layers in the nanotube wall was reduced. After reduction and release, the nanotube suspension optically revealed a better stability. TEM micrographs show a thin, granular iron oxide layer sandwiched between the silica shells for the individual tubes with a narrow size and length distribution of the majority of tubes in the sample (figure 3.24 (a) and (b)).

SQUID measurements of a dried nanotube suspension with a nominal iron oxide wall thickness of 5 nm confirm the possibility to transfer the knowledge achieved on the iron oxide thin films to the nanotubes. Comparison of magnetization isotherms measured at 5 K and 300 K indicates superparamagnetic behavior of the nanotubes by the disappearance of coercivity and remanence at elevated temperatures (figure 3.25 a). Magnetic saturation could not be achieved in the measurement setup used. Thus, high-field ± 40 kOe magnetizations isotherms were performed with a smaller field-step-size around the x-axis intersection, but with a reduced signal-to-noise ratio as displayed in the appendix in figure A.9. Such large saturation fields (> 20 kOe) would explain the ‘apparent’ reduced saturation magnetization observed in iron oxide thin films (section 3.3).¹⁵ The coercive field at 5 K amounts to (1150 ± 50) Oe, and thus is significantly larger than the values obtained for permanent magnetic magnetite films and nanotubes (compare to figure 3.22 in this section and figure 3.11 in section 3.3). Several reasons can cause such a large coercivity: first, the surface anisotropy contribution becomes important due to the increased

¹⁵MPMS-2, Quantum Design, Inc. maximal field range ± 10 kOe; MPMS-XL, Inc. maximal field range ± 50 kOe. The latter shows a lower signal-to-noise ratio than the MPMS-2

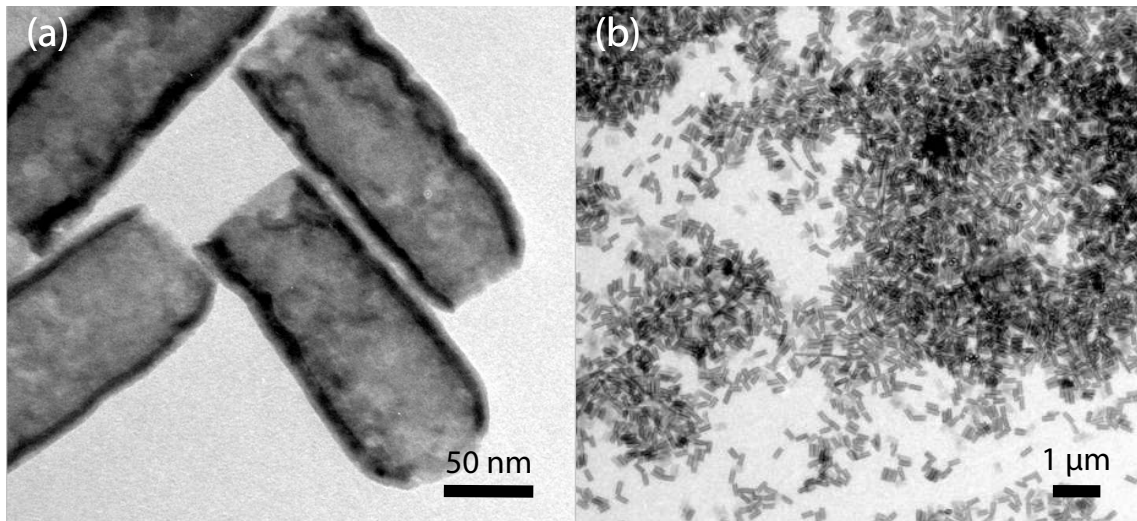


Figure 3.24: TEM micrographs of (190 ± 20) nm long iron oxide nanotubes with a tube diameter of (85 ± 10) nm and a nominal iron oxide wall thickness of 5 nm. (a) A magnified image reveals three-layered structure of the nanotube. The inner silica shell could only partially resolved. Furthermore, the open tube bottom is remarkable and is most likely caused by a too long Ar^+ sputtering. (b) Overview TEM image displays the length and diameter homogeneity of the nanotube sample.

surface-to-volume ratio of the small particles/grains in the nanotube wall. The effective anisotropy is increased and would lead to larger coercivities and higher saturation fields (in randomly distributed particle systems). [Zys04] [Gil05] [Lim10] Second, interaction of (superparamagnetic) nanoparticles, which are aligned in a chain, can raise the coercivity—to values above 1200 Oe—as calculated by Muxworthy and Williams. [Mux09] Third, acidic oxidation—caused by the strongly oxidizing chromic acid in the release step—or subsequent aerobic re-oxidation cannot be excluded from consideration. Formerly prepared magnetite nanotubes might change partially or even completely to maghemite or hematite which could reveal high coercivities at low temperatures in combination with superparamagnetic behavior. [Han77] [Mar98] [Kos02] [Yan11]

Temperature-dependent measurements as displayed in figure 3.25 (b) substantiate the hypothesis of superparamagnetic iron oxide nanotubes. The magnetic moment determined in a remanence measurement (after applying the maximal accessible field of 10 kOe) goes to zero. Furthermore, field-cooled and zero-field-cooled measurements display the typical footprint as expected for superparamagnetic behavior in such measurement routines. A maximum at around (75 ± 10) K is visible in the ZFC-measurement and is attributed to the blocking temperature of the system. Furthermore, the FC-measurement shows the typical progression of superparamagnetic behavior by staying almost constant below the blocking temperature and following

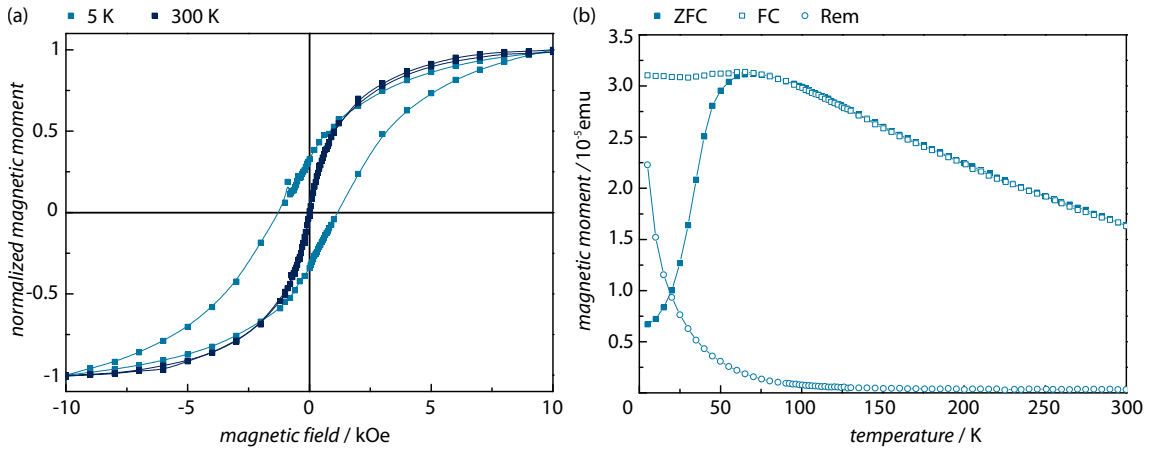


Figure 3.25: SQUID magnetization measurements of the dried nanotube suspension displayed in figure 3.24 reveal superparamagnetic behavior. (a) A magnetizations isotherm measured at 5 K displays an open hysteresis curve (coercive field fairly above 1000 Oe), whereas a measurement at 300 K shows a crossing through the origin indicating superparamagnetic behavior. Saturation could not be achieved even in the highest accessible magnetic field of the measurement setup used. (b) Temperature-dependent magnetization measurements support the hypothesis of the superparamagnetic behavior. The remanent magnetic moment after applying a magnetic field of 10 kOe and measuring during warm-up goes to zero. Additionally, the field-cooled and the zero-field-cooled measurement at a magnetic field of 600 Oe display the typical trend as expected for superparamagnetic behavior. The maximum at around 75 K in the ZFC-measurement is attributed to be the blocking temperature.

the ZFC-behavior above. The splitting temperature—at which the relaxation time of the largest particles becomes comparable to the measurement time—can be estimated to around (130 ± 20) K and coincides with the temperature at which the remanence curve reaches zero.

Iron oxide nanotubes with a nominal wall thickness of ≤ 4 nm reveal similar high coercivities of $\geq (975 \pm 25)$ Oe—showing that the synthesis process is reproducible—and were investigated by magnetic field-dependent ZFC-measurements. The results of which are displayed in figure 3.26 revealing a shift of the blocking temperature to lower values at larger applied magnetic fields (subfigure (a)). This observation is expected for superparamagnetic systems as the energy barrier is reduced by the applied magnetic field. Thus, switching of the magnetization can occur more easily, resulting in a lowered blocking temperature.[Bea59] [Kno08] For a single uniaxial superparamagnetic particle with the magnetic volume V the blocking temperature T_b can be derived as a function of the applied magnetic field H to

$$T_B = \frac{K_u V}{k_B \ln\left(\frac{\tau_N}{\tau_0}\right)} \left(1 - \frac{H}{H_0}\right)^2 \quad (3.1)$$

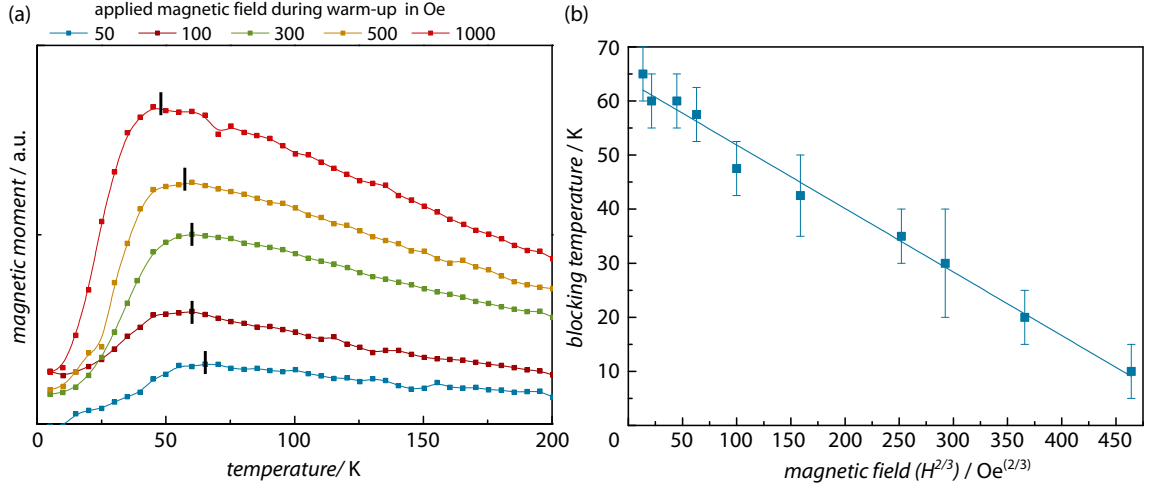


Figure 3.26: (a) Magnetic moment (in arbitrary units) as a function of the temperature for ZFC measurements performed on a dried nanotube suspension (similar to 3.24 but with a reduced, nominal wall thickness of 4 nm) at different applied magnetic fields. A maximum (highlighted by the black lines) can be observed in all curves which is attributed to the (magnetic field-dependent) blocking temperature of a superparamagnetic system. (b) Plot of the determined blocking temperature as a function of the applied magnetic field ($H^{2/3}$) reveals a linear trend which can be attributed to a spin-glassy behavior (see discussion in main text). The lines in (a) serve as guide to the eyes. The error bar in (b) are caused by determining the blocking temperature.

in which K_u and H_0 denote an uniaxial anisotropy constant and a field parameter related to the anisotropy field with $H_0 = \frac{2K_u}{M_s}$, respectively.[Zha98] τ_0 and τ_N denote a material-dependent, characteristic time in the range from 10^{-9} s to 10^{-10} s and the Néel relaxation time, respectively (section 2.1) The equation generally changes for a standard laboratory setup (measurement time 100 s) to

$$T_B = \frac{KV}{25k_B} \left(1 - \frac{H}{H_0}\right)^\alpha \quad (3.2)$$

assuming an interacting system of superparamagnetic nanoparticles with a general anisotropy constant K —reflected in H_0 . The exponent α ranges from 1.5 to 2 depending on the interaction strength, the symmetry of the magnetocrystalline anisotropy, and the magnetic field direction with respect to the magnetic easy axes of the nanoparticle.[Bro63] [Vic89] The latter equation is only valid if the magnetic energy is much smaller than the energy barrier ($mH \ll E$).

If the energy barrier is significantly decreased by large applied magnetic fields, the behavior changes to a

$$T_B \propto -H^{2/3} \quad (3.3)$$

relation.[Wen84] [Dor87] The authors of both publications predict a crossover to the quadratic behavior if the applied magnetic field approaches zero. The plot of the determined blocking temperature as a function of the applied magnetic field (in terms of $H^{\frac{2}{3}}$) is displayed in figure 3.26 (b). Such a linear dependence is often attributed to spin glass systems. However, the previously mentioned publications of Wenger and Mydosh as well as Dormann and co-workers showed that the $H^{\frac{2}{3}}$ -behavior of the blocking temperature is not an unique property of spin glasses. Several authors demonstrate the difficulty to distinguish experimentally clearly between a superparamagnetic behavior and a spin glass-like one.[Goy04] [Ban06] [Ped08] Furthermore, measurements by Luo *et al.* on frozen ferrofluids reveal spin-glassy behavior which is caused by an interacting particle system with a random magnetic anisotropy.[Luo91] The latter explanation is also conceivable for the system of randomly distributed, interacting grains closed to each other in the nanotube's wall.

Superparamagnetic nanotubes were recently achieved by Pitzschel utilizing ALD of nickel and cobalt-doped nickel as well as by Chong for cobalt ferrite ALD.[Pit12] [Cho11] The latter publication clearly demonstrates the influence of the deposited wall thickness—which determines the grain size in the wall—on the coercive field, remanence and blocking temperature. However, no magnetic field-dependent study of the blocking temperature was performed.

To conclude, we could demonstrate the ability of synthesizing superparamagnetic iron oxide nanotubes by combining porous alumina membranes and ALD. Measurements of the blocking temperature as a function of the applied magnetic field revealed a dependence which is often attributed to spin glasses. Even if there are several publications which showed that this could also be related to pure superparamagnetism, a clear evidence could not be given in the framework of this thesis. To shed more light onto the open question, pursuing magnetic measurements, e.g. AC-susceptibility measurements to determine the energy barrier (distribution) of the grains, are suggested.

3.5 Three-Dimensional Scale-Up: Synthesis of Nickel Nanorods

In this section, a synthesis route is described which overcomes the boundaries of the limited template size. In the preparation approach for iron oxide nanotubes, only the template surface area was increased leading to a two-dimensional scale-up (section 3.1 and 3.4). However, simple template enlargement is generally restricted by experimental and economical setup constraints. Herein, a promising three-dimensional scale-up route is presented utilizing long multisegmented Ni/Cu nanowires electrodeposited into porous AAO membranes as precursor for the synthesis of short nickel nanorods.

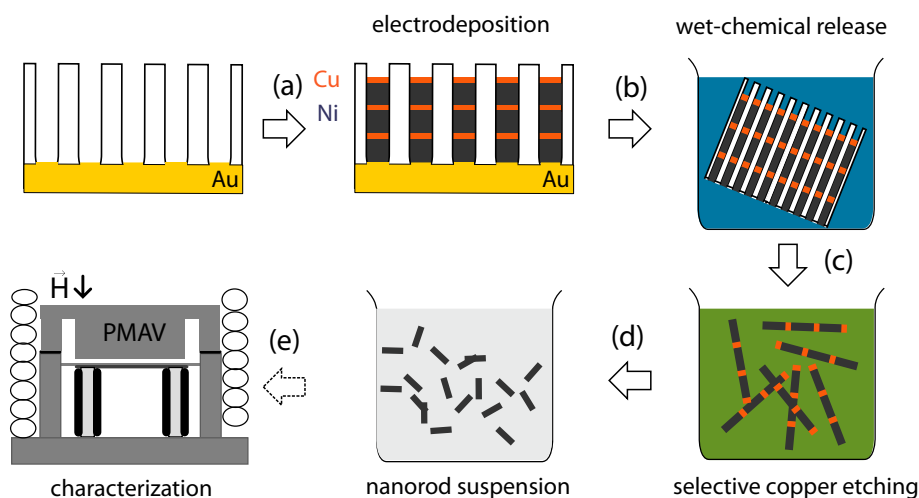


Figure 3.27: Scheme of the preparation route of a magnetic Ni nanorod ferrofluidic suspension. (a) Pulsed electrodeposition of nickel and copper on a through-hole AAO membrane with a gold backside contact results in long multisegmented nanowires embedded in the membrane. (b) Selective etching of the supporting AAO template releases the multisegmented wires. (c) Transfer of the long nanowires to a selective copper etchant, removal of the sacrificial copper phase and (d) subsequent re-dispersion in a carrier medium result in a nickel nanorod liquid suspension, which is ready for magnetic field-dependent viscoelastic characterization (e).

The concept of the synthesis route is schematically illustrated in figure 3.27. Starting point of the preparation path is a nanoporous alumina membrane synthesized by electrolytic oxidation of aluminum (section 3.1). The backside (underlying) aluminum is wet-chemically removed and the closed pores' hemispheres are opened by wet-chemical etching in phosphoric acid or by reactive ion etching. A thin gold layer is then sputtered on one side of the through-hole AAO membrane serving as seed layer for the subsequent electrodeposition of gold (for instance from a commercial Au bath like *AurunaTM 5000*) to thicken the backside electrode and to close the pores. *Pulsed electrodeposition* of nickel and copper (figure 3.27(a)) into such a prepared membrane results in multisegmented nanowires embedded in the AAO template. By sequential switching between two different applied potentials in the range of seconds, selective deposition in a multilayer fashion of two materials from one electrolyte is possible (figure 3.29(a)). Afterwards, the gold working electrode is selectively removed by using potassium triiodine solution to enable the subsequent release of the multisegmented Ni/Cu wires from the supporting alumina template in an alkaline solution (figure 3.27(b)). Subsequently, the long nanowires are filtrated from the alkaline solution, rinsed several times with water, and finally transferred to a selective copper etchant based on isopropyl alcohol (figure 3.27(c)).[Jag94] A short description of the chemical reactions during selective etching is given in

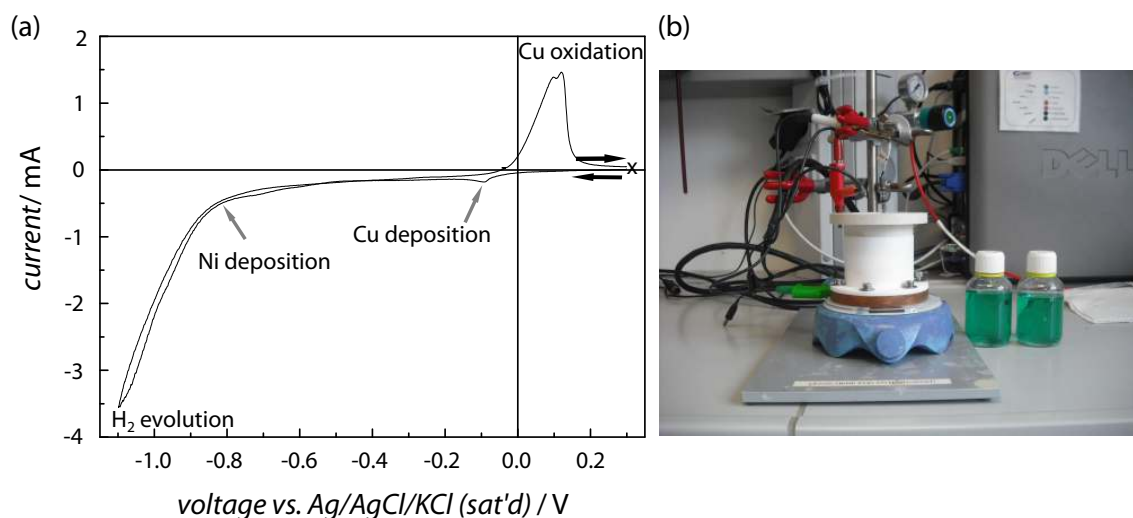


Figure 3.28: A cyclic voltammogram (CV) of the electrolyte is displayed in subfigure (a). The CV was taken in standard conditions on an oxalic acid membrane with a sweep rate of 20 mV s^{-1} . The dip at -140 mV is assigned to the diffusion limited region in the reduction of copper, whereas the reduction of the nickel ions starts at -0.8 V and merges at lower potentials into hydrogen evolution. The photograph (b) displays the three-electrode setup which is connected to a *Gamry* potentiostat.

figure A.5. The copper layers are selectively removed leading to isolated, short magnetic nickel nanorods, which are subsequently transferred—again via filtration and washing—to the carrier medium. Finally, the synthesis procedure leads to a nickel nanorod suspension ready for further magnetic and magnetoviscous characterization (figure 3.27 (d)).

Ni and Cu were chosen—from the broad range of materials able to be electrodeposited—for several reasons. First, for the sake of easiness, since data on the electrodeposition process parameters, and their characterization with respect to stoichiometry, crystallinity and magnetic properties are readily available by several publications of the Searson group.[Che03a] [Che03b] [Sun04] [Che06] Second, nickel and magnetite have almost the same magnetization at room temperature (table 2.2), making the nickel nanorods and the iron oxide nanotubes more easy to compare, since at least one magnetic parameter is kept constant. Third, nickel can easily resist the release process of the multisegmented nanowires from the template in an alkaline solution by forming a thin, native oxide which works as protective layer. Last, the copper layers can be selectively removed without etching the nickel.[Jag94] [Ara04]

The metal ions for the electrodeposition were provided by an electrolyte simultaneously containing nickel and copper ions—in detail, 0.5 M nickel(II) sulfate hexahydrate ($\text{NiSO}_4 \cdot 6 \text{ H}_2\text{O}$), 0.005 M copper(II) sulfate pentahydrate ($\text{CuSO}_4 \cdot 5 \text{ H}_2\text{O}$), and 0.6 M boric acid (H_3BO_3) as pH buffer. To overcome the fact that copper

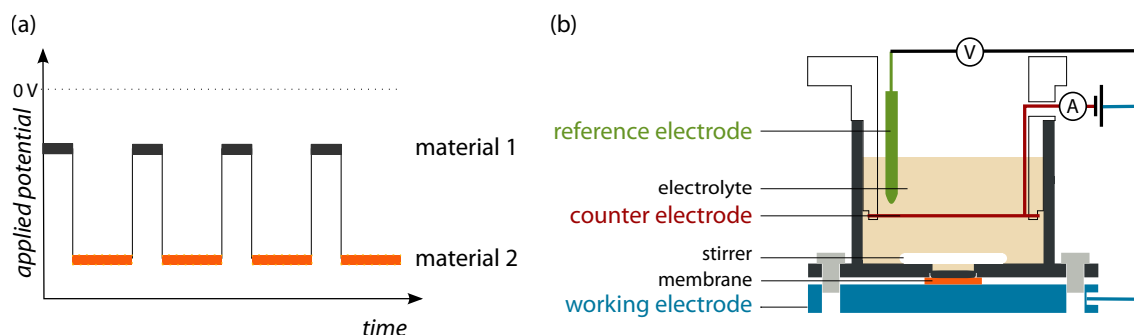


Figure 3.29: (a) Scheme of a three-electrode electrodeposition cell. The electrodeposition takes place on the working electrode by applying a suitable, constant reduction potential between working and reference electrode. The reduction current is read by the counter electrode. Such a system is able to provide a constant potential at the working electrode without fluctuations. (b) Schematic drawing of the applied potential as a function of the experiment time. Sequential switching between two potentials allow for electrodeposition of different materials in a multilayered fashion.

is more noble than nickel, the ratio of ions in the electrolyte is adjusted to be 1:100. Thus, copper incorporation into the deposited nickel during the high potential pulses is minimized and almost pure nickel segments can be obtained. The optimum deposition potentials were determined to be -160 mV and -1.0 V for copper and nickel, respectively, according to cyclic voltammetry which was taken with a three-electrode setup connected to a *Gamry*TM potentiostat in same experimental conditions as used for electrodeposition later (figure 3.28). The deposition technique bases on a three-electrode setup—schematically displayed in figure 3.29 (b) in which a constant voltage is applied between reference and working electrode. The electrical current, necessary for the reduction, is provided by the counter electrode. Thus, a constant potential without fluctuations can be obtained at the working electrode. The duration at the different reduction potentials determines the individual length of the copper and nickel segments. Therefore, the length of the nickel segments can be tailored from disk-like (aspect ratio < 1) to rod-like segments—depending on the template and the duration of the potential—as shown in figure 3.30. More than one hundred magnetic nanoobjects separated by sacrificial Cu layers can be stacked in form of long multilayered wires depending on the template thickness and the length of the individual segments. The surface of a template has to be enlarged by a factor equal to the number of stacked nanoobjects to lead to the same yield as if only one layer is deposited. Such a two-dimensional scale-up process is economically not feasible due to the high consumption of ultra-pure aluminum needed for well-ordered pore structures.

The synthesis of such multilayered (magnetic/non-magnetic) wires or thin films by electrodeposition is well established within the research community of the gi-

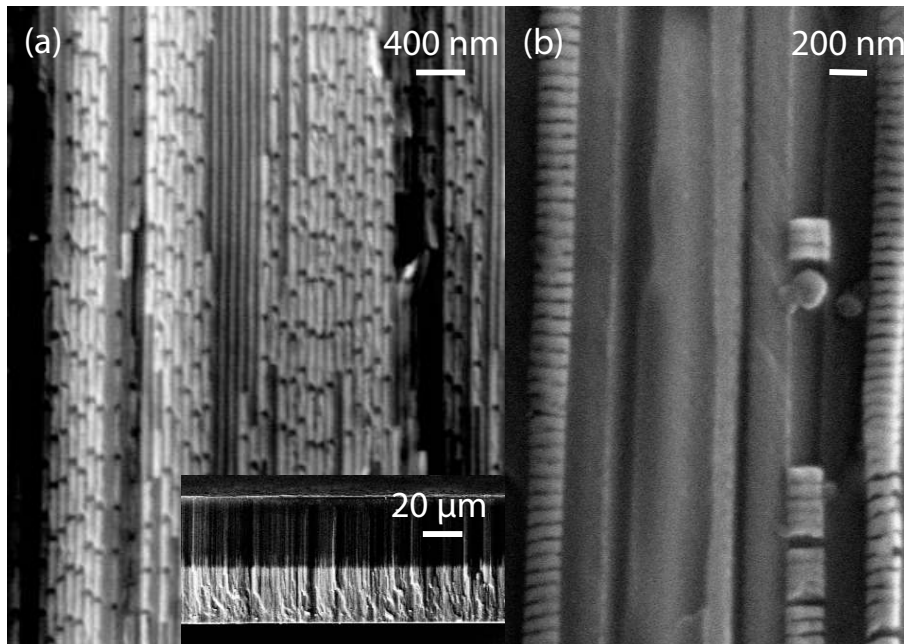


Figure 3.30: SEM images displaying cross-sectional views of AAO membranes filled with multisegmented wires. (a) An oxalic acid porous alumina membrane with a pore diameter of (40 ± 5) nm was filled via multilayer electrodeposition in such a way that long nickel segments with an aspect ratio of ten were received. (b) Deposition into a *Whatman*TM porous alumina membrane (pore diameter (180 ± 50) nm) at a reduced nickel deposition time results in magnetic nanodisks with an aspect ratio of around 0.5. For (a) and (b), the edge of the cross-section was dipped into the selective Cu etchant to enhance the contrast between individual segments. The inset in (a) illustrates the uniformity of pore-filling during electrodeposition.

ant magnetoresistance (GMR) effect.[Bak10] In that specific case, the length of the non-magnetic buffer segments has to be in the range of the exchange length of the magnetic layers, typically below 10 nm to 20 nm. Moreover, the magnetic layer is supposed to provide an easy axis perpendicular to the long axis of the wire—easily achieved by ultra-thin segments due to the enhanced shape anisotropy.[Blo94] [Eva00] In contrast, thicker segments have been synthesized in this thesis for two reasons: first, to achieve well-separated nanorods, and second to introduce a preferred easy axis parallel to the nanorod axis.

Cross-sectional SEM micrographs of filled membranes are presented in figure 3.30. The main SEM images of (a) and (b) exhibit precise control of the electroplating process, and therefore of the segments' lengths, by using alternating deposition potentials for nickel and copper reduction. Moreover, the inset in subfigure (a) provides evidence for the homogeneity of the growth during electrodeposition inside the pores. Figure 3.31 presents SEM images of the different stages during the syn-

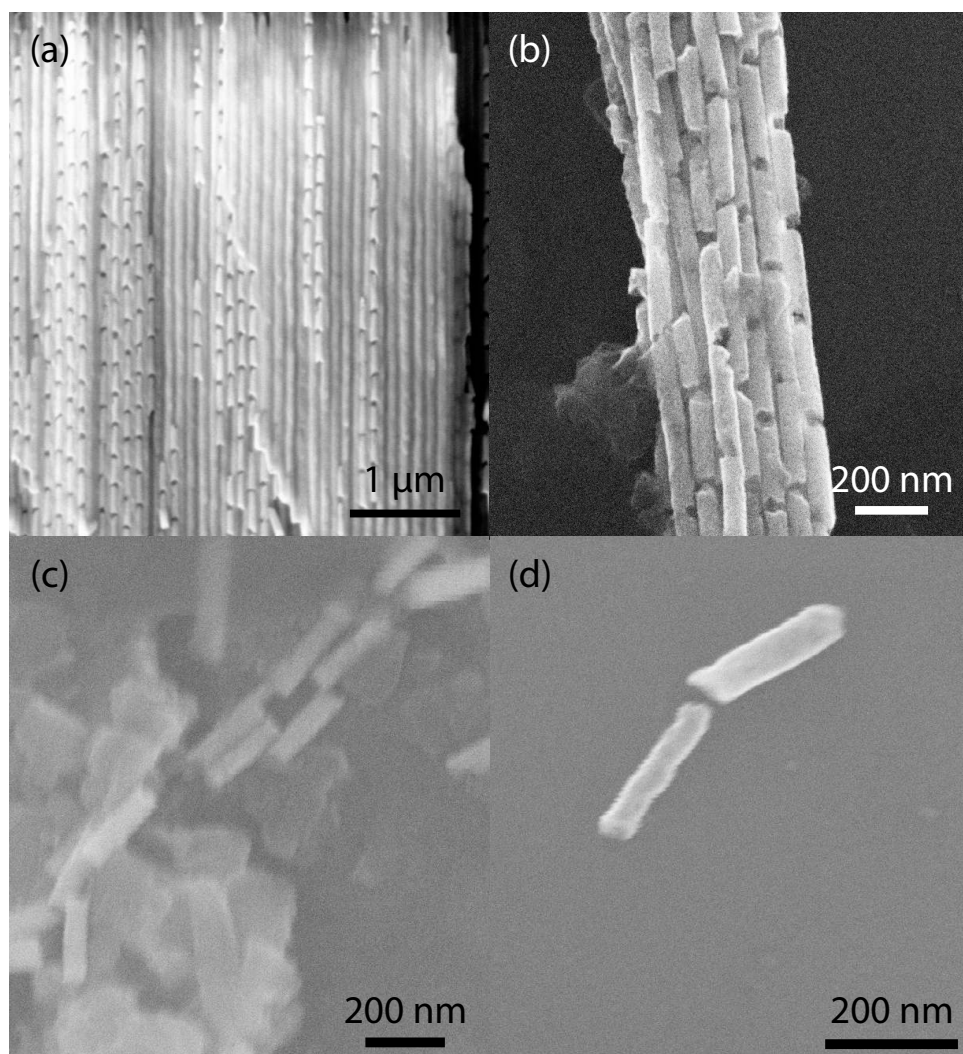


Figure 3.31: SEM micrographs at different points during the synthesis of (220 ± 40) nm long nickel nanorods: (a) multisegmented Ni/Cu wires embedded in the membrane; (b) a bundle of long, multilayered nanowires released from the supporting template and dried on a silicon substrate (selective Cu etching performed at the cross-section and in the dried state to enhance the contrast). (c)+(d) Individual, short nickel nanorods after selective copper etching, washing, and dispersing in the carrier medium (finally dried on a silicon substrate).

thesis of nickel nanorods with a length of (220 ± 40) nm: (a) long, multisegmented nanowires embedded in the membrane; (b) a bundle of multilayered wires released from the membrane; (c)+(d) separated, dispersed short nickel nanorods. Evidently, magnetic nanorods with fully tunable geometrical parameters are feasible by selecting the appropriate template as well as the electrodeposition parameters of the individual nickel and copper segments.

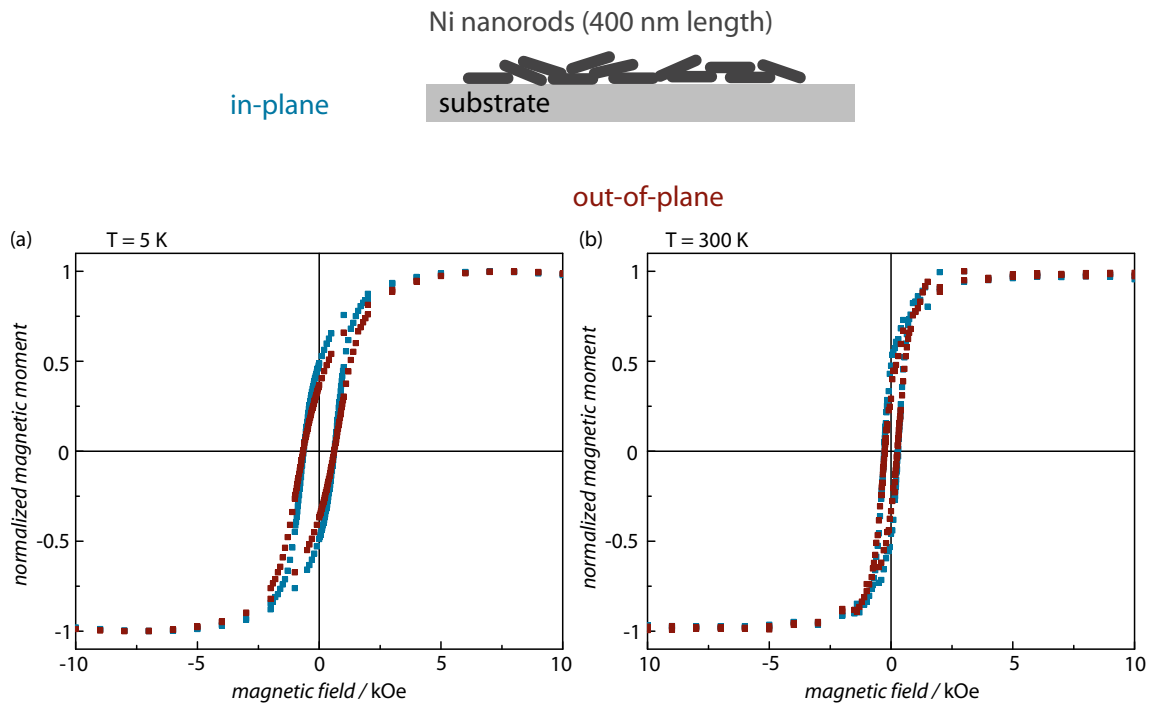


Figure 3.32: Normalized magnetization isotherms of nickel nanorods with a length of (400 ± 40) nm at 5 K (a) and 300 K (b). At both temperatures a reduced squareness in the out-of-plane measurement is obvious compared to the in-plane measurement. An easy axis parallel to the rod's axis can be cautiously concluded even the saturation and the coercive field display no clear difference for the in-plane and out-of-plane configurations at both temperatures. The nickel nanorod liquid suspension was dried on a silicon substrate. The scheme at the top of the figure illustrates the nomenclature for the in-plane and out-of-plane measurement.

The magnetic properties of released nanorods with a length of (400 ± 40) nm and a diameter of (40 ± 5) nm were examined by SQUID magnetometry (figure 3.32) on a dried nanorod suspension. At a temperature of 5 K (displayed in (a)), the in-plane and the out-of-plane measurement reveal the same coercive field of (625 ± 25) Oe. However, the squareness differs significantly for the two different directions and amounts to $(49 \pm 1)\%$ and $(37 \pm 1)\%$, respectively. Raising the temperature to 300 K reduces the coercive fields in both directions to (275 ± 15) Oe, whereas the squareness is only slightly decreased to $(47 \pm 1)\%$ and to $(32 \pm 1)\%$ for the in-plane and the out-of-plane direction, respectively. The measured differences between both configurations indicate an easy axis along the nanorod axis. In the out-of-plane measurement almost all rods are supposed to be perpendicular aligned to the applied magnetic field, whereas in the in-plane measurement a certain amount of nanorods point in field direction (sketched on top in figure 3.32). If no magnetic field is applied during the drying procedure, the pointing direction of the nanorods is sup-

posed to be homogeneously distributed over 180° in the substrate plane. Thus, a large switching field distribution has to be taken into account since the majority of rods has a certain out-of-plane component, which will affect the observed coercive field, the squareness, and the saturation field. The latter is normally used to differentiate between easy and hard axis. Unfortunately, the saturation field is almost the same for both measurements directions. Thus, only the increased remanence—at 5 K and 300 K—of the in-plane measurement compared to the out-of-plane data serves as hint for a preferred easy axis parallel to the rod axis. However, Chen *et al.* published measurements and simulations on multisegmented nanowires which reveal an easy axis parallel to the wire axis.[Che03a] [Che03b] Moreover, Chen and co-workers demonstrated in a following publication that tilted multisegmented nanowires reveal significant differences in the hysteretic behavior compared to non-tilted wires.[Che06] The ‘apparent’ perpendicular—to the wire axis—measurement displays an increase in coercive field and squareness, whereas the ‘apparent’ parallel measurement demonstrate reduced values for both quantities.

One aim of the SQUID measurements was the estimation of the volume concentration of magnetic material in the liquid suspension after viscosity measurements. An additional washing step could not be applied since a certain loss can be expected in such a procedure consisting of filtration and several rinsing steps. Thus, the nanorods suspended in the diethylene glycol/water mixture had to be dried. To overcome the low vapor pressure of diethylene glycol, temperature- and vacuum-assisted evaporation of the solvent was applied. The high drying temperatures (120°C) with respect to the Curie temperature of the magnets¹⁶, the vibrations of the vacuum pump as well as the high viscosity of pure diethylene glycol—the water evaporates first—might had hindered a sufficient alignment in the magnetic field direction. For sure, improvements in the drying setup will lead to better results of the magnetization isotherm measurements.

A versatile synthesis approach was presented in this section which allows for the scaled-up synthesis of nickel nanorods via electrodeposited multilayered Ni/Cu nanowires and subsequent selective etching of the sacrificial copper layers. The combination of AAO membranes with electrodeposition enables the experimentalist to tune all geometric properties of the desired magnetic objects in liquid suspension.

¹⁶The distributor of the NdFeB magnets recommend a maximum application temperature from 80°C to 100°C , since the Curie temperature amounts for the commercial magnets to around 300°C . [Sup13]

4 Magnetic and Magnetorheological Properties of Liquid Suspensions

The synthesis of sufficiently concentrated and voluminous liquid suspensions of magnetic particles is challenging not only for template-based approaches but also for the most sol-based synthesis routes. In general, several mL of these liquid suspensions with volume concentrations above 0.1 vol % are often needed for the magnetic field-dependent viscoelastic characterization in the standard rheometers. In this work, a *piezo-membrane axial vibrator*—specialized to measure fluids with volumes below a tenth of a milliliter—was used to determine the magnetic field-dependent fluid-mechanical properties of the prepared liquid suspensions. In the first part of this chapter, the instrument is shortly introduced and described. Thereafter, magnetic and magnetorheological measurements of a commercial ferrofluid are presented acting as a reference for the elongated particle suspensions. Subsequently, the magnetoviscous effect of elongated particle suspensions is discussed in a separate section, as well as the shear thinning effect. Last but not least, the complex shear modulus of the conventional ferrofluid and an elongated particle suspension is investigated. Finally, a short summary is given including the key ideas and major points of this chapter in terms of a keyword list.

The MVE designated in this chapter is calculated from the absolute value of the complex viscosity in accordance to the standard convention of oscillatory rheological measurements.

4.1 Piezo-Membrane Axial Vibrator

Pipe, capillary, rotational cylinder, cone or plate rheometer, to name a few, are standard measurement systems used for rheological characterization of liquids, melts, polymers, and colloidal liquid suspensions.[Mez06] A rheometer in a magnetic field allows for the determination of magnetic field-dependent fluid-mechanical properties. However, volumes above one milliliter are needed, making the use of these rheometers not suitable for this work. Pechhold and co-workers developed a piezo-membrane axial vibrator (PMAV) at the *Institut für dynamische Materialprüfung* (Ulm) which enables to determine the viscoelastic properties of liquids with a volume down to 50 μL . Detailed information about the setup, theory and measurement of the PMAV can be found in the work of Kirschenmann.[Kir03] Thus, only a short

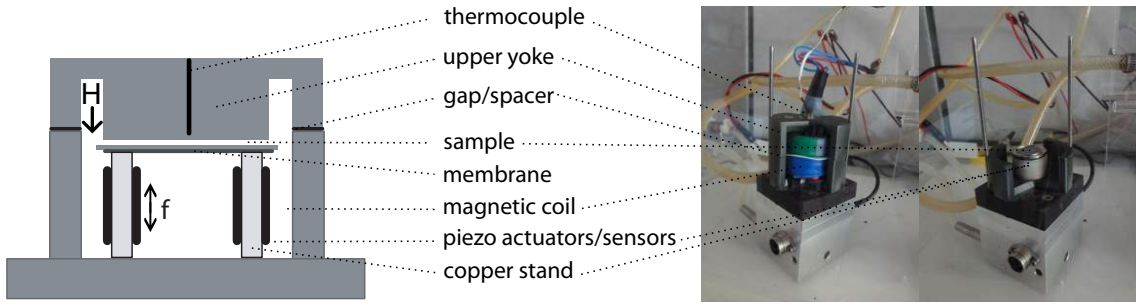


Figure 4.1: Scheme (left) and photograph (right) of the PMAV setup. The major components are labeled.

introduction is given at this position. Magnetic coils around the PMAV setup allow for applying a magnetic field in the range from 0 mT to 110 mT by controlling the electrical current through the coils.[Wu06] [Wu11] The complex shear modulus/viscosity can be determined in a shear frequency range from 8 Hz to 200 Hz under *squeeze flow* conditions. Individual viscosity measurements were found to be reproducible within $\pm 3\%$. All viscoelastically characterized liquid suspensions based on a carrier medium consisting of a diethylene glycol-water mixture with a volume ratio of seven to three. A total volume of $(95 \pm 5) \mu\text{L}$ liquid suspension was used to determine the magnetic field-dependent viscoelastic properties. During the measurement, the setup was kept at a constant temperature of $(20.0 \pm 0.3)^\circ\text{C}$ controlled by an external cooling system (not displayed in figure 4.1).

A scheme and a photograph of the PMAV are presented in figure 4.1. The PMAV setup basically consists of a pair of yokes. The upper yoke is rigid and covered with a thin glass plate. The lower yoke is the active (working) part of the PMAV with a stainless steel membrane. A liquid sample can be placed on the stainless steel plate in the gap between the two yokes. The height of the gap can be adjusted by adding thin spacing layers. The membrane is connected to eight piezo elements mounted on copper stands. Four of them work as actuators and their elongation is controlled by a lock-in amplifier. The amplifier excites the actuators at a desired frequency within the range from 8 Hz to 200 Hz, which results in a vertical oscillation of the membrane with an amplitude of approximately 5 nm. The other four piezo elements are separated from the actuators and work as sensors to detect the response of the system. The liquid sample in the gap is squeezed and experiences a ‘squeeze flow’ perpendicular to the oscillation of the membrane.[Lau92] [She98] [Kir03] [Cra05] [Eng05]

The complex spring constant K^* of a fluid can be determined from the ratio of the dynamic displacements in unloaded and loaded state. Pechhold derived the spring constant to

$$K^* = \frac{3\pi}{2} \cdot R \cdot \left(\frac{R}{d}\right)^3 \cdot \frac{G^*}{1 + \frac{\rho\omega^2 d^2}{10G^*} + \theta} \quad (4.1)$$

assuming the dynamic squeeze flow model of an incompressible fluid with linear viscoelasticity and without wall slipping. G^* and ρ are properties of the fluid, namely complex shear modulus and density, respectively; plate radius R , gap distance d and shear frequency ω are setup parameters. Neglecting terms of higher order of the frequency (expressed by θ) in the denominator results in a quadratic equation for the complex shear modulus

$$0 = G^{*2} - G^* \frac{K^*}{K_0} \frac{1}{c} - \frac{b}{c} \frac{K^*}{K_0} \quad (4.2)$$

with $b = \frac{\rho\omega^2 d^2}{10}$, $c = \frac{3}{2}\pi R \left(\frac{R}{d}\right)^3 \frac{1}{K_0}$ and $K_0 = \frac{K_{01}K_{02}}{K_{01}+K_{02}}$. K_{01} denotes the spring constant of the active part of the copper stand (highlighted in dark grey at the copper stand in figure 4.1) and K_{02} the spring constant of the passive part. Taking only the positive solution of this equation into account results in

$$G^* = \frac{1}{c} \frac{K^*}{K_0} \frac{1}{1 - bc \frac{K_0}{K^*}}. \quad (4.3)$$

With the limitation to low frequencies ($f < 1000$ Hz) the inertia correction $bc \frac{K_0}{K^*}$ is negligible small. Therefore, the real part of the shear modulus amounts to

$$G' = \frac{1}{c \left(\frac{K_0}{K}\right)'} \quad (4.4)$$

and the imaginary part to

$$G'' = -\frac{1}{c \left(\frac{K_0}{K}\right)''}. \quad (4.5)$$

$\left(\frac{K_0}{K}\right)'$ and $\left(\frac{K_0}{K}\right)''$ are directly related to the output signals of the 2-channel lock-in amplifier allowing for the calculation of the loss and storage modulus. For a more detailed derivative of this solution and its relation to the lock-in measurement signals, it is referred to Kirschenmann's PhD thesis to the chapter nine and ten as well as to the appendix A3.[Kir03]

4.2 Reference Ferrofluid Based on Spherical Nanoparticles

A commercially available ferrofluid¹ was used to prepare the reference ferrofluidic suspension—to be compared with the elongated liquid suspensions—and to work as staple for the hybrid suspensions. The commercial product is based on (superpara)magnetic cobalt ferrite (CoFe_2O_4) nanoparticles which are suspended in pure

¹LCE-25TM by (former) *SusTech GmbH*

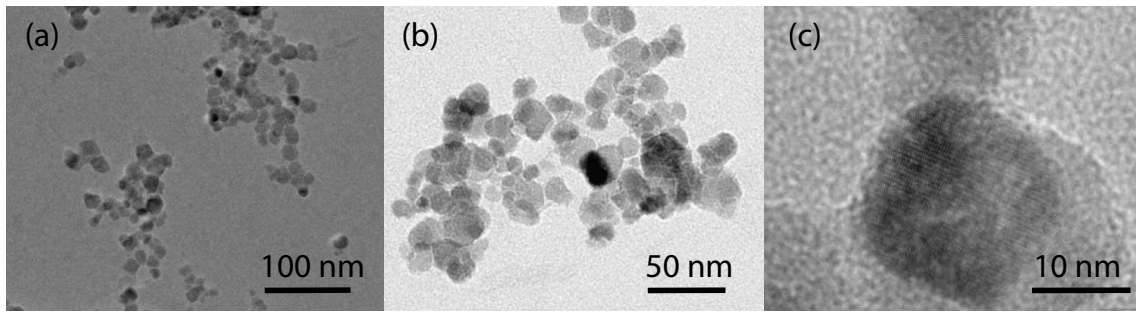


Figure 4.2: HR-TEM micrographs (a)-(c) of the reference ferrofluid’s cobalt ferrite particles at different magnifications. (a)-(b) A large size distribution with a mean diameter of about 20 nm is apparent.[Fau12]. (c) Image of a single-crystalline nanoparticle.

diethylene glycol (DEG) with a volume concentration (solid/liquid) of 25 %. The reference ferrofluid used in this work was prepared (if not otherwise denoted) by dilution of the initial LCE-25 with water and DEG to a volume concentration of $(0.66 \pm 0.03) \%$ (solid/liquid) suspended in a 7:3 DEG-water mixture.

4.2.1 Aging of the Reference Ferrofluid

The major part of the cobalt ferrite nanoparticles is supposed to be superparamagnetic, and thus to exhibit diameters less than 10 nm after synthesis 2007. However, TEM analysis in the years between 2008 and 2010 indicated already an increased particle diameter ranging from 10 nm to 18 nm, until in 2012 statistical analysis of HR-TEM images (figure 4.2)² revealed a mean diameter of around 20 nm far above the superparamagnetic limit.[Fau12] Such ‘volume growth’ with time is known as aging effect in (aqueous) nanoparticle suspensions and can be caused by nanoparticle clustering/agglomeration or Ostwald ripening.[Pro99] [Tom07] Since the particle’s volume determines the magnetic and magnetoviscous behavior, both properties will change with time.³

Blocked nanoparticles act as permanent magnets since Néel relaxation is not possible; thus, an open magnetization hysteresis is observed. However, in liquid suspension Brownian rotational relaxation is possible. In figure 4.3 (a) magnifications of three (isothermal) magnetization hysteresis curves are displayed. A large coercive field of (8600 ± 100) Oe as well as a saturation field above 45 000 Oe can be

²HR-TEM and statistical analysis of which was performed by Dr. Johannes Biskupek (Ulm University) and Rene Faust (supervised bachelor student, Physic Department, University of Hamburg, 2012), respectively.

³If (later in this thesis) data of hybrid suspensions are compared to pure reference ferrofluid measurements both experiments are performed at the time. Thus, magnetoviscous data of the reference suspension can differ slightly depending at the measurement point during the PhD work.

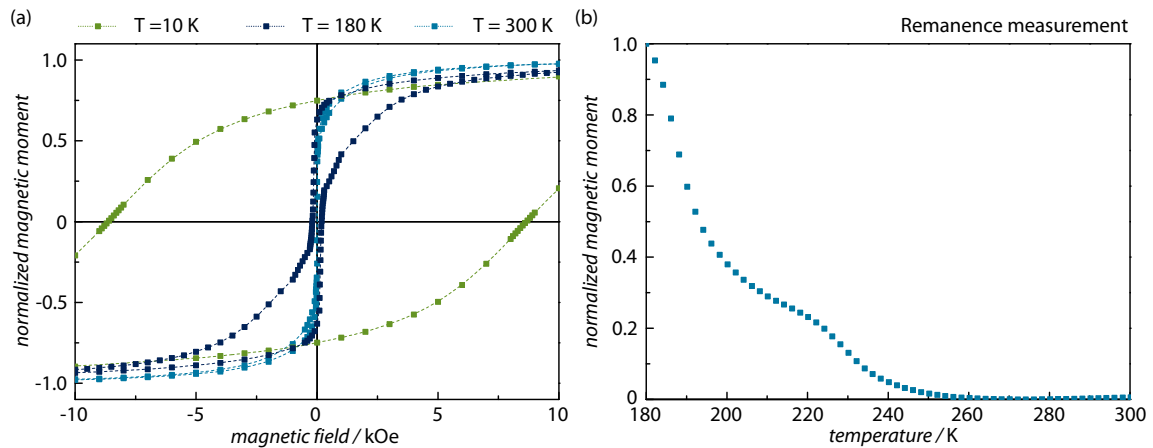


Figure 4.3: (a) Inset in magnetization isotherms of a liquid reference ferrofluid (cobalt ferrite particle, 0.66 vol %) measured at different temperatures (green 10 K, dark blue 180 K, bright blue 300 K). The ferrimagnetism of the frozen cobalt ferrite particles is obvious in the 10 K measurement by the open hysteresis curve. At 300 K a closed magnetization isotherm curve can be observed indicating superparamagnetic behavior. The wasp-waisted shape of the magnetization isotherm measured at 180 K can be explained by a large size distribution of the superparamagnetic nanoparticles. The complete measurements are shown in the appendix figure A.10. The dashed lines serve as guide to the eyes. (b) Temperature-dependent remanence measurement after applying a magnetic field of 50 kOe. A decay related to Néel relaxation is apparent, until the carrier medium melts at around 220 K. Therefore, Brownian rotation of the suspended particles is possible and the remanent magnetic moment of the sample vanishes.

determined at a temperature of 10 K. Such values are typical for hard ferromagnets and match well with literature values reported on cobalt ferrite.[Maa09] [Bal07] The (fixed) magnetic moment of the frozen (immobilized) nanoparticles can be released by raising the temperature. The thermal energy increases and overcomes the (volume-dependent) anisotropy energy of the individual nanoparticles. Particles below the temperature-corresponding critical volume reveal an unblocked (superparamagnetic) state without remanence and coercive field due to the Néel relaxation, whereas nanoparticles with a larger volume stay blocked. The coexistence of these both states can result in a wasp-waisted shape of the magnetization isotherm.[Rob95] Such a shape can be identified in a magnetization isotherm measured at 180 K (dark blue curve) validating the large diameter distribution determined by TEM image analysis. Increasing the temperature to 300 K—above the melting temperature of the carrier liquid—reveals a magnetization isotherm with vanishing coercive field and remanence due to the superposition of the two relaxation mechanisms. This idea is supported by the temperature-dependent remanence measurement displayed in figure 4.3 (b). A single exponential decay is observed until the melting temperature is reached at around 220 K. At that point, the diethylene glycol-water

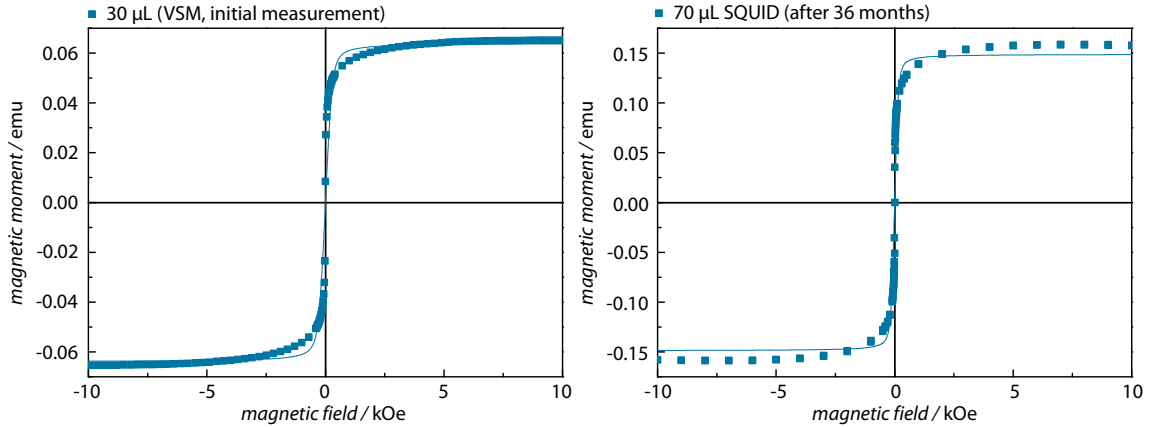


Figure 4.4: Magnetization isotherm measurements of the reference ferrofluid in liquid state (solid points) and the corresponding fit with the Langevin formalism (line). Left image displays the initial VSM measurement of 30 μL (2009) at room temperature. Right panel shows the analysis via a SQUID measurement of 70 μL after 36 months (2012) at 300 K. The fitting parameters and the calculated values are presented in the table 4.1.

mixture melts and thus allows for rotational (Brownian) relaxation. However, the high viscosity of several thousand mPas at the melting point hinders the relaxation by Brownian motion.[MEG13] [Cor13] Further temperature rise results in an exponential—Arrhenius type—viscosity decrease which lowers the Brownian relaxation time about four orders of magnitude—from several hundreds of milliseconds to few microseconds. Thus, the measurement time becomes significantly longer than the relaxation time, and above 250 K only a zero remanent net magnetic moment can be determined by SQUID magnetometry.

Magnetization isotherm measurements of the ferrofluid in liquid state reveal further indication for a volume growth with time. A measurement of the magnetic field-dependent magnetic moment of a suspension of superparamagnetic nanoparticles can be fitted by the Langevin formalism for paramagnets leading to the number

	initial measurement	after 36 months
Measurement system	VSM	SQUID
Liquid volume	$(30 \pm 1) \mu\text{L}$	$(70 \pm 1) \mu\text{L}$
Magnetic nanoparticles	$(2.3 \pm 0.1) \times 10^{12} \mu\text{L}^{-1}$	$(1.3 \pm 0.1) \times 10^{12} \mu\text{L}^{-1}$
Magnetic moment per nanoparticle	$(9.2 \pm 0.4) \times 10^{-16} \text{emu}$	$(16.0 \pm 1.0) \times 10^{-16} \text{emu}$
Mean diameter	$(17.2 \pm 0.3) \text{nm}$	$(20.4 \pm 0.4) \text{nm}$

Table 4.1: Experimental parameter as well as the fit results of the magnetization isotherms in figure 4.4 by the Langevin formalism allow for the calculation of the mean particle diameter from the initial measurement and a repeated experiment after 36 months under the assumption of the volume magnetization of bulk cobalt ferrite.

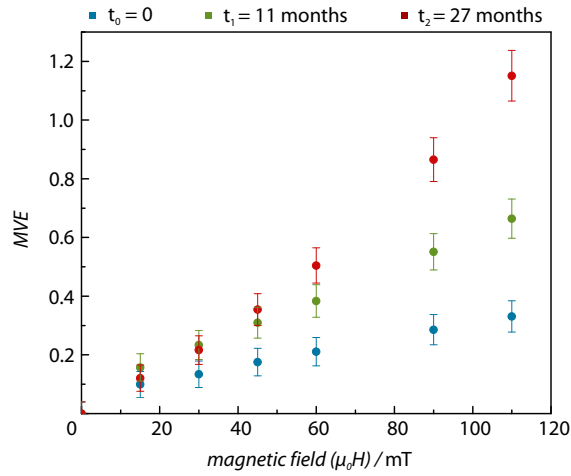


Figure 4.5: MVE data (shear frequency: 18 Hz) of the reference ferrofluid as a function of the applied magnetic field at three different dates. The increase of the magnetoviscous response over time is attributed to an increased volume fraction of larger nanoparticles over time due to volume growth by nanoparticle agglomeration or Oswald ripening.

of nanoparticles in the sample and the mean magnetic moment per nanoparticle. Figure 4.4 presents two magnetization isotherm measurements and their corresponding Langevin formalism fits at different times during the PhD. At a first glance, it is obvious that the fit of the repeated measurement after 36 months is worse than the fit to the initial data indicating a strong deviation from the Langevin formalism. Furthermore, the amount of nanoparticles per microliter shrank on the one hand, but on the other hand the magnetic moment per nanoparticles increased, keeping the absolute magnetic moment per microliter, and therefore the magnetic volume concentration, constant—fitting parameters are presented in the table 4.1. Assuming the bulk mass magnetization of cobalt ferrite and a spherical shape allows for the calculation of the mean particle diameters in the initial experiment and 36 months later to (17.2 ± 0.3) nm and (20.4 ± 0.4) nm, respectively. These data are in good agreement with the TEM image analysis and supports the idea of volume growth with time. The deviation of the fitting curve from the data is caused by the non-appropriate use of the Langevin formalism to describe the magnetic field-dependent magnetization behavior of the larger (blocked) nanoparticles correctly.

As already mentioned, the aging of the reference fluid with time is also obvious in the magnetoviscous properties displayed in figure 4.5. The determined MVE of the reference ferrofluid (at a magnetic field of 110 mT) is increased about 4 times within 27 months. This observation is another indication for nanoparticle growth since the experimentally observed MVE depends on the volume fraction of large particles in the magnetic fluid. [Thu03] The ferrofluid LCE-25 was stored in the fridge to minimize aging effects between the comparative measurements. If the diluted reference fluid (volume concentration of (0.66 ± 0.03) % (solid/liquid) suspended in

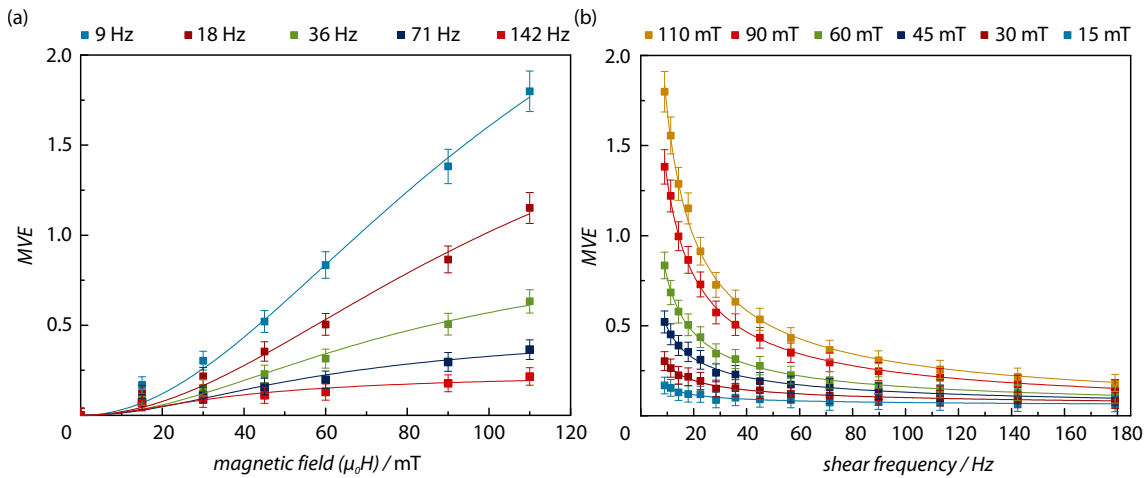


Figure 4.6: The determined MVE for the reference ferrofluid as a function of the applied magnetic field (a) as well as of the shear frequency (b). (a) The MVE shows a non-linear behavior which can be qualitatively well fitted by equation 2.49 for each shear frequency. The increase in the viscosity is caused by cluster and chain formation which hinders the flow. (b) The decay of the MVE as a function of the shear frequency is attributed to the so-called shear thinning in which higher shear forces destroy the clusters and chains. The lines drawn in (b) are fits corresponding to a power-law function (according to equation 2.26).

a 7:3 DEG-water mixture) is stored at ambient conditions for some months, aging is exceedingly intensified leading to a non-physical high MVE > 10 . [Fau12]⁴ Therefore, diluted reference fluids were prepared freshly from the concentrated LCE-25 every time and measured in between one week.

4.2.2 Magnetoviscous Characterization of the Reference Ferrofluid

The magnetoviscous properties of the reference ferrofluid presented on the next pages are based on data sets taken in January 2013. Figure 4.6 (a) displays the MVE as a function of the applied magnetic field at different shear frequencies. For ‘ideal’, highly diluted (non-interacting) ferrofluids the viscosity increase as a function of the applied magnetic field can be calculated by equation 2.39 and would result in an increase below one percent as shown in figure 2.7. However, measurements reveal magnetoviscous effects two orders of magnitude larger than predicted by the simple model of rotational viscosity. A fit of the data using equation 2.49 (parameters determined from the fit are the correction factor C_n as well as the magnetic moment per nanoparticle m) reflects the trend and the shape of the MVE qualita-

⁴Similar experiments and observations are discussed in the Bachelor thesis of Rene Faust (Physics Department, University of Hamburg, 2012)

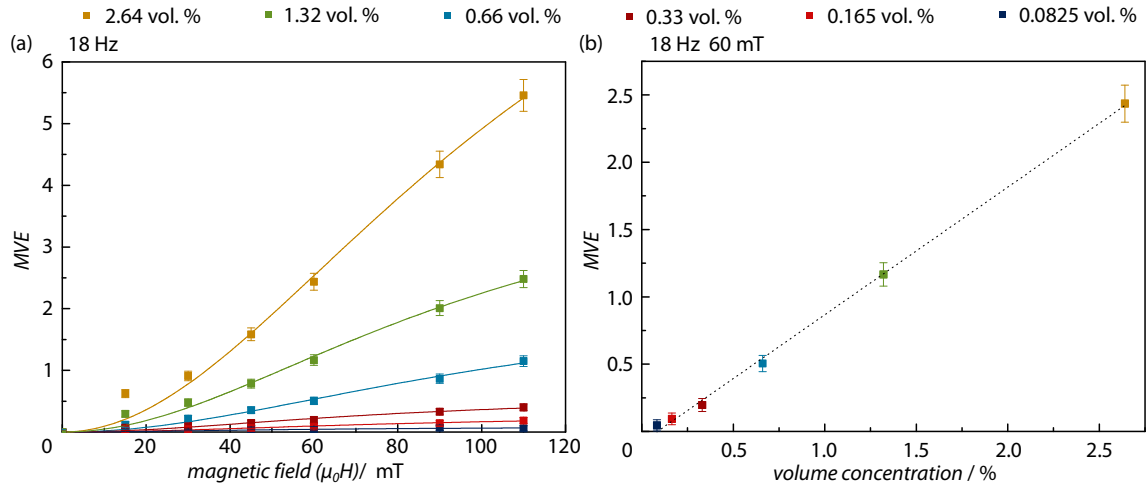


Figure 4.7: (a) MVE at 18 Hz shear frequency vs. magnetic field measurements for differently concentrated ferrofluid liquid suspensions based on the LCE-25. The error bars of the MVE are smaller than the height of the squares. The lines in (a) are fits of the rotational viscosity model for elongated particles (equation 2.49). (b) Plot of the MVE in dependence of the volume concentration c of the liquid suspension at a depicted magnetic field of 60 mT and a shear frequency of 18 Hz. The drawn line represents a linear fit $MVE = (-0.08 \pm 0.02) + (0.95 \pm 0.02) (\%)^{-1}c$. The deviation from the origin to a positive intercept with the x-axis can be explained by the uncertainty of the nanoparticles' volume concentration as well as the sensitivity and the reproducibility of the PMAV measurements especially at low volume concentrations.

tively well.[Ode02a] On the one hand, the magnetic moment amounts for all fits to a physically reasonable value—allowing for an estimation of the particle diameter to about 14 nm by assuming the bulk magnetization of cobalt ferrite. The determined mean diameter is close to the previously calculated values based on the TEM image analysis and the isothermal magnetization measurements. But on the other hand, the correction factor amounts to unexpected values at least two orders of magnitude larger than expected— C_n would amount to 1.5 for non-interacting, ideal spheres (compare equation 2.39 with 2.49). However, one can state that the concept of flow hindrance seems to be valid even if the observed magnitude of the MVE cannot be explained by hindrance of the flow through rotation of individual, spherical particles. Instead, (cluster or) chain formation has to be taken into account. Assuming the chains/clusters as rigid objects would result in a correction factor similar to the shape function C_n for cylindrical particles (equation 2.49). Consequently, the MVE is scaled by this correction factor. Furthermore, the assumption of cluster or chain formation also explains another feature of the measurements: the non-linear MVE decrease with increasing shear frequencies as impressively shown in figure 4.6 (b). The MVE at a fixed applied magnetic field, e.g. 110 mT, decreases rapidly by almost a factor of three from 1.75 at 10 Hz to 0.6 at around 110 Hz until it finally seems

to reach a constant value in the applicable frequency range. The phenomenon of decreasing MVE with increasing shear frequency is called shear thinning (effect) and is attributed to the breaking of chains/clusters at higher shear frequencies. A detailed discussion and interpretation of the MVE increase, the fit parameters and the shear thinning effect is given in section 4.4.

Magnetic field-dependent viscosity measurements of differently concentrated ferrofluids allow for determining the MVE as a function of concentration of that liquid suspensions. The corresponding MVE values are presented in figure 4.7 (a). The magnitude of the viscosity response at any magnetic field is a linear function of the volume concentration of nanoparticles in the liquid suspension as exemplarily shown in the figure 4.7 (b) for a shear frequency of 18 Hz and an applied magnetic field of 60 mT. Since the measurements of the commercial ferrofluid are only the prerequisite for the following data interpretation of the MVE of elongated particles, a more detailed investigation of spherical nanoparticle suspensions was out of the scope of this thesis.

To summarize this section: an aging effect in a commercial ferrofluid consisting of spherical cobalt ferrite nanoparticles was observed. The mean diameter of the particles increased with time, probably caused by agglomeration of individual particles. The volume growth of the spherical particles resulted in a four times enhanced magnetoviscous effect after 27 months. However, the fluid-mechanical properties of a reference ferrofluid were determined in dependence of the applied magnetic field, the shear frequency and the concentration. The results allow for comparison with measurements of elongated nanoparticle liquid suspensions, namely nanotubes or nanorods. In section 4.4 it is referred again to the measurements shown herein.

4.3 Elongated Nanoparticle Liquid Suspensions

Well-dispersed ferrofluidic suspension can be achieved by suspending iron oxide nanotubes as well as nickel nanorods in a carrier liquid. The permanent magnetic nanotubes and nanorods interact with externally applied magnetic fields as shown in a photograph in figure 4.8. A magnetic field gradient is applied by a solid permanent magnet at one side of the sample container and allows for the collection of the tubes at the container's wall. Simple shaking of the container reverts the suspension in its initial well-dispersed state.

4.3.1 Stability: A Problem?

Application of ferrofluidic suspensions and especially magnetorheological fluids suffer from an instability on the long-term. Agglomeration and sedimentation change the magnetoviscous properties with time and do not allow for a long-term reproducibility of viscoelastic properties upon an applied magnetic field. Surface function-

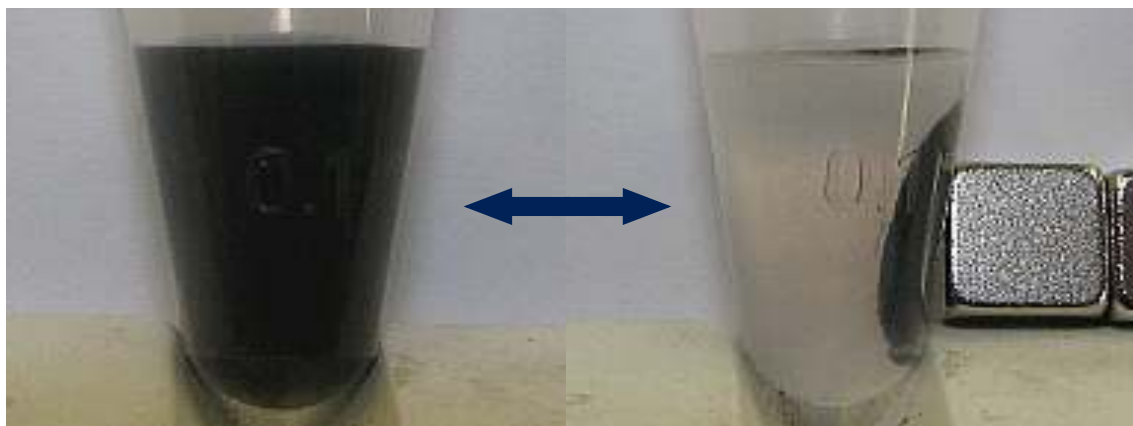


Figure 4.8: Photographs of a liquid suspension of iron oxide nanotubes. The left image shows a well-dispersed liquid suspension. The magnetite nanotubes can be collected by applying a magnetic field gradient with a permanent magnet (right). Simple shaking up reverts the suspension in its well-dispersed initial state.

alization of nanoparticles is a challenging (hot-topic) area, and requires fundamental knowledge of (surface) chemistry and special laboratory infrastructure. However, on the few hours time-scale in the experiments applied herein, the measurements were reproducible as shown in figure 4.9 (a) and (b) for iron oxide nanotubes.

Figure 4.9 (a) displays the magnetic field-dependent MVE of a nanotube suspension measured five times in 2.5 h. The first measurement (drawn in blue) reveals a significant lower MVE than all the following measurements which are equal in the range of the error—reproducibility of the viscosity measurements in the PMAV setup. The observed shift can be attributed to two reasons: first, the temperature after mounting the sample has not reached the constant value of 20 °C. The average laboratory temperature was higher than 20 °C. Thus, the zero-field viscosity is lowered leading to a higher observed MVE. Second, sedimentation (of larger agglomerates) might happen mainly in the first minutes until a steady-state is reached, which is almost stable for few hours. Moreover, no influence on the MVE can be observed with the number switching events between applied and zero magnetic field studied on a different (more diluted) nanotube liquid suspension (figure 4.9 (a) and (b)). After each on-state the MVE vanishes back to zero in the off-state, thus magnetic field-induced formation of non-redispersible agglomerates can be neglected. Comparison of the interplay between absolute viscosity and MVE over time and switching is displayed in the appendix in figure A.11. A slight shift in the absolute viscosity, which might be attributed to sedimentation, does not result in a significant change of the determined MVE.

To conclude, viscosity measurements of liquid suspensions consisting of elongated nanoparticles are reproducible (after a short settling time) and can be used to achieve insights into the promising MVE behavior of such novel ferrofluids, even if the long-

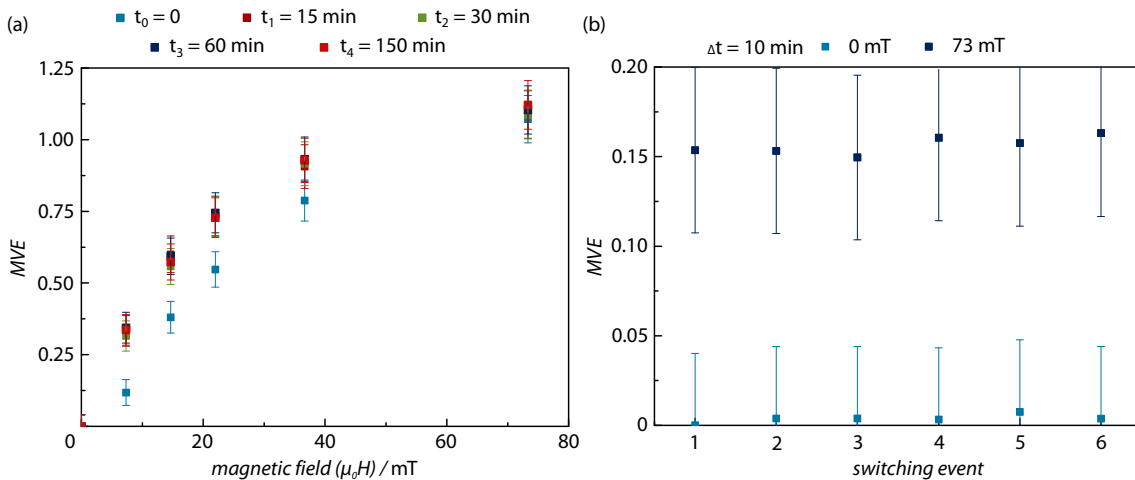


Figure 4.9: The determined MVE of nanotube liquid suspensions reveals a sufficient stability over time and switching event. (a) After a settling time of 15 min, a stable response of the MVE as a function of the applied magnetic field is observed for a liquid suspension of nanotubes (with a length of (740 ± 20) nm, a diameter of (65 ± 10) nm, and a magnetite wall thickness of (8 ± 2) nm). (b) Highly-diluted nanotube (length (210 ± 10) nm, diameter (65 ± 10) nm, wall thickness (8 ± 2) nm) liquid suspension reveals no change in the MVE in the ‘on’ state (applied magnetic field 73 mT) and zero-field-state over several switching cycles.

time stability over several days is not given because of the sedimentation of the elongated nanoparticles. A prospective surface functionalization route is under investigation in collaboration with the Weller group⁵ (Chemistry Department, University of Hamburg). A triblock copolymer is bind to the silica shell and should lead to improvements with regard to long-term stability of the liquid suspensions.

4.3.2 Quantifying the Loss of Elongated Particles during Synthesis

In general, template-based synthesis approaches for ferrofluids struggle for a sufficient yield of nanoparticles per batch. Two scale-up routes were described to overcome the limitations. However, several filtration, washing and re-dispersing steps are necessary until the final magnetic fluid can be achieved. Each of the processes causes a certain loss of nanoparticles missing at the end in the liquid suspension.

To estimate the loss, the amount of elongated particles can be calculated at a theoretically possible 100 % yield from the template’s pore density of 1×10^{10} pores cm^{-2} and the template area.[Nie02] For iron oxide nanotubes this estimate would result in

⁵PhD students Hauke Kloust and Christian Schmidtke, Chemistry Department, University of Hamburg (2013)

a total number of 6.4×10^{11} nanoobjects; for nickel nanorods with a nanoporous deposition area of 80 mm^2 and 60 stacks to a theoretical maximum number of 4.8×10^{11} particles.

VSM measurements of four representative nanotube ferrofluids (nominal iron oxide wall thickness 8 nm) are displayed in the appendix (figure A.12). The saturation magnetic moment enables the calculation of the magnetic volume concentration in the liquid suspension taking the saturation magnetization to be $(450 \pm 25) \text{ emu cm}^{-3}$ as determined in section 3.2 (figure 3.15). Based on these results, the amount of nanotubes per μL liquid suspension can be further estimated by considering the geometric tube parameters, e.g. length, diameter, wall thicknesses of SiO_2 and Fe_3O_4 . For a complete ‘standard’ characterization (TEM, SQUID/VSM, PMAV) of a liquid suspension, the released nanotubes were finally suspended in $150 \mu\text{L}$ carrier liquid. Thus, the total number of synthesized nanotubes per ‘standard’ batch can be estimated to be around $(1.5 \pm 0.5) \times 10^{11}$ nanotubes resulting in a loss of 70 % to 85 %.

A similar calculation can be performed for the nickel nanorod suspension. The volume concentration is estimated to $(0.010 \pm 0.002) \text{ vol } \%$ using the saturated magnetic moment of the SQUID measurements and a reduced saturation magnetization for the electrodeposited nickel as reported by Sun and co-authors.[Sun04] The total amount of nanorods, which were finally dispersed in $200 \mu\text{L}$, amounts to $(4.0 \pm 1.2) \times 10^{10}$ by assuming a length of $(400 \pm 40) \text{ nm}$ and a diameter of $(40 \pm 5) \text{ nm}$. Thus, the total loss is larger than 90 % for this synthesis route.

In general, these high losses are caused by the number of steps during release of the nanoobjects from the template and final preparation of the liquid suspension:

- selective etching of the alumina template in chromic acid ($> 50 \text{ mL}$ in a glass beaker) or in 1 M potassium hydroxide ($\approx 2 \text{ mL}$ in an *Eppendorf* tube) for the nanotubes or the multisegmented nanowires (as precursor for the nickel nanorods), respectively.
- vacuum-enhanced filtration utilizing ion track-etched polycarbonate membranes (*Whatman*TM) for the separation of nanotubes/nanowires from the template’s etchant. This procedure includes rinsing with DI-water for several times.
- the release of the elongated objects from the (polycarbonate) filter into the *Eppendorf* centrifuge tube by ultrasonication. Whereas the iron oxide nanotubes are released into the diethylene glycol-water mixture, the multilayered wires are dispersed into the selective copper etchant. In the latter case, another filtration step is necessary to achieve the individual nanorods and to disperse them into the carrier medium.
- centrifugation to reduce the total volume of the liquid suspension and to achieve the maximum concentrated magnetic fluid.

The additional selective Cu etching step and the second filtration step followed by another release procedure of the nanorods from the filtration membranes are identified as reason for the increased loss in the second (three-dimensional) synthesis route compared to the two-dimensional scale-up approach. One may wonder about these high losses, but private communications by other researchers dealing with large-scale synthesis routes of nanoparticles, and especially with template-based approaches, reveal similar experiences.⁶ Further improvements and developments in the release procedures are inevitable to compete with sol-based synthesis routes in (far) future. Magnetic field enhanced filtration or sedimentation as well as improved filter membranes—which allow for an easier and (more) complete release of the nanoobjects—might be the first steps to higher yields.

4.3.3 Magnetic Field-Dependent MVE Studies of Elongated Nanoparticle Ferrofluids

Besides the developing and establishing of the two novel, scaled-up synthesis approaches, the characterization of the elongated particle suspensions was a goal of the thesis. In detail, differences in the magnetic field-dependent viscoelastic properties compared to a commercial ferrofluid—consisting of spherical nanoparticles—have been worked out and conceivable explanations are given. For this purpose, magnetic field-dependent viscosity measurements were carried out on liquid suspensions of iron oxide nanotubes and nickel nanorods.

The data presented in this section were taken on an elongated particle ferrofluid based on the magnetite nanotubes (characterized in section 3.4) and on the nickel nanorods synthesized by the three-dimensional scale-up approach (section 3.5). The length and the iron oxide wall thickness of the nanotubes was (190 ± 10) nm and (8 ± 2) nm, respectively. Thus, the magnetic volume concentration of that liquid suspension has been estimated to be (0.024 ± 0.003) vol % (measurement (d) in figure A.12 in the appendix). The nickel nanorods were the same as introduced in section 3.5 (length 400 nm, diameter 40 nm, concentration (0.010 ± 0.002) vol %).

The MVE was determined as a function of the applied magnetic field at different constant shear frequencies for both suspensions as displayed in figure 4.10. At a first glance—neglecting the different geometries and volume concentrations—liquid suspensions of magnetite nanotubes or nickel nanorods show a saturating behavior of the MVE, whereas the reference ferrofluid displays a monotonic increasing MVE (figure 4.6 (a)) in the applicable magnetic field range. Similar saturating trends were already observed by Lang and Günther for iron nanorod and nickel nanorod suspensions, respectively (figure 2.9).[Lan05] [Gün11] An explanation can

⁶Hauke Kloust, Research Group Weller, Chemistry Department, University of Hamburg (Germany); Research group of Birringer, Saarland University (Germany); Kirsten Pondman, University of Twente (Netherlands)

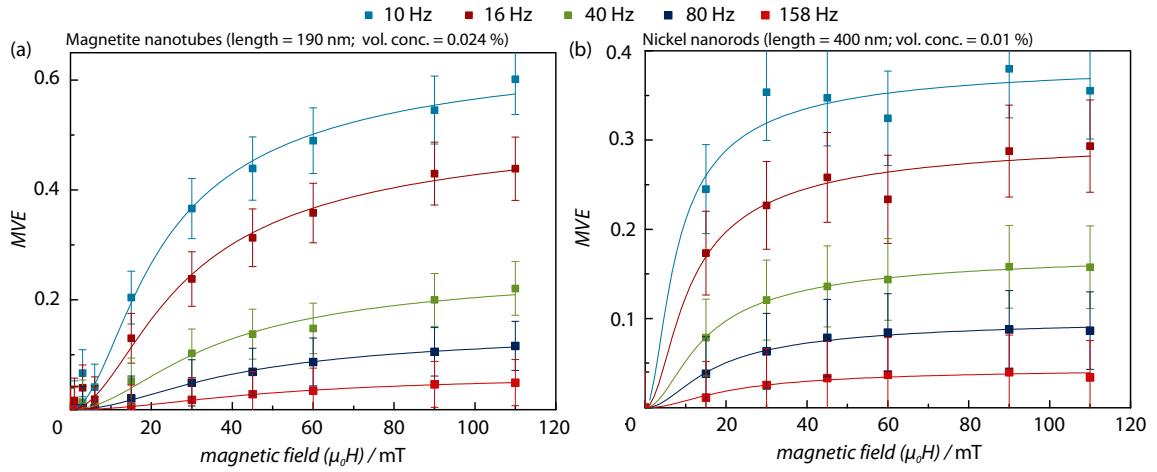


Figure 4.10: Magnetic field-dependent MVE of iron oxide nanotubes (a) and nickel nanorods (b) at five depicted shear frequencies. The saturating behavior of the elongated particle liquid suspensions differs significantly from the steadily increasing MVE of the reference ferrofluid (figure 4.6 (a)). Shear thinning can be clearly identified by the reduced MVE at higher shear frequencies. The drawn lines present fits of equation 2.49 to the data.

be given by taking the intrinsic reason for the viscosity increase into account. Spherical nanoparticles in liquid suspension tend to form chains in an applied magnetic field, whose length increases with increasing magnetic field.[Zub00] [Men04] If the maximum chain length is reached, the MVE of spherical nanoparticle suspension saturates, too. The maximum chain length is determined by the absolute number of nanoparticles in the suspension and the interplay between shear force, magnetic field strength and (dipolar) interaction strength between the particles.[Men04] [Zub06] The (MVE-) saturation magnetic field could not be reached for the reference ferrofluids in the PMAV setup used herein. However, a trend to saturation can be identified in figure 4.7 (a) for lower volume concentrations. The hindrance of the flow becomes stronger as a consequence of longer chains; the MVE increases therefore. In contrast, elongated particles—with an easy axis parallel to the long axis—will align parallel to the magnetic field direction. If all nanotubes/nanorods are aligned, no additional flow hindrance is formed anymore, and the MVE should saturate. The differences in the magnetic field-dependent MVE response between the nanotube and the nanorod suspension can be attributed to the increased magnetic moment per particle as well as to the reduced volume concentration for the latter one.

The magnetic field-dependent MVE is a function of the shear frequency applied during measurement: the higher the shear frequency is, the lower the MVE increase as well as the saturated MVE at higher fields are. The decrease of the MVE as a function of shear frequency follows a similar, monotonic decreasing trend as the MVE of the reference ferrofluid (figure 4.6 (b)) and is displayed in the appendix in

figure A.14. In contrast to these results (and the shear frequency-dependent measurement by Günther [Gün08]), Lang reported in his PhD thesis—later published by Birringer and co-authors—a maximum of the shear frequency-dependent MVE at various magnetic fields (compare 10 Hz, 32 Hz, and 178 Hz in figure 2.9 (a)). [Lan05] “This shift supports the idea that, apart from mere orientational relaxation behavior of the nanorods, resonance behavior becomes superimposed with the applied homogeneous magnetic field acting as the restoring torque.” [Bir08] None of the measurements during the PhD work showed such a non-monotonic (resonance) behavior. The reason might be attributed to the different sample geometry—connected chain of spheres by Lang (TEM images as displayed in figure 2.9 (a))—and to the different diameter, which is at least a factor of four smaller. The three-dimensional scale-up approach in combination with ALD of Al_2O_3 allows for the template-based synthesis of Ni nanorods with a similar geometry leading to prospective experiments. The observed shear thinning (effect) of the elongated particle suspensions prepared in this thesis is discussed in section 4.4 in detail.

Several preliminary statements can be drawn from the comparison of the MVE of elongated particle suspensions with the MVE of ferrofluids based on spherical particles (figure 4.11).

1. Liquid suspensions of elongated magnetic nanoparticles show a different magnetic field-dependent MVE than ferrofluids consisting of spherical nanoparticles. In the applicable magnetic field range, elongated particle suspensions show a saturating MVE behavior, whereas the spherical particle ferrofluids reveal a continuously increasing MVE.
2. At lower magnetic fields a stronger—more sensitive—response in the MVE is observed for the elongated particle suspensions. This fact can be attributed to an easier alignment of the elongated particles in a magnetic field compared to the formation of a chain consisting of spherical particles.
3. The maximum MVE at a magnetic field of 110 mT is similar for the elongated particle suspensions with a more than fifteen times diluted volume concentration compared to the spherical particle ferrofluids at various concentrations. Taking the reduced saturation magnetization of cobalt ferrite compared to magnetite or nickel into account (table 2.2), still results in a ten times diluted ‘magnetic concentration’ (ΦM_s)—a reduced saturation magnetization of the total liquid suspension with the unit emu mL^{-1} .
4. A decrease of the MVE with increasing shear frequency is observed. A detailed discussion of this phenomenon is given in section 4.4.
5. Measurements of a superparamagnetic nanotube suspension showed no response of the MVE within the error range to an applied magnetic field (dis-

played in the appendix in figure A.13). This suggests that only elongated particles with a fixed magnetic moment contribute to the magnetic field-dependent MVE similar to the assumptions made by Shliomis, Martsenyuk and Raïkher for the model of rotational magnetoviscosity for spherical nanoparticles. [Shl72] [Mar73] [Shl80]

The statements (1)–(3) need a more detailed comment: a stronger increase of the MVE at lower fields and an earlier saturation is predicted by the concept of rotational magnetoviscosity for non-interacting (single-domain) particles with a larger magnetic moment without any shape considerations— independent whether the larger magnetic moment is caused by the material or the size of the particle (compare figure 2.7). Thus, further viscosity measurements are inevitable to validate that the obtained results are caused by the elongated shape and not only by the increased magnetic moment per particle. However, the realization of such a control experiment would be challenging: synthesis of monodisperse spherical particle suspensions with different particle sizes/magnetic moments (above the superparamagnetic limit), equal concentration (< 0.1 vol% to avoid or at least to minimize interaction), and with a sufficient liquid suspension volume (> 90 μL) volume is by far not trivial.

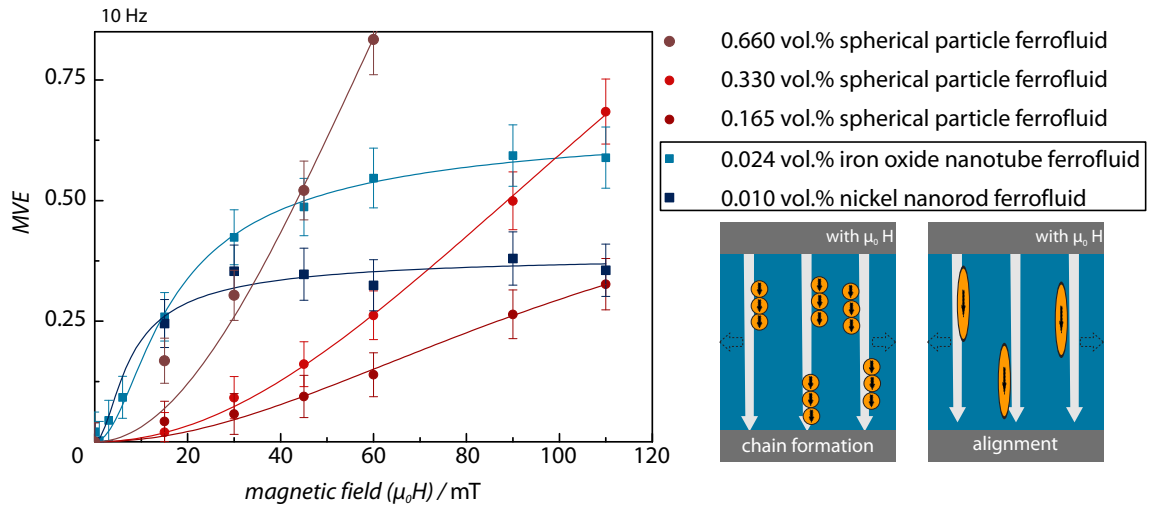


Figure 4.11: Magnetic field-dependent MVE for the two elongated nanoparticle suspensions and three ferrofluids consisting of spherical particles with different volume concentration drawn in blue and red, respectively. The figure supports the following enumeration of the conclusions drawn from a comparison between elongated and spherical particle liquid suspension. The different reasons for the MVE enhancement of both suspension are sketched on the right hand side. Chain formation of spherical particles causes the observed MVE increase in standard ferrofluids, whereas parallel alignment of the elongated particles to the external field can be treated as main reason for the MVE enhancement in elongated particle suspensions. The drawn lines present fits of the rotational viscosity model to the data.

4.3.4 Preliminary Results: MVE of Nanotube Liquid Suspensions Differing in Length and Concentration

At that point, one has to emphasize again that the theory of ferrofluids bases on the magnetic volume concentration Φ which depends on the absolute number of nanoparticles as well as the magnetic volume $V_m = mM_s^{-1}$ of the individual nanoparticle. Therefore, comparison of different liquid suspensions differing in the individual particle volume, the magnetic material, and/or the absolute number of particles by means of the volume concentration should be done only qualitatively as well as with reservation.

Magnetic iron oxide nanotube suspensions with different length and concentration were explored with respect to their magnetic field-dependent MVE behavior. The MVE as a function of the applied magnetic field is displayed in figure 4.12 for four different nanotube ferrofluids. The suspensions (1)–(3) contain the same absolute number of nanotubes ($(1.0 \pm 0.2) \times 10^9$) per μL and differ primarily in length (but also in diameter (1) & (2) with an outer diameter of 50 nm, (3) outer diameter of 85 nm). Suspension (4) contains only half of the amount of nanotubes. The nanotubes of suspension (1), (2) and (4) were prepared in an early state of the thesis without an applied pore-widening step leading to a nail-head end of the tube on one side as displayed in figure A.2 in the appendix. The synthesis route of suspension (3) already contained the pore-widening step resulting in that nanotubes which were characterized in section 3.4. It is obvious that longer nanotubes will hinder the flow more effectively resulting in an increased MVE as shown in figure 4.12 (1)–(3). Moreover, a liquid suspension with a reduced amount of nanotubes results in a reduced hindrance of the flow. Therefore, the determined MVE is reduced (compare suspension (3) with (4) at similar geometric parameters). Two (preliminary) statements can be made for elongated nanoparticles, which have to be validated by further experiments:

1. The longer the elongated particles, the larger the MVE (at the same absolute number of nanotubes).
2. A reduced number of nanoobjects results in a lower MVE (at similar length).

The volume concentration Φ , and thus also the reduced saturation magnetization (ΦM_s) of the liquid suspension, is increased with increasing length, whereas Φ is decreased with reducing the amount of nanotubes in the liquid suspension. To determine whether the observed differences are due to the change of the geometry or only due to the volume concentration remains open or further studies. Several questions can be tackled based on the established synthesis routes, which allow for independent fine tuning of the geometry and material: How is the interplay between volume concentration Φ , absolute amount of (elongated) particles and geometry/volume of the particles with respect to the MVE? What is the influence of the outer diameter? What is the influence of the ends of the nanotubes/nanorods?

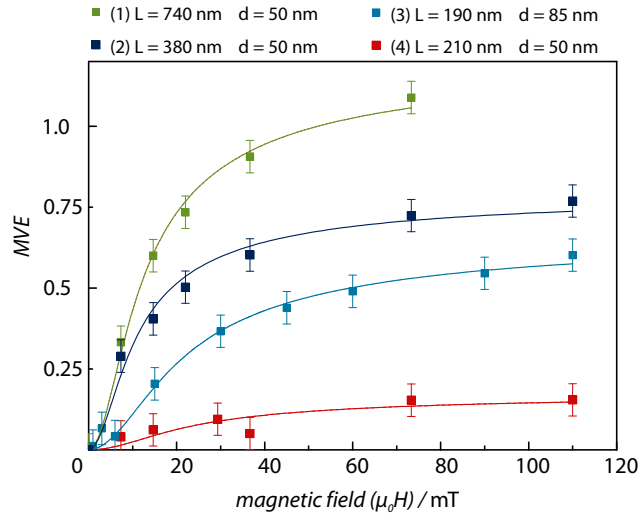


Figure 4.12: Magnetic field-dependent MVE of four different nanotubular ferrofluids determined at a constant shear frequency of 10 Hz. The MVE displays a strong increase at fields $\lesssim 45$ mT and seems to saturate at larger field values. For the suspensions (1)–(3) and (4) the quantity of nanotubes per μL amounts to $(1.0 \pm 0.2) \times 10^9$ and to $(0.5 \pm 0.1) \times 10^9$, respectively. The geometric parameter length and outer diameter are given on top of the graph. The nominal nanotube wall consists of an 8 nm thick magnetite layer sandwiched between two silica layers each with a thickness of 5 nm. The lines drawn correspond to fits by equation 2.49.

4.4 Shear Thinning in Ferrofluidic Suspensions

In general, a viscosity decrease upon increased shear frequencies is called shear thinning. Such behavior is well-known for ferrofluids based on spherical nanoparticles in an applied magnetic field. Magnetic field-induced microstructures, which hinder the flow, can break under high shear forces leading to a reduced hindrance which consequently results in an apparent viscosity decrease. The magnetic field-dependent MVE obtained at a constant shear frequency was fitted according to the rotational viscosity model. Subsequently, the fit parameters can be investigated with respect to their evolution as a function of the shear frequency. Additionally, the apparent viscosity decay as a function of the shear frequency can be phenomenologically modeled by the Herschel-Bulkley relation (equation 2.27). Based on these analyses, one can shed light onto the shear thinning effect.

The section is structured accordingly. First, fits according to the rotational viscosity model are presented and reviewed. Second, it is discussed whether the MVE as relative value or the absolute viscosity data should be used as basis for the analysis of the shear thinning effect. Based on that discussion, the shear thinning effect is phenomenologically analyzed for the elongated particle suspensions and the reference ferrofluid.

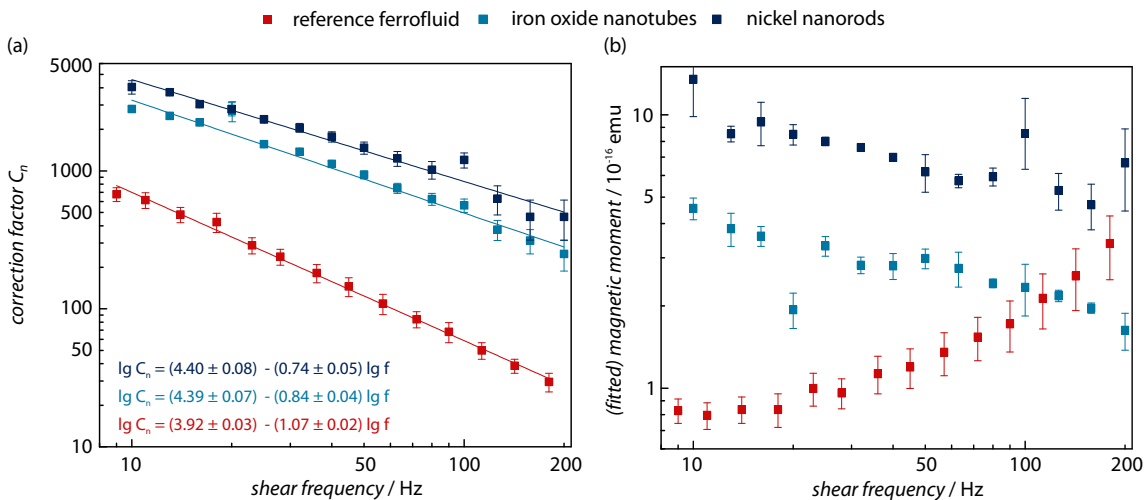


Figure 4.13: Double-logarithmic plot of the correction factor C_n and the magnetic moment m in (b) as a function of the shear frequency in subfigure (a) and (b), respectively, for the reference ferrofluid (red), an iron oxide nanotube suspension (bright blue) and a ferrofluid consisting of nickel nanorods (dark blue). Both values are determined from fits of equation 2.49 to the magnetic field-dependent MVE data of the corresponding liquid suspension. The lines in (a) are linear fits with respect to the double-logarithmic plot. The drawn error bars are errors of the fit.

4.4.1 A Detailed Look at the MVE Based on the Rotational Magnetoviscosity Concept

The model of rotational viscosity for elongated particles (equation 2.49) was fitted to the determined MVE—of the reference ferrofluid, the nickel nanorod suspension, and the magnetite nanotube ferrofluid—as a function of the applied field at different constant shear frequencies (figure 4.6 (a), 4.7 (a) and 4.10). Two fit parameters were adjusted: the correction factor C_n as well as the magnetic moment m of the individual nanoparticle, which contributes to the MVE. Both fit parameters are plotted as a function of the shear frequency in figure 4.13.

The linear decrease of C_n in the double-logarithmic plot indicates a power-law dependence of the fit parameter as a function of the shear frequency for all three liquid suspensions (figure 4.13 (a)). It is striking that the correction factor for all particle suspensions is one to two orders of magnitude larger than expected. Using the derived correction function of Brenner for cylinders (appendix A.3) results for the iron oxide nanotubes to an aspect ratio ranging from 175 to 50 for shear frequencies from 10 Hz to 200 Hz; the calculated aspect ratios for nickel nanorods are even higher. Applying a similar approximation for the chains of the reference ferrofluid and treating them as a rigid cylinder results in aspect ratios between 80 and 12. One can conclude that large clusters and chains are formed upon an applied

magnetic field. These clusters/objects change in size (and shape) with increasing shear frequency. Since the exact mathematical description of the correction function strongly depends on the knowledge of the shape, the estimated aspect ratios possess a large error. For this reason, the correction factor is further used in this thesis as a measure for the size of the object, which hinders the flow, but without converting it to an exact aspect ratio.

The slope of the shear frequency-dependent C_n is a measure for the strength of shear thinning effect—in other words for the size reduction of the objects, which hinder the flow. The decrease in the correction factor of ferrofluids based on spherical particles has its origin in the shear-dependent breaking of the chains, which becomes shorter with increasing shear frequency. However, breaking of the elongated nanoobjects is rather unlikely. Therefore, other explanations must be found. First, microstructure formation due to magnetic interaction have to be considered as a reason in the elongated particle suspensions, too, even if they are strongly diluted. Such microstructures, which would hinder the shear flow, will also break at high shear frequencies similar to the chain breaking in the reference ferrofluid. Thus, the cluster size decreases and the correction factor, which is related to the size of the microstructure, is reduced. As a consequence, the observed MVE is decreased. Second, higher shear frequencies can rotate an increased number of elongated objects with their long axis parallel to the shear direction—away from the perpendicular direction. The effective length which can hinder the flow becomes smaller and the determined correction factor would decrease consequently. Further viscosity measurements (if possible with other rheometers), and additional in-situ experiments, for instance neutron or photon scattering techniques, are necessary to determine the exact origin of the reduced correction factor for the elongated particle suspensions in dependence of the shear frequency.

The second fit parameter, the magnetic moment m of the particle, which contributes to the MVE, is plotted in figure 4.13 (b) as a function of the shear frequency. Noticeably, the trend is different for the reference ferrofluid compared to the elongated particle suspension. The mean magnetic moment in the standard ferrofluid increases with increasing shear frequencies, whereas it shrinks in both elongated particle suspensions. The reason for the increasing magnetic moment in the reference ferrofluid could be the formation of nonlinear microstructures. As mentioned in the introductory part, drop- or ring-like structures could be formed in ferrofluids under an applied magnetic field.[Zub06] [Yoo10] [Tan12] Such structures can show magnetic flux closure patterns.[Li01] A reduced ‘mean’ magnetic moment is measured as a consequence, since not all magnetic moments point parallel to the external applied magnetic field. The microstructures break at higher shear frequencies and the released uniaxial particles contribute to the overall magnetization—the ‘mean’ magnetic moment increases.

Evaluation of the determined magnetic moment for the two elongated particle suspensions reveals two surprising facts. First, the calculated ‘mean’ magnetic moment is up to three orders of magnitude smaller compared to the estimated value from the geometrical parameters. Second, the magnetic moment seems to decrease with increasing shear frequency. The latter observation was also discovered and discussed by Lang.[Lan05] He revealed a shear frequency-dependent shrinkage of the magnetic moment up to a factor of five in a comparable frequency range from 10 Hz to 178 Hz—herein a factor of 2 to 3 is discovered. A magnetic field-dependent magnetization is assumed in the concept of rotational magnetoviscosity which can be described by the Langevin formalism $M(B) = M_s L(\alpha)$ and which is independent of the shear frequency. Both assumptions are not fulfilled in the situation of elongated particles.

The Langevin formalism can be used to describe the phenomenon of paramagnetism in which non-interacting localized atomic magnetic moments are randomly oriented due to thermal energy. Applying an external magnetic field results in a certain alignment of the magnetic moments, and thus in an increase of the overall magnetization. This formalism can be expanded to ‘intrinsic’ and ‘extrinsic’ superparamagnetic behavior as long as the prerequisites ‘non-interacting’ and ‘localized magnetic moments’, which can follow an external magnetic field, are fulfilled. It was shown in the previous chapter in section 3.4 that the iron oxide nanotubes consist of different grains with different directions which, moreover, magnetically interact with each other. A similar structure is also conceivable for the nickel nanorods. Thus, it is not allowed to use the Langevin formalism, *per se*, since the magnetic moments of the individual grains do not easily align in an externally applied magnetic field. As a consequence, the magnetic moment per particle will be underestimated. Appropriate, physically meaningful fits of the Langevin function to VSM measurements of iron oxide nanotube suspensions or nickel nanorod ferrofluids were not possible (appendix, figure A.12) confirming that the formalism cannot be applied for the elongated particle suspensions.

Moreover, Lang discusses (in the appendix B of his thesis) a shear frequency-dependent magnetization of nanorod suspensions, which can be easily a factor ten smaller than the magnetization without shearing.[Lan05] Other researchers also studied the (shear frequency-dependent) off-equilibrium magnetization states and their influence on the fluid-mechanical properties of the ferrofluids under various flow conditions.[Mül01] [Ode02b] [Mül06] [Emb06] [Les06] [Alt12] The model of the rotational viscosity as derived by Shliomis bases on the interplay between mechanical torque, due to the shear flow, and magnetic torque induced by the external magnetic field. The change of the magnetization can be neglected for weak shear frequencies and spherical particles. However, the influence of shear forces onto the particle orientation distribution function cannot be ignored for (long) elongated particles.[Bre74] As a consequence, the magnetic moments—in the ideal case par-

allel fixed to the particle axes—are not perfectly aligned. Thus, the magnetization component perpendicular to the shear flow is drastically reduced since it depends on the shear rate, the exact flow conditions in the setup, and the external magnetic field.

One can conclude that the use of the Langevin formalism as well as the shear frequency-dependent interplay between mechanical torque and magnetic field-induced torque can result in a reduced magnetization, which finally ends up in a reduced magnetic moment per nanoparticle determined by the fits. The experimentalist has to determine the magnetic field-dependent magnetization of the liquid suspension under the same flow conditions, namely flow geometry and shear frequency, to adjust the model of rotational magnetoviscosity appropriately to elongated particle ferrofluids. A future extension of the PMAV setup to an induction magnetometer might be challenging but not impossible. Pick-up coils—exactly located around the sample position—might allow for the in-situ determination of the z-component of the magnetic moment.⁷

4.4.2 Shear Thinning: MVE or Absolute Viscosity?

One has to emphasize again that the MVE is a relative value which consists of a viscosity difference ($\eta(\mu_0 H) - \eta_0$) normalized to the zero-field viscosity. This approach is correct for ferrofluids with a zero-field viscosity which is independent of the shear frequency. The MVE as a function of the shear frequency is then only determined by the shear frequency-dependent viscosity at a certain applied magnetic field. If the latter as well as the zero-field viscosity are a function of the shear frequency, the interpretation of the relative MVE becomes more complex.

Figure 4.14 displays the absolute viscosity of an iron oxide nanotube suspension, the reference ferrofluid, and the carrier liquid⁸ at zero applied magnetic field. A decay of the absolute viscosity is clearly observable for the nanotube ferrofluid: the viscosity drops from above 13 mPa s to the carrier liquid value of around 10.5 mPa s in the explored shear frequency range. In contrast, only a slight decrease from around 11 mPa s to 10.5 mPa s can be observed for the reference ferrofluid as well as the pure carrier liquid. The observed shear thinning effect of the nanotube suspension is related to the elongated geometry of the particles. A simplified picture is sketched at the right-hand side of figure 4.14. At zero field, the spherical particles are homogeneously distributed. A few loosely-bounded (small) agglomerates might be present, which break easily at low shear frequencies. In general, the ferrofluid's viscosity equals the viscosity of the carrier liquid. A slight decrease with increasing shear frequency can be observed for the carrier liquid which must be related to the

⁷Sensitivity should be not an issue since the expected magnetic moment of the sample is supposed to be larger than 10 memu

⁸Diethylene glycol-water-mixture with a volume ratio of 7:3.

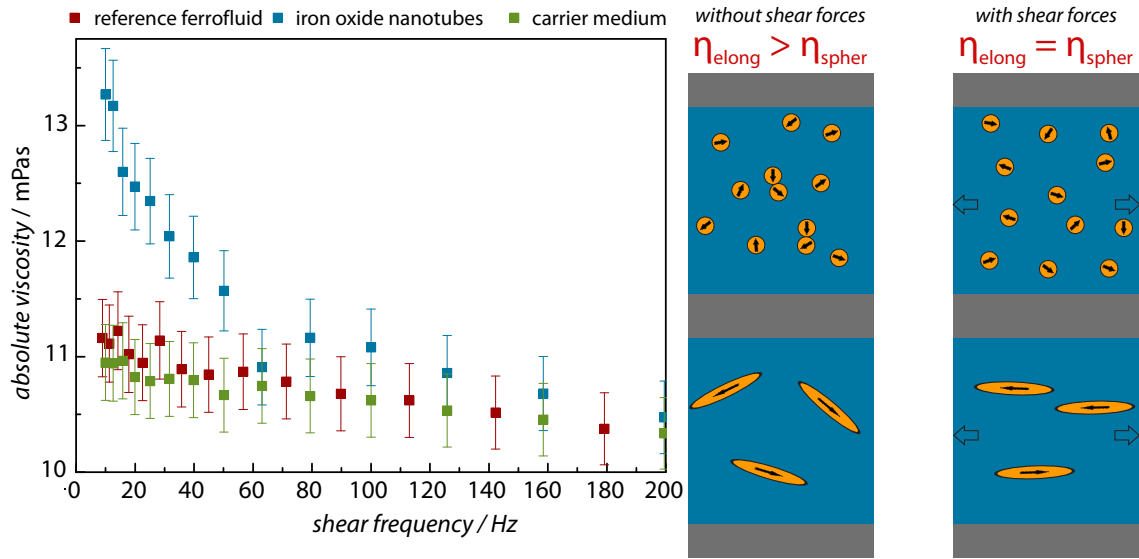


Figure 4.14: Plot of the absolute viscosity as a function of the shear frequency for the reference ferrofluid (red), the nanotube liquid suspension (blue) and the carrier medium (green). A significant decrease of the absolute viscosity can be observed for the nanotube suspension, whereas the reference fluid stays almost constant in the shear frequency range and reveals the same trend as the newtonian carrier liquid does. The slight viscosity decrease of the latter is attributed to the PMAV setup. Simplified sketches display the origin of the different, experimentally observed behaviors. The particles in the reference ferrofluid are homogeneously distributed, only few, small microstructures can be observed. With increasing shear frequency, the loosely bound microstructures might break, but the nanoparticles are still homogeneously distributed and only the viscosity of the carrier medium is measured. In contrast, the flow is hindered in the elongated particle suspension due to the distribution of the pointing directions of the elongated particles. When the shear force increases, more and more particles align parallel and the absolute viscosity decreases until the carrier medium viscosity is reached.

measurement system since a diethylene glycol-water-mixture is supposed to be a Newtonian liquid—the viscosity is independent of the shear frequency. However, a completely different picture can be drawn for a well-dispersed nanotube suspension. The pointing directions of the nanotubes extend homogeneously across the solid angle of the half space (2π). Thus, the most nanotubes have a projection of their long axis which is perpendicular to the flow and which would hinder a shear flow. Depending on the shear force, the nanotubes align parallel and the hindrance of the flow is reduced. As a result, the apparent viscosity decreases until all elongated objects are aligned parallel to the flow—the hindrance is minimized—and only the carrier medium viscosity is measured.

The apparent zero-field shear thinning has to be taken into account for an exact comparison of the liquid suspensions consisting of differently shaped nanoparticles.

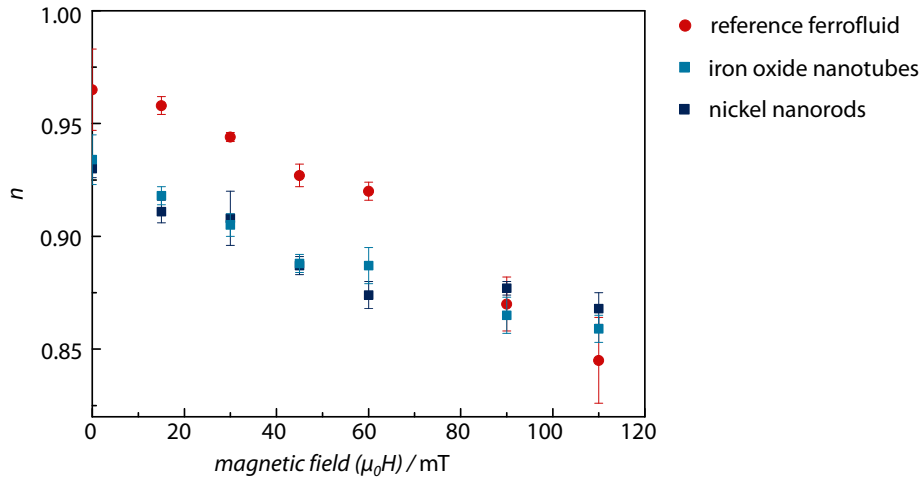


Figure 4.15: The fit parameter n of the Herschel-Bulkley model (equation 2.27) as a function of the applied magnetic for the reference ferrofluid (red), the nanotube liquid suspension (bright blue), and the nickel nanorod ferrofluid (dark blue). The error bars correspond to the errors of the fit.

The Herschel-Bulkley model is a phenomenological description of the absolute viscosity (equation 2.27) often used in engineering to describe the shear frequency-dependent viscous behavior of a fluid. The decrease of the shear thinning effect is mainly determined by the flow behavior index n which is plotted in figure 4.15 as a function of the applied magnetic field. When n equals one (at a negligibly small yield stress as observed here), the viscosity is independent of the shear frequency and the liquid is a Newtonian fluid.

The flow index n decreases with increasing magnetic field for all three liquid suspensions. It can be concluded that the ‘strength’ of the shear thinning effect is increased with increasing magnetic field. On the one hand, long chains of spherical nanoparticles are formed at large magnetic fields. However, long chains will break more easily at high shear frequencies than short chains since the number of possible breaking points is increased. Hence, the observed shear thinning effect is stronger for large magnetic fields. The situation in the case of elongated particles is much more complex. First, a significant shear thinning effect can be already observed without applied magnetic field, as explained above. The situation is slightly changed in an externally applied magnetic field. An additionally magnetic torque is induced which tries to align the particle perpendicular to the flow direction. The total hindrance of the flow is increased since more particles are aligned with the applied magnetic field. However, if more particles are aligned, more particles can slightly rotate at higher shear frequencies and the viscosity will decrease more strongly— n decreases. This theory is supported by the decrease of the correction factor C_n (subsection 4.4.1) which can be explained by a rotation of the elongated particles—

additional to cluster breaking. The projection of the long axis perpendicular to the flow decreases, as a consequence the hindrance, and thus the apparent viscosity, is reduced. It seems that the flow index of the reference ferrofluid decreases faster than n of the liquid suspensions consisting of elongated particles. This observation indicates that it is easier to brake long chains than to rotate elongated particles in high magnetic fields. However, further magnetic field-, shear frequency-, and concentration-dependent viscosity measurements have to be performed to validate a trend.

4.5 Shear Moduli of Ferrofluids

The complex shear modulus of a liquid consists of the real part G' which is related to the elastic properties—stored energy during deformation—of the liquid and the imaginary part G'' which represents the viscous behavior, thus being a measure for the dissipation of energy during deformation.[Mez06] The magnetorheological investigation of the reference ferrofluid (circles) as well as of the nickel nanorod suspension (squares) is displayed in figures 4.16 and 4.16 and reveals fluid-like behavior $G'' > G'$ in the complete experimentally accessible parameter space of shear frequency and magnetic field.

Shear frequency-dependent measurements of G' and G'' at constant magnetic fields of 15 mT and 110 mT are shown in figure 4.16 (a) and (b), respectively. Both shear moduli of the nickel nanorod suspension are higher at 15 mT and low frequencies < 40 Hz than the corresponding ones of the reference ferrofluid. That matches well with the MVE data shown in figure 4.11 in which the magnetic field-dependent MVE response at 15 mT is larger for the elongated particle suspension than for the differently concentrated, conventional ferrofluids. At the upper end of the shear frequency range, the loss moduli of the reference ferrofluid as well as the nickel nanorod suspension match well with the loss modulus of the pure carrier liquid (green stars, measured without field). The storage moduli of both liquid suspensions rise with increasing shear frequency, whereas the storage modulus of the pure carrier liquid (not displayed in figure 4.16) remains constant and at least two orders of magnitude below the liquid suspensions. It seems that the reference ferrofluid reveals a stronger increase (despite the shifted point at 50 Hz). This observation can be explained with the microstructure formation. The concentration of magnetic particles is much higher (0.66 vol %) compared to the nickel nanorod suspensions (0.01 vol %), thus cluster formation is more likely. A large amount of small clusters would not result in a large hindrance of the flow, but would be capable to store more energy than isolated particles. Raising the applied magnetic field to 110 mT results in a different picture of the situation at frequencies below 40 Hz. Both moduli of the reference ferrofluid are higher than the corresponding ones of the nickel nanorod suspension. This fact mirrors the MVE at large magnetic fields in which the refer-

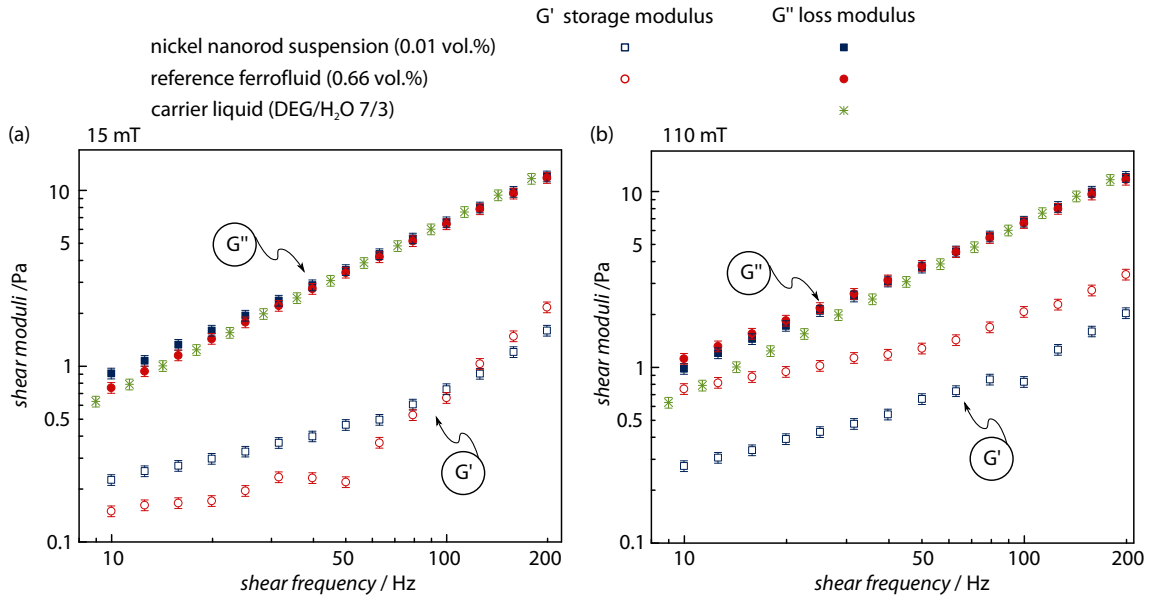


Figure 4.16: Double-logarithmic plot of the storage shear modulus G' (open symbols) and the loss modulus G'' (filled symbols) of the pure nickel nanorod suspension (blue squares) and the reference ferrofluid (red circles) as a function of the shear frequency at constant magnetic field ((a) 15 mT; (b) 110 mT). A measurement of the loss modulus of the carrier liquid is plotted in green stars. The storage modulus of the carrier liquid is not displayed since it amounts almost to zero. G'' is always larger than G' in the accessible parameter space indicating liquid-like behavior.

ence fluid overcomes the pure nickel nanorod suspension (figure 4.11). Moreover, the increased storage modulus of the reference ferrofluid indicates a significant amount of stored energy in magnetic field-induced networks/clusters of spherical particles compared to the nanorod suspension. The shear moduli also give insight into the shear thinning effect: first, an equalization of the loss moduli is apparent for the two different liquid suspensions matching with the values of the carrier liquid at high shear frequencies. Second, the increase of the storage modulus of the nickel nanorod suspension seems to be larger than the slope of the reference ferrofluid. The long chains/clusters, which are formed in the reference ferrofluid at large magnetic fields, break more easily at higher shear frequencies. Thus, less energy can be stored than without cluster breaking. The nickel nanorod suspension and the clusters formed therein seem to be less effected by the shear thinning than the reference ferrofluid, as already indicated by the reduced shear thinning effect observed in the correction factor (subsection 4.4.1) and in the flow behavior index (subsection 4.4.2).

Magnetic field-dependent measurements at a constant shear frequency are displayed in figure 4.17. The storage modulus G' is constant for all magnetic fields larger than 15 mT for the nickel nanorod suspension at a shear frequency of 20 Hz (a). The observations indicate that—besides the initial change—no further magnetic field-

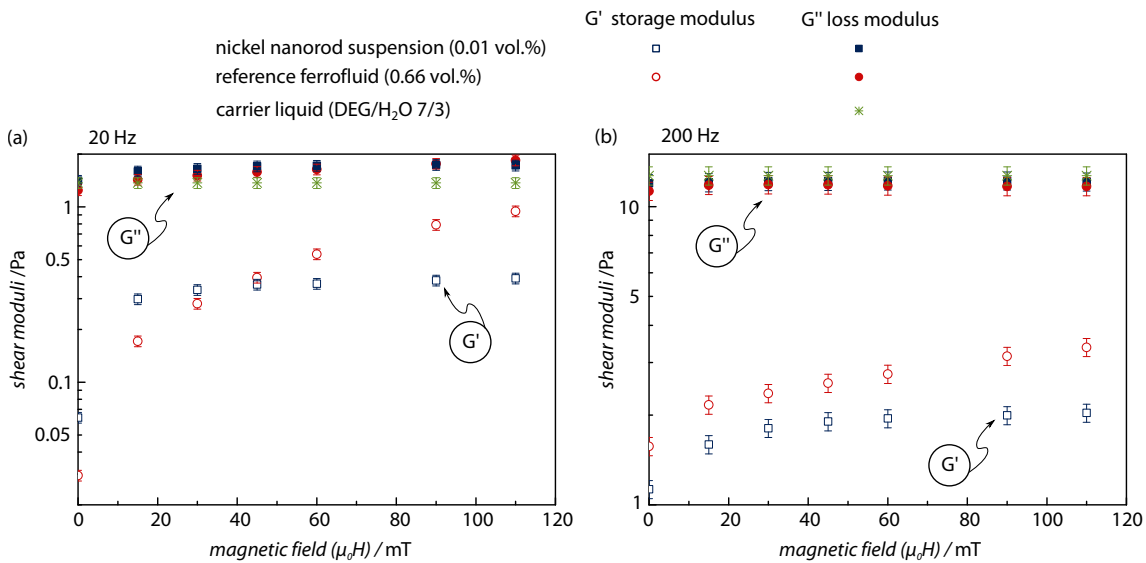


Figure 4.17: Log-lin plot of the storage shear modulus G' (open symbols) and the loss one G'' (filled symbols) of the pure nickel nanorod suspension (blue squares) and the reference ferrofluid (red circles) as a function of the applied magnetic field at a constant shear frequency ((a) 20 Hz; (b) 200 Hz). A measurement of the loss modulus of the carrier liquid is plotted in green stars. The storage modulus of the carrier liquid is not displayed since it amounts almost to zero. G'' is always larger than G' indicating liquid-like behavior.

dependent network formation occurs that would allow for the storage of energy. Increasing the shear frequency to 200 Hz (b) leads to a saturation field of > 30 mT. It is reasonable that larger shear forces would need a higher magnetic field to reach the same amount of cluster formation as without or with less shearing (compare to figure 4.10). In contrast, the G' -modulus of the reference ferrofluid increases with the magnetic field for both experiments ((a) and (b)), suggesting a magnetic field-dependent cluster/network formation which would allow for the storage of a greater amount of energy during deformation. The loss moduli (filled symbols), the representatives for the viscous behavior, follow the same trend as the MVE does: G'' increases for the nanorod suspension at 20 Hz—until all nanorods are aligned—with the applied magnetic field and saturation follows (> 15 mT). In contrast, G'' of the reference ferrofluid increases in the applied magnetic field range implying a magnetic field-dependent cluster formation which hinder the flow in the suspension. Increasing the shear frequency to 200 Hz gives for both liquid suspension the same result in the range of the error. Moreover, the measured values match well with the pure carrier liquid. One can conclude that the observed remaining MVE—based on the absolute values of the viscosity—at high shear frequencies is only due to the elastic part of the viscosity.

To summarize, the reference ferrofluid as well as the nickel nanorod suspension reveal liquid-like behavior ($G'' > G'$) in the accessible magnetic field and shear

frequency range of the measurement setup. The determined MVE behavior as well as the shear thinning effect could be confirmed in the shear moduli dependence upon magnetic field and shear frequency. Moreover, additional information is obtained: first, the analysis of the shear moduli support the derived model of cluster and chain formation. Second, the observed (but reduced) MVE at higher shear frequencies is mainly correlated to the storage modulus, and thus to the remaining interacting clusters, since the loss modulus almost equals the pure carrier suspension.

4.6 Magnetorheological Properties of Ferrofluids: A Wrap-Up

Several experiments were performed and data evaluation with various models was proceeded to shed light onto the magnetic field- and shear frequency-dependent properties of liquid suspensions. This sections is thought to give a summary and comprehensive overview of the results.

Reference Ferrofluid

- Commercial ferrofluids suffer from aging
⇒ MVE increases with time.
- An increase of the nanoparticle concentration in the liquid suspension
⇒ results in an increased MVE.
- Rotational magnetoviscosity model is not capable to describe the observed MVE of the spherical particle ferrofluid
⇒ introducing the correction factor C_n .
- Spherical nanoparticles form long chains in applied magnetic fields
⇒ chain length increases with increased magnetic field.
- Higher shear frequencies reduce the observed MVE since the chain break
⇒ C_n decreases,
⇒ the flow index n decreases with increasing magnetic field.
- Flux closure structures are formed
⇒ the magnetic moment increases with increasing shear frequency since the flux closure structures break.
- Reference ferrofluids reveal liquid-like behavior
⇒ $G'' > G'$ (in the experimental accessible parameter space).

Elongated Particle Suspension

- Elongated particle ferrofluids can be prepared by template-based approaches
⇒ magnetic field-dependent MVE observable.
- Saturating behavior in MVE observed
⇒ parallel alignment of the particles to the external magnetic field.
- Length and concentration influence the MVE
⇒ longer objects/larger concentration results in increased MVE.
- Shear thinning observable
⇒ C_n decreases,
⇒ magnetic moment decreases,
⇒ the flow index n decreases with increasing magnetic field,
⇒ caused by breaking of cluster and rotation of the elongated particles.
- Shear thinning effect in zero applied magnetic field
⇒ caused by particle orientation distribution.
- Elongated particle suspensions reveal liquid-like behavior
⇒ $G'' > G'$. (in the experimental accessible parameter space).

The less negative slope of the correction factor C_n as well as the reduced decrease in the flow index n are strong indications for a reduced shear thinning effect in elongated particle suspensions compared to the reference ferrofluid consisting of spherical particles. Further experiments are in progress to validate these observations.

5 Hybrid Magnetic Fluids

We showed—under the lead of collaboration partners from Ulm and Stuttgart in the framework of the *German Research Foundation Priority Program 1165*—that tobacco mosaic viruses can be used as a prospective additive to ferrofluids.[Wu10c] Further detailed investigation of Wu and co-workers revealed a magnetic field-dependent viscosity increase of the hybrid suspension by several orders of magnitude compared to the (reference) ferrofluid.[Wu10b] The authors attribute electrostatic interaction of the surface charges of both species to be the reason for (quasi-linear) cluster formation—nanoparticles bind to the viruses—which leads to the observed drastically enhanced MVE. The published results were the starting point and the motivation to explore inorganic iron oxide nanotubes and nickel nanorods as promising additives in conventional ferrofluids.

This chapter is divided into three parts. First, measurements on hybrid suspensions consisting of nickel nanorods and spherical cobalt ferrite particles are presented. Second, superparamagnetic iron oxide nanotubes are explored as additives. Last, conclusive explanations are derived for the observed phenomena in such inorganic hybrid suspensions.

5.1 Nickel Nanorods as Additive

Preparation of the Hybrid Suspensions

The remains of the nickel nanorod suspension (0.01 vol %)—after PMAV and SQUID measurements approximately 40 μL —as well as the reference ferrofluid (0.66 vol %) served as precursors for the synthesis of hybrid magnetic fluids. The volume concentration of the spherical cobalt ferrite particles was kept constant at 0.66 vol % in all hybrid suspensions. Only the concentration of nanorods was changed. The highest nanorod concentration in the hybrid suspension was chosen to be 0.002 vol % (20 ppm), which in absolute numbers, corresponds to one nanorod per 4×10^4 nanoparticles. Subsequently, 50 μL of this hybrid sample was diluted by the addition of 50 μL of the reference ferrofluid. Thereby, the ratio between the number of nanoparticles and nanorods was doubled—the concentration in ppm of the nanorods was halved. This procedure was repeated four times, until the final ratio of one nanorod per 64×10^4 nanoparticles (1.25 ppm) was reached (figure 5.1). The absolute volume concentration—total volume of solid magnetic material to liquid volume—changed slightly from $\Phi_{\text{initial}} = 0.662 \text{ vol } \%$ to $\Phi_{\text{final}} = 0.660 \text{ vol } \%$,

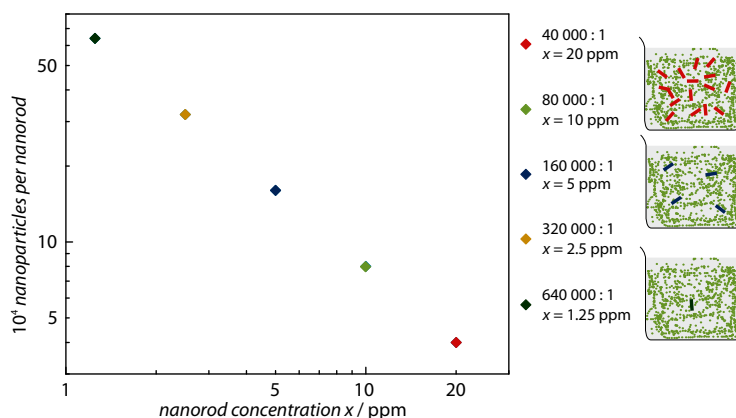


Figure 5.1: Double-logarithmic plot of the amount of nanoparticles per nanorod as a function of the volume concentration of nanorods. Scheme at the right side illustrates the dilution series. The color assignment of the individual nickel nanorod concentrations is valid for the complete section dealing with nickel nanorod hybrid suspensions (section 5.1).

which is in the error range of the volume concentration of the reference ferrofluid $\Delta\Phi = 0.030$ vol %. Hence, all observed phenomena are attributed to the amount of nickel nanorods in the hybrid suspension, and not to the overall increased volume concentration of the magnetic material.

On the Reversibility between the ‘On’- and the ‘Off’-Magnetic Field-Dependent Viscoelastic Properties

The reversibility between magnetic field ‘off’ and ‘on’ was explored by sequential switching between 0 mT and 110 mT, respectively, within few minutes and measuring the corresponding viscoelastic properties at each state. The data are shown in figure 5.2 for (a) the most concentrated hybrid suspension with a nickel concentration of 20 ppm and (b) for a hybrid magnetic fluid containing 2.5 ppm nickel nanorods. In detail, the most concentrated hybrid suspension reveals a significant increase in the storage modulus G' and the loss modulus G'' (at both magnetic field states) between consecutive switching events. At least for the ‘on’ state the trend of the shear moduli seems to saturate; however, in the time frame of the measurements no evident saturation is reached. One can conclude that additional, non-reversible, large (interacting) structures/clusters are formed at each ‘on’ event allowing for an increased hindrance of the flow but also for storing more energy in these clusters. Moreover, the formed (permanent) microstructures also lead to an increased loss and shear modulus in the subsequent ‘off’ state indicating that an applied magnetic field (each time) triggers the formation of new (permanent) clusters or increases the size of the existing ones. Consequently, the shear moduli G' and G'' are raised, compared to the prior ‘on’ state. When the amount of nanorods is decreased, the switching

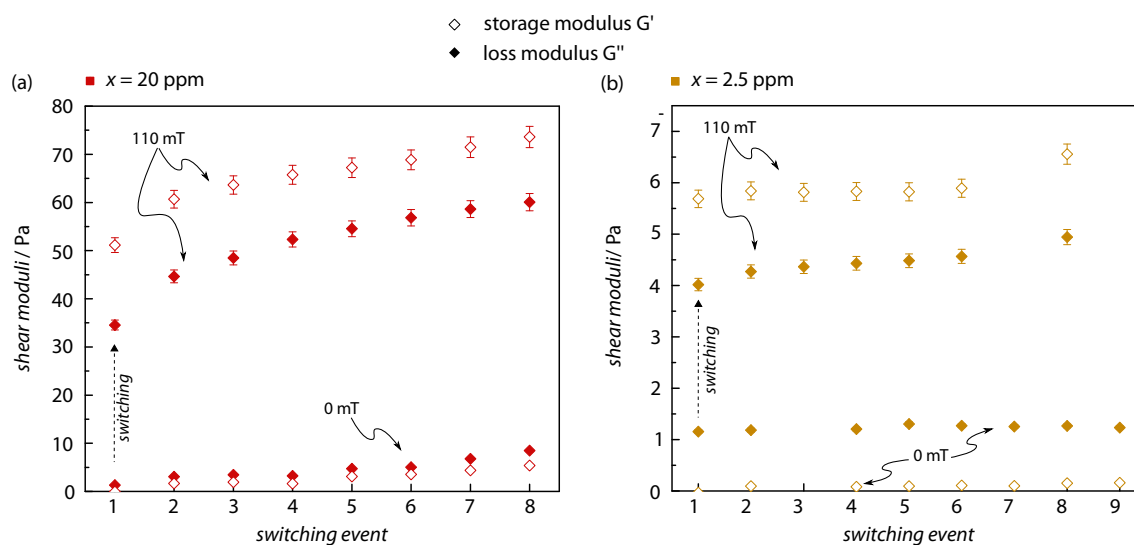


Figure 5.2: Plot of the shear moduli (open symbols: storage modulus G' ; filled symbols: loss modulus G'') in dependence of the switching event for two different liquid suspensions (a) 20 ppm nickel nanorod hybrid suspension and (b) a hybrid fluid containing 2.5 ppm nickel nanorods. The shear frequency was kept constant at 20 Hz during the measurement. Each switching event consisted of an ‘off’ magnetic field measurement (lower values), directly followed by a measurement at 110 mT (denoted by the higher shear moduli values). The waiting time between each switching amounted to 5 min. Detailed information to subfigure (b): the missing ‘off’ data set at switching event (3) is explained by a corrupted data file. Furthermore, switching (7) to (9) are different to the other values. (7) represents the last ‘off’ measurement of a day, (8) denotes a complete switching measurement after 10 h, subsequently it was measured once more in ‘off’-state (9). A shift in the ‘on’ field measurement (8) is observed, compared to the previous ones, which can be caused by water evaporation which would lead to a higher (magnetic) volume concentration or by further microstructure formation due to interaction between the nickel nanorods and the cobalt ferrite particles.

behavior changes as displayed in figure 5.2 (b) for a diluted hybrid suspension which contains 32×10^4 nanoparticles per nanorod. The storage modulus reveals an almost constant value in the ‘on’ state (switching events (2)–(6)), whereas an increase of the loss modulus is observed. In the ‘off’ state both shear moduli increase slightly as a function of the switching events ((1)–(6)). However, the zero-field shear moduli of the hybrid suspension are in a similar range as those of the pure nickel nanorod suspension (compare figure 4.17 (a)).

An increasing amount of permanent microstructures will result in an additional hindrance of the flow—increase in G'' —but also in an increase of the stored energy—raise of G' . However, when the (permanent) cluster size is small and/or the amount of clusters is drastically reduced, the ability of the formed microstructures to store energy as well as to hinder the flow of the surrounding carrier medium is reduced.

When the cluster size is sufficiently small, already small shear frequencies can rotate the clusters in the ‘off’ magnetic field state leading to shear moduli similar to the pure ferrofluidic suspensions. Applying a magnetic field aligns/fixes the clusters and thus leads to the significantly increased shear moduli.

Consequently, the magnetic history of the hybrid suspension plays an important role in determining the magnetic field-dependent viscoelastic properties of such a hybrid magnetic fluid. In the consecutive experiments, following procedure was used: a freshly prepared suspension was mounted in the PMAV setup and the magnetic field was sequentially switched to 110 mT and 0 mT for four times—a waiting time of 5 min between two ‘on’ measurements was implemented to avoid excess heating of the sample caused by the current flowing through the solenoid. Subsequently, a waiting period was implemented until the setup’s temperature reached $(20.0 \pm 0.2)^\circ\text{C}$ and one PMAV measurement series—from 0 mT to 110 mT—could be started.

The Loss Factor: Sol-Gel Transition

The reader might have noticed that the storage modulus in the ‘on’ state in figure 5.2 (a) and (b) is larger than the loss modulus. Hence, the hybrid suspensions do not behave like a liquid anymore, instead a gel-like behavior is observed.

The loss factor describes the phase shift between storage and loss modulus (equation 2.33) and is used to distinguish between a sol-like and a gel-like behavior. Loss factors greater than unity and below unity denote a liquid-like and a gel-like behavior, respectively. At the sol-gel transition point both moduli are identical and the loss factor equals one. The loss factors of three hybrid liquid suspensions, the nickel nanorod suspension, and two differently concentrated standard ferrofluids—consisting of spherical cobalt ferrite particles—are plotted in figure 5.3 as a function of the shear frequency at a constant magnetic field (a) and in dependence of the magnetic field at a constant shear frequency (b).

On the one hand, the colloidal suspensions only consisting of nickel nanorods and spherical nanoparticles as well as the most diluted hybrid suspension (64×10^4 nanoparticles per nanorod, 1.25 ppm) manifest liquid-like behavior (loss factor > 1) in the shear frequency range from 10 Hz to 200 Hz (subfigure (a)). In detail, the loss factor of the standard ferrofluid with a volume concentration of 2.64% and the most diluted hybrid suspension reveal a permanently increasing loss factor, whereas the reference ferrofluid (0.66 vol%) and the pure nickel nanorod suspension display a maximum at 50 Hz and 100 Hz, respectively, randomly seen in several other measurement rounds. Further experiments have to be conducted to explore whether this maximum is attributed to the samples themselves or to the measurement setup. The latter explanation is reasonable, since these features occur exactly at a multiple of the power supply frequency. Nevertheless, the positive slope of the curves (at shear frequencies below the maximum) can be explained by more dissipated than stored energy. Increasing shear frequencies suppress the formation of interacting

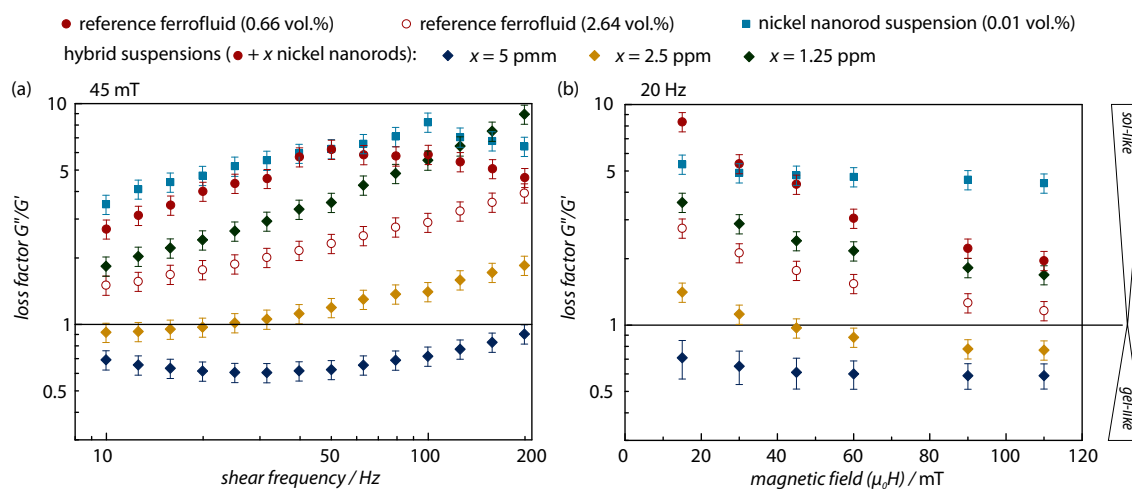


Figure 5.3: A double-logarithmic plot of the loss factor— G'' normalized to G' —as a function of the shear frequency (a) and a log-lin plot of the loss factor in dependence of the applied magnetic field (b) for two differently concentrated standard ferrofluids, a pure nickel nanorod suspension, and three hybrid suspensions differing in the additive amount of nickel nanorods. The sol-gel transition at unity is highlighted by a horizontal line in both subfigures. The measurements of the hybrid suspension containing 5 ppm nanorods reveals a gel-like behavior, whereas a sol-gel transition—indicated by the intersection with the horizontal line—can be observed in measurements of the hybrid suspension containing $x = 2.5$ ppm nanorods. All the other liquid suspensions behave like a liquid. For the sake of clarity, the hybrid nanorod suspensions containing 20 ppm and 10 ppm nickel nanorods are not presented in the figure; they remain in a gel-like state like the 5 ppm hybrid suspension.

clusters/chains which would allow for storing energy. On the other hand, the loss factors of hybrid suspensions with higher concentrations of nanorods ($x = 5$ ppm, 10 ppm and 20 ppm; for the sake of clarity, the latter two concentrations are not shown in figure 5.3) remain below unity and almost constant with a minimum at around 50 Hz; the exact reason for which remains unclear and is attributed to the response behavior of the setup. In spite of that, the general, constant trend indicates the formation of a gel-like *network* which is rigid enough to withstand the applied shear forces. A different behavior of the shear frequency-dependent loss factor is shown by the $x = 2.5$ ppm concentrated hybrid suspension which reveals a sol-gel transition at around 25 Hz (at an applied magnetic field of 45 mT). Below 25 Hz the viscoelastic behavior is gel-like, whereas the behavior is liquid-like above this transition frequency. A magnetic field-induced network formation can be overcome by high shear forces, and the hybrid ‘gel’ is released into a liquid state as a consequence. Similar behavior is observed in polymer solutions with a high degree of entanglement of the individual polymer chains, but also in physically or chemically cross-linked polymers.[Mez06] In general, these particular cases can be identified by shear moduli

measurements in a wide range of shear frequencies as accessible by standard (oscillatory/rotational) rheometers ranging from $1 \times 10^{-3} \text{ s}^{-1}$ to $1 \times 10^2 \text{ s}^{-1}$. An accurate differentiation between these two cases is not possible in the scope of this work since the PMAV setup only allows for measurements in the range from 8 Hz to 200 Hz. However, physical interaction—and therefore cross-linking—is most likely due to the (attractive) magnetism in our case. Thus, the word ‘network’ is used regardless of whether pure entanglement or attractive interaction are responsible for the observed sol-gel transition.

Figure 5.3 (b) presents the loss factor as a function of the applied magnetic field at a fixed shear frequency (20 Hz). Obviously, the loss factor of the spherical nanoparticle suspensions (both concentrations) decreases with increasing magnetic field, whereas the ratio of the two shear moduli of the pure nickel nanorod fluid stays almost constant. An explanation for this behavior can be given in terms of the origin of the shear moduli: chain-like microstructures are formed in the standard ferrofluids upon an applied magnetic field. Thus, the sample becomes stiffer and allows for storing more energy. As a consequence, a drop in the loss factor is observed, when the storage modulus G' increases faster than the loss modulus G'' (compare figure 4.17). In contrast, the shear moduli of the pure nickel nanorod suspension stay constant (after initial saturation) as a function of the applied magnetic field, thus the loss factor also remains constant. Adding 5 ppm nanorods (or more) to the reference ferrofluid results in gel-like properties (loss factor < 1) even at the smallest applied magnetic field of 15 mT. Again, and in contrast, the hybrid suspension with a ratio of 32×10^4 nanoparticles per one nanorod ($x = 2.5$ ppm) shows a magnetic field-dependent transition from a liquid-like to a gel-like state. At low magnetic fields (below 45 mT) the shear frequency hinders the formation of an interacting network. However, when the magnetic field is further increased, network formation occurs (G' overcomes G'') and the sample changes its behavior from sol- to gel-like.

It is obvious that the fluid-mechanical properties of a hybrid suspension (with a constant concentration of spherical nanoparticles) depend on the concentration of nanorods. Hybrid suspensions with a larger concentration of nickel nanorods show the tendency to form stronger (interacting) clusters or networks which are stiffer and allow for the storage of more energy. When the amount of nanorods is reduced, a sol-gel transition point occurs which depends on the experimental parameters, shear frequency and magnetic field. Further lowering of the nanorod concentration results in hybrid suspensions which reveal liquid-like behavior and which resemble the behavior of the standard ferrofluid consisting only of spherical particles.

The transition frequency, at which the sol-gel transition occurs at a fixed magnetic field, is plotted in a semi-log graph displayed in figure 5.4. The linear trend in the lin-log graph denotes a logarithmic function of the transition frequency in dependence of the magnetic field. In other words, the dashed line separates the two different states: liquid-like behavior is determined for experimental parameters

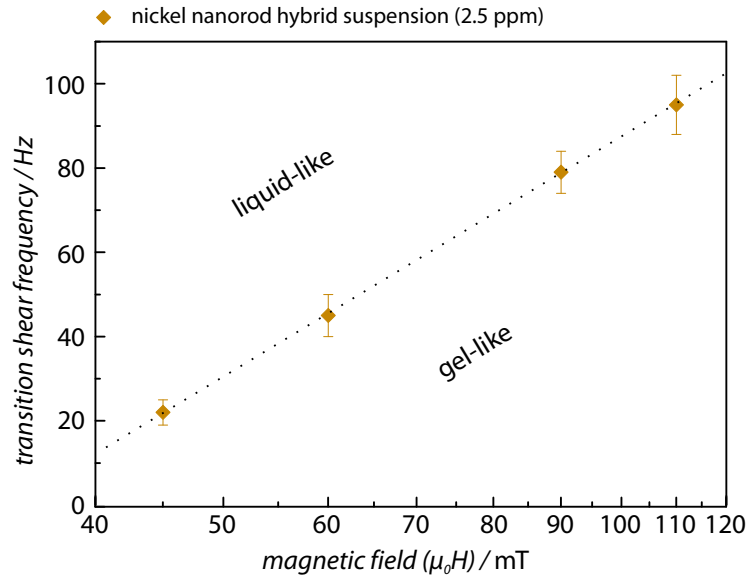


Figure 5.4: Lin-log plot of the transition shear frequency f_{trans} in dependence of the applied magnetic field for a hybrid suspension containing $x = 2.5$ ppm nanorods (32×10^4 nanoparticles per nanorod). The linear trend denotes a logarithmic function of the transition frequency upon an applied magnetic field. The dashed line is a linear fit separating the two regions, namely liquid-like (above) and gel-like (below) behavior and amounts to $f_{\text{trans}} = (-291 \pm 3) \text{ Hz} + (189 \pm 2) \text{ Hz} \cdot \lg(B \text{ mT}^{-1})$. The error bars arise from the determination of the transition point.

which have their corresponding intersection (in the diagram) above the ‘transition’ line, whereas gel-like properties are observed when the used experimental conditions lead to an intersection below the line. At a vanishing shear frequency, the minimum applied magnetic field to transform the liquid into a gel amounts to 35 mT. The observed increase of the transition frequency with increasing magnetic field supports the concept of network formation. One can imagine that higher magnetic fields result in a stiffer network which would need larger shear forces to be released in the liquid state. The inverse function of the logarithmic magnetic field-dependent transition frequency ($f_{\text{trans}} \propto \ln B$) derives to an exponential function of the magnetic field which is at least needed to change such a hybrid suspension from the liquid-like into a gel-like state at a certain shear frequency.

MVE and Shear Thinning Effect

As defined in section 2.3, ferrofluids are supposed to reveal liquid-like properties in the experimentally accessible magnetic field and shear frequency range. However, some of the hybrid suspensions investigated here, revealed a gel-like or a transitional behavior. Hence, on the one hand, the theory of the MVE for (elongated particle)

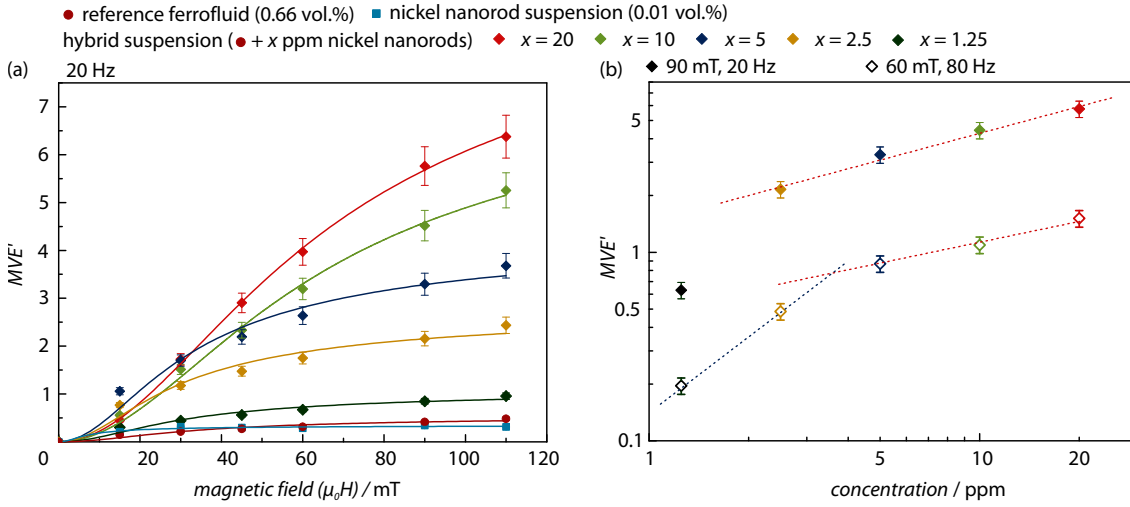


Figure 5.5: (a) Plot of the MVE' as function of the applied magnetic field for differently concentrated hybrid suspensions, the nickel nanorod suspension and the reference ferrofluid. Viscosity measurements were conducted at a constant shear frequency of 20 Hz. The influence of the nickel nanorod concentration on the magnitude of the measured MVE' is obvious. All drawn lines represent fit results of equation 2.49 to the data. (b) The MVE' is double-logarithmically plotted as a function of the concentration for two parameter sets. filled symbols denote data taken at an applied magnetic field of 90 mT and a shear frequency of 20 Hz, whereas open symbols correspond to measurements performed at 60 mT and 80 Hz. The dashed lines serve as guide to the eyes and indicate two different response regions depending whether the hybrid suspension behaves like a gel (red) or like a liquid (blue).

liquid suspensions (equation 2.49) might not be valid in such suspensions, since the viscosity is a property of fluids. On the other hand, the oscillatory PMAV measurement provides the real part as well as the imaginary part of the viscosity at the same time. The real part of the viscosity describes the viscous behavior, whereas the imaginary part describes the elastic properties. Therefore, the following qualitative discussion is only based on the real part of the measured viscosity—prime symbols are used for the sake of clarity.

The calculated MVE' is displayed as a function of the applied magnetic field in figure 5.5 (a) for the reference ferrofluid, the nickel nanorod suspension and the differently concentrated hybrid magnetic fluids. At a first glance, the observed behavior is similar to the ‘pure’ ferrofluids as shown in the previous chapter (compare to figures 4.6 and 4.10); but, the apparent viscosity is drastically increased in an applied magnetic field. A maximum MVE' of about 6.5 is observed for the most concentrated hybrid suspension ($x = 20$ ppm) at an applied magnetic field of 110 mT and a shear frequency of 20 Hz. The magnitude of the magnetoviscous effect decreases as the concentration of nanorods is reduced. The MVE' is plotted as a function

of the nickel nanorod concentration for two different experimental conditions: first, for a shear frequency of 20 Hz and an applied magnetic field of 90 mT, and second for 80 Hz and 60 mT. In the first case, the hybrid suspension with a concentration of 2.5 ppm nickel nanorods reveals gel-like behavior, whereas liquid-like behavior is observed for the second experimental conditions (figure 5.4). Two regions can be identified in the plot: the first region is defined by all hybrid suspensions which reveal gel-like behavior in the measurements, and the second region is defined by the hybrid suspensions which act as liquids. Both regions differ in the slope of the MVE' increase in dependence of the concentration. When the hybrid suspension behaves as a liquid, the sensitivity to the nickel nanorod concentration seems to be more significant than in a gel-like state. These preliminary results have to be supported by further measurements. Synthesis and investigation of further hybrid suspensions—ideally with concentrations ranging from 2.5 ppm to 5 ppm—are inevitable to shed more light on the magnetic field- and shear frequency-dependent sol-gel transition.

Equation 2.49 of the rotational magnetoviscosity model for elongated particles was fitted to the determined MVE' values (figure 5.5 (a)) at different nickel nanorod concentrations and shear frequencies. Again, a significantly reduced magnetic moment is determined, and shows the same trend as discussed in the previous chapter. The explanations given in subsection 4.4.1 might be also valid for the hybrid suspensions in this chapter. However, the second fit parameter C'_n reveals a clear dependence of the concentration and is plotted as a function of the shear frequency for all hybrid suspensions in figure 5.6. For a better comparison, the ‘real’ correction factor of the pure nickel nanorod suspension as well as the correction factor of reference ferrofluid are displayed in the same graph. The slope is a measure for the magnitude of the shear thinning effect. It is obvious that the (negative) slope decreases with decreasing nickel nanorod concentration. The correction factor changes only by less than 50 % at the highest nanorod concentration of 20 ppm within the applied shear frequency range, whereas a drop from more than 500 to less than 20 is observed for the lowest concentration investigated. Moreover, the slope of the hybrid suspensions approaches the slope of the reference ferrofluid, when the concentration of nanorods is decreased. It is striking that the correction factor of the pure nickel nanorod suspension is the highest at low shear frequencies. On the one hand, this fact indicates a strong cross-linking in the hybrid suspension with a high amount of nickel nanorods ($x = 20$ ppm, 10 ppm) instead of chain or (individual) cluster formation. But on the other hand, the correction factor scales the effect of flow hindrance. Now, one can argue about whether gels really ‘flow’ or are only ‘plastically deformed’. In the latter case the use of the correction is only valid for less diluted suspensions ($x \lesssim 5$ ppm) being in a liquid-like state (or at least near to the sol-gel transition).

To conclude, the obtained results display promising magnetoviscous/-elastic properties of the nanorod hybrid suspensions. Continuing studies, such as cryogenic TEM

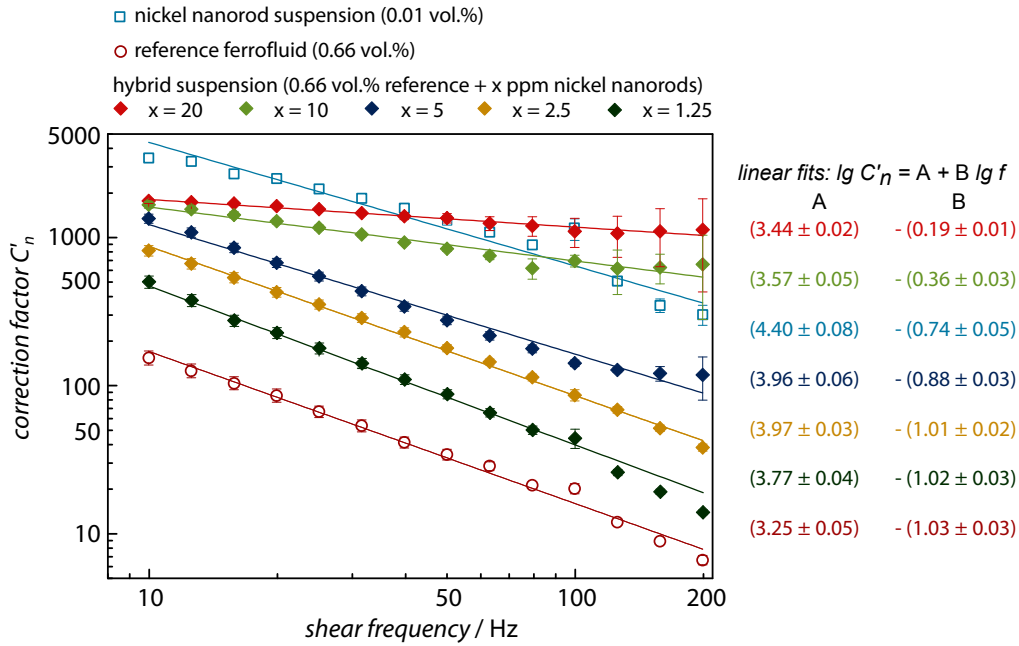


Figure 5.6: Log-log plot of the correction factor C'_n as a function of the shear frequency for differently concentrated hybrid suspensions, the nickel nanorod suspension and the reference ferrofluid. The correction factors reflect the length of the formed clusters, and thus the hindrance of the flow. Therefore, the slope of the shear frequency-dependent C'_n is a measure for the magnitude of the shear thinning effect: a more negative slope indicates a stronger shear thinning effect than a decrease with a less negative slope. The errors bars correspond to the fits results. The drawn lines are linear fits to the data.

investigations, neutron scattering experiments, or even shear moduli measurements over a wide range of shear frequencies, just to name a few, can be utilized to explore the magnetic field-dependent internal microstructure and cluster formation of these hybrid suspensions. Besides the enumerated complex techniques, even further PMAV measurements can extend the findings of this section. Particular attention should be paid to the synthesis and the characterization of more hybrid suspensions which show the sol-gel transition. Especially, changing the numbers of nanoparticles per nanorod—at a constant concentration of nanorods—will give insight in the clustering behavior around the nanorods. For future experiments, collaborations with researchers investigating polymers and polymer solutions are highly recommended since the hybrid suspensions reveal commonalities with these kind of fluids.

5.2 Superparamagnetic Iron Oxide Nanotubes as Additive

Viscosity measurements of a suspension containing superparamagnetic nanotubes (length 190 nm, diameter 85 nm, iron oxide wall thickness 5 nm; as presented in subsection 3.4.2) reveal no magnetoviscous effect (displayed in figure A.13 in the appendix). An exact ‘magnetic’ solid phase concentration cannot be determined since a reduced saturation magnetization has to be taken into account for reduced film thicknesses as displayed in figure 3.15 (subsection 3.3.2). Unfortunately, the decrease of the saturation magnetization at around 5 nm is quite steep leading to a large change in the magnetization at a small thickness change. Therefore, the uncertainty in the saturation magnetization is too large to denote an exact value. Nevertheless, an initial hybrid suspension had been prepared by adding superparamagnetic nanotubes to the pure reference ferrofluid ((0.66 ± 0.03) vol %) to achieve a hybrid suspension. The initial suspension was then further diluted keeping the spherical particles’ volume concentration constant and reducing the amount of nanotubes to the half. The shear moduli in dependence of the number of switching events are displayed for the initial nanotube hybrid suspension in figure 5.7. After

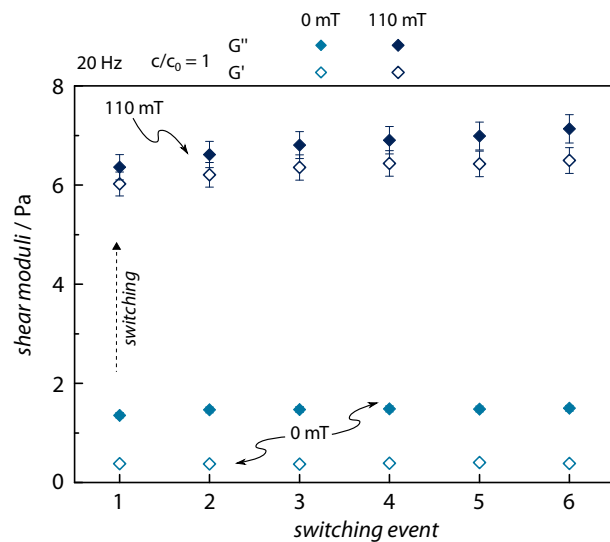


Figure 5.7: Shear moduli of the initial nanotube hybrid suspension plotted in dependence of the switching event. An individual switching event consists of a zero-field (‘off’) measurement and a measurement at 110 mT (‘on’ state) both taken at a shear frequency of 20 Hz (measurements are color coded). The loss modulus G'' and the storage modulus G' are plotted in filled and open symbols, respectively. Only a small increase with increasing number of switching events can be observed indicating that the formation of a network by strongly interacting clusters is rather unlikely. The error bars for the ‘off’ measurement are within the symbol size.

an increase between the first and the second switching event, the shear moduli at zero applied magnetic field stay (almost) constant. A slight increase can be identified for the loss as well as the storage modulus in the ‘on’-state at 110 mT. However, significant contributions to permanent (interacting) cluster formation can be excluded (compare with similar measurements at nickel nanorod hybrid suspensions in figure 5.2). Moreover, the switching event measurements reveal that the hybrid suspension remains liquid at the highest magnetic field (110 mT) and at a low shear frequency (20 Hz) since the loss modulus is larger than the storage modulus.

The MVE is plotted in figure 5.8 (a) as a function of the applied magnetic field for the initial (bright blue) as well as the half-concentrated (dark blue) hybrid suspensions at two different shear frequencies (20 Hz: filled symbols; 80 Hz: open symbols). The data of the reference ferrofluid are plotted in red circles. Three conclusions can be stated:

- the apparent (normalized) viscosity increases by about 800 % for a hybrid nanotube suspension. Thus, the observed increase is larger than the sum of both effects (MVE of around 1.5 for the reference ferrofluid and a negligible effect of the superparamagnetic nanotube suspension).
- A shear thinning effect can be observed similar to all other ferrofluids investigated in this thesis.
- The MVE depends on the concentration of nanotubes in the suspension. Half of the concentration of nanotubes results in only 50 % of the MVE compared to the starting hybrid suspension.

The latter observation is in good agreement with the results determined from the nickel nanorod hybrid suspension in liquid state (compare to figure 5.5 (b): 60 mT, 80 Hz, for hybrid suspensions containing 1.25 ppm and 2.5 ppm nanorods). Again, the magnetic field-dependent MVE can be fitted by the adopted model of rotational viscosity (equation 2.49) including the correction factor C_n . The latter is plotted as a function of the shear frequency in figure 5.7. Similar to the previous studies (figures 4.13 and 5.2), the correction factor decreases with increasing shear frequency. Noticeably, the three lines have the same slope and are only shifted in the absolute value. One can conclude that the reference ferrofluid mainly determines the shear thinning effect; and the nanotubes (also nickel nanorods in the most diluted hybrid suspensions, compare to figure 5.6) only influence the (elongated) cluster size.

It has been shown that even additives in terms of superparamagnetic nanotubes—which reveal no MVE by themselves—can increase the MVE of a conventional ferrofluid. The problem of the unknown volume concentration of superparamagnetic iron oxide nanotubes has to be overcome for future studies. Applying UV/VIS-spectroscopy and measuring the absorption/transmission of the liquid suspension could be the experiment of choice to determine the iron oxide concentration. A

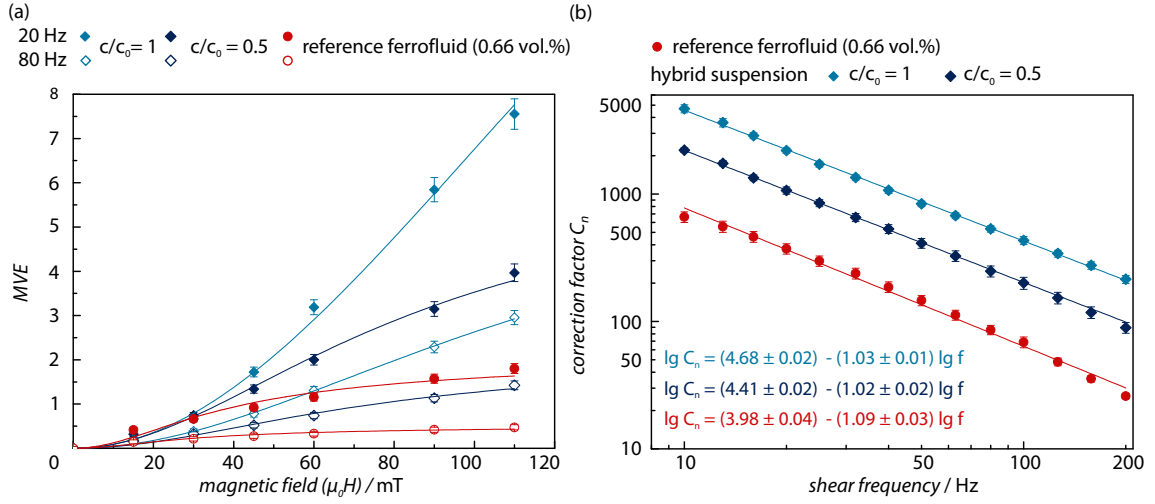


Figure 5.8: (a) MVE as a function of the applied magnetic field for two shear frequencies (coded by symbol filling). The MVE of the reference ferrofluid is displayed with circles, whereas the MVE of the two hybrid nanotube suspensions—different concentrations—are color coded—are plotted with polygonal symbols. It is obvious that the magnitude of the MVE depends on the shear frequency as well as on the nanotube concentration in the hybrid suspension. The drawn lines are fits of equation 2.49 to the data. (b) The correction factor of the reference ferrofluid (red) as well as of the two differently concentrated hybrid nanotube suspensions (blue) are double-logarithmically plotted as a function of the shear frequency. The slope of the decrease of C_n is similar for all three liquid suspensions indicating that the shear thinning effect is mainly determined by the spherical particles in the hybrid suspension. The solid lines are linear fits to the data.

conventional (magnetite) particle ferrofluid with a known concentration can serve as starting point for a dilution series leading to a calibration curve, which would further allow for the determination of the iron oxide nanotube concentration in a liquid suspension.

5.3 A Hypothesis for the Enhanced MVE in Hybrid Suspensions

The key question is: what happens in such a hybrid suspension? Wu *et al.* explored (non-magnetic) tobacco mosaic virus additives to the (same) reference ferrofluid and observed a magnetic field-dependent viscosity increase over several orders of magnitude depending on the concentration of the additives and of the reference ferrofluid.[Wu10b] [Wu10c] The authors state an electrostatic binding of the spherical reference particles—negatively charged due to surface functionalization—to the positively charged surface residues of the virus particles. A control experiment with

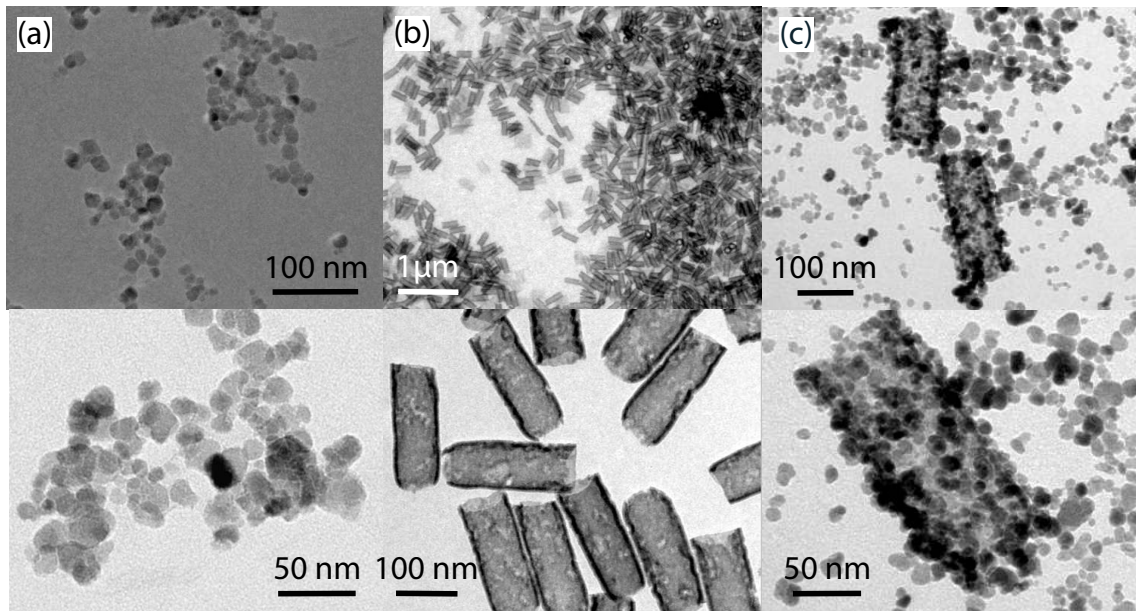


Figure 5.9: TEM images of (a) the pure reference ferrofluid, (b) the superparamagnetic iron oxide nanotubes (length 190 nm, diameter 85 nm, iron oxide wall thickness 5 nm), and (c) the hybrid suspension as a mixture of both. Significant spherical particle clustering around the superparamagnetic iron oxide nanotubes is obvious. These large clusters are suggested to be the reason for the enhanced magnetic field-dependent MVE response.

negatively charged surface residues on the viruses confirmed their suggestion since no significant viscosity increase was observed. Repulsive electrostatic forces hinder the binding of the nanoparticles to the viruses in this specific case.

Transmission electron microscopy of the inorganic hybrid nanotube suspensions (5.9 (c)) revealed a significant clustering of the spherical particles (a) around the magnetic nanotubes (b). It is well known that large objects such as clusters predominantly determine the MVE in ferrofluidic suspensions.[Ode00] [Thu03] [Ode04] [Zub05] The viscosity measurements of hybrid suspensions—with additives of nickel nanorods or iron oxide nanotubes—indicate interactions between spherical particles and elongated inorganic nanoobjects, and therefore cluster formation.

Wu *et al.* investigated hybrid suspensions with a ratio of about 8000 cobalt ferrite nanoparticles (based on the same reference ferrofluid, 0.66 vol %) per elongated, virus additive particle (length: 300 nm) and observed a MVE in the order of 30 (graph in figure 2.11 (a) in subsection 2.3.3). The highest nickel nanorod concentration which was explored in this thesis amounted to 20 ppm corresponding to about 40 000 nanoparticles per nanorod. As already mentioned, the exact concentration of the (initial) superparamagnetic iron oxide hybrid suspension is unknown. However, the upper limit of the nanoparticle to nanotube ratio is 1×10^5 to 1 estimated using the saturated magnetic moment determined in VSM measurements and a reduced

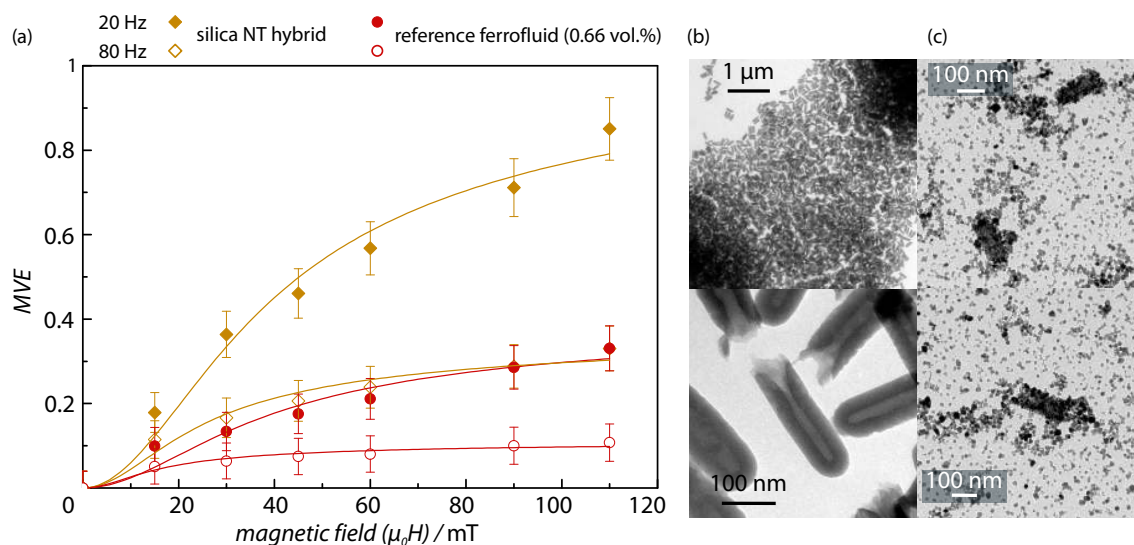


Figure 5.10: (a) MVE of the silica nanotube hybrid suspension (yellow polygonal symbols) and the reference ferrofluid (red circles) as a function of the applied magnetic field for two shear frequencies (coded by the filling of the symbols). A three times enhanced MVE can be observed in the ‘non-magnetic additive’ hybrid suspension compared to the reference ferrofluid. All drawn lines represent fit results of equation 2.49 to the data. (b) TEM micrographs of the pure silica nanotubes. (c) Transmission electron microscopy reveals significant clustering around the nanotubes which is attributed to electrostatic interactions.

magnetization of a 5 nm thin film (compare to subsection 3.3.2 and figure 3.15). Thus, the observed MVE of the hybrid suspensions investigated in this chapter is in a comparable range to the results of Wu and co-workers.[Wu10b]

Electrostatic interactions were assigned by Wu and co-workers to cause the agglomeration of the reference ferrofluid particles around the tobacco mosaic viruses (figure 2.11 (d)). On a first glance, magnetic (attractive) interactions might be a possible reason for the agglomeration around the inorganic nanoobjects. In fact, even pure silica nanotubes (concentration unknown) revealed a magnetic field-dependent MVE increase when added to a reference ferrofluid (figure 5.10(a)). TEM images of the hybrid suspension display a significant clustering of the cobalt ferrite nanoparticles around the silica nanotubes (subfigure (b)). In this particular case, the attraction via magnetic interaction can be excluded: the surface potential of pure, untreated silica is supposed to be negative at a pH-value of 5—pH of the carrier liquid (DEG/H₂O)—which would result in a repulsive electrostatic force.[Par65] Thus, no agglomeration is expected since the spherical particles have been (surface) functionalized by negative charges.[Fau12] However, it was shown that silica which was prior exposed to aluminum or chromium ions revealed a positive surface potential at pH = 5.[Hor78] [Zak92] [Leo05] During the synthesis process aluminum ions as

well as chromium ions are present at various concentrations and pH-values due to the consecutive release and washing steps of the nanotubes. Therefore, adsorption of these ions on the silica surface is likely. A positive surface charge would attract the negatively charged spherical particles and would lead to the formation of (elongated) agglomerates. Taking these facts into account, the cluster formation of the superparamagnetic iron oxide nanotubes and silica nanotubes with the spherical particles is mainly attributed to electrostatic interaction.¹

In the case of the nickel nanorods, both reasons—electrostatic as well as dipolar magnetic interaction—may play a role. On the one hand, nickel tends to form a native oxide layer, especially when alkaline processes are involved in the synthesis route. The nickel oxide reveals a positive surface charge, therefore being attractive for the spherical particles of the reference ferrofluid.[Par65] [Ots11] On the other hand, the increasing shear modulus with the number of switching events (figure 5.2) indicates interacting, permanent cluster formation which is triggered by the magnetic field. These experimental results cannot only be explained by electrostatic interaction. Control measurements as a function of time without applying a magnetic field reveal (almost) constant shear moduli. However, a distinct separation of both processes is not possible and remains open for future experiments.

Inorganic elongated particle additives reveal promising magnetoviscous properties can be applied to enhance the magnetoviscous properties of a standard ferrofluid consisting of spherical particles. Nickel nanorods can be used to change the properties of a hybrid suspension from a liquid-like state to gel-like behavior depending on the nanorod concentration in the hybrid suspension, the applied magnetic field and the shear frequency. Such hybrid suspensions working at the cutting edge of ferrofluids and magnetorheological fluids: the first group stays liquid upon an applied magnetic field, whereas the latter solidifies. Furthermore, superparamagnetic iron oxide as well as pure silica nanotubes—both pure liquid suspensions show no magnetic field-dependent MVE—can also be applied to improve the magnetic field-dependent response of a hybrid suspension. At least two different attractive interactions have to be considered as reason for the apparent agglomeration of the spherical particles around the elongated object. In the case of silica and (superparamagnetic) iron oxide nanotubes, electrostatic interactions are supposed to be the driving forces, whereas in the case of nickel nanorods a combination of electro- and magnetostatic interactions has to be considered. Further experiments dealing with the tuning of the surface potential are suggested to shed more light on the hybrid suspensions, e.g. viscosity measurements of hybrid suspensions as a function of the pH-value, with different functionalized surfaces of the additives or the commercial ferrofluid, and differently pretreated silica bead/nanotube additives.

¹Rene Faust (supervised Bachelor student, Physics Department, University of Hamburg (2012)) performed control experiments with commercial (untreated) silica beads as additive at similar additive concentrations as used by Wu and co-workers. An increase in the magnetic field-dependent MVE could not be detected at all.

6 Summary and Outlook

To synthesize sufficiently concentrated ferrofluids by template-based approaches, scale-up of the yield per batch is inevitable to finally allow for magnetic field-dependent viscosity measurements. Two preparation routes were presented in this thesis which overcame the inherent limitation of the template size. Tailor-made iron oxide nanotubes were synthesized by an enlargement of the porous template area in combination with atomic layer deposition, whereas nickel nanorods were prepared by utilizing the third dimension—the pore length—of a nanoporous alumina membrane for multilayered electrodeposition.

An improved thermal reduction process of the iron oxide films deposited by ALD led to stoichiometric and crystalline magnetite films. First principle studies of the magnetic properties of magnetite thin films revealed the occurrence of the Verwey transition and the isotropic point—both features are only attributed to high-quality magnetite samples. Furthermore, FORC studies and angular-dependent isothermal magnetization measurements indicated a change of the micromagnetic structure in the thin film depending on whether the magnetic field was applied in parallel or perpendicular to the magnetite film. When the film thickness was reduced below 10 nm, the saturation magnetization as well as the coercive field significantly decreased indicating the occurrence of superparamagnetic behavior. Based on these results, magnetite nanotubes with low aspect ratios ≤ 15 were synthesized and structurally investigated. The polycrystalline, granular structure of the thin films could be confirmed in the walls of the nanotubes. Indeed, reducing the wall thickness ≤ 5 nm resulted in superparamagnetic iron oxide nanotubes. The second synthesis approach based on multilayered electrodeposition of nickel and copper from a single electrolyte in a porous alumina membrane. Long, multisegmented nanowires served as precursor for the short nickel nanorods, which were synthesized by a selective etching of the sacrificial copper phase. At the end, both preparation routes resulted in liquid suspensions of elongated magnetic nanoparticles.

As a reference, the magnetic field- and shear frequency-dependent fluid-mechanical properties of a commercial ferrofluid were investigated. Aging of the reference ferrofluid was observed, which resulted in a change of the magnetoviscous properties with time. Comparative MVE studies of a nickel nanorod and a magnetite nanotube suspension revealed significant differences between spherical and elongated nanoparticle suspensions in the magnetic field-dependent MVE response and in the shear thinning effect (expressed by the correction factor). The observed results were attributed to two different mechanisms in the corresponding suspensions: chain/cluster

formation and breaking were identified in the case of the reference ferrofluid, whereas for the elongated particles their rotation seemed to play an important role.

Hybrid suspensions were prepared by adding elongated objects to the reference ferrofluids. Already small amount of additives in the ppm range caused a drastic increase of the apparent MVE. Moreover, it was shown that the properties of a hybrid suspension could be turned from sol- to gel-like by adjusting the applied magnetic field or the shear frequency. Clustering of the spherical particles around the elongated objects was suggested as possible reason. In detail, magnetic interactions between nickel nanorods and cobalt ferrite particles were likely, whereas electrostatic interactions were suggested in the case of superparamagnetic nanotube and silica nanotube additives.

To conclude, magnetite thin films and nanotubes have been produced by ALD for the first time in such a high quality that the Verwey transition and the isotropic point could be determined. Further experiments on films as well as nanotubes are planned, namely AC susceptibility studies to explore the energy barrier with respect to superparamagnetism, and temperature-, angular- as well as thickness-dependent FORC measurements to investigate the micromagnetic structure in detail. Utilizing HR-TEM, AFM (atomic force microscopy), and (GI-)XRD would allow for determining the grain size as a function of the iron oxide thickness in films as well as in the nanotube walls. Other studies are already in the implementation; in detail, one has to mention the temperature-dependent Raman spectroscopy (Foncuberta i Morral, EPFL (Switzerland)), the investigation of epitaxial growth of iron oxide on (001) MgO (Barth, TU Vienna (Austria)), the experiments on the magnetic circular dichroism (Campo, University of Florence (Italy)), the study of the thermal reduction process's dynamics (Detavernier, Ghent University (Belgium)), and the electrical characterization (in our group by Johannes Gooth, University of Hamburg (Germany)). The viscosity measurements presented herein revealed promising results which can serve as starting point for further studies. Particularly, the response behavior of the elongated particle suspensions as well as the fascinating properties of the hybrid suspensions—working at the cutting edge of ferrofluids and magnetorheological fluids—may attract researchers to improve the existing synthesis routes or to develop novel preparation methods, which would allow for the controlled synthesis of tailor-made elongated nanoparticle suspensions in such concentrations and volumes that magnetoviscous measurements are possible. Additionally, experiments have to be planned which allow for the detection of the elongated particle orientation distribution function in dependence of the magnetic field and shear frequency. Neutron-scattering experiments as already performed on spherical particle ferrofluids or optical relaxation measurements can help to study the magnetic field- and shear frequency-dependent behavior of the elongated particles and clusters in liquid suspensions.[Wie06] [Kle09] [Sch12]

Besides the applications in magnetic fluids, (superpara)magnetic nanoparticles are utilized in medical applications, such as magnetic resonance imaging, drug- or gene-delivery, and hyperthermia therapy, to name a few. Especially, the iron oxide nanotubes with their inner free space seem to be ideal candidates for drug-delivery applications. Two collaboration projects have already been planned to explore the use of the nanotubes as medical containers. (Pondman, University of Twente (Netherlands); Pané i Vidal, ETH Zurich (Switzerland)) However, one might argue about the yield of nanotubes with respect to ‘real’ applications. Recently, our group explored and published a synthesis route which exploits the third dimension of a nanoporous template for the preparation of nanotubular objects. Selective surface protection by organic self-assembled monolayers and cycling anodization allows for stacking of separated nanotubes in the membranes. [Bae13] The nickel nanorod synthesis route might be explored in terms of cancer cell destruction by manipulating magnetic nano-/microdisks with AC magnetic fields. The magnetic ground state of a nano-/microdisc can be the vortex state depending on the exact geometry. When cancer cells are interfaced with these disks and an AC magnetic field is applied, the vortex in the disc shifts and induces an oscillation of the disk. As a consequence, a mechanical force is transferred onto the cell membrane and induces the cell apoptosis—the programmed cell death. [Kim10] The permalloy microdiscs in this publication were synthesized by a lithographic preparation route. 1×10^8 discs (1 μm in diameter and 60 nm thick) can be prepared in one batch with the proposed synthesis route by Kim and co-workers. Using multisegmented nanowires in an appropriate template as precursor will drastically increase the yield of such disks. The combination of the two- and the three-dimensional approach presented in this thesis would easily allow for a three orders of magnitude larger yield with which first clinical studies are in close vicinity.¹

¹Phosphoric acid membrane (pore density $5 \times 10^7 \text{ cm}^{-2}$), pores are widened to 400 nm diameter, 64 cm^2 template area, 100 stacks with periodicity of 50 nm of electrodeposited permalloy [Sal12] and 50 nm of the sacrificial copper layer.

Bibliography

- [Abe76] K. Abe, Y. Miyamoto, and S. Chikazumi. *Magnetocrystalline anisotropy of low-temperature phase of magnetite*. Journal of the Physical Society of Japan **41** (6), 1894–1902 (1976).
- [Aer13] National Aeronautics and Space Administration. *Amazing magnetic fluids*. Article on http://science1.nasa.gov/science-news/science-at-nasa/2002/23aug_mrfluids/ (31.05.2013).
- [Aha96] A. Aharoni. *Introduction to the Theory of Ferromagnetism*. Oxford University Press Inc., New York, 1996.
- [Alb10] O. Albrecht, R. Zierold, C. Patzig, J. Bachmann, C. Sturm, B. Rheinländer, M. Grundmann, D. Görlitz, B. Rauschenbach, and K. Nielsch. *Tubular magnetic nanostructures based on glancing angle deposited templates and atomic layer deposition*. Physica Status Solidi B **247** (6), 1365–1371 (2010).
- [Alb11] O. Albrecht, R. Zierold, S. Allende, J. Escrig, C. Patzig, B. Rauschenbach, K. Nielsch, and D. Görlitz. *Experimental evidence for an angular dependent transition of magnetization reversal modes in magnetic nanotubes*. Journal of Applied Physics **109** (9), 093910 (2011).
- [Alt12] S. Altmeyer, Y. Do, and J. M. Lopez. *Influence of an inhomogeneous internal magnetic field on the flow dynamics of a ferrofluid between differentially rotating cylinders*. Physical Review E **85** (6), 066314 (2012).
- [Ana09] S. Anandakumar, V. S. Rani, B. P. Rao, S. S. Yoon, J. R. Jeong, and C. Kim. *Template synthesis of cobalt nanowires using PS-*b*-PMMA block copolymer*. IEEE Transactions on Magnetics **45** (10), 4063–4066 (2009).
- [Ara86] R. Aragón, R. J. Rasmussen, J. P. Shepherd, J. W. Koenitzer, and J. M. Honig. *Effect of stoichiometry changes on electrical-properties of magnetite*. Journal of Magnetism and Magnetic Materials **54** (57), 1335–1336 (1986).
- [Ara04] S. Arai, T. Hasegawa, and N. Kaneko. *Fabrication of three-dimensional Cu/Ni multilayered microstructure by wet process*. Electrochimica Acta **49** (6), 945–950 (2004).

- [Ara07] S. Aravamudhan, K. Luongo, P. Poddar, H. Srikanth, and S. Bhansali. *Porous silicon templates for electrodeposition of nanostructures*. Applied Physics A: Materials Science & Processing **87** (4), 773–780 (2007).
- [Aro08] M. Aronniemi, J. Saino, and J. Lahtinen. *Characterization and gas-sensing behavior of an iron oxide thin film prepared by atomic layer deposition*. Thin Solid Films **516** (18), 6110–6115 (2008).
- [Ash96] O. Ashour, C. A. Rogers, and W. Kordonsky. *Magnetorheological fluids: materials, characterization, and devices*. Journal of Intelligent Material Systems and Structures **7** (2), 123–130 (1996).
- [Bac07] J. Bachmann, J. Jing, M. Knez, S. Barth, H. Shen, S. Mathur, U. Gösele, and K. Nielsch. *Ordered iron oxide nanotube arrays of controlled geometry and tunable magnetism by atomic layer deposition*. Journal of the American Chemical Society **129** (31), 9554–9555 (2007).
- [Bac08] J. Bachmann, R. Zierold, Y. T. Chong, R. Hauert, C. Sturm, R. Schmidt-Grund, B. Rheinländer, M. Grundmann, U. Gösele, and K. Nielsch. *A practical, self-catalytic, atomic layer deposition of silicon dioxide*. Angewandte Chemie International Edition **47** (33), 6177–6179 (2008).
- [Bac09] J. Bachmann, J. Escrig, K. Pitzschel, J. M. M. Moreno, J. Jing, D. Görlitz, D. Altbir, and K. Nielsch. *Size effects in ordered arrays of magnetic nanotubes: Pick your reversal mode*. Journal of Applied Physics **105** (7), 07B521 (2009).
- [Bae11] C. Bae, H. Shin, and K. Nielsch. *Surface modification and fabrication of 3D nanostructures by atomic layer deposition*. MRS Bulletin **36** (11), 887–897 (2011).
- [Bae13] C. Bae, R. Zierold, J. M. M. Moreno, H. Kim, H. Shin, J. Bachmann, and K. Nielsch. *Multisegmented nanotubes by surface-selective atomic layer deposition*. Journal of Materials Chemistry C **1** (4), 621–625 (2013).
- [Bak10] I. Bakonyi and L. Péter. *Electrodeposited multilayer films with giant magnetoresistance (GMR): progress and problems*. Progress In Materials Science **55** (3), 107–245 (2010).
- [Bal07] G. Baldi, D. Bonacchi, C. Innocenti, G. Lorenzi, and C. Sangregorio. *Cobalt ferrite nanoparticles: the control of the particle size and surface state and their effects on magnetic properties*. Journal of Magnetism and Magnetic Materials **311** (1), 10–16 (2007).

- [Ban06] M. Bandyopadhyay and S. Dattagupta. *Memory in nanomagnetic systems: superparamagnetism versus spin-glass behavior*. Physical Review B **74** (21), 214410 (2006).
- [Bat06] A. Bataille, E. Vincent, S. Gota, and Gaut. *Finite size effects in the Verwey transition of magnetite thin films*. arXiv:cond-mat/0610291 (2006).
- [Bea59] C. P. Bean and J. D. Livingston. *Superparamagnetism*. Journal of Applied Physics **30** (4), 120S (1959).
- [Bel08] R. C. Bell, J. O. Karli, A. N. Vavreck, D. T. Zimmerman, G. T. Ngatu, and N. M. Wereley. *Magnetorheology of submicron diameter iron microwires dispersed in silicone oil*. Smart Materials & Structures **17** (1), 015028 (2008).
- [Ben11] P. Bender, A. Günther, A. Tschöpe, and R. Birringer. *Synthesis and characterization of uniaxial ferrogels with Ni nanorods as magnetic phase*. Journal of Magnetism and Magnetic Materials **323** (15), 2055–2063 (2011).
- [Ber96] B. M. Berkovsky and V. Bashtovoy. *Magnetic Fluids and Applications Handbook*. Begell House, Wallingford, 1996.
- [Bic57] L. R. Bickford, J. M. Brownlow, and R. F. Penoyer. *Magnetocrystalline anisotropy in cobalt-substituted magnetic single crystals*. Proceedings of the Institution of Electrical Engineers **B104**, 238–244 (1957).
- [Bic06] I. Bica. *Advances in magnetorheological suspension: production and properties*. Journal of Industrial and Engineering Chemistry **12** (4), 501–515 (2006).
- [Bir08] R. Birringer, H. Wolf, C. Lang, A. Tschöpe, and A. Michels. *Magnetic nanorods: genesis, self-organization and applications*. Zeitschrift für Physikalische Chemie **222** (2-3), 229–255 (2008).
- [Blo94] A. Blondel, J. P. Meier, B. Doudin, and J. P. Ansermet. *Giant magnetoresistance of nanowires of multilayers*. Applied Physics Letters **65** (23), 3019–3021 (1994).
- [Bol05] A. Bollero, M. Ziese, R. Höhne, H. C. Semmelhack, U. Köhler, A. Setser, and P. Esquinazi. *Influence of thickness on microstructural and magnetic properties in Fe_3O_4 thin films produced by PLD*. Journal of Magnetism and Magnetic Materials **285** (1-2), 279–289 (2005).
- [Bos02] G. Bossis, S. Lacis, A. Meunier, and O. Volkova. *Magnetorheological fluids*. Journal of Magnetism and Magnetic Materials **252** (1-3), 224–228 (2002).

- [Bre74] H. Brenner. *Rheology of a dilute suspension of axisymmetric brownian particles*. International Journal of Multiphase Flow **1**, 195–341 (1974).
- [Bro60a] S. Broersma. *Rotational diffusion constant of a cylindrical particle*. Journal of Chemical Physics **32** (6), 1626–1631 (1960).
- [Bro60b] S. Broersma. *Viscous force constant for a closed cylinder*. Journal of Chemical Physics **32** (6), 1632–1635 (1960).
- [Bro63] W. F. Brown. *Thermal fluctuations of a single-domain particle*. Physical Review **130** (5), 1677–1686 (1963).
- [Bro81] S. Broersma. *Viscous force and torque constants for a cylinder*. Journal of Chemical Physics **74** (12), 6989–6990 (1981).
- [But03a] K. Butter, P. H. Bomans, P. M. Frederik, G. J. Vroege, and A. P. Philipse. *Direct observation of dipolar chains in ferrofluids in zero field using cryogenic electron microscopy*. Journal of Physics: Condensed Matter **15** (15), S1451–S1470 (2003).
- [But03b] K. Butter, P. H. Bomans, P. M. Frederik, G. J. Vroege, and A. P. Philipse. *Direct observation of dipolar chains in iron ferrofluids by cryogenic electron microscopy*. Nature Materials **2** (2), 88–91 (2003).
- [Car05] D. Carlier, C. Terrier, C. Arm, and J. P. Ansermet. *Preparation and magnetic properties of Fe_3O_4 nanostructures grown by electrodeposition*. Electrochemical and Solid-State Letters **8** (3), C43–C46 (2005).
- [Cha80] R. W. Chantrell, A. Bradbury, J. Popplewell, and S. W. Charles. *Particle cluster configuration in magnetic fluids*. Journal of Physics D: Applied Physics **13** (7), L119–L122 (1980).
- [Cha01] B. S. Chae, A. M. Lane, and J. M. Wiest. *On the Cox-Merz rule for magnetic dispersions*. Rheologica Acta **40** (6), 599–602 (2001).
- [Che03a] M. Chen, P. C. Searson, and C. L. Chien. *Micromagnetic behavior of electrodeposited Ni/Cu multilayer nanowires*. Journal of Applied Physics **93** (10), 8253–8255 (2003).
- [Che03b] M. Chen, L. Sun, J. E. Bonevich, D. H. Reich, C. L. Chien, and P. C. Searson. *Tuning the response of magnetic suspensions*. Applied Physics Letters **82** (19), 3310–3312 (2003).
- [Che06] M. Chen, C. L. Chien, and P. C. Searson. *Potential modulated multilayer deposition of multisegment Cu/Ni nanowires with tunable magnetic properties*. Chemistry of Materials **18** (6), 1595–1601 (2006).

- [Chi01] B. D. Chin, J. H. Park, M. H. Kwon, and O. O. Park. *Rheological properties and dispersion stability of magnetorheological (MR) suspensions*. *Rheologica Acta* **40** (3), 211–219 (2001).
- [Cho10a] Y. T. Chong, D. Görlitz, S. Martens, M. Y. E. Yau, S. Allende, J. Bachmann, and K. Nielsch. *Multilayered core/shell nanowires displaying two distinct magnetic switching events*. *Advanced Materials* **22** (22), 2435–2439 (2010).
- [Cho10b] Y. T. Chong, E. M. Y. Yau, K. Nielsch, and J. Bachmann. *Direct atomic layer deposition of ternary ferrites with various magnetic properties*. *Chemistry of Materials* **22** (24), 6506–6508 (2010).
- [Cho11] Y. T. Chong, M. Y. E. Yau, Y. Yang, M. Zacharias, D. Görlitz, K. Nielsch, and J. Bachmann. *Superparamagnetic behavior in cobalt iron oxide nanotube arrays by atomic layer deposition*. *Journal of Applied Physics* **110** (4), 043930 (2011).
- [Coe71] J. M. D. Coey. *Noncollinear spin arrangement in ultrafine ferrimagnetic crystallites*. *Physical Review Letters* **27** (17), 1140–1142 (1971).
- [Cor01] N. Cordente, M. Respaud, F. Senocq, M. J. Casanove, C. Amiens, and B. Chaudret. *Synthesis and magnetic properties of nickel nanorods*. *Nano Letters* **1** (10), 565–568 (2001).
- [Cor03] M. R. Cornell and U. Schwertmann. *The Iron Oxides: Structure, Properties, Reactions, Occurrences and Uses*. Wiley-VCH; 2nd, Completely Revised and Extended Edition, 2003.
- [Cor13] Huntsman Corporation. *Ethylene glycol, diethylene glycol, triethylene glycol brochure*. Data sheet on http://www.huntsman.com/performance_products/a/Products/Glycols (20.05.2013).
- [Cox58] W. P. Cox and E. H. Merz. *Correlation of dynamic and steady flow viscosities*. *Journal of Polymer Science* **28** (118), 619–622 (1958).
- [Cra05] J. J. Crassous, R. Regisser, M. Ballauff, and N. Willenbacher. *Characterization of the viscoelastic behavior of complex fluids using the piezoelectric axial vibrator*. *J. Rheol.* **49** (4), 851–863 (2005).
- [Cul09] B.D. Cullity and C.D. Graham. *Introduction to Magnetic Materials (2nd Edition)*. IEEE Press and John Wiley & Sons, Inc. Hoboken, New Jersey, 2009.
- [Dig69] J. W. Diggle, T. C. Downie, and C. W. Goulding. *Anodic oxide films on aluminum*. *Chemical Reviews* **69** (3), 365–405 (1969).

- [Doe07] F. Doebrich, A. Michels, and R. Birringer. *Synthesis of a nanorod ferrofluid and characterisation by magnetic-field-dependent small-angle X-ray scattering*. Journal of Magnetism and Magnetic Materials **316** (2), E779–E782 (2007).
- [Dor87] J. L. Dormann, D. Fiorani, and M. Elyamani. *Field-dependence of the blocking temperature in the superparamagnetic model - $H^{2/3}$ coincidence*. Physics Letters A **120** (2), 95–99 (1987).
- [dR02] M. de Ridder, P. C. van de Ven, R. G. van Welzenis, H. H. Brongersma, S. Helfensteyn, C. Creemers, P. Van Der Voort, M. Baltés, M. Mathieu, and E. F. Vansant. *Growth of iron oxide on yttria-stabilized zirconia by atomic layer deposition*. Journal of Physical Chemistry B **106** (51), 13146–13153 (2002).
- [Dun02a] D. J. Dunlop. *Theory and application of the day plot (m_{rs}/m_s versus h_{cr}/h_c) 1. Theoretical curves and tests using titanomagnetite data*. Journal of Geophysical Research: Solid Earth **107** (B3), EPM4 (2002).
- [Dun02b] D. J. Dunlop. *Theory and application of the day plot (m_{rs}/m_s versus h_{cr}/h_c) 2. Application to data for rocks, sediments, and soils*. Journal of Geophysical Research: Solid Earth **107** (B3), EPM5 (2002).
- [dV09] J. de Vicente, J. P. Segovia-Gutiérrez, E. Andablo-Reyes, F. Vereda, and R. Hidalgo-Álvarez. *Dynamic rheology of sphere- and rod-based magnetorheological fluids*. Journal of Chemical Physics **131** (19), 194902 (2009).
- [dV10] J. de Vicente, F. Vereda, J. P. Segovia-Gutiérrez, M. D. Morales, and R. Hidalgo-Álvarez. *Effect of particle shape in magnetorheology*. Journal of Rheology **54** (6), 1337–1362 (2010).
- [dV11] J. de Vicente, D. J. Klingenberg, and R. Hidalgo-Álvarez. *Magnetorheological fluids: a review*. Soft Matter **7** (8), 3701–3710 (2011).
- [Eer04] W. Eerenstein, T. Hibma, and S. Celotto. *Mechanism for superparamagnetic behavior in epitaxial Fe_3O_4 films*. Physical Review B **70** (18), 184404 (2004).
- [Emb06] J. P. Embs, S. May, C. Wagner, A. V. Kityk, A. Leschhorn, and M. Lücke. *Measuring the transverse magnetization of rotating ferrofluids*. Physical Review E **73** (3), 036302 (2006).
- [Eng05] J. Engmann, C. Servais, and A. S. Burbidge. *Squeeze flow theory and applications to rheometry: a review*. Journal of Non-Newtonian Fluid Mechanics **132** (1-3), 1–27 (2005).

- [Esc08] J. Escrig, J. Bachmann, J. Jing, M. Daub, D. Altbir, and K. Nielsch. *Crossover between two different magnetization reversal modes in arrays of iron oxide nanotubes*. *Physical Review B* **77** (21), 214421 (2008).
- [Eva00] P. R. Evans, G. Yi, and W. Schwarzacher. *Current perpendicular to plane giant magnetoresistance of multilayered nanowires electrodeposited in anodic aluminum oxide membranes*. *Applied Physics Letters* **76** (4), 481–483 (2000).
- [Fan89] P. C. Fannin and S. W. Charles. *The study of a ferrofluid exhibiting both Brownian and Néel relaxation*. *Journal Of Physics D: Applied Physics* **22** (1), 187–191 (1989).
- [Fau12] Rene Michael Faust. *Hybride Ferrofluide basierend auf länglichen Nanoobjekten*. Bachelor’s thesis, Physics Department, University of Hamburg, 2012.
- [Fer04] J. D. Ferguson, E. R. Smith, A. W. Weimer, and S. M. George. *ALD of SiO_2 at room temperature using TEOS and H_2O with NH_3 as the catalyst*. *Journal of the Electrochemical Society* **151** (8), G528–G535 (2004).
- [Gar99] J. M. García, A. Asenjo, J. Velázquez, D. García, M. Vázquez, P. Aranda, and E. Ruiz-Hitzky. *Magnetic behavior of an array of cobalt nanowires*. *Journal of Applied Physics* **85** (8), 5480–5482 (1999).
- [Gau85] J. S. Gau and C. F. Brucker. *Angular variation of the coercivity in magnetic recording thin-films*. *Journal of Applied Physics* **57** (8), 3988–3990 (1985).
- [Gav07] J. P. Gaviña, A. Bohé, A. Pasquevich, and D. M. Pasquevich. *Hematite to magnetite reduction monitored by Mössbauer spectroscopy and X-ray diffraction*. *Physica B: Condensed Matter* **389** (1), 198–201 (2007).
- [Gem12] J. Gemmer, Y. Hinrichsen, A. Abel, and J. Bachmann. *Systematic catalytic current enhancement for the oxidation of water at nanostructured iron(III) oxide electrodes*. *Journal of Catalysis* **290**, 220–224 (2012).
- [Geo10] S. M. George. *Atomic layer deposition: an overview*. *Chemical Reviews* **110** (1), 111–131 (2010).
- [Gil05] K. Gilmore, Y. U. Idzerda, M. T. Klem, M. Allen, T. Douglas, and M. Young. *Surface contribution to the anisotropy energy of spherical magnetite particles*. *Journal of Applied Physics* **97** (10), 10B3011 (2005).

- [Gin96] J. M. Ginder, L. C. Davis, and L. D. Elie. *Rheology of magnetorheological fluids: models and measurements*. International Journal of Modern Physics B **10** (**23-24**), 3293–3303 (1996).
- [Gin98] J. M. Ginder. *Behavior of magnetorheological fluids*. MRS Bulletin **23** (**8**), 26–29 (1998).
- [Gon06] F. D. Goncalves, J. H. Koo, and M. Ahmadian. *A review of the state of the art in magnetorheological fluid technologies – part I: MR fluid and MR fluid models*. Shock and Vibration Digest **38** (**3**), 203–219 (2006).
- [Goy04] G. F. Goya and M.P. Morales. *Field dependence of blocking temperature in magnetite nanoparticles*. Journal of Metastable and Nanocrystallite Materials **20–21**, 673–678 (2004).
- [Goy08] G. F. Goya, V. Grazu, and M. R. Ibarra. *Magnetic nanoparticles for cancer therapy*. Current Nanoscience **4** (**1**), 1–16 (2008).
- [Gün08] A. Günther, S. Monz, A. Tschöpe, R. Birringer, and A. Michels. *Angular dependence of coercivity and remanence of Ni nanowire arrays and its relevance to magnetoviscosity*. Journal of Magnetism and Magnetic Materials **320** (**7**), 1340–1344 (2008).
- [Gün11] Annegret Günther. *Hydrodynamische Eigenschaften von magnetischen Nickelnanostäben in kolloidaler Suspension*. Dissertation, Saarland University, 2011.
- [Han77] K. Haneda and A. H. Morrish. *Magnetite to maghemite transformation in ultrafine particles*. Journal De Physique **38** (**3**), 321–323 (1977).
- [Hay75] C. F. Hayes. *Observation of association in a ferromagnetic colloid*. Journal of Colloid and Interface Science **52** (**2**), 239–243 (1975).
- [Hil79] R. J. Hill, J. R. Craig, and G. V. Gibbs. *Systematics of the spinel structure type*. Physics and Chemistry of Minerals **4** (**4**), 317–339 (1979).
- [Hil10] D. Hiller, R. Zierold, J. Bachmann, M. Alexe, Y. Yang, J. W. Gerlach, A. Stesmans, M. Jivanescu, U. Müller, J. Vogt, H. Hilmer, P. Löper, M. Künle, F. Munnik, K. Nielsch, and M. Zacharias. *Low temperature silicon dioxide by thermal atomic layer deposition: investigation of material properties*. Journal of Applied Physics **107** (**6**), 0643149 (2010).
- [Hor78] J. M. Horn and G. Y. Onoda. *Surface-charge of vitreous silica and silicate-glasses in aqueous-electrolyte solutions*. Journal of the American Ceramic Society **61** (**11-1**), 523–527 (1978).

-
- [Huc00] A. Huczko. *Template-based synthesis of nanomaterials*. Applied Physics A: Materials Science & Processing **70** (4), 365–376 (2000).
- [Igl12] G. R. Iglesias, M. T. Lopez-Lopez, J. D. G. Duran, F. Gonzalez-Caballero, and A. V. Delgado. *Dynamic characterization of extremely bidisperse magnetorheological fluids*. Journal of Colloid and Interface Science **377** (1), 153–159 (2012).
- [Ilg02] P. Ilg and M. Kröger. *Magnetization dynamics, rheology, and an effective description of ferromagnetic units in dilute suspension*. Physical Review E **66** (2), 021501 (2002).
- [Ilg03] P. Ilg and M. Kröger. *Erratum: Magnetization dynamics, rheology, and an effective description of ferromagnetic units in dilute suspension (vol 66, art no 021501, 2002)*. Physical Review E **67** (4), 049901 (2003).
- [Jac55] I. S. Jacobs and C. P. Bean. *Approach to elongated fine-particle magnets*. Physical Review **100** (4), 1060–1067 (1955).
- [Jag94] R. Jagannathan, S. Purushothaman, and S.A. Sikorski. *Methods for etching a less reactive material in the presence of a more reactive material*. US Patent US5304284 – 10/18/1991 (1994).
- [Jes98] O. Jessensky, F. Müller, and U. Gösele. *Self-organized formation of hexagonal pore arrays in anodic alumina*. Applied Physics Letters **72** (10), 1173–1175 (1998).
- [Jil91] D. C. Jiles. *Introduction to Magnetism and Magnetic Materials*. Chapman & Hall, London, 1991.
- [Jol99] M. R. Jolly, J. W. Bender, and J. D. Carlson. *Properties and applications of commercial magnetorheological fluids*. Journal of Intelligent Material Systems and Structures **10** (1), 5–13 (1999).
- [Kan02] S. Kantorovich and A. O. Ivanov. *Formation of chain aggregates in magnetic fluids: an influence of polydispersity*. Journal of Magnetism and Magnetic Materials **252** (1-3), 244–246 (2002).
- [Kel53] F. Keller, M. S. Hunter, and D. L. Robinson. *Structural features of oxide coatings on aluminium*. Journal of the Electrochemical Society **100** (9), 411–419 (1953).
- [Kes11] W. M. M. Kessels and M. Putkonen. *Advanced process technologies: plasma, direct-write, atmospheric pressure, and roll-to-roll ALD*. MRS Bulletin **36** (11), 907–913 (2011).

- [Kim10] D. H. Kim, E. A. Rozhkova, I. V. Ulasov, S. D. Bader, T. Rajh, M. S. Lesniak, and V. Novosad. *Biofunctionalized magnetic-vortex microdiscs for targeted cancer-cell destruction*. *Nature Materials* **9** (2), 165–171 (2010).
- [Kir03] Ludwig Kirschenmann. *Aufbau zweier piezoelektrischer Sonden (PRV / PAV) zur Messung der viskoelastischen Eigenschaften weicher Substanzen im Frequenzbereich 0,5 Hz - 2 kHz bzw. 0,5 Hz - 7 kHz*. Dissertation, Ulm University, 2003.
- [Kla11] B. M. Klahr, A. B. F. Martinson, and T. W. Hamann. *Photoelectrochemical investigation of ultrathin film iron oxide solar cells prepared by atomic layer deposition*. *Langmuir* **27** (1), 461–468 (2011).
- [Kle95] C. A. Kleint, H. C. Semmelhack, M. Lorenz, and M. K. Krause. *Structural and magnetic-properties of epitaxial magnetite thin-films prepared by pulsed-laser deposition*. *Journal of Magnetism and Magnetic Materials* **140-144** (Part 1), 725–726 (1995).
- [Kle09] T. Klein, A. Laptev, A. Günther, P. Bender, A. Tschöpe, and R. Birringer. *Magnetic-field-dependent optical transmission of nickel nanorod colloidal dispersions*. *Journal of Applied Physics* **106** (11), 114301 (2009).
- [Kne07] M. Knez, K. Nielsch, and L. Niinisto. *Synthesis and surface engineering of complex nanostructures by atomic layer deposition*. *Advanced Materials* **19** (21), 3425–3438 (2007).
- [Kno08] M. Knobel, W. C. Nunes, L. M. Socolovsky, E. De Biasi, J. M. Vargas, and J. C. Denardin. *Superparamagnetism and other magnetic features in granular materials: a review on ideal and real systems*. *Journal of Nanoscience and Nanotechnology* **8** (6), 2836–2857 (2008).
- [Kod96] R. H. Kodama, A. E. Berkowitz, E. J. McNiff, and S. Foner. *Surface spin disorder in $NiFe_2O_4$ nanoparticles*. *Physical Review Letters* **77** (2), 394–397 (1996).
- [Koł12] T. Kołodziej, A. Kozłowski, P. Piekarczyk, W. Tabiś, Z. Kakol, M. Zając, Z. Tarnawski, J. M. Honig, A. M. Oleś, and K. Parlinski. *Nuclear inelastic scattering studies of lattice dynamics in magnetite with a first- and second-order Verwey transition*. *Physical Review B* **85** (10), 104301 (2012).
- [Kos02] A. Kosterov. *Low-temperature magnetic hysteresis properties of partially oxidized magnetite*. *Geophysical Journal International* **149** (3), 796–804 (2002).

- [Kri10] K. M. Krishnan. *Biomedical nanomagnetism: a spin through possibilities in imaging, diagnostics, and therapy*. IEEE Transactions on Magnetics **46** (7), 2523–2558 (2010).
- [Krö03] M. Kröger, P. Ilg, and S. Hess. *Magnetoviscous model fluids*. Journal of Physics: Condensed Matter **15** (15), S1403–S1423 (2003).
- [Lam13] Charlie Le Lam. *Magnetic properties of magnetite thin films synthesized by ALD and subsequent reduction*. Master’s thesis, Physics Department, University of Hamburg 2013.
- [Lan78] J. I. Langford and A. J. C. Wilson. *Scherrer after 60 years: survey and some new results in determination of crystallite size*. Journal of Applied Crystallography **11** (2), 102–113 (1978).
- [Lan05] Christian Lang. *Nanostab-Ferrofluide*. Dissertation, Saarland University, 2005.
- [Lau92] H. M. Laun. *Rheometry towards complex flows: squeeze flow technique*. Makromolekulare Chemie: Macromolecular Symposia **56** (1), 55–66 (1992).
- [Leg77] A. J. Leggett. *Superfluid $^3\text{He-A}$ is a liquid ferromagnet*. Nature **270** (5638), 585–586 (1977).
- [Leo05] Y. K. Leong. *Yield stress and zeta potential of nanoparticulate silica dispersions under the influence of adsorbed hydrolysis products of metal ions - Cu(II), Al(III) and Th(IV)*. Journal of Colloid and Interface Science **292** (2), 557–566 (2005).
- [Les06] A. Leschhorn, J. P. Embs, and M. Lücke. *Magnetization of rotating ferrofluids: the effect of polydispersity*. Journal of Physics: Condensed Matter **18** (38), S2633–S2642 (2006).
- [Les11] M. Leskelä, M. Ritala, and O. Nilsen. *Novel materials by atomic layer deposition and molecular layer deposition*. MRS Bulletin **36** (11), 877–884 (2011).
- [Lev97] M. L. Levin, D. É. Poleskii, and I. V. Prokhorov. *Some features of the magnetorheological effect*. Journal of Engineering Physics and Thermophysics **70** (5), 769–772 (1997).
- [Li98a] A. P. Li, F. Müller, A. Birner, K. Nielsch, and U. Gösele. *Hexagonal pore arrays with a 50–420 nm interpore distance formed by self-organization in anodic alumina*. Journal of Applied Physics **84** (11), 6023–6026 (1998).

- [Li98b] F. Li, L. Zhang, and R. M. Metzger. *On the growth of highly ordered pores in anodized aluminum oxide*. Chemistry of Materials **10** (9), 2470–2480 (1998).
- [Li98c] X. W. Li, A. Gupta, G. Xiao, and G. Q. Gong. *Transport and magnetic properties of epitaxial and polycrystalline magnetite thin films*. Journal of Applied Physics **83** (11), 7049–7051 (1998).
- [Li01] S. P. Li, D. Peyrade, M. Natali, A. Lebib, Y. Chen, U. Ebels, L. D. Buda, and K. Ounadjela. *Flux closure structures in cobalt rings*. Physical Review Letters **86** (6), 1102–1105 (2001).
- [Lie05] M. Lie, H. Fjellvåg, and A. Kjekshus. *Growth of Fe_2O_3 thin films by atomic layer deposition*. Thin Solid Films **488** (1-2), 74–81 (2005).
- [Lim10] E. Lima, E. De Biasi, M. V. Mansilla, M. E. Saleta, F. Effenberg, L. M. Rossi, R. Cohen, H. R. Rechenberg, and R. D. Zysler. *Surface effects in the magnetic properties of crystalline 3 nm ferrite nanoparticles chemically synthesized*. Journal of Applied Physics **108** (10), 103919 (2010).
- [Liu06] L. Liu, H. Z. Kou, W. L. Mo, H. J. Liu, and Y. Q. Wang. *Surfactant-assisted synthesis of α - Fe_2O_3 nanotubes and nanorods with shape-dependent magnetic properties*. Journal of Physical Chemistry B **110** (31), 15218–15223 (2006).
- [Liv81] J. D. Livingston. *A review of coercivity mechanisms*. Journal of Applied Physics **52** (3), 2544–2548 (1981).
- [LL05] M. T. Lopez-Lopez, J. de Vicente, G. Bossis, F. Gonzalez-Caballero, and J. D. G. Duran. *Preparation of stable magnetorheological fluids based on extremely bimodal iron-magnetite suspensions*. Journal of Materials Research **20** (4), 874–881 (2005).
- [LL07] M. T. Lopez-Lopez, G. Vertelov, G. Bossis, P. Kuzhir, and J. D. G. Duran. *New magnetorheological fluids based on magnetic fibers*. Journal of Materials Chemistry **17** (36), 3839–3844 (2007).
- [Lon13] C.J. Longhurst. *The suspension bible*. Article on http://www.carbibles.com/suspension_bible.html (31.05.2013).
- [Lu07] A. H. Lu, E. L. Salabas, and F. Schuth. *Magnetic nanoparticles: synthesis, protection, functionalization, and application*. Angewandte Chemie International Edition **46** (8), 1222–1244 (2007).

- [Luo91] W. L. Luo, S. R. Nagel, T. F. Rosenbaum, and R. E. Rosensweig. *Dipole interactions with random anisotropy in a frozen ferrofluid*. Physical Review Letters **67** (19), 2721–2724 (1991).
- [Maa09] K. Maaz, M. Usman, S. Karim, A. Mumtaz, S. K. Hasanain, and M. F. Bertino. *Magnetic response of core-shell cobalt ferrite nanoparticles at low temperature*. Journal of Applied Physics **105** (11), 113917 (2009).
- [Mac94] C.W. Macosko. *Rheology: Principles, Measurements, and Applications*. Advances in interfacial engineering series. Wiley-VCH, 1994.
- [Mar73] M. A. Martsenyuk, Y. L. Raïkher, and M. I. Shliomis. *Kinetics of magnetization of suspensions of ferromagnetic particles*. Zhurnal Eksperimentalnoi I Teoreticheskoi Fiziki **65** (2), 834–841 (1973).
- [Mar74] M. A. Martsenyuk, Y. L. Raïkher, and M. I. Shliomis. *On the kinetics of magnetization of suspensions of ferromagnetic particles*. Soviet Physics - JETP **38** (2), 413–416 (1974).
- [Mar94] C. R. Martin. *Nanomaterials: a membrane-based synthetic approach*. Science **266** (5193), 1961–1966 (1994).
- [Mar96] D. T. Margulies, F. T. Parker, F. E. Spada, R. S. Goldman, J. Li, R. Sinclair, and A. E. Berkowitz. *Anomalous moment and anisotropy behavior in Fe_3O_4 films*. Physical Review B **53** (14), 9175–9187 (1996).
- [Mar98] B. Martínez, X. Obradors, L. Balcells, A. Rouanet, and C. Monty. *Low temperature surface spin-glass transition in γ - Fe_2O_3 nanoparticles*. Physical Review Letters **80** (1), 181–184 (1998).
- [Mar11] A. B. F. Martinson, M. J. DeVries, J. A. Libera, S. T. Christensen, J. T. Hupp, M. J. Pellin, and J. W. Elam. *Atomic layer deposition of Fe_2O_3 using ferrocene and ozone*. Journal of Physical Chemistry C **115** (10), 4333–4339 (2011).
- [Mas95] H. Masuda and K. Fukuda. *Ordered metal nanohole arrays made by a two-step replication of honeycomb structures of anodic alumina*. Science **268** (5216), 1466–1468 (1995).
- [McT69] J. P. McTague. *Magnetoviscosity of magnetic colloids*. Journal of Chemical Physics **51** (1), 133–136 (1969).
- [MEG13] MEGlobal. Data sheet on http://www.meglobal.biz/media/product_guides/MEGlobal_DEG.pdf (20.05.2013).

BIBLIOGRAPHY

- [Men04] V. S. Mendeleev and A. O. Ivanov. *Ferrofluid aggregation in chains under the influence of a magnetic field*. Physical Review E **70** (5), 051502 (2004).
- [Mew11] J. Mewis and N. J. Wagner. *Colloidal Suspension Rheology*. Cambridge Series in Chemical Engineering. Cambridge University Press, 2011.
- [Mez06] Thomas G. Mezger. *The Rheology Handbook: For Users of Rotational and Oscillatory Rheometers*. Vincentz Network GmbH&Co KG, 2006.
- [Mii13] V. Miikkulainen, M. Leskelä, M. Ritala, and R. L. Puurunen. *Crystallinity of inorganic films grown by atomic layer deposition: overview and general trends*. Journal of Applied Physics **113** (2), 021301 (2013).
- [Mou04] J. B. Moussy, S. Gota, A. Bataille, M. J. Guittet, M. Gautier-Soyer, F. Delille, B. Dieny, F. Ott, T. D. Doan, P. Warin, P. Bayle-Guillemaud, C. Gatel, and E. Snoeck. *Thickness dependence of anomalous magnetic behavior in epitaxial $Fe_3O_4(111)$ thin films: effect of density of antiphase boundaries*. Physical Review B **70** (17), 174448 (2004).
- [Mux00] A. R. Muxworthy and E. McClelland. *Review of the low-temperature magnetic properties of magnetite from a rock magnetic perspective*. Geophysical Journal International **140** (1), 101–114 (2000).
- [Mux02] A. R. Muxworthy and D. J. Dunlop. *First-order reversal curve (FORC) diagrams for pseudo-single-domain magnetites at high temperature*. Earth and Planetary Science Letters **203** (1), 369–382 (2002).
- [Mux09] A. R. Muxworthy and W. Williams. *Critical superparamagnetic/single-domain grain sizes in interacting magnetite particles: implications for magnetosome crystals*. Journal of the Royal Society Interface **6** (41), 1207–1212 (2009).
- [Mül01] H. W. Müller and M. Liu. *Structure of ferrofluid dynamics*. Physical Review E **64** (6), 061405 (2001).
- [Mül06] O. Müller, D. Hahn, and M. Liu. *Non-newtonian behaviour in ferrofluids and magnetization relaxation*. Journal of Physics: Condensed Matter **18** (38), S2623–S2632 (2006).
- [Nga08] G. T. Ngatu, N. M. Wereley, J. O. Karli, and R. C. Bell. *Dimorphic magnetorheological fluids: exploiting partial substitution of microspheres by nanowires*. Smart Materials & Structures **17** (4), 045022 (2008).
- [Nie02] K. Nielsch, J. Choi, K. Schwirn, R. B. Wehrspohn, and U. Gösele. *Self-ordering regimes of porous alumina: the 10 % porosity rule*. Nano Letters **2** (7), 677–680 (2002).

- [Ode98] S. Odenbach and H. Störk. *Shear dependence of field-induced contributions to the viscosity of magnetic fluids at low shear rates*. Journal of Magnetism and Magnetic Materials **183** (1-2), 188–194 (1998).
- [Ode00] S. Odenbach and K. Raj. *The influence of large particles and agglomerates on the magnetoviscous effect in ferrofluids*. Magnetohydrodynamics **36** (4), 312–319 (2000).
- [Ode02a] S. Odenbach. *Magnetoviscous Effects in Ferrofluids*. Springer, Berlin, 2002.
- [Ode02b] S. Odenbach and H. W. Müller. *Stationary off-equilibrium magnetization in ferrofluids under rotational and elongational flow*. Physical Review Letters **89** (3), 037202 (2002).
- [Ode04] S. Odenbach. *Recent progress in magnetic fluid research*. Journal of Physics: Condensed Matter **16** (32), R1135–R1150 (2004).
- [Orn10] J. Orna, P. A. Algarabel, L. Morellón, J. A. Pardo, J. M. de Teresa, R. L. Antón, F. Bartolome, L. M. García, J. Bartolomé, J. C. Cezar, and A. Wildes. *Origin of the giant magnetic moment in epitaxial Fe_3O_4 thin films*. Physical Review B **81** (14), 144420 (2010).
- [Ost33] W. Ostwald. *Über die rechnerische Darstellung des Strukturgebietes der Viskosität*. Kolloid Zeitschrift **65** (1), 44–62 (1933).
- [Ots11] A. Otsuki, S. Barry, and D. Fornasiero. *Rheological studies of nickel oxide and quartz/hematite mixture systems*. Advanced Powder Technology **22** (4), 471–475 (2011).
- [Pan09] Q. A. Pankhurst, N. K. T. Thanh, S. K. Jones, and J. Dobson. *Progress in applications of magnetic nanoparticles in biomedicine*. Journal of Physics D: Applied Physics **42** (22) (2009).
- [Par65] G. A. Parks. *Isoelectric points of solid oxides solid hydroxides and aqueous hydroxo complex systems*. Chemical Reviews **65** (2), 177–198 (1965).
- [Par00] S. J. Park, S. Kim, S. Lee, Z. G. Khim, K. Char, and T. Hyeon. *Synthesis and magnetic studies of uniform iron nanorods and nanospheres*. Journal of the American Chemical Society **122** (35), 8581–8582 (2000).
- [Par01] J. H. Park, B. D. Chin, and O. O. Park. *Rheological properties and stabilization of magnetorheological fluids in a water-in-oil emulsion*. Journal of Colloid and Interface Science **240** (1), 349–354 (2001).

- [Pau78] D. N. Paulson and J. C. Wheatly. *Evidence for electronic ferromagnetism in superfluid $^3\text{He-A}$* . Physical Review Letters **40** (9), 557–561 (1978).
- [Ped08] D. Peddis, C. Cannas, A. Musinu, and G. Piccaluga. *Coexistence of superparamagnetism and spin-glass like magnetic ordering phenomena in a $\text{CoFe}_2\text{O}_4\text{-SiO}_2$ nanocomposite*. Journal of Physical Chemistry C **112** (13), 5141–5147 (2008).
- [Pik99] C. R. Pike, A. P. Roberts, and K. L. Verosub. *Characterizing interactions in fine magnetic particle systems using first order reversal curves*. Journal of Applied Physics **85** (9), 6660–6667 (1999).
- [Pik01] C. R. Pike, A. P. Roberts, and K. L. Verosub. *First-order reversal curve diagrams and thermal relaxation effects in magnetic particles*. Geophysical Journal International **145** (3), 721–730 (2001).
- [Pik05] C. R. Pike, C. A. Ross, R. T. Scalettar, and G. Zimanyi. *First-order reversal curve diagram analysis of a perpendicular nickel nanopillar array*. Physical Review B **71** (13), 134407 (2005).
- [Pin06] A. Pineau, N. Kanari, and I. Gaballah. *Kinetics of reduction of iron oxides by H_2 - part I: Low temperature reduction of hematite*. Thermochemica Acta **447** (1), 89–100 (2006).
- [Pin07] A. Pineau, N. Kanari, and I. Gaballah. *Kinetics of reduction of iron oxides by H_2 - part II. low temperature reduction of magnetite*. Thermochemica Acta **456** (2), 75–88 (2007).
- [Pit09] K. Pitzschel, J. M. M. Moreno, J. Escrig, O. Albrecht, K. Nielsch, and J. Bachmann. *Controlled introduction of diameter modulations in arrayed magnetic iron oxide nanotubes*. ACS Nano **3** (11), 3463–3468 (2009).
- [Pit12] Kristina Pitzschel. *Magnetic nanowires and nanotubes with modulated diameters*. Dissertation, University of Hamburg, 2012.
- [Pri05] V. M. Prida, M. Hernández-Vélez, K. R. Pirota, A. Menéndez, and M. Vázquez. *Synthesis and magnetic properties of Ni nanocylinders in self-aligned and randomly disordered grown titania nanotubes*. Nanotechnology **16** (11), 2696–2702 (2005).
- [Pro99] T. Prozorov, R. Prozorov, K. V. P. M. Shafi, and A. Gedanken. *Self-organization in ferrofluids prepared by sonochemical radiation method*. Nanostructured Materials **12** (5-8), 669–672 (1999).

- [Puu05] R. L. Puurunen. *Surface chemistry of atomic layer deposition: A case study for the trimethylaluminum/water process*. Journal of Applied Physics **97** (12), 121301 (2005).
- [Ran90] R. Ranjan, R., J. S. Gau, and N. Amin. *Comparison of angular variation of coercivity in various magnetic media*. Journal of Magnetism and Magnetic Materials **89** (1-2), 38–46 (1990).
- [Rao09] C. N. R. Rao and A. Govindaraj. *Synthesis of inorganic nanotubes*. Advanced Materials **21** (42), 4208–4233 (2009).
- [Reg81] A. E. Regazzoni, G. A. Urrutia, M. A. Blesa, and A. J. G. Maroto. *Some observations on the composition and morphology of synthetic magnetites obtained by different routes*. Journal Of Inorganic & Nuclear Chemistry **43** (7), 1489–1493 (1981).
- [Ren13] K. Renger. *Die anfängliche Suszeptibilität von Eisen und Magnetit in Abhängigkeit von der Temperatur*. Dissertation, University of Zurich, 1913.
- [Rob95] A. P. Roberts, Y. L. Cui, and K. L. Verosub. *Wasp-waisted hysteresis loops: mineral magnetic characteristics and discrimination of components in mixed magnetic systems*. Journal of Geophysical Research: Solid Earth **100** (B9), 17909–17924 (1995).
- [Rob00] A. P. Roberts, C. R. Pike, and K. L. Verosub. *First-order reversal curve diagrams: a new tool for characterizing the magnetic properties of natural samples*. Journal of Geophysical Research: Solid Earth **105** (B12), 28461–28475 (2000).
- [Rob06] A. P. Roberts, Q. S. Liu, C. J. Rowan, L. Chang, C. Carvallo, J. Torrent, and C. S. Horng. *Characterization of hematite (α - Fe_2O_3), goethite (α - $FeOOH$), greigite (Fe_3S_4), and pyrrhotite (Fe_7S_8) using first-order reversal curve diagrams*. Journal of Geophysical Research: Solid Earth **111** (B12), B12S35 (2006).
- [Roo08] M. Rooth, A. Johansson, K. Kukli, J. Aarik, M. Boman, and A. Harsta. *Atomic layer deposition of iron oxide thin films and nanotubes using ferrocene and oxygen as precursors*. Chemical Vapor Deposition **14** (3-4), 67–70 (2008).
- [Ros69] R. E. Rosensweig, R. Kaiser, and G. Miskolcz. *Viscosity of magnetic fluid in a magnetic field*. Journal of Colloid and Interface Science **29** (4), 680–686 (1969).
- [Ros85] Rosensweig. *Ferrohydrodynamics*. Cambridge University Press, 1985.

- [Sal03] A. K. Salem, P. C. Searson, and K. W. Leong. *Multifunctional nanorods for gene delivery*. *Nature Materials* **2** (10), 668–671 (2003).
- [Sal11] N. Salamun, H. X. Ni, S. Triwahyono¹, A. A. Jalil, and A. H. Karim. *Synthesis and characterization of Fe₃O₄ nanoparticles by electrodeposition and reduction methods*. *Journal of Fundamental Sciences* **7** (1), 89–92 (2011).
- [Sal12] M. S. Salem, P. Sergelius, R. Zierold, J. M. M. Moreno, D. Görlitz, and K. Nielsch. *Magnetic characterization of nickel-rich NiFe nanowires grown by pulsed electrodeposition*. *Journal of Materials Chemistry* **22** (17), 8549–8557 (2012).
- [Sch18] P. Scherrer. *Bestimmung der Grösse und der inneren Struktur von Kolloidteilchen mittels Röntgenstrahlen*. *Nachrichten von der Gesellschaft der Wissenschaften zu Göttingen, Mathematisch-Physikalische Klasse* **1918**, 98–100 (1918).
- [Sch09] J. R. Scheffe, A. Frances, D. M. King, X. H. Liang, B. A. Branch, A. S. Cavanagh, S. M. George, and A. W. Weimer. *Atomic layer deposition of iron(III) oxide on zirconia nanoparticles in a fluidized bed reactor using ferrocene and oxygen*. *Thin Solid Films* **517** (6), 1874–1879 (2009).
- [Sch11] J. R. Scheffe, M. D. Allendorf, E. N. Coker, B. W. Jacobs, A. H. McDaniel, and A. W. Weimer. *Hydrogen production via chemical looping redox cycles using atomic layer deposition-synthesized iron oxide and cobalt ferrites*. *Chemistry of Materials* **23** (8), 2030–2038 (2011).
- [Sch12] S. Schrittwieser, F. Ludwig, J. Dieckhoff, K. Soulantica, G. Viau, L. Lacroix, S. M. Lentijo, R. Boubekri, J. Maynadié, A. Hütten, Hubert Brückl, and Jörg Schotter. *Modeling and development of a biosensor based on optical relaxation measurements of hybrid nanoparticles*. *ACS Nano* **6** (1), 791–801 (2012).
- [Sen97] S. P. Sena, R. A. Lindley, H. J. Blythe, C. Sauer, M. Al-Kafarji, and G. A. Gehring. *Investigation of magnetite thin films produced by pulsed laser deposition*. *Journal of Magnetism and Magnetic Materials* **176** (2-3), 111–126 (1997).
- [Ser11] Philip Sergelius. *FORC-Messungen an magnetischen Nanostab-Arrays*. Bachelor’s thesis, Physics Department, University of Hamburg, 2011.
- [She98] J. D. Sherwood and D. Durban. *Squeeze-flow of a Herschel-Bulkley fluid*. *Journal of Non-Newtonian Fluid Mechanics* **77** (1-2), 115–121 (1998).

- [Shi04] K. Shimada, S. Shuchi, T. Fujita, T. Miyazaki, A. Shibayama, and S. Kamiyama. *Newly improved magnetic compound fluid (MCF) for more stability of particle dispersion*. International Journal of Applied Electromagnetics and Mechanics **19** (1-4), 351–354 (2004).
- [Shl72] M. I. Shliomis. *Effective viscosity of magnetic suspensions*. Soviet Physics - JETP **34** (6), 1291–1294 (1972).
- [Shl80] M. I. Shliomis and Y. L. Raikher. *Experimental investigations of magnetic fluids*. IEEE Transactions on Magnetics **16** (2), 237–250 (1980).
- [Spa10] N.A. Spaldin. *Magnetic Materials*. Cambridge University Press, 2010.
- [Sto48] E. C. Stoner and E. P. Wohlfarth. *A mechanism of magnetic hysteresis in heterogeneous alloys*. Philosophical Transactions Of The Royal Society Of London Series A: Mathematical And Physical Sciences **240** (826), 599–642 (1948).
- [Sun04] L. Sun, C. L. Chien, and P. C. Searson. *Fabrication of nanoporous nickel by electrochemical dealloying*. Chemistry of Materials **16** (16), 3125–3129 (2004).
- [Sup13] Supermagnete.de. Online-Shop <http://www.supermagnete.de/Q-10-10-03-N> (20.05.2013).
- [Syo65] Y. Syono. *Magnetocrystalline anisotropy and magnetostriction of Fe_3O_4 - Fe_2TiO_4 series—with special application to rock magnetism*. Japanese Journal of Geophys **4**, 71–143 (1965).
- [Tad10] T.F. Tadros. *Rheology of Dispersions*. Wiley, 2010.
- [Tan91] Z. X. Tang, C. M. Sorensen, K. J. Klabunde, and G. C. Hadjipanayis. *Size-dependent curie-temperature in nanoscale $MnFe_2O_4$ particles*. Physical Review Letters **67** (25), 3602–3605 (1991).
- [Tan12] B. M. Tanygin, V. F. Kovalenko, M. V. Petrychuk, and S. A. Dzyan. *Molecular dynamics study of the primary ferrofluid aggregate formation*. Journal of Magnetism and Magnetic Materials **324** (23), 4006–4010 (2012).
- [Tao01] R. Tao. *Super-strong magnetorheological fluids*. Journal of Physics: Condensed Matter **13** (50), R979–R999 (2001).
- [Tej09] A. S. Teja and P. Y. Koh. *Synthesis, properties, and applications of magnetic iron oxide nanoparticles*. Progress in Crystal Growth and Characterization of Materials **55** (1-2), 22–45 (2009).

- [Thu03] S. Thurm and S. Odenbach. *Particle size distribution as key parameter for the flow behavior of ferrofluids*. *Physics of Fluids* **15** (6), 1658–1664 (2003).
- [Tir80] M. M. Tirado and J. G. de la Torre. *Rotational-dynamics of rigid, symmetric top macromolecules: application to circular cylinders*. *Journal of Chemical Physics* **73** (4), 1986–1993 (1980).
- [Tir84] M. M. Tirado, C. L. Martínez, and J. G. de la Torre. *Comparison of theories for the translational and rotational diffusion-coefficients of rod-like macromolecules: application to short DNA fragments*. *Journal of Chemical Physics* **81** (4), 2047–2052 (1984).
- [Tom07] E. Tombácz, E. Illés, A. Majzik, A. Hajdú, N. Rideg, and M. Szekeres. *Ageing in the inorganic nanoworld: example of magnetite nanoparticles in aqueous medium*. *Croatica Chemica Acta* **80** (3-4), 503–515 (2007).
- [Uli10] J. C. Ulicny, K. S. Snavely, M. A. Golden, and D. J. Klingenberg. *Enhancing magnetorheology with nonmagnetizable particles*. *Applied Physics Letters* **96** (23), 231903 (2010).
- [vdH96] P. A. A. van der Heijden, P. J. H. Bloemen, J. M. Gaines, J. T. W. M. van Eemeren, R. M. Wolf, P. J. van der Zaag, and W. J. M. de Jonge. *Magnetic interface anisotropy of MBE-grown ultra-thin (001)Fe₃O₄ layers*. *Journal of Magnetism and Magnetic Materials* **159** (3), L293–L298 (1996).
- [vdZ96] P. J. van der Zaag, W. F. J. Fontijn, P. Gaspard, R. M. Wolf, V. A. M. Brabers, R. J. M. van de Veerdonk, and P. A. A. van der Heijden. *A study of the magneto-optical Kerr spectra of bulk and ultrathin Fe₃O₄*. *Journal of Applied Physics* **79** (8), 5936–5938 (1996).
- [Ver39] E. J. W. Verwey. *Electronic conduction of magnetite (Fe₃O₄) and its transition point at low temperatures*. *Nature* **144**, 327–328 (1939).
- [Vic87] R. H. Victora. *Quantitative theory for hysteretic phenomena in CoNi magnetic thin-films*. *Physical Review Letters* **58** (17), 1788–1791 (1987).
- [Vic89] R. H. Victora. *Predicted time-dependence of the switching field for magnetic-materials*. *Physical Review Letters* **63** (4), 457–460 (1989).
- [Voo98] F. C. Voogt, T. T. M. Palstra, L. Niesen, O. C. Rogojanu, M. A. James, and T. Hibma. *Superparamagnetic behavior of structural domains in epitaxial ultrathin magnetite films*. *Physical Review B* **57** (14), R8107–R8110 (1998).

- [Wal02] F. Walz. *The Verwey transition—a topical review*. Journal of Physics: Condensed Matter **14** (**12**), R285–R340 (2002).
- [Wan91] H. Wan and G. C. Hadjipanayis. *Thickness dependence of coercivity in CoNi thin-films*. Journal of Applied Physics **70** (**10**), 6059–6061 (1991).
- [Wan08] N. Wang, Y. Cai, and R. Q. Zhang. *Growth of nanowires*. Materials Science and Engineering: Reports **60** (**1-6**), 1–51 (2008).
- [Wan09] Z. X. Wang, L. M. Wu, M. Chen, and S. X. Zhou. *Facile synthesis of superparamagnetic fluorescent Fe_3O_4/ZnS hollow nanospheres*. Journal of the American Chemical Society **131** (**32**), 11276–+ (2009).
- [Wel95] D. Weller, J. Stöhr, R. Nakajima, A. Carl, M. G. Samant, C. Chappert, R. Megy, P. Beauvillain, P. Veillet, and G. A. Held. *Microscopic origin of magnetic-anisotropy in Au/Co/Au probed with X-ray magnetic circular-dichroism*. Physical Review Letters **75** (**20**), 3752–3755 (1995).
- [Wen84] L. E. Wenger and J. A. Mydosh. *Nonuniqueness of $H^{2/3}$ and H^2 field-temperature transition lines in spin-glasses*. Physical Review B **29** (**7**), 4156–4158 (1984).
- [Wer06] N. M. Wereley, A. Chaudhuri, J. H. Yoo, S. John, S. Kotha, A. Suggs, R. Radhakrishnan, B. J. Love, and T. S. Sudarshan. *Bidisperse magnetorheological fluids using Fe particles at nanometer and micron scale*. Journal of Intelligent Material Systems and Structures **17** (**5**), 393–401 (2006).
- [Whi93] T. M. Whitney, J. S. Jiang, P. C. Searson, and C. L. Chien. *Fabrication and magnetic-properties of arrays of metallic nanowires*. Science **261** (**5126**), 1316–1319 (1993).
- [Wie06] A. Wiedenmann, U. Keiderling, R. P. May, and C. Dewhurst. *Dynamics of field-induced ordering processes in ferrofluids studied by polarised small-angle neutron scattering*. Physica B: Condensed Matter **385–386** (**Part 1**), 453–456 (2006).
- [Wil95] W. Williams and D. J. Dunlop. *Simulation of magnetic hysteresis in pseudo-single-domain grains of magnetite*. Journal of Geophysical Research: Solid Earth **100** (**B3**), 3859–3871 (1995).
- [Wil96] G. Wilde, G. P. Görlner, and R. Willnecker. *Hypercooling of completely miscible alloys*. Applied Physics Letters **69** (**20**), 2995–2997 (1996).
- [Wu06] Zhenyu Wu. *Synthesis and Magnetoviscosity of Nanotube and Nanorod Ferrofluids*. Master’s thesis, Ulm University, 2006.

- [Wu10a] W. Wu, X. H. Xiao, S. F. Zhang, J. A. Zhou, L. X. Fan, F. Ren, and C. Z. Jiang. *Large-scale and controlled synthesis of iron oxide magnetic short nanotubes: Shape evolution, growth mechanism, and magnetic properties*. Journal of Physical Chemistry C **114** (**39**), 16092–16103 (2010).
- [Wu10b] Z. Y. Wu, A. Mueller, S. Degenhard, S. E. Ruff, F. Geiger, A. M. Bittner, C. Wege, and C. E. Krill. *Enhancing the magnetoviscosity of ferrofluids by the addition of biological nanotubes*. ACS Nano **4** (**8**), 4531–4538 (2010).
- [Wu10c] Z. Y. Wu, R. Zierold, A. Mueller, S. E. Ruff, C. C. Ma, A. A. Khan, F. Geiger, B. A. Sommer, M. Knez, K. Nielsch, A. M. Bittner, C. Wege, and C. E. Krill. *Preparation and magnetoviscosity of nanotube ferrofluids by viral scaffolding and ALD on porous templates*. Physica Status Solidi B: Basic Solid State Physics **247** (**10**), 2412–2423 (2010).
- [Wu11] Zhenyu Wu. *Preparation and Characterization of Nanotube Ferrofluids by Template-Directed Methods*. Dissertation, Ulm University, 2011.
- [Yan11] Y. Yang, J. B. Yi, X. L. Huang, J. M. Xue, and J. Ding. *High-coercivity in α - Fe_2O_3 formed after annealing from Fe_3O_4 nanoparticles*. IEEE Transactions on Magnetics **47** (**10**), 3340–3342 (2011).
- [Yoo10] M. Yoon and D. Tománek. *Equilibrium structure of ferrofluid aggregates*. Journal of Physics: Condensed Matter **22** (**45**), 455105 (2010).
- [Yue11] Z. G. Yue, W. Wei, Z. X. You, Q. Z. Yang, H. Yue, Z. G. Su, and G. H. Ma. *Iron oxide nanotubes for magnetically guided delivery and pH-activated release of insoluble anticancer drugs*. Advanced Functional Materials **21** (**18**), 3446–3453 (2011).
- [Zak92] M. I. Zaki, S. A. A. Mansour, F. Taha, and G. A. H. Mekheimer. *Chromia on silica and alumina catalysts - surface structural consequences of interfacial events in the impregnation course of aquated Cr(III) ions*. Langmuir **8** (**2**), 727–732 (1992).
- [Zep89] W. B. Zeper, F. J. A. M. Greidanus, P. F. Carcia, and C. R. Finchner. *Perpendicular magnetic-anisotropy and magneto-optical Kerr effect of vapor-deposited Co/Pt-layered structures*. Journal of Applied Physics **65** (**12**), 4971–4975 (1989).
- [Zha98] Y. D. Zhang, J. I. Budnick, W. A. Hines, C. L. Chien, and J. Q. Xiao. *Effect of magnetic field on the superparamagnetic relaxation in granular Co-Ag samples*. Applied Physics Letters **72** (**16**), 2053–2055 (1998).

- [Zha01] Y. P. Zhao, R. M. Gamache, G. C. Wang, T. M. Lu, G. Palasantzas, and J. T. M. De Hosson. *Effect of surface roughness on magnetic domain wall thickness, domain size, and coercivity*. Journal of Applied Physics **89** (2), 1325–1330 (2001).
- [Zhu12] X. C. Zhu, X. J. Jing, and L. Cheng. *Magnetorheological fluid dampers: a review on structure design and analysis*. Journal of Intelligent Material Systems and Structures **23** (8), 839–873 (2012).
- [Zie11] R. Zierold, Z. Y. Wu, J. Biskupek, U. Kaiser, J. Bachmann, C. E. Krill, and K. Nielsch. *Magnetic, multilayered nanotubes of low aspect ratios for liquid suspensions*. Advanced Functional Materials **21** (2), 226–232 (2011).
- [Zub92] A. Y. Zubarev. *On the theory of magnetic fluids with chain-like aggregates*. Magnetohydrodynamics **28** (1), 18–23 (1992).
- [Zub00] A. Y. Zubarev and L. Y. Iskakova. *Effect of chainlike aggregates on dynamical properties of magnetic liquids*. Physical Review E **61** (5), 5415–5421 (2000).
- [Zub02] A. Y. Zubarev, S. Odenbach, and J. Fleischer. *Rheological properties of dense ferrofluids. Effect of chain-like aggregates*. Journal of Magnetism and Magnetic Materials **252** (1-3), 241–243 (2002).
- [Zub05] A. Y. Zubarev, J. Fleischer, and S. Odenbach. *Towards a theory of dynamical properties of polydisperse magnetic fluids: effect of chain-like aggregates*. Physica A: Statistical Mechanics and Its Applications **358** (2-4), 475–491 (2005).
- [Zub06] A. Y. Zubarev and L. Y. Iskakova. *Rheological properties of ferrofluids with microstructures*. Journal of Physics: Condensed Matter **18** (38), S2771–S2784 (2006).
- [Zys04] R. D. Zysler, M. V. Mansilla, and D. Fiorani. *Surface effects in α - Fe_2O_3 nanoparticles*. European Physical Journal B **41** (2), 171–175 (2004).

A Appendix

A.1 Templated Synthesis & Structural Investigation

Anodization Setup

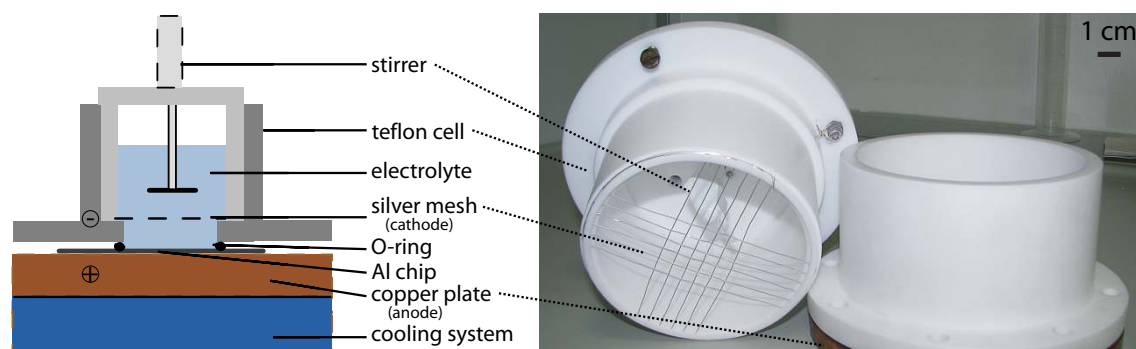


Figure A.1: Scheme (left) of the anodization cell and a photograph (right) of the scaled-up version used in this work. The major components of the setup are labeled. The scale-up of the anodization cell allows for the preparation of 600 billion nanotubes in one batch.

Length control of pores in anodic alumina via time

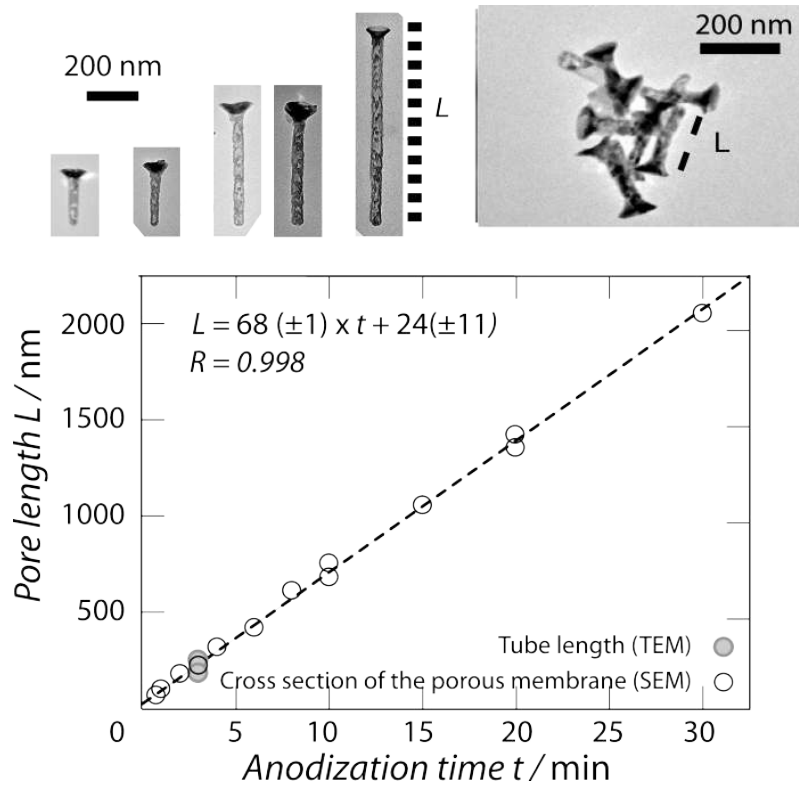


Figure A.2: Plot of the pore and tube length L as a function of anodization time t . The linear relationship amounts to $(68 \pm 1) \text{ nm min}^{-1}t + (24 \pm 11) \text{ nm}$ and allows for setting the tube length by controlling the time. A TEM micrograph of released nanotubes and a selection of individual nanotubes are presented on top of the figure. The nanotubes were prepared in an early state of the thesis, thus showing a nail-head structure since no pore-widening was applied.(section 3.4)

Home-made reduction setup

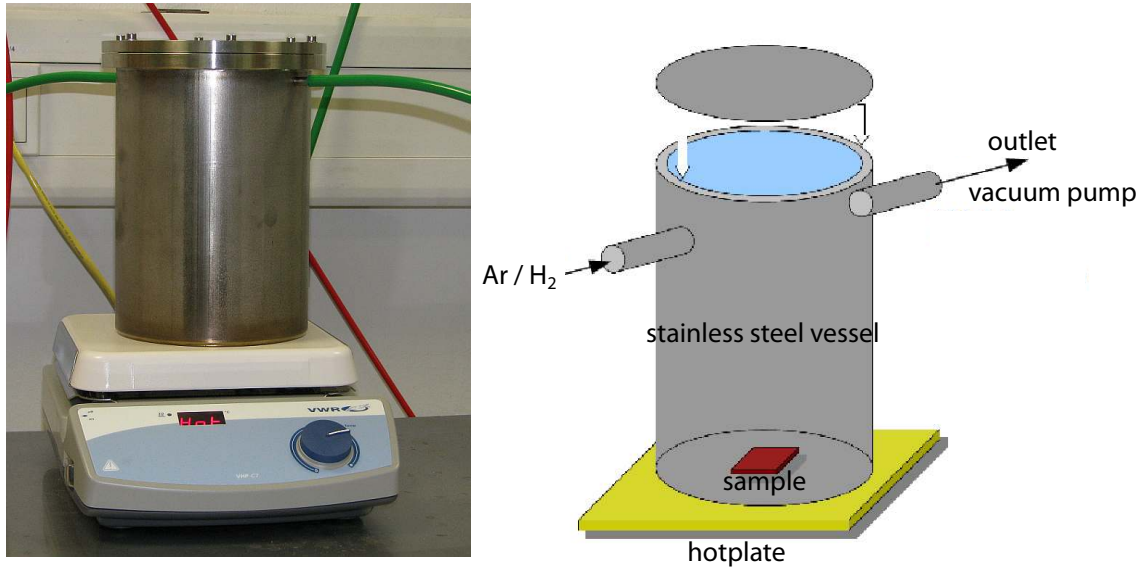


Figure A.3: Photograph (a) and schematic drawing (b) of the home-made reduction oven consisting of an O-ring sealed stainless steel vessel which is placed on a hot plate to provide the elevated temperatures needed for the reduction. (b) Scheme of the setup.

Figure A.3 displays a photograph (a) as well as schematic sketch (b) of this setup. A stainless steel vessel constructed by the mechanical workshop (Physics Department, University of Hamburg) was connected to a needle valve which allowed for the flow control of the forming gas. A argon/hydrogen mixture with a volume ratio of 95 to 5 was used as reduction atmosphere. Prior the start of the reduction process, the stainless steel vessel was evacuated by a rotary vane pump and subsequently filled with the forming gas up to atmospheric pressure. The flow rate of the argon/hydrogen was set to (160 ± 10) ccm determined by a standard ball type flow meter until the complete process was finished. To start the reduction the vessel was placed on a hot plate heated to $400\text{ }^{\circ}\text{C}$ (set) temperature. After one hour the vessel was removed from the hot plate and put on a steel block to quench the reduction.

In-Situ XRD analysis of iron oxide thin films

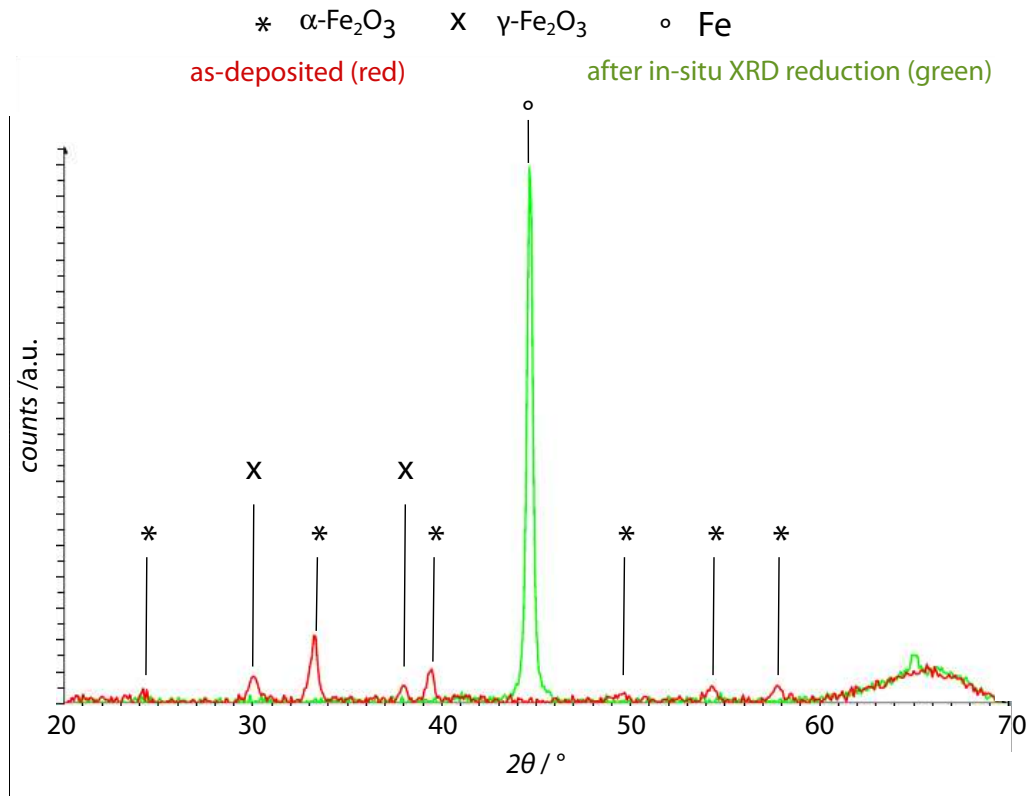


Figure A.4: $\Theta/2\Theta$ XRD measurement of an as-deposited iron oxide thin film (deposition temperature 230 °C, thickness 45 nm) (red) and a complete reduced sample after the in-situ experiment (green). The as-deposited sample consists of a mixture of hematite (JCPDS 80-2377) and maghemite (JCPDS 39-1346), the converted sample is pure iron (JCPDS 87-0721)

Reactive Ion Etching to remove interconnects

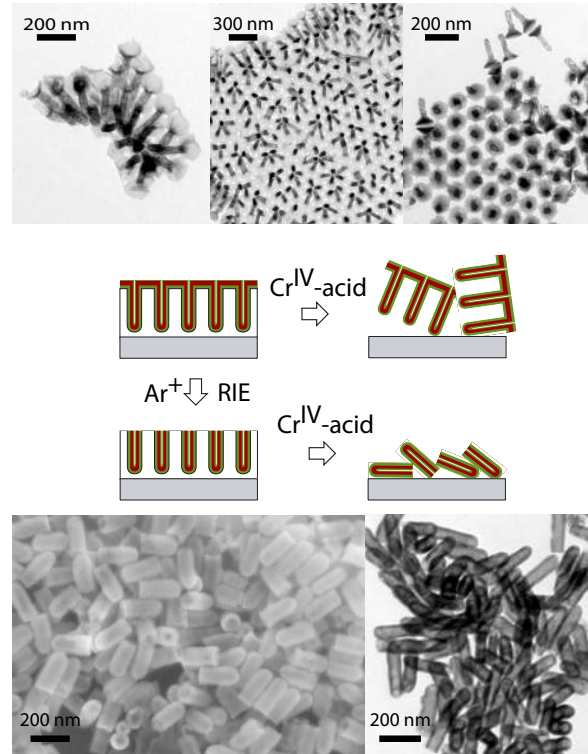


Figure A.5: TEM micrographs of released nanotubes are displayed at the top and the bottom of the figure. The middle panel shows a scheme which clarifies the importance of the dry etching procedure. In the first row, neither a silica RIE process nor Ar⁺ sputtering is applied to the nanotubes embedded in the membrane. Releasing the still interconnected nanotubes from the template results in large blocks and clusters (shown in the micrographs on top of the scheme) which do not allow for a homogeneous dispersion of nanotubes necessary for further fluid-mechanical characterization. In contrast, applying the dry etching processes allows for the synthesis of separated nanotubes which can be well dispersed in a carrier medium as schematically shown in the lower row of the scheme and proven by TEM micrographs displayed at the bottom of the figure. Please note that the lower images are taken at a later point of the thesis. Pore-widening and optimized reduction process parameters lead to a straight tube with a homogeneously coated iron oxide layer along the tube.

HR-TEM analysis of a single magnetite nanotube

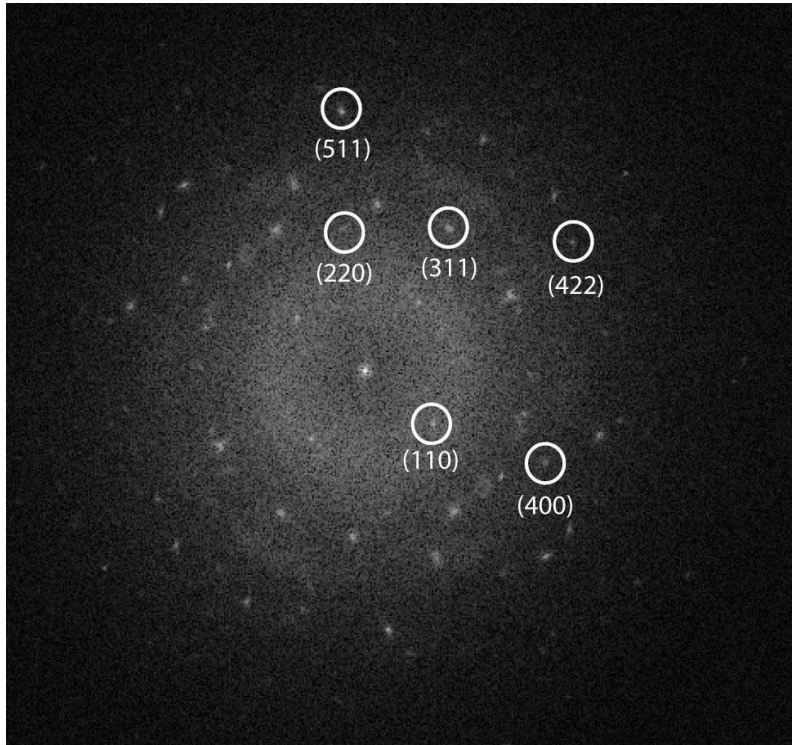


Figure A.6: The spots in the Fast Fourier transform pattern of the HR-TEM image in figure 3.18 (c) reveal a polycrystalline structure within a single nanotube.

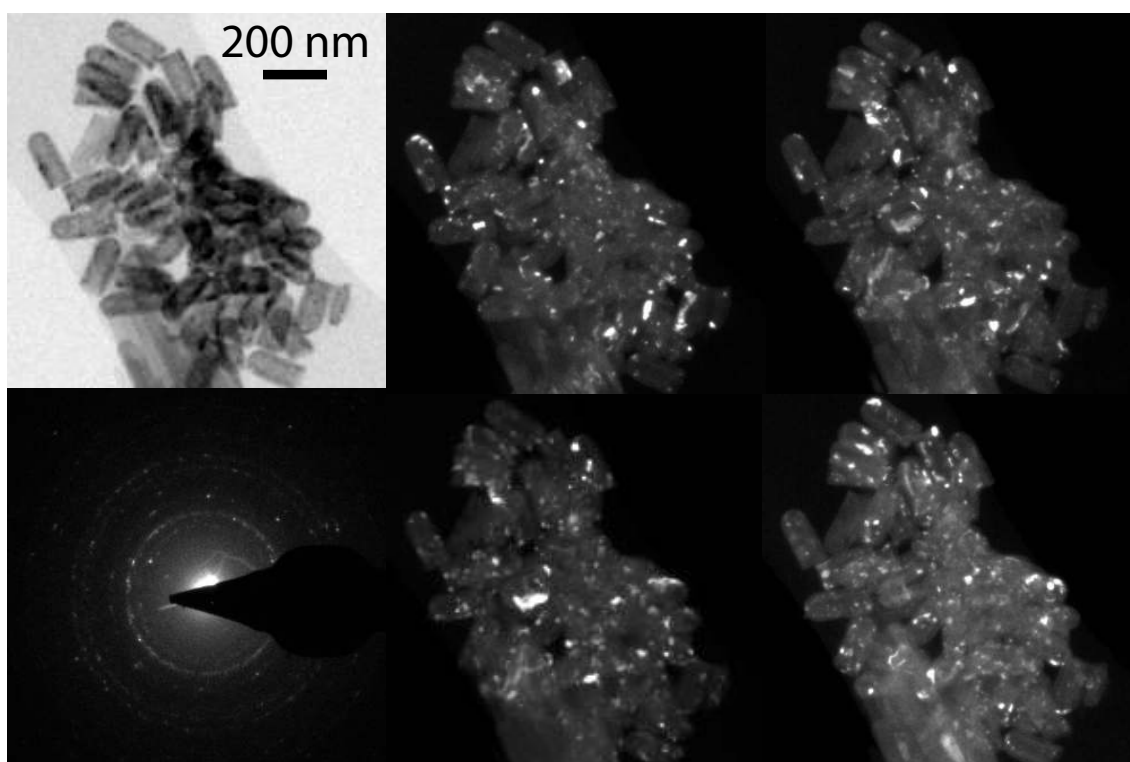


Figure A.7: The original dark-field micrographs of figure 3.21. Reference is made to section 3.4 for a detailed discussion.

Selective Copper Dissolution

The selective copper etching bases on the US patent "Methods for etching a less reactive material in the presence of a more reactive material".[Jag94] Therein, the selectivity of the etchant is proven at the example of copper and cobalt; but it works for selective copper etching in the presence of nickel in the same way (Figure A.8).

Both, copper and nickel, are exposed to a non-oxidative (water-free) solution based on isopropyl alcohol. The etchant contains Cu^{2+} from a copper salt (copper (II) tetra fluoroborate) and a complexing agent (cis-2-butene-1,4-diol) drawn as CA in the scheme. A stable Cu^+ -Complex is formed by a one-electron-transfer process from the metallic copper to the Cu^{2+} ions in suspension. Thereby, Cu^+ from the metallic Cu goes into the environmental etching solution.

Since a mono-cationic state of nickel—even in a complexed state—is energetically not likely in this etching solution, the dissolution due to a one-electron-transfer is not possible. Thus, the etchant works with a high selectivity.

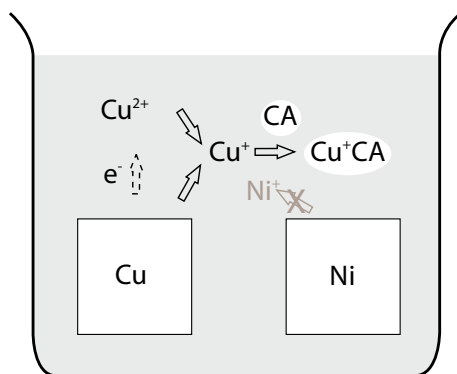


Figure A.8: Scheme of the chemical processes involved in the selective dissolution of copper.

A.2 Physical Properties of Particles and Ferrofluids

Shape Functions of Prolate Spheroids

Nanorods are often assumed as prolate spheroids in a first approximation. Shape correction terms were calculated by Brenner as well as Ilg and co-workers. Other approaches directly assumed cylindrical objects and found numerical correction values. Herein, only the solutions of the different approaches are presented without a detailed derivation of them. Reference is made to the corresponding literature for detailed information. [Bre74] [Tir84] [Ilg02] [Ilg03]

$$c_n^{\text{Ilg,spheroid}} = \frac{2}{3} \left(1 - \frac{1}{n^4}\right) n^2 \left[\frac{2n^2 - 1}{2n\sqrt{n^2 - 1}} \ln \left(\frac{n + \sqrt{n^2 - 1}}{n - \sqrt{n^2 - 1}} \right) - 1 \right]^{-1} \quad (\text{A.1})$$

$$c_n^{\text{Brenner,spheroid}} = \frac{1}{6} \cdot \frac{(2 \ln n - \ln 4 + 1)(n^2 + 1)}{6(\ln n)^2} \quad (\text{A.2})$$

$$c_n^{\text{Brenner,cylinder}} = \frac{2}{9} \left(\frac{n^2}{\ln n} + \frac{n^2}{(\ln n)^2} (\ln 2 - 1) + \frac{3L}{8\pi} \right) \quad (\text{A.3})$$

L denotes a numerical constant which critically depends on the exact end of the cylinder: for a circular, blunt-ended cylinder an experimentally determined value amounts to $L \approx 5.45$.

$$c_n^{\text{Tirado,cylinder}} = \frac{1}{3} n^2 \left(\ln n - 0.662 + \frac{0.917}{n} - \frac{0.05}{n^2} \right)^{-1} \quad (\text{A.4})$$

High-Field Magnetization Isotherms of Superparamagnetic Nanotubes

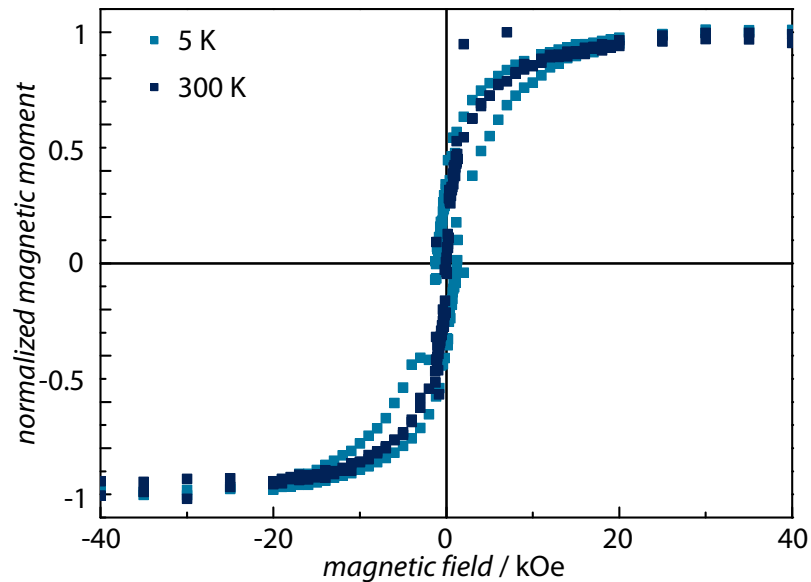


Figure A.9: High-field magnetization isotherms of a dried superparamagnetic nanotube suspension taken at 5 K and 300 K. Saturation could be reached in magnetic field larger than 20 kOe. At elevated temperatures coercivity and remanence vanish, thus indicating superparamagnetic behavior. It seems that the magnetization isotherm at 5 K displays a wasp-waisted shape. Such curves can be caused by a broad distribution of particle/grain sizes and are discussed in section 4.2

SQUID Magnetization Isotherms of the Reference Ferrofluid

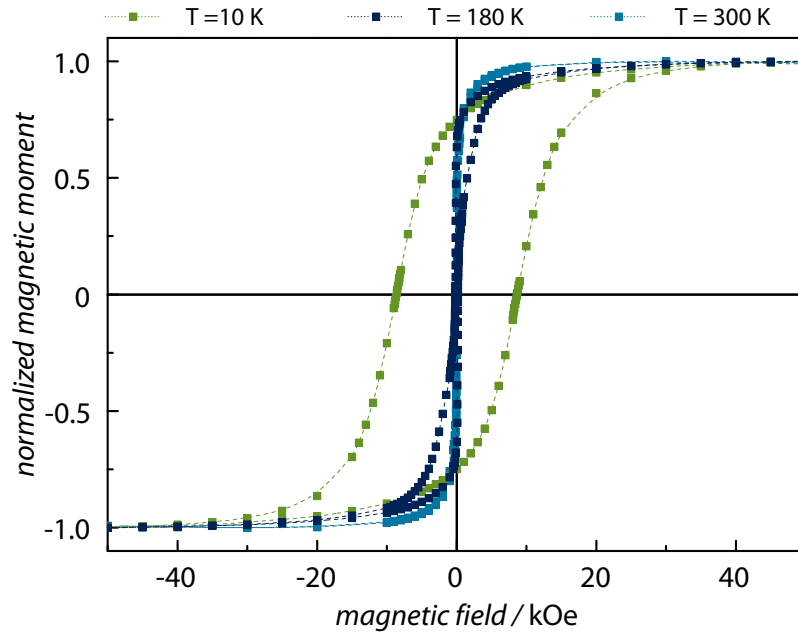


Figure A.10: Complete magnetization isotherms of figure 4.3 measured at different temperatures (green 10 K, dark blue 180 K, bright blue 300 K). The dashed lines serve as guide to the eyes.

Stabilization of Nanotube Ferrofluids

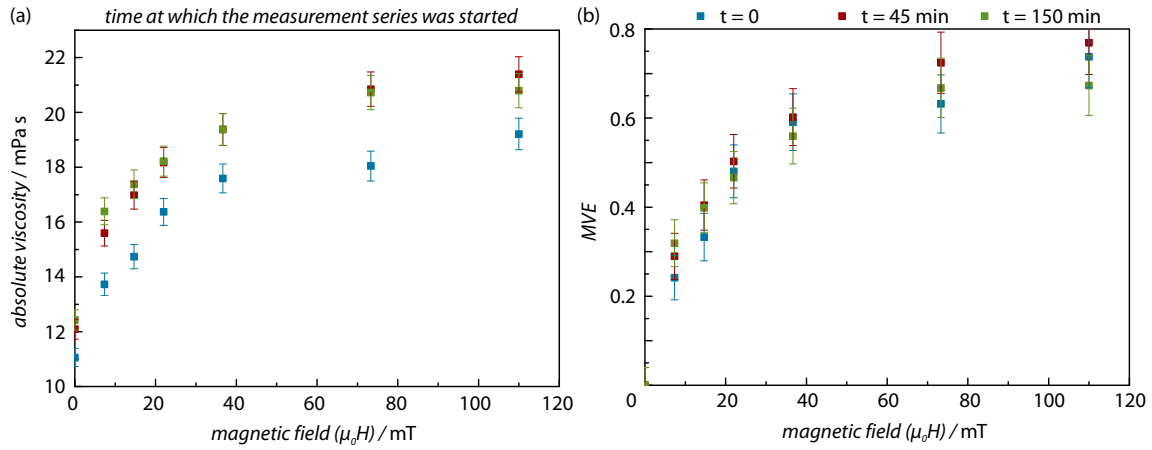


Figure A.11: Viscosity measurements (a) at three different times and the calculated MVE (b) of an iron oxide nanotube liquid suspension (length (380 ± 20) nm, diameter (65 ± 10) nm, iron oxide wall thickness (8 ± 2) nm). A shift can be observed in the viscosity measurements, whereas the calculated MVE behavior stays almost constant.

Iron Oxide Nanotubes

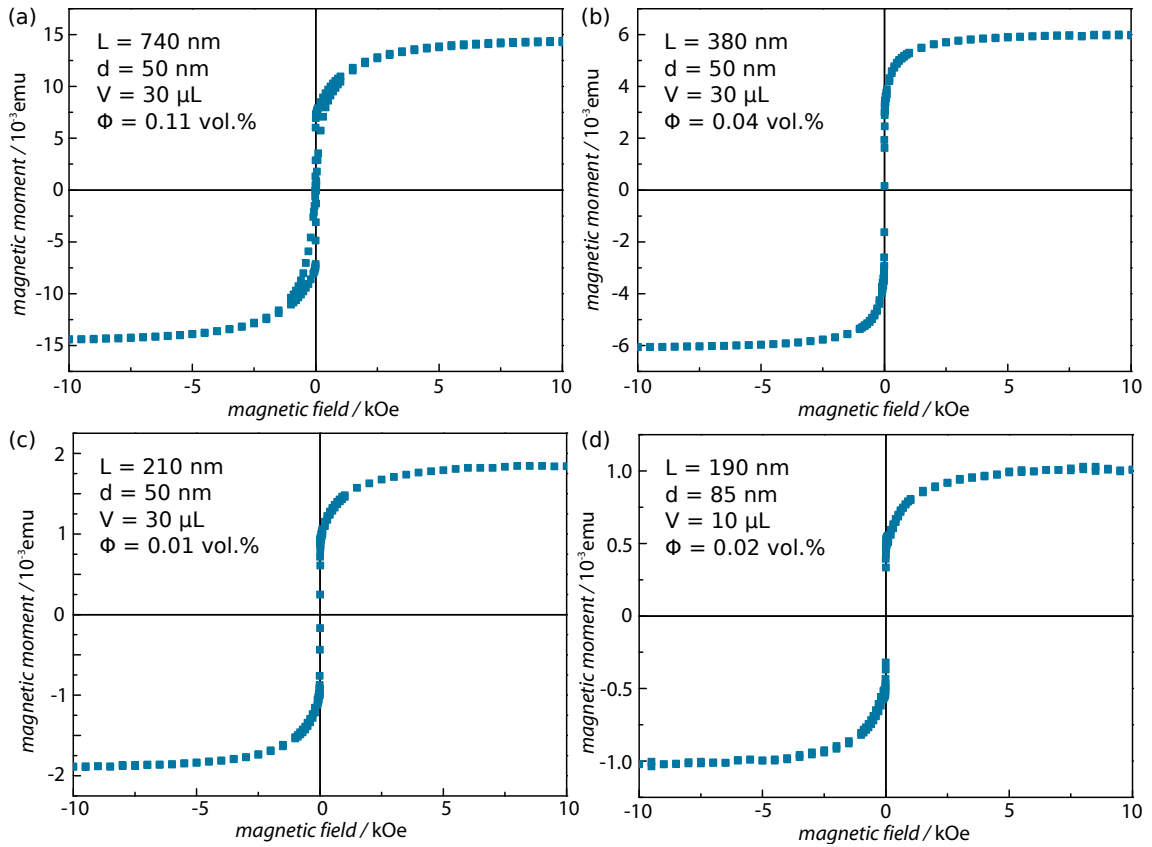


Figure A.12: SQUID magnetization isotherms of various iron oxide nanotubes suspensions. The saturation magnetic moment was used to estimate the volume concentration of the nanotube ferrofluidic suspensions.

MVE of Superparamagnetic Nanotubes

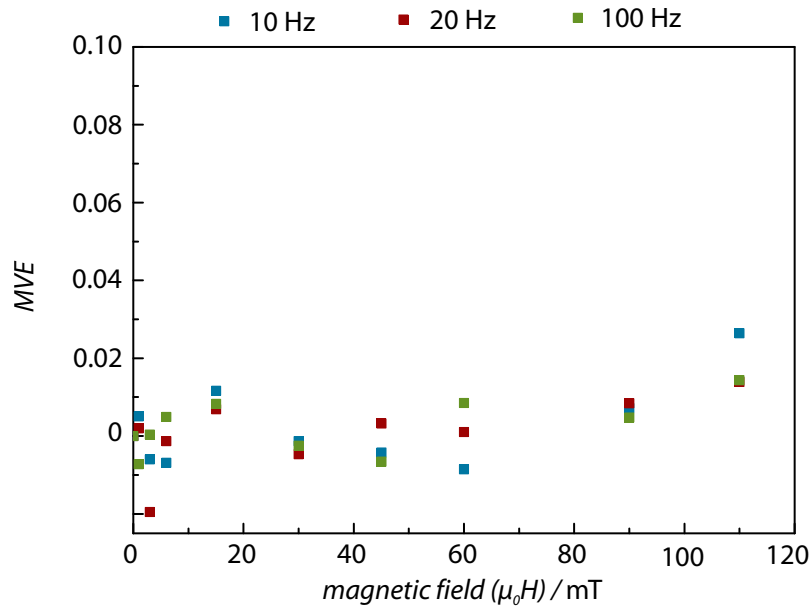


Figure A.13: The determined MVE of a superparamagnetic nanotube suspension as a function of the applied magnetic determined at three different shear frequencies. No response onto a magnetic field can be observed in such kind of liquid suspension. The error of the MVE bases on the reproducibility of the viscosity and amounts to $\Delta MVE \approx 0.04$

Shear Thinning Effect

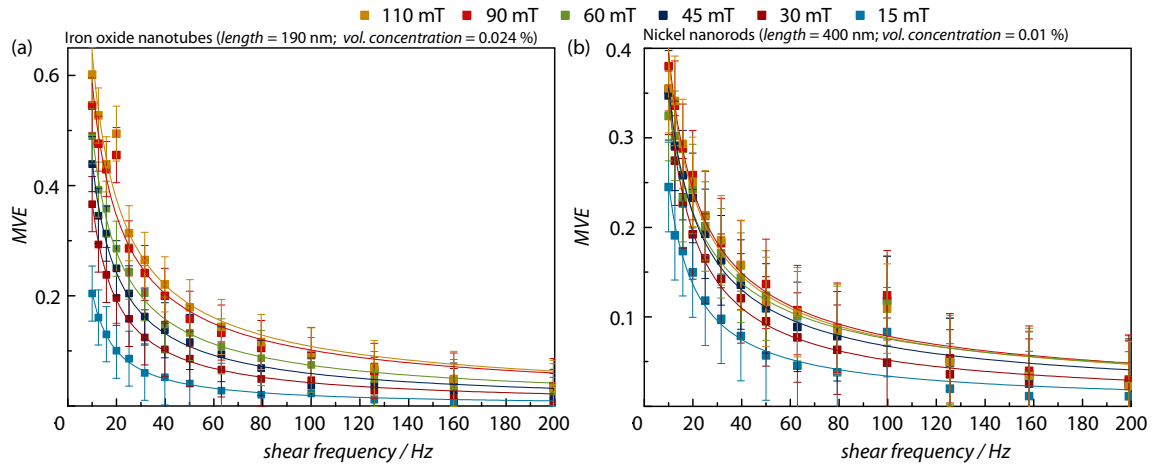


Figure A.14: Plot of the shear frequency-dependent MVE of (a) an iron oxide nanotube and (b) a nickel nanorod suspension at various magnetic fields. The lines drawn are fits corresponding to a power-law function (according to equation 2.26).

Danksagung

Zu guter Letzt möchte ich mich an dieser Stelle bei all den Menschen bedanken, ohne die diese Arbeit nicht entstanden wäre. Ich bedanke mich bei:

Prof. Kornelius Nielsch für die Betreuung der Arbeit und die vielen, vielen Möglichkeiten, die er mir während meiner Doktorandenzeit geboten hat. Außerdem möchte ich ihm an diese Stelle nochmal explizit danken, dass er mich aus Halle nach Hamburg mitgenommen hat.

Prof. Julien Bachmann, der gerade am Anfang immer für mich da war, von dem ich viel gelernt habe und der immer, wenn ich Rat gebraucht habe, ein offenes Ohr hatte.

Prof. Carl E. Krill III (Universität Ulm) für die Leihgabe des PMAV-Setups.

Dr. Josep M. Montero Morono und Dr. Detlef Görlitz für die vielen wissenschaftlichen Diskussionen aber auch aufbauenden Worte, wenn man gerade einmal in einem Tief steckte.

Dr. Zhenyu Wu für die PMAV Messungen zu Beginn der Arbeit und dann elektronischer Fernunterstützung als die kleineren oder größeren Probleme auftraten.

Reinhold Meißner, der E-Werkstatt, der mechanischen Werkstatt sowie dem Heliumteam für das Lösen der kleinen und großen technischen Probleme.

der Transmissionselektronmikroskopie-Arbeitsgruppe von Prof. Ute Kaiser (Universität Ulm) und vor allem Dr. Johannes Biskupek.

Dr. Jolien Dendooven aus der Arbeitsgruppe von Christoph Detavernier (Universität Ghent) für die in-situ XRD-Messungen.

Philip und Tim für die FORC-Messungen.

Soham Banerjee (und dem DAAD für die Bereitstellung der Finanzierung) für seine Arbeit an den Nickelnanostäbchen.

Rene Faust und Charlie Le Lam die mit ihrer Bachelor- bzw. Masterarbeit einen Beitrag zu dieser Dissertation geleistet haben.

Ole, der mich damals in Hamburg willkommen geheißen hat, mich in den Magnetismus einführte und mit dem ich viele lustige Stunden Schreibtisch an Schreibtisch oder auf dem Rad verbracht habe.

Stephan für die klaren Erläuterungen zur Physik, ohne die ich wahrscheinlich noch manches Problem wälzen würde.

Martin für seine Designkünste, sein Englisch, dafür, dass er da war, als man ihn brauchte und dafür, dass man sich immer auf ihn verlassen konnte.

Maik, Kathrin, Thomas, Falk, Tina, Sonja, Tim, William, Christian, Sebastian, Jojo und Michi für die vielen schönen Momente während der Arbeit und/oder für die Stunden der Ablenkung und des Energiesammelns.

Karo und Alex. Es ist gut zu wissen, dass es euch gibt.

Kerstin, dafür dass es dich in meinem Leben gibt und vor Allem für die Geduld und das Verständnis in den letzten Wochen der Arbeit.

meinen Eltern Gundula und Andreas sowie meinen Geschwistern Cora und Konrad, dafür dass sie immer an mich geglaubt haben und mich immer unterstützt haben, ohne Wenn und Aber.

Für meine Großeltern Ruth und Kurt